The Pennsylvania State University
The Graduate School
Intercollege Graduate Program in Materials

PHASE DIAGRAMS FOR GUIDING SILICON THIN FILM DEPOSITION IN PHOTOVOLTAICS APPLICATIONS AS DERIVED BY REAL TIME SPECTROSCOPIC ELLIPSOMETRY

A Thesis in

Materials

by

Andre Santarosa Ferlauto

© 2001 Andre Santarosa Ferlauto

Submitted in Partial Fulfillment
of the Requirements
for the Degree of

Doctor of Philosophy

December 2001

We approve the thesis of Andre Santarosa Ferlauto.

Date of Signature

Robert W. Collins
Professor of Physics and Materials Research
Thesis Co-Adviser
Chair of Committee

Christopher R. Wronski
Leonhard Professor of Microelectronic Devices and Materials
Thesis Co-Adviser

Thomas N. Jackson
Professor of Electrical Engineering

Russell Messier
Professor of Engineering Science and Mechanics

Barbara A. Shaw
Associate Professor of Engineering Science and Mechanics
Chair of the Intercollege Graduate Program in Materials

ABSTRACT

Real time spectroscopic ellipsometry measurements of the evolution of the microstructural and optical properties of hydrogenated silicon (Si:H) films during growth have been applied to develop deposition phase diagrams. These diagrams provide guidance for the optimization of rf plasma-enhanced chemical vapor deposition (PECVD) of hydrogenated amorphous silicon (a-Si:H) films for applications in high performance, high stability solar cells. In the deposition phase diagrams, transitions lines are drawn that identify the bulk layer thicknesses (d_b) separating different film growth regimes as a function of one key deposition variable. The identified transitions include (i) an onset of surface roughening from a stable-surface growth regime such that the Si:H film is amorphous on both sides of the onset [a→a]; (ii) an onset of surface roughening associated with the nucleation of Si microcrystals, leading to a mixed-phase growth regime [a→(a+μc)]; and (iii) an onset of surface smoothening associated with the coalescence of the microcrystals, leading to a single-phase microcrystalline Si:H (μc-Si:H) growth regime [(a+μc)→μc].

RTSE measurements of several Si:H film depositions, complemented by atomic force microscopy (AFM) images were employed in investigations of the physical mechanisms underlying such transitions. Using such insights, the deposition phase diagrams were applied in studies of the effect of H_2-dilution and substrate on Si:H layer deposition. Comparisons of the phase diagrams and solar cell performance results have indicated that optimum rf PECVD of a-Si:H intrinsic layers (i-layers) is performed in the amorphous growth regime with the maximum possible H_2-dilution level $R=[H_2]/[SiH_4]$ while avoiding the amorphous-to-(mixed-phase microcrystalline) transition [a→(a+μc)]. Furthermore, optimization requires the largest possible thickness onset for the roughening transition detected in the amorphous regime [a→a], thus ensuring film growth with a smooth, stable surface throughout deposition of a relatively thick layer (>1000Å).

The phase diagrams were also applied in investigations of the effects of the rf PECVD parameters on Si:H film growth in order to obtain insights into i-layer deposition processes at high rates. The phase diagram results indicate that increases in rf plasma power lead to detrimental effects on film growth, and that a moderate increase in substrate temperature exerts only a weak reversal of the effects of high power due in part to a shift of the a→(a+μc) transition to lower R. In contrast, increases in the total gas pressure lead to a shift of the a→(a+μc) transition to much larger R values. As a result, a large window opens in R, whereby the films are amorphous and exhibit smooth, stable surfaces up to relatively large d_b values (d_b>2000 Å). These results suggest that the total gas pressure, together with the H_2-dilution can be used in the optimization of Si:H PECVD processes at higher rates.

A database for the optical properties of the different materials used in multijunction a-Si:H-based solar cells was also established. In most cases, the optical functions of the different materials were described in terms of simple analytical expressions based on a few physically-relevant, wavelength-independent parameters. In particular, new analytical expressions have been developed for the optical functions of amorphous semiconductor absorber layers and doped microcrystalline layers. It was shown that for a set of high electronic quality thin films, including intrinsic a-Si:H and its alloys with Ge and C, the optical properties throughout the visible range can be described in terms of a single parameter, the optical band-gap.

TABLE OF CONTENTS

LIST OF FIGURES **viii**

LIST OF TABLES **xx**

ACKNOWLEDGEMENTS **xxi**

CHAPTER 1 INTRODUCTION **1**

1.1 BACKGROUND 1

1.2 THESIS OBJECTIVES 4

1.3 THESIS ORGANIZATION 6

CHAPTER 2 REAL TIME SPECTROSCOPIC ELLIPSOMETRY **8**

2.1 INTRODUCTION 8

2.2 BASICS OF ELLIPSOMETRY 10

2.2.1 Polarized light 10

2.2.2 Reflection from multilayer thin films 11

2.2.3 Effective medium theories 16

2.3 ROTATING-COMPENSATOR MULTICHANNEL ELLIPSOMETER 17

2.3.1 Instrument set-up 17

2.3.2 Data Acquisition and Reduction 18

2.3.3 Calibration of compensator retardance 26

2.4 DATA ANALYSIS 31

2.4.1 Least-squares regression analysis 31

2.4.2 Mathematical inversion 33

2.4.3 Global $\overline{\sigma}$-minimization method for RTSE data analysis 34

CHAPTER 3 MICROSTRUCTRAL EVOLUTION IN Si:H THIN FILM GROWTH **42**

3.1 INTRODUCTION 42

3.2 DEPOSITION PROCESSES OF Si:H FILMS 44

3.3 EXPERIMENTAL DETAILS 49

3.4 OVERVIEW OF MICROSTRUCTURAL EVOLUTION IN Si:H GROWTH 49

3.5 MICROSTRUCTURAL EVOLUTION IN THE AMORPHOUS GROWTH REGIME 57

3.5.1 General treatment of thin film growth 57

3.5.2 AFM study and comparison with RTSE measurements 60

3.5.3 Discussion and Summary 68

3.6 DETAILS OF THE AMORPHOUS TO MICROCRYSTALLINE TRANSITION 73

3.6.1 AFM study and comparison with RTSE measurements 75

3.6.2 Phenomenological model 80

3.6.3 Virtual interface analysis 89

3.6.4 Discussion and Summary 93

CHAPTER 4 DEPOSITION PHASE DIAGRAMS FOR THE GUIDANCE OF SOLAR CELL OPTIMIZATION 100

4.1 INTRODUCTION 100

4.2 EXPERIMENTAL DETAILS 103

4.2.1 Deposition conditions 103

4.2.2 RTSE data analysis 104

4.3 DEPOSITION PHASE DIAGRAMS – THE SUBSTRATE EFFECT 105

4.3.1 c-Si substrate 105

4.3.2 a-Si:H substrate 107

4.3.3 p-μc-Si:H substrate 108

4.3.4 Comparison among substrates 112

4.4 GUIDANCE FOR SOLAR CELL OPTIMIZATION 117

4.5 SUMMARY 123

CHAPTER 5 APPROACHES FOR HIGH RATE DEPOSITION OF INTRINSIC LAYER a-Si:H 124

5.1 INTRODUCTION 124

5.2 EXPERIMENTAL DETAILS 127

5.3 EFFECT OF PLASMA POWER AT LOW TEMPERATURE 129

5.4 EFFECT OF TEMPERATURE AT HIGH PLASMA POWER 138

5.5 EFFECT OF PRESSURE 145

5.6 SUMMARY 160

CHAPTER 6 OPTICAL PROPERTIES OF a-Si:H BASED SOLAR CELL MATERIALS 163

6.1 INTRODUCTION 163

6.2 THEORY OF OPTICAL PROPERTIES OF AMORPHOUS AND MICROCRYSTALLINE SEMICONDUCTORS 166

6.3 EXPERIMENTAL APPROACH FOR THE OPTICAL CHARACTERIZATION OF a-Si:H AND ITS ALLOYS 169

6.4 RESULTS FOR AMORPHOUS SILICON AND ALLOYS 170

6.5 OTHER COMPONENT MATERIALS 182

6.5.1 Microcrystalline silicon μc-Si:H doped layers 182

6.5.2 Transparent conducting oxides (TCOs) 185

6.5.3 Metals 189

6.6 APPLICATIONS 193

6.7 SUMMARY 195

CHAPTER 7 CONCLUSION AND FUTURE WORK 198

7.1 CONCLUSION 198

7.2 FUTURE WORK 201

APPENDIX Kramers-Kronig Transformation for Amorphous and Microcrystalline Semiconductors 205

REFERENCES 209

LIST OF FIGURES

Fig. 2.1 Schematic representation of the electric field vector trajectory **E**(z_0,t) for an elliptically polarized light wave. For a given $z=z_0$, **E** traces out an ellipse over time. The sense of rotation determines whether the light wave exhibits left or right-handed polarization. Q is the tilt angle between the ellipse major axis a and the x-axis, measured in counterclockwise-positive sense when facing the light beam. χ is the ellipcity angle given by $\tan^{-1}$(b/a). 12

Fig. 2.2 Schematic representation of the non-normal incidence of a plane wave on a multilayer structure. The structure consists of m layers plus the substrate and the ambient. θ_0 is the angle of incidence and θ_j is the angle of incidence at the interface between the layers j and j+1. The wavevector at the (j, j+1) interface an within the ambient and substrates are shown as arrows. 15

Fig. 2.3 Schematic drawing of a rotating-compensator multichannel ellipsometer apparatus attached to a PECVD reactor. Details of the set-up are given in the text. 19

Fig. 2.4 Results for the Fourier expansion applied in the *in situ* calibration of the compensator retardance. (a) $|B_4|^{-1}$ is plotted versus analyzer angular setting 2A for the pixel group corresponding to a photon energy of 3.2 eV. The open symbols are the experimental data, and the solid line represents the values calculated from the best fit Fourier coefficients obtained in the Fourier analysis. (b) The difference between the experimental and calculated values of $|B_4|^{-1}$ is plotted. 29

Fig. 2.5 (a) Measured retardance δ spectrum (points) and its best-fit (line) versus photon energy for the MgF_2 biplate compensator. The measured spectrum was obtained through the in situ calibration method described in the text and in Fig. 2.3. Equation 2.40 was used for the fit with the thickness fixed d at 8864 nm. The best-fit results of the polynomial coefficients c_k (k=0 to 4) for the MgF_2 birefringence are listed in the Fig. in units of $deg\cdot nm^{-1}\cdot(eV)^{-(k+1)}$. In (b) the difference between the experimental and best-fit spectra in δ is shown. 30

Fig. 2.6 Representation of the optical model used in the analysis of thin film growth. This model includes two layers with variable thicknesses: a bulk layer with thickness d_b, and surface roughness layer with thickness d_s. The dielectric function of the roughness layer is determined by the EMA assuming an equal mixture of film material and void [f_v(void) =0.5]. 38

Fig. 2.7 Flow chart of the global $\bar{\sigma}$-minimization method for RTSE data analysis. 39

Fig. 2.8 Time-averaged unbiased estimator in the LRA ($\bar{\sigma}$) versus the two trial microstructural parameters – the bulk layer (d_b) and roughness layer (d_s) thicknesses – for an a-Si:H deposition. The minimum in $\bar{\sigma}$ defines the correct values of (d_b, d_s) at a given time $t=t_i$. 40

Fig. 2.9 Example of the results of the $\bar{\sigma}$-minimization method: (a) real and imaginary parts of the dielectric function (ε_1, ε_2) for an a-Si:H film at a given time $t=t_i$, obtained from mathematical inversion from the values of (d_b, d_s); time evolution of (b) the unbiased estimator σ, (c) the bulk layer thickness d_b , and (d) the roughness layer thickness d_s , all obtained from the LRA by using the (ε_1, ε_2) spectra obtained in (a). 41

Fig. 3.1 Schematic diagram of the processes in Si:H plasma-enhanced chemical vapor deposition, including (i) gas phase/plasma processes, (ii) surface processes, and (iii) sub-surface processes. 45

Fig. 3.2 Schematic diagram of the concentrations of different radicals in the plasma during PECVD of electronic quality a-Si:H; adapted from (Matsuda, 1998). 47

Fig. 3.3 Schematic of the surface processes occurring during a-Si:H growth by PECVD; adapted from (Robertson, 2000b). 47

Fig. 3.4 Surface roughness layer thickness (d_s) versus bulk layer thickness (d_b) for the deposition of a-Si:H films on c-Si substrates at 200°C with H_2-dilution ratios of R=0 and 10. 50

Fig. 3.5 Surface roughness layer thickness (d_s) versus bulk layer thickness (d_b) for the deposition of Si:H films on c-Si substrates at 200°C with H_2-dilution ratios of R=20 and 40. 51

Fig. 3.6 Schematic diagram of the cross-section of a Si:H film. This diagram depicts the Si:H phase evolution with thickness, beginning with an a-Si:H growth regime at the substrate interface followed by an intermediate mixed-phase (a+μc)-Si:H growth regime, and finally a single-phase μc-Si:H growth regime. 56

Fig. 3.7 Series of AFM images of a-Si:H films deposited with a H_2-dilution ratio of R=0, a plasma power of P=0.08W/cm^2, and a substrate temperature T=200ºC. Each image corresponds to a film deposited to a different thickness including (a) ~4 Å, (b) 240 Å, (c) 780 Å, (d) 1900 Å, and (e) 5200 Å. All images have the same dimensions of 500×500 nm^2. The full-scale ranges for the surface heights (i.e., the gray scale) are (a) 15 Å, (b) 20 Å, (c) 50 Å, (d) 100 Å, and (e) 120 Å. 61

Fig. 3.8 Values for the surface roughness layer thickness versus bulk layer thickness d_b, including the roughness d_s (filled squares), obtained from RTSE, and the corrected RMS roughness $d_{c,rms}$ (open circles), obtained from the AFM images of Fig. 3.7. 62

Fig. 3.9 Height-height correlation function G(ρ) versus the in-plane length scale ρ. The experimental results for the surface of the R=0 a-Si:H film at a thickness of 1900 Å [see Fig. 3.7(d)] are shown as open circles. These experimental results are deduced from Eq. 3.5. The solid lines correspond to a fit based on Eq. 3.6, and the best fit parameter ξ defines the correlation length. 65

Fig. 3.10 (a) Surface roughness layer thickness d_s (from RTSE) and (b) surface roughness in-plane correlation length ξ (from AFM) versus the bulk layer thickness d_b for the R=0 a-Si:H film series of Fig. 3.7. 66

Fig. 3.11 Stability parameter (ω) versus the in-plane wavelength (λ) of the surface perturbations. The values for ω are calculated from Eq. 3.7, by assuming a deposition rate of J=1 Å/s, an atomic radius of δ=3 Å, and different values for the surface diffusion length λ_0 (40–100 Å). The diffusion length λ_0 corresponds to a root of Eq. 3.7 and separates the perturbations that will grow with time (ω>0) from those that will decay with time (ω<0). 69

Fig. 3.12 (a) One dimensional profiles of the surface height function z(x) simulating the surface roughness on an a-Si:H film. The solid line corresponds to the initial profile (t=0), and the dashed line corresponds to the same profile after 500 s of simulated evolution, obtained by using the values for ω determined in Fig. 3.11 (with λ_0=100 Å). (b) Evolution of the RMS roughness d_{rms} versus time starting from the initial profile in (a) assuming different values of λ_0. The time evolution of such a profile is calculated from Eqs. 3.1 and 3.7. 70

Fig. 3.13 Results from RTSE analysis using a two-layer optical model for a Si:H film deposition in which the amorphous–to–microcrystalline transition is observed. The results are plotted versus the bulk layer thickness d_b and include (a) the surface roughness layer thickness d_s and (b) the unbiased estimator σ of the mean square deviation obtained in the least-squares regression analysis. The relevant thicknesses that can be deduced from the analysis are identified by the arrows in (a). 74

Fig. 3.14 Series of AFM images for R=20 Si:H films deposited on 500 Å R=0 a-Si:H substrates. The fixed conditions included a H_2-dilution ratio of R=20, a plasma power of P=0.08 W/cm^2, and a substrate temperature of T=200ºC. Each image corresponds to a film deposited with a different thickness including (a) 430 Å, (b) 880 Å, (c) 2050 Å, and (d) 3500 Å. All images have the same area of 2×2 μm^2. The full scale range for the surface height distributions (i.e., the gray scales) are (a) 500 Å, (b) 500 Å, (c) 1000 Å, and (d) 2000 Å. 77

Fig. 3.15 Combined RTSE and AFM results for the R=20 Si:H film series of Fig. 3.14 plotted versus bulk layer thickness d_b. The results include (a) μc-Si:H fractional surface area coverage from AFM, (b) μc-Si:H nuclei density from AFM, and (c) roughness layer thickness d_s from RTSE (obtained from the 3500 Å Si:H deposition) and corrected RMS roughness $d_{c,rms}$ from AFM. 78

Fig. 3.16 Bearing ratios of the surface height distributions obtained from the AFM images for the R=20 Si:H film series of Figs. 3.14 and 3.15. 79

Fig. 3.17 Schematic diagrams of the cone growth model that describes the evolution of the microstalline phase in the mixed-phase (a+μc)-Si:H growth regime, including (a) a cross-sectional view and (b) a top view. 81

Fig. 3.18 Increase in the surface roughness layer thickness Δd_s versus bulk layer thickness d_b as deduced from RTSE (open circles). The onset of roughening in Δd_s in the initial stages of the mixed-phase growth regime can be fit according to Eq. 3.13 (solid line). The values for the best fit parameters a and $d_{b,tr0}$ are listed within the plot. 84

Fig. 3.19 (a) Cone angle θ and (b) nucleation density N_d versus the a→(a+μc) transition thickness $d_{b,tran}$ for several Si:H films deposited under different conditions. The values for θ and N_d (open circles) are deduced by the cone growth model as described in the text. Values extracted from AFM study of Fig. 3.14 (solid circles), as well as from the RTSE, AFM and TEM study presented elsewhere (solid squares and triangles) (Fujiwara *et al.*, 2001b) are also included for comparison. 88

Fig. 3.20 Schematic of the four-medium optical model used in the RTSE virtual interface (VI) analysis of the amorphous–to–microcrystalline transition in Si:H films. The free parameters in this model are (i) the volume fraction $f_{\mu c}$ of the μc-Si:H phase in the outerlayer of thickness d_o and (ii) the surface roughness layer thickness d_s. 94

Fig. 3.21 Time-averaged unbiased estimator $\overline{\sigma}$ versus the value of the surface roughness layer thickness $d_{s,coal}$ at the (a+μc)→μc transition thickness $d_{b,coal}$. The minimum in $\overline{\sigma}$ defines the value of $d_{s,coal}$ used to deduce the dielectric function $\varepsilon_{\mu c}$ of the μc-Si:H phase. This dielectric function is used in the least-squares regression analysis of the (ψ, Δ) spectra vs. time during the mixed-phase (a+μc)-Si:H growth regime. 94

Fig. 3.22 Results of the virtual interface (VI) analysis applied to RTSE data for a Si:H film as plotted versus the bulk layer thickness d_b (open circles). The results include (a) the microcrystalline volume fraction $f_{\mu c}$ in the outerlayer , (b) the surface roughness layer thickness d_s, and (c) the unbiased estimator σ. The results of the VI analysis are compared to (a) results predicted by the cone growth model of Sec. 3.6.2 (solid line), and (b, c) results obtained in the standard RTSE analysis using the two-layer model (solid squares). 95

Fig. 3.23 Dielectric function spectra (ε_1, ε_2) at different bulk layer thicknesses d_b for a Si:H film that undergoes the amorphous–to–microcrystalline transition. The squares represent the spectra in (ε_1, ε_2) at d_b=200 Å; here the film is in the a-Si:H growth regime. Such spectra are obtained in the standard RTSE analysis using the two-layer optical model. The circles represent the spectra in (ε_1, ε_2) at d_b=2200 Å; here the Si-H film is in the single-phase μc-Si:H growth regime immediately after the (a+μc)→μc transition. Such spectra are obtained from the virtual interface analysis, which is described in the text and in Figs. 3.22 and 3.23. The solid lines correspond to fits to the experimental spectra obtained by using the analytical expressions described in Chapter 6. 96

Fig. 4.1 Evolutionary phase diagram for Si:H PECVD under standard low rf power conditions (0.08 W/cm^2) on c-Si substrates held at a temperature of 200°C. 106

Fig. 4.2 Roughness layer thickness (d_s) versus bulk layer thickness (d_b) for the deposition of Si:H films on R=0 a-Si:H substrates at 200°C using hydrogen dilution ratios of R=15, 30 and 80. 109

Fig. 4.3 Evolutionary phase diagram for Si:H PECVD under standard low rf power conditions (0.08 W/cm^2) on R=0 a-Si:H substrates held at a temperature of 200°C. 110

Fig. 4.4 Comparison of the roughness layer thickness (d_s) versus bulk layer thickness (d_b) for deposition of Si:H films with R=40 on c-Si (open circles) and a-Si:H (R=0) (solid circles) substrates. The substrate temperature in both cases was 200°C. 111

Fig. 4.5 In (a) the roughness layer thickness (d_s) is plotted versus bulk layer thickness (d_b) for the deposition of Si:H films on p-type μc-Si:H substrates. Results for depositions with H_2-dilution ratios of R=5 and 10 are shown for comparison. In (b) the imaginary parts of the dielectric functions (at 200°C) for thicknesses of d_b~170-180Å are presented for the same two films. 113

Fig. 4.6 Simplified phase diagrams in the plane of versus R and d_b for the PECVD of Si:H films on different substrates; the data values and connecting lines represent the a→(a+μc) transitions for the a-Si:H and c-Si substrates, and the a→μc direct transition for the μc-Si:H substrate. 114

Fig. 4.7 (a) Open circuit voltage (V_{oc}) and (b) fill factor (FF) for a-Si:H p-i-n solar cells prepared at 200°C, plotted as a function of the bulk i-layer H_2-dilution ratio R for one-step i-layers (open symbols) and as a function of the p/i interface layer R value for two-step i-layers (closed symbols). The thickness of the p/i interface layers was 200 Å for 20≤R≤40 and 100Å for 60≤R≤80. The total i-layer thickness was fixed at 4000 Å for all cells. In (b) results are shown for the annealed-state FF (circles) and the 100 h AM1.5 degraded-state FF (squares). 120

Fig. 4.8 (a) Annealed-state fill factor (FF) plotted as a function of the bulk i-layer thickness for p-i-n solar cells having i-layer prepared with H_2-dilution ratios of R=0 (squares), R=10 (circles), and R=20 (triangles). 122

Fig. 5.1 Roughness layer thickness d_s vs. bulk layer thickness d_b for the deposition of Si:H films on c-Si with H_2-dilution ratios of (a) R=0 and 10; and (b) R=20 and 40. The fixed deposition conditions include a rf plasma power of P=0.83 W/cm^2 and a substrate temperature of T=200°C. 130

Fig. 5.2 Surface roughness layer thickness d_s vs. bulk layer thickness d_b for a-Si:H films deposited on c-Si with fixed T=200°C and R=10, but at different rf power levels of P=0.08 W/cm^2 (solid circles) and 0.83 W/cm^2 (open squares). For the higher P film, an amorphous-to-amorphous surface roughening transition (a→a) occurs near d_b=500 Å (arrow), whereas for the lower P film, any such transition must occur for d_b>4000 Å. 131

Fig. 5.3 Values of the surface roughness layer thickness d_s at nuclei contact d_s(2.5 Å) (squares) and the smoothening magnitude Δd_s due to nuclei coalescence in the first 100 Å bulk layer growth (triangles) both plotted versus the H_2-dilution ratio R for Si:H films of the low power series with P=0.08 W/cm^2 (series I – solid symbols and solid lines) and the high power series with P=0.83 W/cm^2 (series II – open symbols and dashed lines). 132

Fig. 5.4 Surface roughness layer thickness d_s vs. bulk layer thickness d_b for Si:H films prepared on c-Si with fixed T=200°C and R=40, but different rf power levels of P=0.08 W/cm^2 (solid circles) and 0.83 W/cm^2 (open squares). For the lower P film, μc-Si:H nucleates immediately from the substrate, whereas for the higher P film, an amorphous–to–(mixed-phase) transition [a→(a+μc)] occurs near d_b=170 Å, and a (mixed-phase)–(single-phase) microcrystalline transition [(a+μc)→μc] occurs near 850 Å. 134

Fig. 5.5 Comparison between the phase diagrams for Si:H film deposition on c-Si at 200°C and two different rf powers levels: 0.08 W/cm^2 (series I - circles) and 0.83 W/cm^2 (series II - squares). The open symbols and broken lines indicate amorphous-to-amorphous roughening transitions [a→a], and the solid symbols and solid lines indicate amorphous-to-(mixed-phase-microcrystalline) [a→(a+μc)] transitions. The (up, down) arrows indicate that the transitions occur (above, below) the indicated thicknesses. 136

Fig. 5.6 Annealed state (solid symbols) and degraded state (open symbols) fill factors versus i-layer deposition rate for solar cells having 4000 Å i-layers deposited at R=10 with different rf plasma power levels (circles), and at R=0 with the lowest plasma power (squares). 137

Fig. 5.7 Roughness layer thickness (d_s) versus bulk layer thickness (d_b) for deposition of Si:H films on c-Si substrates with H_2-dilution ratios of R=0, R=7.5, R=15, and R=20. The fixed deposition conditions include a rf plasma power of P=0.83 W/cm^2; and a substrate temperature of T=260°C. 140

Fig. 5.8 Roughness layer thickness d_s vs. bulk layer thickness d_b for a-Si:H films deposited on c-Si with fixed R=0 and P=0.83 W/cm^2, but different substrate temperatures of T=200°C and 260°C. For the T=200°C film, amorphous phase surface roughening begins immediately, whereas for the T=260°C film, the a→a roughening transition occurs near d_b=60 Å. 141

Fig. 5.9 Values of the surface roughness layer thickness d_s at nuclei contact d_s(2.5 Å) (squares), and the smoothening magnitude Δd_s due to nuclei coalescence in the first 100 Å of bulk layer growth (triangles) both plotted versus the H_2-dilution ratio R for Si:H films deposited with a plasma power of P=0.83 W/cm^2 and at two different substrate temperatures of T=200°C (series II – open symbols and dashed line) and 260°C (series III – solid symbols and solid line). 142

Fig. 5.10 Surface roughness layer thickness d_s vs. bulk layer thickness d_b for Si:H films deposited on c-Si with fixed R=10 and P=0.8 W/cm^2, but different substrate temperatures of T=200°C and 260°C. For the T=200°C film, the a→a roughening transition occurs near d_b=500 Å, whereas for the T=260°C film, the a→(a+μc) roughening transition occurs near d_b=700 Å. 143

Fig. 5.11 Comparison between the phase diagrams for Si:H film deposition on c-Si at $P=0.83\ W/cm^2$ and two different substrate temperatures: T=200°C (series II - squares) and 260°C (series III - circles). The open symbols and broken lines indicate the amorphous-to-amorphous roughening transitions [a→a], and the solid symbols and solid lines indicate the amorphous-to-(mixed-phase-microcrystalline) transitions [a→(a+μc)]. The up arrows indicate that the transition occurs above the indicated thicknesses. 144

Fig. 5.12 Deposition rate versus total gas pressure (p_{tot}) for Si:H films prepared with R=10 (squares) and R=40 (circles). The fixed deposition conditions include a rf plasma power of $P=0.34\ W/cm^2$ and a substrate temperature of T=200°C. 146

Fig. 5.13 Surface roughness layer thickness (d_s) versus bulk layer thickness (d_b) for the deposition of Si:H films on c-Si substrate using R=10 and with total pressured of p_{tot}=0.3 (solid squares) and p_{tot}=4.0 Torr (open circles). The fixed deposition conditions include a rf plasma power of $P=0.34\ W/cm^2$ and a substrate temperature of T=200°C. 149

Fig. 5.14 Surface roughness layer thickness (d_s) versus bulk layer thickness (d_b) for the deposition of Si:H films on c-Si substrates with R=40 and with total pressures ranging from 0.9 to 4.0 Torr. The fixed deposition conditions include a plasma power of $P=0.34\ W/cm^2$ and a substrate temperature of T=200°C. 150

Fig. 5.15 Extended phase diagram for Si:H film deposition on c-Si with R=40, $P=0.34\ W/cm^2$, and T=200°C. Note that in this case the phase diagram is plotted in the parameter space of the bulk layer thickness and total gas pressure (d_b-p_{tot}). The open circles and dotted line indicate the amorphous roughening transitions [a→a], the open squares and solid line indicate the amorphous-to-(mixed-phase-microcrystalline) transition [a→(a+μc)], and the solid squares and dashed line indicate the (mixed-phase)–(single-phase) microcrystalline transition [(a+μc)→μc]. 151

Fig. 5.16 Surface roughness layer thickness (d_s) versus bulk layer thickness (d_b) for deposition of a-Si:H films on c-Si substrates with H_2-dilution ratios of R=10, 20, 40, and 60. The fixed deposition conditions include a rf plasma power of $P=0.34\ W/cm^2$, a total pressure of p_{tot}=4.0 Torr; and a substrate temperature of T=200°C. 153

Fig. 5.17 Surface roughness layer thickness (d_s) versus bulk layer thickness (d_b) for deposition of Si:H films on c-Si substrates with H_2-dilution ratios of R=60, 80 and 100. The fixed deposition conditions include a rf plasma power of $P=0.34\ W/cm^2$, a total pressure of p_{tot}=4.0 Torr; and a substrate temperature of T=200°C. 154

Fig. 5.18 Values of the surface roughness layer thickness d_s at nuclei contact d_s(2.5 Å) (solid squares), and smoothening magnitude Δd_s due to nuclei coalescence in the first 100 Å of bulk layer growth (open circles) both plotted versus the H_2-dilution ratio R for Si:H films deposited with a plasma power of P=0.34 W/cm^2, a substrate temperature of T=200°C, and a total pressure of p_{tot}=4.0 Torr. 155

Fig. 5.19 Parameters obtained from the analysis of the dielectric functions versus H_2-dilution ratio R, for the Si:H films of series IV. The plasma power was P=0.34 W/cm^2; the substrate temperature was T=200°C; and the total pressure was p_{tot}=4.0 Torr. In (a) the relative void volume fraction f_v [voids] is plotted. In (b) the optical band gap obtained by the extrapolation method (solid squares) and from fits to a parameterized equation (open circles) are shown. (See Chapter 6 for a detailed description of these two methods.) In (c) the Lorentz oscillator broadening parameter Γ obtained from fits to the same parameterized equation is provided. (See again Chapter 6 for detailed description.) 156

Fig. 5.20 Comparison between the phase diagrams for Si:H film deposition on c-Si substrates using P=0.83 W/cm^2 and p_{tot}<1.0 Torr (series II – squares), and using P=0.34 W/cm^2 and p_{tot}=4.0 Torr (series IV – circles). The open symbols and broken lines indicate the amorphous roughening transition [a→a], and the solid symbols and solid lines indicate the amorphous-to-(mixed-phase-microcrystalline) transition [a→(a+μc)]. The up arrows indicate that the transition occurs above the indicated thicknesses. 159

Fig. 5.21 Surface roughness layer thickness (d_s) vs. bulk layer thickness (d_b) for one selected film of each of the four series described in the text. The films were deposited under nominally "optimum conditions" for each series, i.e., with maximum H_2-dilution possible without crossing the a→(a+μc) transition for a 4000 Å a-Si:H film. The R value for each film is provided; other conditions are listed in Table 5.1. 162

Fig. 6.1 Multijunction a-Si:H-based solar cell structures based in the p-i-n and n-i-p configurations. In these hypothetical structures, a-$Si_{1-x}C_x$:H, a-Si:H, and a-$Si_{1-x}Ge_x$:H are used as the wide-gap, mid-gap, and narrow-gap components, respectively. In addition, all contact layers are assumed to be μc-Si:H:(B,P). 164

Fig. 6.2 Optical properties of a-$Si_{1-x}Ge_x$:H expressed as (ε_1, ε_2) (top) and (n, logα) (bottom) versus photon energy (open symbols). These results were obtained ex-situ at room temperature by combining DBPC, T&R, and SE measurements. The solid lines are fits to the data using a seven parameter optical model including Urbach sub-gap, Cody near-gap, and Lorentz above-gap contributions. 172

Fig. 6.3 Optical properties of a-Si:H expressed as (ε_1, ε_2) (top) and (n, logα) (bottom) versus photon energy (open symbols). These results were obtained ex-situ at room temperature by combining DBPC, T&R, and SE measurements. The solid lines are fits to the data using a seven parameter optical model including Urbach sub-gap, Cody near-gap, and Lorentz above-gap contributions. 173

Fig. 6.4 Optical properties of a-$Si_{1-x}C_x$:H expressed as (ε_1, ε_2) (top) and (n, logα) (bottom) versus photon energy (open symbols). These results were obtained ex-situ at room temperature by combining DBPC, T&R, and SE measurements. The solid lines are fits to the data using a seven parameter optical model including Urbach sub-gap, Cody near-gap, and Lorentz above-gap contributions. 174

Fig. 6.5 Determination of E_G from T&R data alone via the method proposed by Cody for the three samples of Figs. 6.2-6.4. This analysis assumes parabolic valence and conduction band densities of states, a constant dipole matrix element versus photon energy, and no states below the parabolic band edges. Room temperature gap values of 1.31, 1.69, and 1.94 eV are obtained for the a-$Si_{1-x}Ge_x$:H, a-Si:H, and a-$Si_{1-x}C_x$:H, respectively. 176

Fig. 6.6 Free parameters of the Lorentz oscillator (A_{1b}, E_{01}, Γ_{1b}) in the analytical expression for the dielectric function, obtained in the best fits to data such as those of Figs. 6.2-6.4.. The results are plotted versus the optical gap E_G(T&R), obtained according to the method of Fig. 6.5. Results from 12 different photovoltaic-quality a-Si:H, a-$Si_{1-x}Ge_x$:H, and a-$Si_{1-x}C_x$:H materials are correlated, yielding the piecewise linear functions shown. 177

Fig. 6.7 Free parameters of the gap function G(E) {(E_U, E_T), (E_G, E_P)} in the analytical expression for the dielectric function, obtained in the best fits to data such as those of Figs. 6.2-6.4. The results are plotted versus the optical gap E_G(T&R), obtained according to the method of Fig. 6.5. Results from 12 different photovoltaic-quality a-Si:H, a-$Si_{1-x}Ge_x$:H, and a-$Si_{1-x}C_x$:H materials are correlated, yielding the piecewise linear functions shown. 178

Fig. 6.8 Room temperature optical properties (n, logα) for hypothetical a-Si:H alloys computed on the basis of a single specification of the optical band gap E_G(T&R) as determined from a conventional T&R measurement. These results were deduced from the relationships in Figs. 6.6 and 6.7 and from the analytical expression for the dielectric function. 181

Fig. 6.9 Dielectric function at 200°C for the μc-Si:H:B p-layer obtained in the actual device configuration (glass/SnO_2/ZnO/μc-Si:H) from an analysis of rotating-compensator RTSE data. Seven free parameters were used in the analytical expression for the dielectric function including near-gap Tauc behavior and two Lorentz oscillators. 184

Fig. 6.10 Index of refraction and extinction coefficient for an Asahi U-type textured SnO_2 film on glass measured at room temperature using rotating-compensator RTSE. The model applied for the optical properties includes the four-parameter interband Tauc-Lorentz contribution, along with the two-parameter intraband Drude contribution (solid lines). The broken line depicts results for the extinction coefficient extracted from transmission measurements. 187

Fig. 6.11 Dielectric functions of two different types of ZnO films used in a-Si:H-based solar cells: (a) a film used as the dielectric spacer layer in the back-reflector structure, and (b) a thinner film used as the protective layer on a glass/SnO_2 structure. 188

Fig. 6.12 (a) Dielectric function of Ag measured at room temperature as reported by (Palik, 1985) (solid lines) demonstrating its decomposition into intraband (dotted lines) and interband (dashed lines) components. For the intraband component, the Drude expression was used with variable amplitude and broadening parameters, and for the interband component a tabular listing was deduced from the decomposition. (b) Room temperature dielectric functions of thin film Ag prepared by evaporation on glass (solid lines) and by magnetron sputtering on stainless steel (points), both obtained at room temperature by ex situ rotating-analyzer SE. 191

Fig. 6.13 (a) Calculated dielectric function for Al at room temperature (solid lines), including a decomposition into intraband (dotted lines) and interband (dashed lines) components. (See text for details.) (b) Room temperature dielectric functions of thin film Al as reported in (Shiles *et al.*, 1980) (solid lines) and as obtained by rotating-polarizer RTSE during evaporation on a room-temperature silicon wafer substrate (points) (Nguyen *et al.*, 1993). 192

Fig. 6.14 (a) Predicted increase in the i-layer absorbance spectrum (upper panel) for an a-Si:H-based single-junction p-i-n solar cell obtained by assuming a 45 nm microscopic roughness layer at the SnO_2/p-layer interface, over that for an "ideal" device without the interface roughness. The lower panel shows the difference (rough − ideal) in the solar cell reflectance; (b) potential current gain due to the antireflection effect of microscopic roughness of thickness d_i at the SnO_2/p-layer interface. 196

Fig. 6.15 (a) Predicted increase in parasitic absorbance (upper panel) of the ZnO/Ag interface in the a-Si:H p-i-n solar cell obtained upon introduction of a 13 nm ZnO/Ag interlayer (21/79 vol.% ZnO/Ag). The lower panel shows the difference (interlayer − ideal) in the solar cell reflectance spectra; (b) potential current gain generated by the elimination of all parasitic absorbance at the ZnO/Ag interface, plotted versus the ZnO/Ag interface layer thickness d_i. 197

LIST OF TABLES

Table 5.1 Summary of the conditions for four deposition series. For each series the minimum and maximum hydrogen-to-silane gas flow ratios R=[H_2]:[SiH_4] are shown, along with the corresponding total and silane (partial) pressures and the measured deposition rates. Note that for series IV the total pressure is kept constant at 4.0 Torr, in contrast to the other three series for which the silane partial pressure is kept relatively constant at (0.05 ± 0.02) Torr. The entries in bold are the values differing from those of the standard series I. 128

ACKNOWLEDGEMENTS

I would like to express my sincere gratitude to Dr. Robert W. Collins for his dedicated guidance throughout the course of this thesis work. His expertise and friendly advice were essential to the successful completion of this PhD thesis at Penn State. Additional thanks is given to Rob for the careful revision of this manuscript. Special thanks is directed to Dr. Christopher R. Wronski, my thesis co-adviser, for his support and knowledgeable guidance in this collaborative research. I also thank the other committee members, Dr. Russell Messier and Dr. Thomas N. Jackson for the fruitful discussions and collaborations during this work.

I would like to thank all the colleagues that have made the completion of this thesis work possible: Randy Koval, Joohyun Koh, Gelio Ferreira, Hiroyuki Fujiwara, Ilsin An, Yeeheng Lee, Lihong Jiao, Joshua Pearce, Antonio Zapien, and Chi Chen. Special thanks to my friend Pablo Rovira, who has motivated me to come to Penn State and has been deeply involved in every aspect of this research.

My gratitude is dedicated to all my family in Brasil for giving me love and support, specially my mother, Vane, my father and his wife, Luiz Felipe and Tatiana, and my sister and brothers, Adriana, Marcelo e Alexandre. I am also very pleased to thank all my friends, Rodrigo (Zauro), Rodrigo (Sad), Glauco, Rogerio, Daniel (Woody), Fabio (Pica Pau), Max, and many others, who have accompanied me along the journey.

This thesis is dedicated to my wife, Danusa, for her love and inspiration during all these years.

Finally, I greatly appreciated the financial support from the National Renewable Energy Laboratory (NREL) and the National Science Foundation (NSF).

To Danusa

CHAPTER 1

INTRODUCTION

1.1 BACKGROUND

The development of viable renewable energy sources is a major technological challenge for the transformation of the present economies based on fossil fuels into truly sustainable economies of the future (Flavin and Dunn, 1999). The photovoltaic (PV) conversion of solar energy is among the most important alternative renewable energy sources. Although at present the PV contribution to overall energy production is still very small, the production of PV panels has been increasing steadily at a rate of ~25% annually (Maycock, 2000). Reductions in the production costs are required, however, in order for PV technology to compete with current fossil-fuels technology for large-scale energy production. Approximately 80% of the PV market consists of solar cells based on crystalline silicon (c-Si). Such solar cells have relatively high efficiencies but the costs of production are high due to the large amount of material required in fabrication. As a result, thin film solar cell technologies have arisen as viable alternatives for the low cost production of solar cell modules (Shah *et al.*, 1999). Such technologies are attractive because the amount of material used is much reduced as compared to c-Si modules. In addition, thin film solar modules can be deposited over large areas and on inexpensive substrates by using low cost processes, such as the roll-to-roll method (Shah *et al.*, 1999). Among the thin-film technologies, solar cells based on hydrogenated amorphous silicon (a-Si:H) have attracted the most interest over the past two decades or more (Guha *et al.*, 2000).

The interest in a-Si:H as an optoelectronic material began with the pioneering work of Chittick et al. that demonstrated the semiconducting properties of a-Si:H

prepared by the glow discharge of silane (Chittick *et al.*, 1969). A few years later, the doping of a-Si:H was reported by Spear and LeComber (Spear and LeComber, 1975), and soon after, the first photovoltaic devices were developed by Carlson and Wronski (Carlson and Wronski, 1976). At present, state-of-the-art a-Si:H-based solar cells are fabricated in the multijunction configuration, such that two or three p-i-n structures are stacked in the same device (Guha *et al.*, 2000). The intrinsic (i) absorber layers are made from a-Si:H and its alloys with Ge or C, and the doped (p and n) layers can be either amorphous or microcrystalline silicon (or its alloys).

Several different deposition techniques have been used in the preparation of a-Si:H films and devices (Luft and Tsuo, 1993; Perrin, 1995). Most commonly, a-Si:H thin films are deposited by plasma enhanced chemical vapor deposition of silane (SiH_4) at low temperatures ($T<300°C$). The optical and electronic properties of a-Si:H and the associated device performance can vary strongly according to the fabrication methods and deposition conditions. As a result, extensive efforts have been devoted to investigations of the relationships among (deposition processes)/(film properties)/(device performance). These efforts can be separated into two parallel lines of research, both intending to generate further reductions in production costs (Guha *et al.*, 2000).

One line of research aims to increase the final solar cell efficiency, which is in part limited by the light-induced degradation generated by the Staebler-Wronski effect (Staebler and Wronski, 1977). Many studies have revealed that a-Si:H and its alloys (with C or Ge) deposited by using moderate hydrogen dilution of SiH_4 exhibit improved electronic quality and reduced light-induced degradation (Matsuda and Tanaka, 1987; Lee *et al.*, 1996; Okamoto *et al.*, 1996; Rech *et al.*, 1996; Tsu *et al.*, 1997).

A second line of research focuses on increasing the deposition rates for the intrinsic layers while avoiding losses in the device efficiency. Several efforts have been directed toward the optimization of the rf PECVD process at high rates (Matsuda, 1998; Takai *et al.*, 2000). In addition, alternative deposition methods have been developed that can potentially produce high electronic quality materials at increased rates. These methods include PECVD but at higher excitation frequencies in the vhf (50-100 MHz)

(Curtins *et al.*, 1987) and microwave (2.45 GHz) (Guha *et al.*, 1995) ranges, hot-wire CVD (Mahan *et al.*, 1991), and expanding thermal plasma CVD (Kessels *et al.*, 2001).

In this thesis research, real time spectroscopic ellipsometry has been applied in investigations of the relationships among (deposition processes)/(film properties)/(device performance) for rf-PECVD a-Si:H films. RTSE can provide accurate information on the time evolution of the microstructural parameters in thin film growth, as well as the optical properties of the films. RTSE have been used extensively to characterize the growth of a-Si:H and a-$Si_{1-X}C_X$:H films, as well as μc-Si:H films (An *et al.*, 1991b; Li *et al.*, 1992; Lu *et al.*, 1993; Nguyen and Collins, 1993). In particular, it has been applied to characterize different processes employed in the deposition of p-i-n and n-i-p solar cells in the actual device configuration (Koh *et al.*, 1995; Fujiwara *et al.*, 1999a; Koh *et al.*, 1999b; Rovira *et al.*, 2000a).

Finally, improvements in the conversion efficiency of the a-Si:H-based solar cells are also expected to arise from advances in the optical design of the cells. State-of-the-art solar cell modules consist of a stack of several layers of different materials. The complexity of such structures imposes great difficulties for the optimization of these devices when attempted by simple empirical variations in the materials properties and device configuration. Therefore, emphasis has been given to the development of computer programs that simulate the optical characteristics of solar cells. These programs have been developed in attempts to provide guidance for further improvements in the solar cell conversion efficiency (Schropp and Zeman, 1998; Sopori *et al.*, 1999). An important aspect in the development of such simulation programs is the utilization of reliable optical functions for the component materials. Therefore, a part of this thesis research has been devoted to the measurement and analysis of the optical properties of the component materials of a-Si:H-based solar cells.

1.2 THESIS OBJECTIVES

The first and primary objective of this research is to establish systematic descriptions of the growth processes of Si:H thin films prepared by rf plasma enhanced chemical vapor deposition (PECVD). The intent of such descriptions is to provide guidance for the optimization of the deposition processes for a-Si:H intrinsic layers incorporated into a-Si:H based solar cells.

The basis of this investigation is the in situ characterization of the microstructural evolution and optical properties during Si:H film growth by real time spectroscopic ellipsometry (RTSE). Specifically, RTSE is capable of providing the evolution of the surface roughness layer thickness (d_s) versus the bulk layer thickness (d_b). Such results exhibit several different features that demarcate different Si:H film growth regimes. Atomic force microscopy (AFM) is also used to complement the RTSE results, by providing the topography of the surface of the Si:H films at high spatial resolution. The results of RTSE and AFM are interpreted by means of semi-empirical thin film growth models in order to obtain a fundamental understanding of Si:H film growth mechanisms. In addition, novel approaches are developed for RTSE data analysis in the complicated situation in which the Si:H films undergo an amorphous-to-microcrystalline phase transition as a function of the accumulated thickness.

The Si:H thin film growth characterization efforts by RTSE provide the groundwork for the development of deposition phase diagrams. The purpose of these phase diagrams is to provide a succinct description of the different Si:H thin film growth regimes as a function of the bulk layer thickness and one key deposition parameter. The key parameter to be investigated is the H_2-dilution level, which can affect not only the final electronic quality of the Si:H film but also its phase, which ranges from amorphous to single-phase microcrystalline. In addition, deposition phase diagrams, as deduced by RTSE, are applied to Si:H film growth on different substrates. As a result, the Si:H PECVD processes are investigated in a similar configuration as the counterpart Si:H intrinsic layers in solar cells. Such an approach enables direct correlation between film

growth and device performance. Thus, the phase diagrams studies can provide guiding principles for the optimization of a-Si:H processes for photovoltaics applications.

Finally, the phase diagram framework is used to investigate high rate PECVD processes for Si:H intrinsic layers. Phase diagrams in the d_b-R plane are derived from four series of Si:H depositions in which the PECVD parameters are systematically varied. The variable parameters in addition to R include the rf plasma power, the substrate temperature, and the total gas pressure. The effects of such parameters on the growth processes are investigated through comparisons of RTSE results and the corresponding phase diagrams. The intent of these comparisons is to provide insights into the optimization of high-rate deposition processes for the intrinsic layers incorporated into a-Si:H based solar cells.

The second objective of this research is to develop a comprehensive database for the optical functions of the different component materials used in a-Si:H-based multijunction solar cells. Such a database provides the inputs for modeling programs that are designed to simulate the optical characteristics of multilayer solar cells. The approach initiated here is to derive this database from analytical expressions that can describe the optical functions of each component material in terms of a few physically-meaningful, wavelength-independent parameters. In particular, new expressions are proposed for the description of the optical functions for amorphous, nanocrystalline, and microcrystalline semiconductors. These latter expressions are used to describe the experimental spectra in the optical functions for a set of representative intrinsic amorphous materials, including a-Si:H and its alloys with Ge and C. A unique combination of optical spectroscopic techniques is used for the measurement of the optical properties of such samples over the entire visible spectral range.

1.3 THESIS ORGANIZATION

This thesis is organized according to the sequence of objectives described above.

First, Chapter 2 provides a description of the real time spectroscopic ellipsometry (RTSE) technique, including the details of the experimental set up, the methods for data acquisition and reduction, and the basic data analysis approaches. Improvements in both the experimental set up and the data analysis procedures performed during this study will be highlighted.

The results of this research are separated into two major parts. The first (main) part includes Chapters 3, 4, and 5, which focus on the investigation of Si:H deposition processes for optimization of a-Si:H intrinsic layer materials for solar cells. The second part includes Chapter 6, which focuses on the development of a database for the optical properties of a-Si:H-based solar cell components.

In Chapter 3, an overall description of the microstructural evolution for Si:H thin films is presented, as deduced by RTSE. Different features of the microstructural evolution include a surface roughening onset associated with the amorphous growth regime, and roughening and smoothening onsets associated with the amorphous-to-microcrystalline transition. Section 3.5 presents RTSE and AFM measurements of Si:H films in the amorphous growth regime. A theoretical approach is presented to interpret the roughening onset in terms of limitations on the diffusion of absorbed radicals on the film surface. Section 3.6 presents RTSE and AFM measurements of Si:H depositions for which the amorphous–to–microcrystalline transition versus accumulated thickness is observed. A phenomenological model is also proposed to interpret the RTSE analyses results in terms of the preferential growth of the crystalline phase. Finally, a novel self-consistent method is developed to analyze the RTSE data on Si:H films that undergo the amorphous–to–microcrystalline transition.

In Chapter 4, the concept of the extended phase diagram is proposed and developed for the description of PECVD Si:H film growth. This concept is applied to the study of Si:H films prepared using different H_2-dilution levels on different types of

substrates. The implications of these results for the optimization of solar cell fabrication processes and for the correlations of materials and device properties are discussed.

In Chapter 5, the effects of PECVD parameters on the phase diagrams are investigated. Different series of Si:H depositions are described that generate different phase diagrams. Within each series, a wide range in the H_2-dilution level is explored, while other parameters are fixed. The different series explore the effects of rf plasma power, substrate temperature, and total gas pressure. The implications of the phase diagram results for the development of a high-rate Si:H PECVD process are discussed.

Chapter 6 describes a study of the optical properties of the component materials of multijunction solar cells. First, the theoretical development is presented leading to analytical expressions that describe the optical properties of amorphous, nanocrystalline, and microcrystalline semiconductors. Such derivations are further detailed in the Appendix. Second, the experimental approach is described by which the optical properties of a set of representative samples of a-Si:H and its alloy films are measured. The measurement results are used to establish a database for the optical properties of intrinsic amorphous layers. In addition, similar approaches are described to analyze the optical functions of the other solar cell materials, including microcrystalline silicon doped layers, transparent conducting oxide layers and metal contacts. The first application of an optical simulation program is presented in which case the impact of microscopically rough interfaces on the optical response of a-Si:H-based solar cells is investigated.

Finally, in Chapter 7, the overall conclusions of this study are drawn and future extensions of this study are proposed.

CHAPTER 2

REAL TIME SPECTROSCOPIC ELLIPSOMETRY

2.1 INTRODUCTION

Ellipsometry belongs to a broad class of optical characterization techniques that involves the interaction of polarized light with matter. In particular, ellipsometry refers to the measurement of the relative amplitudes and phase shift between two orthogonal electric field components of a polarized light beam and how these values change upon reflection of the beam from a sample. The fact that *two relative* quantities are measured makes this technique extremely powerful for determination of the optical properties of a reflecting sample, and the fact that the relative phase is measured makes the technique extremely sensitive to the sample structure.

In real time spectroscopic ellipsometry (RTSE), the optical spectral response of the sample, from infrared to ultraviolet wavelengths, is collected *in-situ* on a sufficiently short time scale to follow the changes of interest in the sample structure during a dynamical process. The non-invasive and versatile attributes of RTSE as an optical technique combined with its real time and spectroscopic capabilities makes it a very powerful tool for monitoring a wide variety of surfaces and thin film processes in diverse environments (Collins, 1990; Collins *et al.*, 2001). In particular, RTSE have been used successfully in the study of amorphous and microcrystalline semiconductor thin-film growth, providing information on the chemical composition (Fujiwara *et al.*, 1998), microstructural evolution (An *et al.*, 1990; Koh *et al.*, 1999), optical band gap (An *et al.*, 1991a; Koh *et al.*, 1995; Kim *et al.*, 1996), void volume fraction (Kim *et al.*, 1996), etc.

The most common real time spectroscopic ellipsometers utilize one or more rotating-elements that modulate the polarization state of the light beam, and multichannel

detection systems that can collect several hundred spectral points in parallel (Collins, 1990; Collins *et al.*, 2001). The first automatic rotating-element ellipsometer was introduced in 1969 (Cahan and Spanier, 1969), and this led to the development of automated spectroscopic ellipsometers and single wavelength real-time ellipsometers, both using single-channel photo-multiplier tube detectors (Vedam, 1998). Later, the advent of multichannel detection systems based on a linear array of Si photodiodes stimulated the development of real time spectroscopic ellipsometry (Collins, 1990; An and Collins, 1991). The original RTSE instruments used a continuous wave light source, rotating-polarizer (or analyzer), and a combination of spectrograph and linear photodiode array as a detector. With this configuration, the shortest possible acquisition time for a pair of ellipsometric spectra of 128 spectral points (1.5 to 4.8 eV) was 40 ms. In addition, the instrument precision for typical acquisition times of 1 s, as measured by the standard deviation in the ellipsometric angles (ψ, Δ), was (0.01°, 0.03°) at 2.5 eV (An *et al.*, 1992). This precision provides monolayer thickness resolution in thin film measurements.

Recent advances in RTSE have occurred in several directions. The spectral range has been extended to photon energies up to 6.5 eV, enabling the study of wide band gap materials (Zapien *et al.*, 2000). A rotating-compensator configuration was implemented (Lee *et al.*, 1998a) that offers several advantages as compared to the standard rotating-polarizer (analyzer) configuration, including the determination of the phase shift angle Δ with good precision from -180° to 180° and the capability of separating out the contribution of randomly polarized light resulting from non-ideal samples. This latter capability extended the application of RTSE to more complex, non-ideal measurements. For example, RTSE can now be applied to a-Si:H based solar cell production monitoring where textured substrates with macroscopic roughness are usually used (Rovira *et al.*, 1999).

The results from real time spectroscopic ellipsometry (RTSE) presented in this thesis were obtained with a multichannel spectroscopic ellipsometry instrument attached to a PECVD reactor. During the course of this research, this instrument was modified from its original rotating-polarizing design to a rotating-compensator configuration.

Although, the focus of this study was not the instrumentation itself, I have participated in some stages of the implementation of this new configuration. Therefore, in Sec. 2.3 the details of the instrument set-up, data acquisition, and data reduction are presented. In particular, the implementation of *in-situ* calibration of the compensator retardance in reflection mode is described in Sec 2.3.3. Finally, the real-time data analysis methods, which are the final and critical step in RTSE, are presented in detail in Sec. 2.4. These methods were used to produce the results of Chapters 3-5, and similar approaches are used in the analysis of *ex-situ* SE measurements, which are the subject of Chapter 6.

2.2 BASICS OF ELLIPSOMETRY

2.2.1 Polarized light

The electric field of a polarized monochromatic wave propagating in a medium along the z direction is given by (Wooten, 1972; Hecht, 1987):

$$\tilde{\mathbf{E}}(\mathbf{r},t) = \tilde{\mathbf{E}}_0 \exp\left[i\omega(Nz/c - t)\right], \tag{2.1}$$

where ω and c are the angular frequency and the speed of light in vacuum, respectively. $\tilde{N} = n + ik$ is the complex refractive index of the material that describes its linear optical response, n is the refractive index, and k is the extinction coefficient. Alternatively, the optical response of the medium can be described by its complex dielectric function $\tilde{\varepsilon}$, given by

$$\tilde{\varepsilon} = \varepsilon_1 + i\varepsilon_2 = \tilde{N}^2. \tag{2.2}$$

The relation between the two descriptions is given by

$$\varepsilon_1 = n^2 - k^2, \tag{2.3a}$$

$$\varepsilon_2 = 2nk. \tag{2.3b}$$

The vector $\mathbf{E}_0$ determines the polarization state of the wave. In Cartesian coordinates

$$\mathbf{E}_0 = E_{0x}\hat{\mathbf{x}}\exp(i\gamma_x) + E_{0y}\hat{\mathbf{y}}\exp(i\gamma_y), \tag{2.4}$$

where $\gamma_{x(y)}$ represent the absolute phase of $E_{x(y)}$ at z=0 and t=0. For a general polarization state, the electric field vector traces out an ellipse as a function of time at a fixed value $z=z_0$ in a plane perpendicular to its wavevector over time as depicted in Fig. 2.1. The two limiting cases are (i) linear polarized light such that $\gamma_x = \gamma_y$, and (ii) circularly polarized light such that $\gamma_x = \gamma_y \pm \pi/2$ and $E_{0x} = E_{0y}$. Another useful way to describe the polarization ellipse is by the tilt angle Q (–90° < Q ≤ 90°) between its major axis and the x-axis, and the ellipcity angle χ determined by the ratio of the minor axis (b) and the major axis (a), $\chi = \tan^{-1}(b/a)$ (–45° ≤ χ ≤ 45°) (Azzam and Bashara, 1977). These angles will be useful in the data reduction in Section 2.3.

2.2.2 Reflection from multilayer thin films

In an ellipsometric measurement, the change in the polarization state is measured for a light beam upon reflection from a sample at an oblique angle. The sample response can be described by the complex amplitude reflection coefficients given as

$$\tilde{r}_p = |\tilde{r}_p| \exp(i\delta_p) = \frac{\tilde{E}_p^{\,ref}}{\tilde{E}_p^{\,inc}} , \tag{2.5a}$$

$$\tilde{r}_s = |\tilde{r}_s| \exp(i\delta_s) = \frac{\tilde{E}_s^{\,ref}}{\tilde{E}_s^{\,inc}} , \tag{2.5b}$$

where p and s refers to the directions parallel and perpendicular to the plane of incidence, respectively. $E_{p(s)}$ denotes the p(s) components of the E-field amplitude, and “ref” and “inc” refers to the reflected and incident beams. δ_p and δ_s are the resulting phase shifts of the E-field components upon reflection. The measured quantity in ellipsometry is the complex amplitude reflection coefficient ratio $\tilde{\rho}$, defined by

$$\tilde{\rho} \equiv \frac{\tilde{r}_p}{\tilde{r}_s} = \frac{|\tilde{r}_p|}{|\tilde{r}_s|} \exp[i(\delta_p - \delta_s)]. \tag{2.6}$$

Usually, it is convenient to describe $\tilde{\rho}$ in terms of the pair of ellipsometric angles (ψ, Δ) corresponding to the relative amplitude ($\tan\psi$) and phase shift (Δ) between the p and s

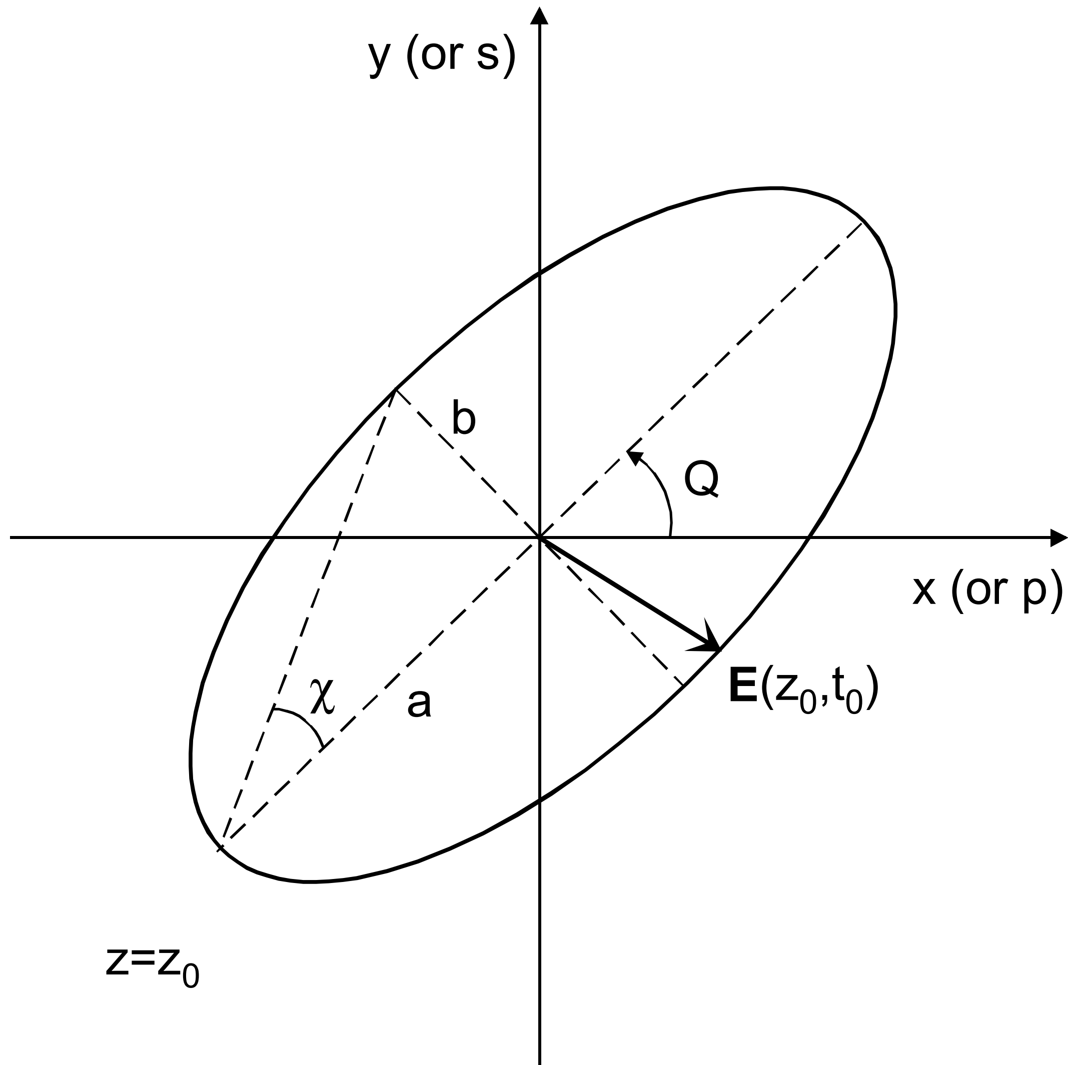

Figure 2.1 Schematic representation of the electric field vector trajectory $\mathbf{E}(z_0,t)$ for an elliptically polarized light wave. For a given $z=z_0$, **E** traces out an ellipse over time. The sense of rotation determines whether the light wave exhibits left or right-handed polarization. Q is the tilt angle between the ellipse major axis a and the x-axis, measured in counterclockwise-positive sense when facing the light beam. χ is the ellipcity angle given by $\tan^{-1}(b/a)$.

components:

$$\tilde{\rho} = \tan\psi \exp i\Delta, \tag{2.7}$$

and thus,

$$\tan\psi = \frac{|\tilde{r}_p|}{|\tilde{r}_s|}, \tag{2.8a}$$

$$\Delta = \delta_p - \delta_s\ . \tag{2.8b}$$

The complex amplitude reflection coefficients depend on the optical properties and the microstructural characteristics of the sample. For an ideal interface between two media (ambient and semi-infinite sample material), the expressions for $\tilde{r}_p$ and $\tilde{r}_s$ can be determined straightforwardly by means of the Fresnel equations (Azzam and Bashara, 1977; Hecht, 1987), and the dielectric function of the reflecting medium can be extracted directly from the measured ellipsometric angles (ψ, Δ) using the following expression

$$\tilde{\varepsilon} = \varepsilon_{amb} \sin^2\theta_i \left[1 + \tan^2\theta_i \left(\frac{1-\tilde{\rho}}{1+\tilde{\rho}} \right)^2 \right], \tag{2.9}$$

where ε_{amb} is the dielectric function of the ambient and θ_i is the angle of incidence (both real values). For more complicated thin film samples, however, one needs to consider a suitable optical model that includes one or more stacked layers on the top of the substrate, including layers of different materials or different chemical compositions, as well as surfaces and interfaces layers. Effective medium theories (EMTs) are used in the treatment of microscopically rough surfaces and interfaces as will be described in the next Section. The optical properties of a multilayer structure can be calculated using a matrix formalism, whereby the 2x2 scattering matrix **S** describes the overall reflection and transmission properties of the structure. Figure 2.2 depicts a schematic of a multilayer structure consisting of m layers, where the ambient is denoted layer 0 and the semi-infinite substrate is layer m+1. In this case, **S** is given by (Azzam and Bashara, 1977)

$$\mathbf{S} = \mathbf{I}_{01} \prod_{j=1}^{m} \mathbf{L}_j \mathbf{I}_{j(j+1)}, \tag{2.10}$$

where **I** and **L** are the interface and layer matrices, respectively. The interface matrix between layer j and (j+1) is

$$\mathbf{I}_{j(j+1)} = \frac{1}{\tilde{t}_{j(j+1)}} \begin{bmatrix} 1 & \tilde{r}_{j(j+1)} \\ \tilde{r}_{j(j+1)} & 1 \end{bmatrix}, \tag{2.11}$$

where t and r are complex amplitude coefficients for transmission and reflection and can be calculated using the Fresnel equations for this interface. The matrix for layer j is given by

$$\mathbf{L}_j = \begin{bmatrix} e^{i\tilde{\beta}_j} & 1 \\ 1 & e^{-i\tilde{\beta}_j} \end{bmatrix}, \tag{2.12}$$

where β_j is the phase shift imposed on the orthogonal components of the E-field when the wave traverses the j layer. This quantity is written as

$$\tilde{\beta}_j = \frac{2\pi}{\lambda} d_j \tilde{N}_j \cos\tilde{\theta}_j. \tag{2.13}$$

Here $\tilde{N}_j$ and d_j are the complex refractive index, and the thickness of layer j, $\tilde{\theta}_j$ is the angle of incidence at the j(j+1) interface, and λ is the wavelength of the light in vacuum. The angle $\tilde{\theta}_j$ is complex in general and can be calculated through Snell's Law by

$$\tilde{N}_j \cos\tilde{\theta}_j = n_0 \cos\theta_0, \tag{2.14}$$

where n_0 and θ_0 are the refractive index of the ambient and the angle of incidence (both assumed to be real). The scattering matrix **S** must be calculated for both p and s polarization components and the complex amplitude reflection coefficient ratio can be extracted according to

$$\tilde{\rho} = \frac{\tilde{r}_p}{\tilde{r}_p} = \frac{\tilde{S}_{p21}}{\tilde{S}_{p11}} \frac{\tilde{S}_{s21}}{\tilde{S}_{s21}}. \tag{2.15}$$

Therefore, a pair of ellipsometric spectra (ψ, Δ) associated with a given sample structure can be calculated if the angle of incidence is known and if the optical properties versus wavelength and the thickness for each layer are also known. Equations 2.10 to 2.15 are used in the analysis methods of the ellipsometric spectra as will be described in Sec. 2.4.

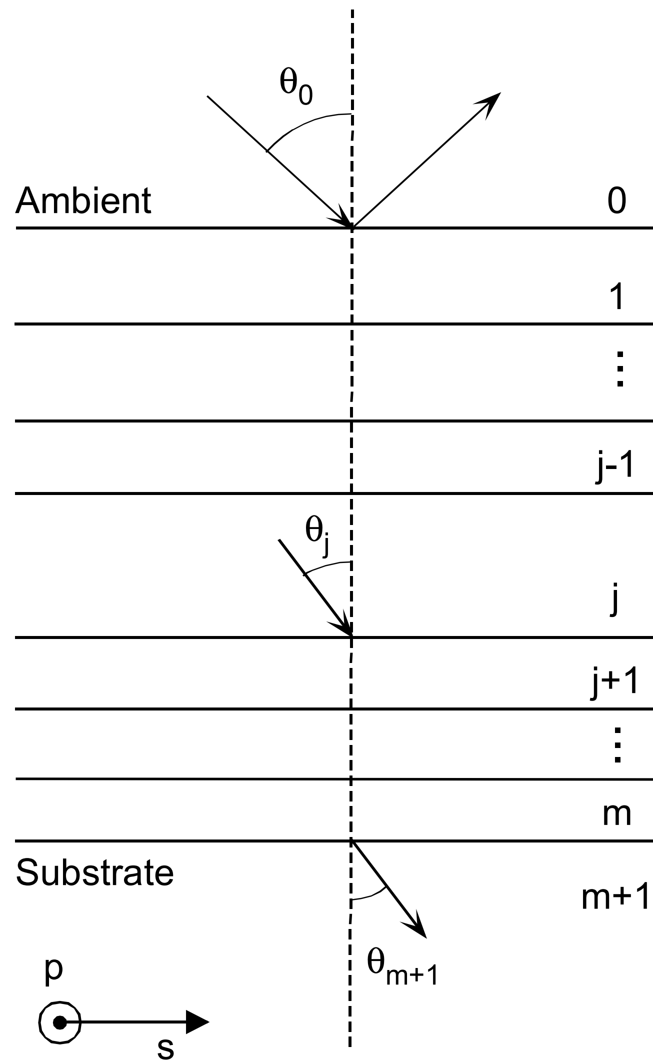

Figure 2.2 Schematic representation of the non-normal incidence of a plane wave on a multilayer structure. The structure consists of m layers plus the substrate and the ambient. θ_0 is the angle of incidence and θ_j is the angle of incidence at the interface between the layers j and j+1. The wavevector at the (j, j+1) interface an within the ambient and substrates are shown as arrows.

2.2.3 Effective medium theories

In order to describe the dielectric response of layers consisting of microscopic mixtures of different materials, such as microscopic surface roughness and interface layers one must rely on effective medium theories (EMT). With these theories an effective dielectric function corresponding to the mixture can be determined from the dielectric functions and volume fractions of the component materials. A general expression for the simplest EMTs is given by

$$\frac{\tilde{\varepsilon}-\tilde{\varepsilon}_h}{\tilde{\varepsilon}+2\tilde{\varepsilon}_h}=\sum_i f_i \frac{\tilde{\varepsilon}_i-\tilde{\varepsilon}_h}{\tilde{\varepsilon}_i+2\tilde{\varepsilon}_h}\ , \tag{2.16}$$

where $\tilde{\varepsilon}$ is the effective dielectric function, $\tilde{\varepsilon}_i$ and f_i are the dielectric function and volume fraction of the ith component and $\tilde{\varepsilon}_h$ is the host dielectric function. Equation 2.16 is valid for isotropic screening, i.e., when the inclusions of the different materials have spherical shapes. Expressions for anisotropic screening have been discussed previously (Aspnes, 1982).

Three cases for the EMT have been considered for the analysis of ellipsometric data in the visible range (Aspnes *et al.*, 1979; Fujiwara *et al.*, 2000a). In the first case, called the Lorentz-Lorenz approximation (LL), the host material is vacuum, i.e., $\tilde{\varepsilon}_h$=1. In the second case, the Maxwell-Garnett approximation (MG) assigns a dominant phase j such that $f_j > f_i$ for all i, and thus $\tilde{\varepsilon}_h=\tilde{\varepsilon}_j$. In the third case, called the Bruggeman approximation (EMA), $\tilde{\varepsilon}$ is found self-consistently by assuming that $\tilde{\varepsilon}=\tilde{\varepsilon}_h$, in other words, the dielectric function of the effective medium and the dielectric function of the host medium are assumed to be the same. The Bruggeman approximation has been the most widely applied for the characterization of isotropic mixtures of semiconducting and dielectric materials when the volume fractions of the different components are of the same order. Recently, Fujiwara et al. have shown, on the basis of RTSE measurements, that the EMA indeed provides a better description over the LL and MG approximations for surface roughness layers on amorphous silicon films (Fujiwara *et al.*, 2000a). Finally, it is important to emphasize that such EMTs are valid only in cases in which the size of

each component region is large enough such that bulk dielectric response of the material is retained, otherwise size-modified component dielectric functions are required. On the other hand, the size and/or the in-plane spacing between these regions must be much smaller than the wavelength of the probing light. For example, for surface roughness layers such that the inhomogeneities are of the order of the light wavelength (called macroscopic roughness), diffusive scattering described in terms of random diffraction will be present (Beckmann and Spizzichino, 1963).

In this research, the Bruggeman approximation, or EMA, is used throughout to describe surface and interface roughness layers. In this approximation, Eq. 2.16 becomes

$$\sum_i f_i \frac{\tilde{\varepsilon}_i - \tilde{\varepsilon}}{\tilde{\varepsilon}_i + 2\tilde{\varepsilon}} = 0. \tag{2.17}$$

2.3 ROTATING-COMPENSATOR MULTICHANNEL ELLIPSOMETER

2.3.1 Instrument set-up

The rotating-compensator multichannel ellipsometry set-up consists of the following elements in sequence from the source to the detector (see Fig. 2.3):

(i) Light source: 75 W Xe arc lamp; emits a continuous spectrum from 1.5 to 5.0 eV.

(ii) Collimating optics: single lens + pinhole + achromatic lens.

(iii) Fixed polarizer: quartz Rochon prism-type; imposes a known linear polarization state on the incident beam. It can be rotated via a stepping motor for calibration purposes.

(iv) Shutter.

(v) Sample: inside the PECVD reactor optically-accessible through strain-free optical windows.

(vi) Continuously rotating compensator: zero-order MgF_2 biplate; modulates the polarization state of the beam reflected from the sample. The typical rotation

frequency is 12 Hz. An optical encoder is attached to the motor shaft that produces pulses to trigger the detector controller.

(vii) Fixed analyzer: MgF_2 Rochon prism; deconvolves the polarization state of the modulated light beam. It can be rotated via a stepping motor for calibration purposes

(viii) Focusing optics.

(ix) Spectrograph: 1/4 m Littrow single prism-type.

(x) Detector: 1024-pixel silicon photodiode array with controller; grouped by eight in all studies.

Instrument control and data acquisition are performed by a computer through an IEEE 488 board.

In addition to the introduction of the rotating-compensator, some modifications were made to the previous rotating-polarizer configuration in order to improve the optical response of this instrument in the near-UV region of the spectra. These modifications included (i) optimization of the collimating optics by the introduction of a pinhole and UV-achromatic lens; (ii) optimization of the detection optics by introduction of a UV-achromatic lens placed right before the entrance slit of the spectrograph. The role of the latter lens is to refocus the light beam (Zapien *et al.*, 2000). Finally (iii) the back surface of the Littrow prism was repolished and recoated by (Universal Thin Films Lab, 232 N Planck Rd, Newburgh, NY 12550, Ph:914-562-0601) in order to reduce stray light.

2.3.2 Data Acquisition and Reduction

In the rotating-element type ellipsometers, the quantities of interest are determined by Fourier analysis of the modulated output irradiance. Specifically, in the rotating-compensator configuration the dc, second, and fourth order Fourier coefficients are non-zero —as opposed to only the dc and second order coefficients in the rotating-polarizer (analyzer) configuration. As a result, the output irradiance detected by each pixel group is given as a function of time by (Lee *et al.*, 1998a)

$$I(t) = I_0[1+\alpha_2'\cos(2\omega_C t)+\beta_2'\sin(2\omega_C t)+\alpha_4'\cos(4\omega_C t)+\beta_4'\sin(4\omega_C t)], \qquad (2.18)$$

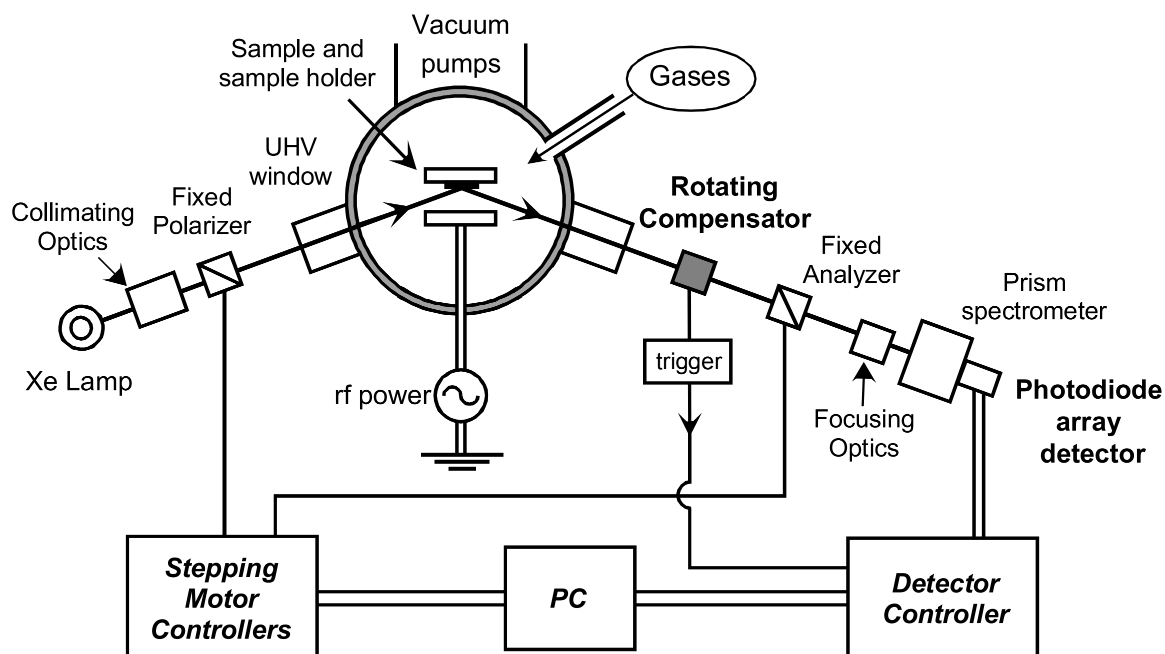

Figure 2.3 Schematic drawing of a rotating-compensator multichannel ellipsometer apparatus attached to a PECVD reactor. Details of the set-up are given in the text.

where I_0 is the time averaged irradiance, and ω_C is the angular frequency of the compensator mechanical rotation. The detection of the spectra in the experimental Fourier coefficients $(\alpha_m', \beta_m'; m = 2,4)$ and the spectra in I_0 is performed in fully parallel mode due to the integration characteristic of the spectrograph/photodiode array detection system. Each group of photodiode pixels along the array continuously accumulates a signal proportional to the number of incoming photons of a given wavelength (with the exception of those photons arriving within a very short readout time). The readout of each pixel group is triggered N times per optical rotation of the compensator by a TTL pulse generated by an optical encoder mounted on the shaft of the compensator motor. One must set $N \geq 5$ in order to extract enough information so that the five independent spectra in the Fourier coefficients can be determined. As a result, the readout of each pixel group is the integration of the modulated irradiance over a fraction 1/N of the compensator optical cycle:

$$S_j = \int_{(j-1)T_C/N}^{jT_C/N} I(t)dt; \quad j = 1,..,N. \tag{2.19}$$

Here T_C is the optical period ($T_C=\pi/\omega_C$) and S_j is the jth integrated readout (or j^{th} sum) for each pixel group. In this instrument, N is set to 8 for compatibility with the original configuration of the optical encoder. I_0 and $(\alpha_m', \beta_m'; m = 2,4)$ can be related to the sums S_j through the following transformations:

$$I_0 = \frac{1}{\pi}\sum_{j=1}^{8} S_j \ , \tag{2.20a}$$

and

$$\mathbf{F} = \mathbf{H} \cdot \mathbf{S}, \tag{2.20b}$$

where $\mathbf{F} = [\alpha_2', \beta_2', \alpha_4', \beta_4']^T$, $\mathbf{S}$ is the eight-component column vector containing the sums S_j and $\mathbf{H}$ is given by

$$\mathbf{H} = \frac{\pi}{2I_0}\begin{bmatrix} 1 & 1 & -1 & -1 & -1 & -1 & 1 & 1 \\ 1 & 1 & 1 & 1 & -1 & -1 & -1 & -1 \\ 1 & -1 & -1 & 1 & 1 & -1 & -1 & 1 \\ 1 & 1 & -1 & -1 & 1 & 1 & -1 & -1 \end{bmatrix}. \tag{2.21}$$

Since five spectra are being derived from eight spectra, there are several possible relations among them. The matrix **H** was chosen with all elements non-zero and of equal magnitude so that each of the $(\alpha_m', \beta_m'; m=2,4)$ spectra is determined by weighting all of the S_j spectra equally, thus minimizing the propagation of random and systematic experimental errors.

The deduced spectra in the Fourier coefficients $(\alpha_m', \beta_m'; m=2,4)$ can be related to the spectral characteristics of the sample by first analyzing the polarization changes in the light beam as it passes through the optical elements of the instrument. In this analysis the Mueller matrix formalism is applied as follows (Azzam and Bashara, 1977). The Stokes vector $\mathbf{S}_{OUT}$ describing the output light beam arriving at the detector in the analyzer frame of reference is given in terms of the Stokes vector $\mathbf{S}_{SAMPLE}$ of the light beam reflected from the sample by

$$\mathbf{S}_{OUT} = I_{00}\frac{I_r}{I_i}\mathbf{M}_A\,\mathbf{R}(A')\mathbf{R}(-C')\mathbf{M}_C(\delta)\mathbf{R}(C')\cdot\mathbf{S}_{SAMPLE}\,. \tag{2.22}$$

Here I_{00} is the spectral throughput of the instrument and (I_r/I_i) is the ratio of reflected to incident irradiance for the polarized light wave reflected from the sample. $\mathbf{M}_A$ and $\mathbf{M}_C(\delta)$ are the Mueller matrices for the analyzer and the compensator, given by (Azzam and Bashara, 1977)

$$\mathbf{M}_A = \begin{bmatrix} 1 & 1 & 0 & 0 \\ 1 & 1 & 0 & 0 \\ 0 & 0 & 0 & 0 \\ 0 & 0 & 0 & 0 \end{bmatrix} \tag{2.23}$$

and

$$\mathbf{M}_C(\delta) = \begin{bmatrix} 1 & 0 & 0 & 0 \\ 0 & 1 & 0 & 0 \\ 0 & 0 & \cos\delta & \sin\delta \\ 0 & 0 & -\sin\delta & \cos\delta \end{bmatrix}. \tag{2.24}$$

In Eq. 2.24, δ is the compensator retardance, which is wavelength dependent for an element of the biplate type. This spectral dependence generates additional complexity in

the instrument characterization/calibration in comparison to the previous rotating-polarizer configuration, which employs only achromatic polarization-modifying elements. Details of the wavelength calibration of the compensator retardance will be given in Sec. 2.3.3. In Eq. 2.22, $\mathbf{R}(\theta)$ designates the Mueller rotation matrix needed to transform to the optical element reference frame from the p-s laboratory frame. The latter frame is established such that the p and s directions are defined as parallel and perpendicular to the plane of incidence, respectively. All angles are defined as measured counterclockwise-positive from the p-direction when facing the light source. $\mathbf{R}(\theta)$ is given by

$$\mathbf{R}(\theta) = \begin{bmatrix} 1 & 0 & 0 & 0 \\ 0 & \cos 2\theta & \sin 2\theta & 0 \\ 0 & -\sin 2\theta & \cos 2\theta & 0 \\ 0 & 0 & 0 & 1 \end{bmatrix}. \tag{2.25}$$

In Eq. 2.22, A' is the true azimuthal angle of the analyzer, given by $A' = A - A_S$, where A is the angular reading and A_S is the correction to the reading. A_S can be determined in calibration using procedures described in details elsewhere (Lee *et al.*, 1998a). Analogously, C' is the true azimuthal angle of the compensator. $\mathbf{S}_{SAMPLE}$ in Eq. 2.22 is the normalized Stokes vector describing the light beam reflected from the sample in a general elliptical polarization state and is given by (Azzam and Bashara, 1977):

$$\mathbf{S}_{SAMPLE} = \begin{bmatrix} 1 \\ p\cos 2\chi \cos 2Q \\ p\cos 2\chi \sin 2Q \\ p\sin 2\chi \end{bmatrix}. \tag{2.26}$$

Here, p is the degree of polarization describing the fraction of light reaching the detector that is completely polarized, $0 \le p \le 1$. Q and χ are the polarization angles defined in Sec. 2.2.1 and depicted in Fig. 2.1 ($-90° < Q \le 90°$ and $-45° \le \chi \le 45°$). After calculating the matrix product in Eq. 2.22, involving extensive manipulations, the theoretical output irradiance is determined as

$$I(t) = I_{00}\frac{I_r}{I_i}\alpha_0[1+\alpha_2\cos 2C' + \beta_2\sin 2C' + \alpha_4\cos 4C' + \beta_4\sin 4C'], \tag{2.27}$$

where

$$\alpha_0 = 1 + \left\{p\cos^2(\delta/2)\cos 2\chi\cos 2(A'-Q)\right\}, \tag{2.28a}$$

$$\alpha_2 = (p\sin\delta\sin 2\chi\sin 2A')/\alpha_0, \tag{2.28b}$$

$$\beta_2 = (-p\sin\delta\sin 2\chi\cos 2A')/\alpha_0, \tag{2.28c}$$

$$\alpha_4 = \left\{p\sin^2(\delta/2)\cos 2\chi\cos 2(A'+Q)\right\}/\alpha_0, \tag{2.28d}$$

$$\beta_4 = \left\{p\sin^2(\delta/2)\cos 2\chi\sin 2(A'+Q)\right\}/\alpha_0 . \tag{2.28e}$$

Because the compensator is continuously rotating, C' is given by $C' = \omega_C t - C_S$, where $-C_S$ is the angle of the compensator fast axis at t=0. This latter angle can be found in calibrations procedures described elsewhere (Lee *et al.*, 1998a). In order to deduce the theoretical spectra in the Fourier coefficients $(\alpha_m, \beta_m;\ m = 2{,}4)$ from the measured spectra $(\alpha_m', \beta_m';\ m = 2{,}4)$, the following rotation transformation is necessary

$$\alpha_m = \alpha_m'\cos(mC_S) + \beta_m'\sin(mC_S), \tag{2.29a}$$

$$\beta_m = -\alpha_m'\sin(mC_S) + \beta_m'\cos(mC_S);\ m = 2,4. \tag{2.29b}$$

The average irradiance I_0 at the detector is given by

$$I_0 = I_{00}\frac{I_r}{I_i}\alpha_0 . \tag{2.30}$$

When the sample is non-depolarizing, I_r/I_i represents the sample reflectance, which can also be used to gain information about the sample (Rovira, 2000).

A summary of the procedures for data collection is described next. First, spectra in the experimental light wave irradiance $\{S_j;\ j=1,\ldots,8\}$ are measured and converted to spectra in the experimental Fourier coefficients $(\alpha_m', \beta_m';\ m = 2{,}4)$. Next, the experimental Fourier coefficients are transformed into their theoretical counterparts $(\alpha_m, \beta_m;\ m = 2{,}4)$ once C_S is obtained through calibration. Finally, the Stokes vector

parameters defining the polarization state of the light beam leaving the sample can be determined, assuming that the analyzer azimuthal angle A' and the spectral retardance of the compensator δ(E) have been determined through previous calibration procedures (Lee *et al.*, 1998a, Lee *et al.*, 2001). From the inversion of Eqs. 2.28, the Stokes vector parameters of the reflected light beam can be described as functions of $(\alpha_m, \beta_m; m=2,4)$, A', and δ, according to

$$Q = \frac{1}{2}\tan^{-1}\left(\frac{\beta_4}{\alpha_4}\right) - A', \tag{2.31a}$$

$$\chi = \frac{1}{2}\tan^{-1}\left[\frac{1}{2}\tan(\delta/2)\left(\frac{\alpha_2^2+\beta_2^2}{\alpha_4^2+\beta_4^2}\right)^{1/2}\right], \tag{2.31b}$$

$$\chi = \frac{1}{2}\tan^{-1}\left[\frac{\alpha_2\cos 2(A'+Q)\tan(\delta/2)}{2\alpha_4\sin 2A'}\right], \tag{2.31c}$$

$$\chi = \frac{1}{2}\tan^{-1}\left[\frac{-\beta_2\sin 2(A'+Q)\tan(\delta/2)}{2\beta_4\cos 2A'}\right], \tag{2.31d}$$

$$p = \frac{\Re_Q}{\cos 2\chi\cos 2(A'-Q)\{1-(1+\Re_Q)\cos^2(\delta/2)}, \tag{2.31e}$$

$$\Re_Q = \alpha_4\cos 4Q + \beta_4\sin 4Q\ . \tag{2.31f}$$

Here the magnitude of χ should be obtained from Eq. 2.31b, while the sign of χ can be determined from either Eq. 2.31c or Eq. 2.31d.

The final step is to determine the ellipsometric angles (ψ, Δ) associated with the sample as a function of the Stokes vector parameters of the beam reflected from the sample and the polarizer azimuthal angle P'. Again, resorting to the Mueller matrix formalism, the Stokes vector reflected from the sample is described by

$$\mathbf{S}_{SAMPLE} = \mathbf{M}_{SAMPLE}\cdot\mathbf{S}_{POL} \tag{2.32}$$

where $\mathbf{M}_{SAMPLE}$ is the Mueller matrix of the sample. For an isotropic non-depolarizing sample, the normalized Mueller matrix can be defined as a function of the ellipsometric angles (ψ, Δ) as (Azzam and Bashara, 1977)

$$\mathbf{M}_{SAMPLE} = \begin{bmatrix} 1 & -\cos 2\psi & 0 & 0 \\ -\cos 2\psi & 1 & 0 & 0 \\ 0 & 0 & \sin 2\psi \cos\Delta & \sin 2\psi \sin\Delta \\ 0 & 0 & -\sin 2\psi \sin\Delta & \sin 2\psi \cos\Delta \end{bmatrix}. \tag{2.33}$$

In Eq. 2.32, $\mathbf{S}_{POL} = [1,\ \cos 2P',\ \sin 2P',\ 0]^T$ is the normalized Stokes vector of the light beam emerging from the polarizer when its azimuthal angle is P'. Comparing the results of the product in Eq. 2.32 with the Stokes vector defined in Eq. 2.22, the following relations are found (Collins *et al.*, 2001):

$$\tan\Delta = -\frac{\tan 2\chi}{\sin 2Q}, \tag{2.34a}$$

$$\tan\psi = |\tan P'|\left[sy + \sqrt{y^2+1}\right], \tag{2.34b}$$

where

$$y = \frac{|\cos 2Q|}{\left|\left(\tan^2 2\chi + \sin^2 2Q\right)^{1/2}\right|}, \tag{2.34c}$$

and $s \equiv \mathrm{sgn}(\psi - |P'|)$.

The sign of Δ can be determined from the following two equations:

$$\cos\Delta = \frac{p\cos 2\chi \sin 2Q\,(1-\cos 2P'\cos 2\psi)}{\sin 2P'\sin 2\psi}, \tag{2.35a}$$

$$\sin\Delta = \frac{-p\sin 2\chi\,(1-\cos 2P'\cos 2\psi)}{\sin 2P'\sin 2\psi}. \tag{2.35b}$$

Equations 2.34 and 2.35 reflect some advantages of the rotating-compensator configuration. First, the sign of Δ can be retrieved from the angle χ, and, second, the measurement sensitivity is uniform over the entire range of Δ (–180°≤Δ≤180°) since it is derived from the inverse tangent function. This enables precise measurements of

transparent films and film growth processes on transparent substrates (where Δ is close to 0° or 180°) (Lee *et al.*, 1998a).

The ability to measure the degree of polarization p for the light beam reaching the detector is also important. First of all, p is very sensitive to non-idealities of the instrument itself. For example, if there is a significant contribution of stray light to the detector output, one finds that $p < 1$. Furthermore, if the measured sample is non-ideal, i.e., part of the light beam loses its polarization upon reflection from the sample, p will also be reduced from unity. An example of the analysis of the depolarization spectra for samples with thickness inhomogeneities has been given previously (Lee *et al.*, 1998b).

2.3.3 Calibration of compensator retardance

The compensator is the principal optical component of a rotating-compensator ellipsometer. Therefore, its selection, alignment and calibration are very important steps for successful implementation and operation of this instrument configuration. The type of compensator chosen for this instrument is a zero-order biplate, and the optical material chosen was MgF_2, which has a high transmittance in the visible and near-UV range and does not exhibit optical activity. Bi-plate compensators consist of two thin plates of a birefringent crystal aligned such that the fast axes are perpendicular. This set-up is very compact and mechanically rigid, making it suitable for applications in which the compensator is rotated continuously. Unfortunately, this type of compensator presents some drawbacks. First, it is chromatic, i.e., its retardance is dependent on the photon energy. As a consequence, for certain photon energy ranges, $\delta(E)$ can be far from the quarter-wavelength condition (δ=90°), where the instrument has the highest overall performance. Second, the compensator must be internally aligned to ensure that the fast axes of the individual plates are precisely perpendicular, otherwise $\delta(E)$ exhibits high frequency oscillations (Aspnes, 1971). In order to perform a relative alignment between the two plates, a procedure was developed as described in detail elsewhere (Rovira, 2000; Lee *et al.*, 2001).

The calibration of the compensator retardance versus wavelength can be performed by several methods (Lee *et al.*, 2001). These methods can be separated into two categories: (i) ex situ calibration, e.g. measurement of the compensator as a "sample" in a rotating polarizer or analyzer spectroscopic ellipsometer; and (ii) in situ calibration, whereby the retardance is determined with the compensator in its actual position in the instrument. The in situ methods are preferable since the compensator is not moved after calibration, and thus any effects of slight misalignment are incorporated into the measured retardance. In (Lee *et al.*, 2001), a good agreement between $\delta(E)$ determined by ex situ and in situ methods was obtained; however the in situ calibration was performed in a straight-through configuration, suitable only for transmission ellipsometry measurements. Here, a method is described that is suitable for in situ calibration in the reflection mode. As a result, $\delta(E)$ is determined in the actual sample measurement configuration, after mounting and aligning the sample and with the compensator continuously rotating.

The first step is the determination of the polarizer calibration angle, P_S, which is performed as described previously (Lee *et al.*, 1998a). Once P_S is found, the polarizer is set at $P' = (P{-}P_S) = 0$ or 90°, in order to generate a linear polarization state upon reflection from an isotropic sample. This ensures that the 2ω Fourier coefficients (α_2', β_2') of the output irradiance vanish, yielding the following relation:

$$\left|B_4'\right|^{-1} \equiv \left(\alpha_4'^2 + \beta_4'^2\right)^{-1/2} = \gamma_0 + \gamma_2 \cos 2A + \eta_2 \sin 2A, \qquad (2.36)$$

where (γ_0, γ_2 and η_2) are the coefficients of a Fourier expansion in the analyzer angular setting A. By relating Eqs. 2.28d, 2.28e and 2.36, the following relationships can be derived:

$$\gamma_0 = [\sin^2(\delta/2)]^{-1}, \qquad (2.37a)$$

$$\gamma_2 = \pm\cos 2A_S \cot^2(\delta/2), \qquad (2.37b)$$

$$\eta_2 = \pm\sin 2A_S \cot^2(\delta/2). \qquad (2.37c)$$

Therefore, by collecting the spectra (α_4', β_4') for several analyzer angular settings A from 0 to 180°, the spectra in (γ_0, γ_2, η_2) can be determined from a Fourier analysis of the spectrum in $|B_4|^{-1}$ versus A. Finally, by combining Eqs. 2.37b and 2.37c, the spectrum in δ can be deduced according to

$$\delta(E) = 2\tan^{-1}\left[\left(\gamma_2{}^2 + \eta_2{}^2\right)^{-1/4}\right]. \tag{2.38}$$

As an example, the results for a calibration performed with a c-Si wafer are presented here. Figure 2.4a depicts the measured $|B_4|^{-1}$ versus analyzer angular setting A for the pixel group corresponding to a photon energy of 3.2 eV (open symbols). The solid line in Fig. 2.4a represents the $|B_4|^{-1}$ values deduced from the calculated Fourier expansion coefficients (γ_0, γ_2, η_2). As seen in Fig. 2.4b, the difference between the measured and calculated $|B_4|^{-1}$ values is smaller than 0.01 for all A, a result that corroborates the validity of this method.

Figure 2.5(a) depicts the measured $\delta(E)$ spectrum, obtained with the polarizer set at P'=0 (symbols). In order to avoid propagation of random experimental errors in the determination of the ellipsometric angles, the utilization of an analytical expression to describe $\delta(E)$ is preferred over the utilization of "raw" experimental data. The theoretical retardance of a biplate compensator can be approximated by

$$\delta(E) = 360\frac{E}{1239.8}d\Delta n \text{ [in degrees].} \tag{2.39}$$

Here E is the photon energy (in eV), d is the thickness difference (in nm) between the two MgF_2 plates and Δn is the birefringence of MgF_2. A possible first approach to deduce an analytical expression for $\delta(E)$ is simply to use reference data for the MgF_2 birefringence (Cotter *et al.*, 1991) and determine d in a least-squares regression analysis (LRA) fit. However, if d is kept fixed at this value, there is a poor agreement between $\delta(E)$ deduced by this approach and $\delta(E)$ obtained in the experiment. Therefore, in a second approach a fixed value for d is determined by the previous approach and then a LRA of $\delta(E)$ is performed by describing Δn as a polynomial function of 4th order. This approach yields an expression of the form:

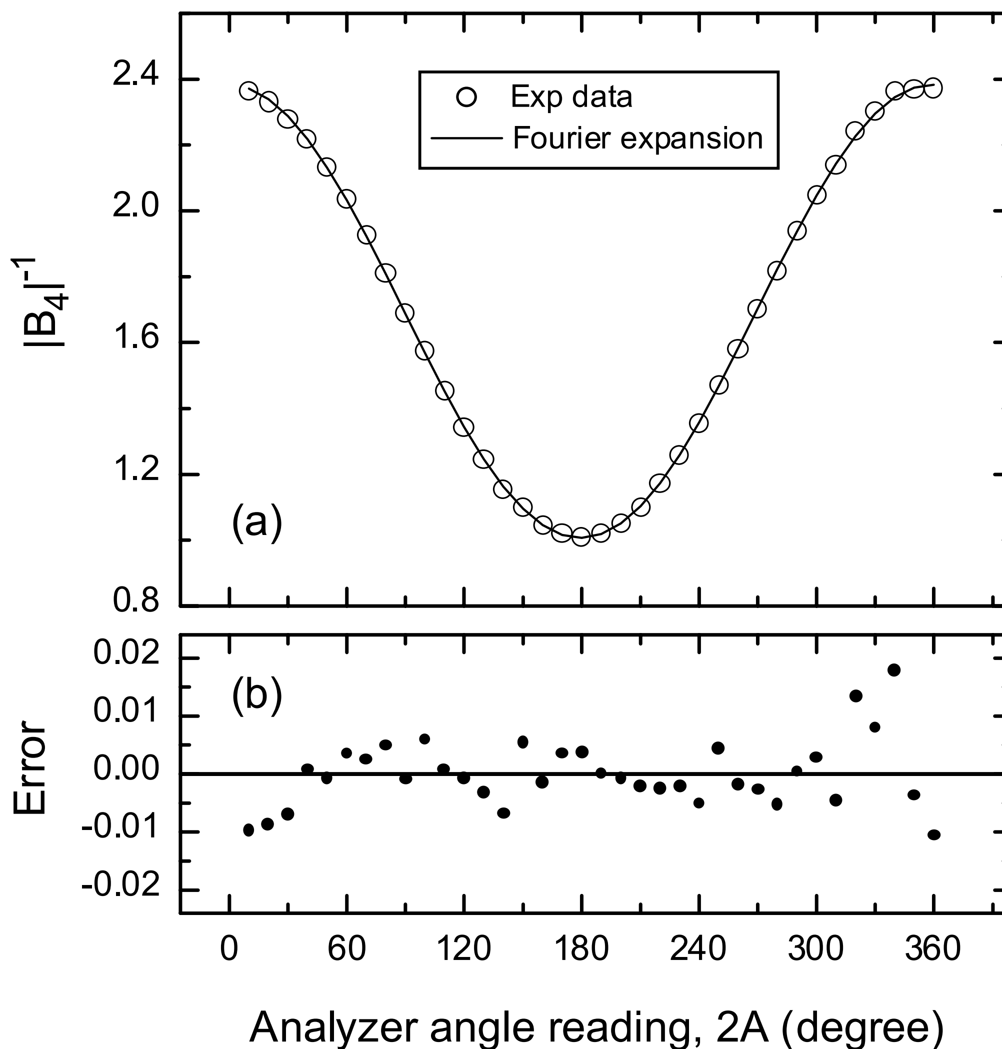

Figure 2.4 Results for the Fourier expansion applied in the in situ calibration of the compensator retardance. (a) $|B_4|^{-1}$ is plotted versus analyzer angular setting 2A for the pixel group corresponding to a photon energy of 3.2 eV. The open symbols are the experimental data, and the solid line represents the values calculated from the best fit Fourier coefficients obtained in the Fourier analysis. (b) The difference between the experimental and calculated values of $|B_4|^{-1}$ is plotted.

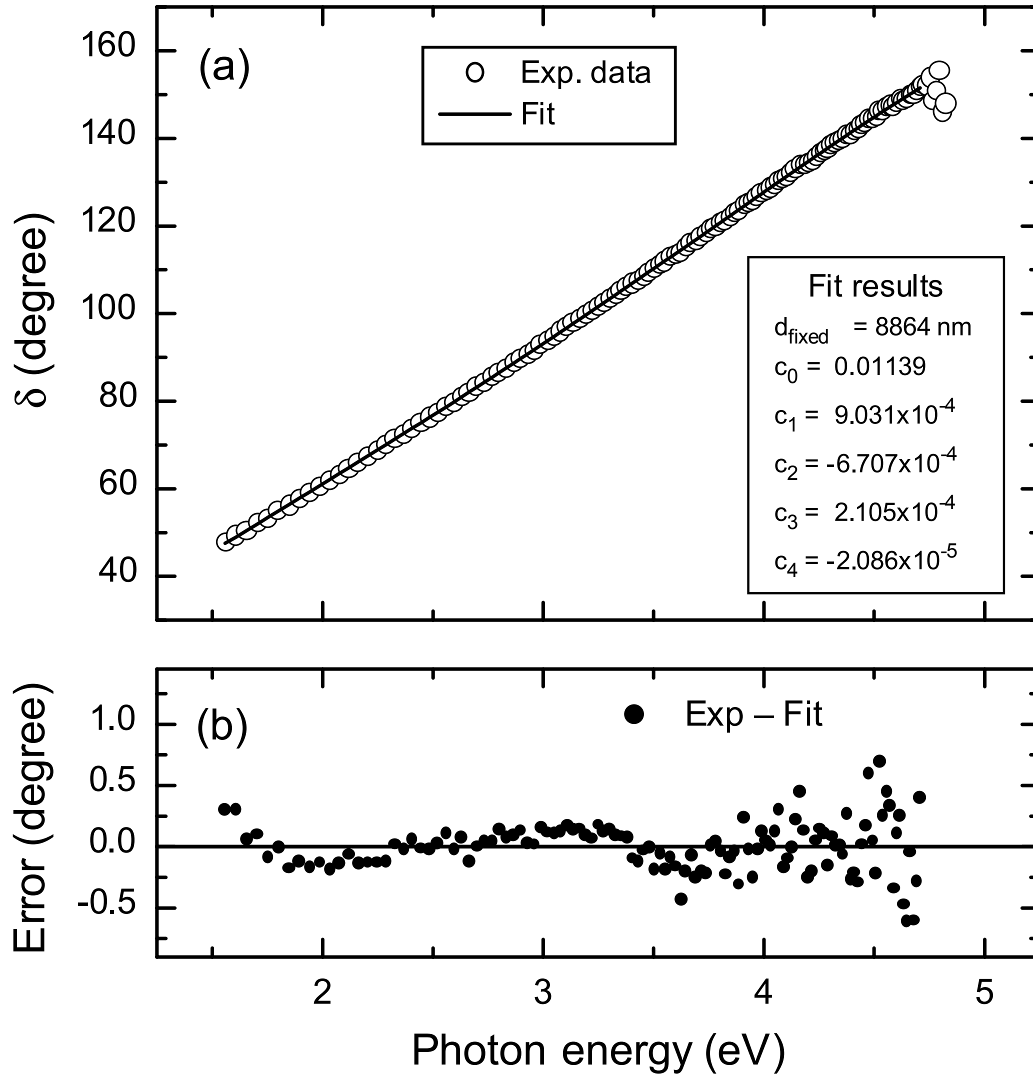

Figure 2.5 (a) Measured retardance δ spectrum (points) and its best-fit (line) versus photon energy for the MgF_2 biplate compensator. The measured spectrum was obtained through the in situ calibration method described in the text and in Fig. 2.3. Equation 2.40 was used for the fit with the thickness fixed d at 8864 nm. The best-fit results of the polynomial coefficients c_k (k=0 to 4) for the MgF_2 birefringence are listed in the figure in units of $\deg\cdot nm^{-1}\cdot(eV)^{-(k+1)}$. In (b) the difference between the experimental and best-fit spectra in δ is shown.

$$\delta(E) = 360 \frac{E}{1239.8} d_{fixed} \sum_{k=0}^{4} c_k E^k . \quad (2.40)$$

The solid line in Fig. 2.5b represents the best-fit results obtained with d_{fixed}= 8864 nm. The best-fit polynomial coefficients c_k are listed in the figure [in units of deg·nm^{-1}·(eV)$^{-(k+1)}$]. The quarter-wave energy is E_Q=2.91 eV (λ_Q=426 nm). Figure 2.5(b) depicts the difference between the data and best-fit spectra in δ, providing an assessment of the accuracy and precision of this method.

2.4 DATA ANALYSIS

In spectroscopic ellipsometry (SE), the interpretation of the experimental data is a critical step for the extraction of useful physical information on the measured sample. SE is an indirect technique in the sense that the measured quantities, i.e., the spectra in the ellipsometric angle [ψ(E), Δ(E)], which represent the changes on the polarization state of a light beam upon reflection from the sample, cannot provide direct quantitative information about the sample properties. Hence, data analysis procedures must begin with a model that includes the optical properties and microstructure of the thin-film sample.

2.4.1 Least-squares regression analysis

The most common approach for the interpretation of SE data sets collected for thin film samples relies on least-squares regression analysis (LRA). If all the component materials of the sample structure and their dielectric functions are known, photon energy-independent parameters describing the sample microstructure, such as layer thicknesses and material volume fractions, can be deduced by fitting the experimental spectra. In addition, if the dielectric function of a certain material is unknown, it can be described as a function of photon energy-independent parameters, and these parameters can be deduced in the LRA as well.

The first step in the LRA is to adopt a physically reasonable multilayer model for the sample structure. The photon energy independent parameters will be the layer thicknesses and the volume fractions of component materials in each layer. The dielectric function of any composite layer is determined from the dielectric functions of each component material through the EMA, as described in Sec. 2.2.3. Surface roughness and interface layers can be simulated in this way. A numerical algorithm is then used to minimize the differences between the spectra calculated from the chosen model and the experimental spectra by minimizing the square of the unbiased estimator. This quantity denoted σ^2 is defined by

$$\sigma^2 = \frac{1}{NM - p - 1}\sum_{j=1}^{M}\sum_{i=1}^{N}\left[g_{j,exp}(E_i) - g_{j,cal}(E_i,\mathbf{x})\right]^2 , \tag{2.41}$$

where N is the number of spectral data points, M is the number of data sets, and p is the number of free parameters. The functions $g_{j,exp}(E_i)$ and $g_{j,cal}(E_i,\mathbf{x})$ represent the experimental and calculated quantities at the photon energy E_i for the jth data set, and $\mathbf{x}$ denotes a vector of size p containing the free parameters (Jellison, 1998).

In ellipsometry, two experimental quantities are measured simultaneously (M=2), corresponding to the pair of ellipsometric spectra (ψ, Δ). In fact, quantities that may be more suitable than (ψ, Δ) are usually chosen for g_j depending on the instrument configuration. For the rotating-compensator configuration, the real and imaginary parts of the complex amplitude reflection ratio $\tilde{\rho}$ are chosen because they provide improved sensitivity over the entire range of Δ ($-180° < \Delta \leq 180°$) and because they preserve the sign of Δ. As a result, Eq 2.41 can be written as

$$\sigma^2 = \frac{1}{2N - p - 1}\sum_{i=1}^{N}\left\{\left[\mathrm{Re}\,\tilde{\rho}_{j,exp}(E_i) - \mathrm{Re}\,\tilde{\rho}_{j,cal}(E_i,\mathbf{x})\right]^2 + \left[\mathrm{Im}\,\tilde{\rho}_{j,exp}(E_i) - \mathrm{Im}\,\tilde{\rho}_{j,cal}(E_i,\mathbf{x})\right]^2\right\}. \tag{2.42}$$

After the minimum in the unbiased estimator σ is found, the best-fit parameter values together with their 90% confidence limits can be deduced. In addition, the degree of correlation between the parameters can be assessed by inspecting the correlation matrix. This statistical information is used in turn to assess the validity of the optical model. For

example, if the confidence limits on a given parameter are larger than the parameter value itself, this parameter is not justified in the model and should be discarded or fixed (if its value is affirmed by other measurements).

2.4.2 Mathematical inversion

If the microstructural parameters are known *a priori* by the utilization of other characterization techniques or if they are assigned trial values as the first step of a more comprehensive analysis, then one can apply the equations based on the multilayer optical analysis to determine one unknown dielectric function from the (ψ, Δ) spectra. However, because the equations of Sec 2.2.2 are highly non-linear, it is impossible to find closed form solutions relating the unknown (ε_1, ε_2) spectra to the experimental (ψ, Δ) spectra. As a result, one must rely on a numerical method. In this method, designated exact inversion, the roots of the error function computed between the experimental and calculated (ψ, Δ) spectra are found by means of an iterative algorithm based on Newton's method.

The exact inversion approach is suitable for the determination of the dielectric functions of opaque thin films when the surface layers can be characterized independently from other techniques. Alternatively, trial values for one or more microstructural parameters such as the roughness layer thickness can be used to generate a trial result for the unknown dielectric function, which can then be compared to results from other techniques. This approach is used in Chapter 6. In this Chapter, the extinction coefficient k spectra (or α) obtained from exact inversion of SE data and from transmission and reflection spectroscopy (T&R) are compared in order to determine the value of the surface roughness layer thickness d_s for which the two spectra overlap. The surface roughness layer (which is modeled with the EMA) is introduced in the optical model to account for the roughness *and* the native oxide layers on the film surface. Due to the complexity of the surface and the similarities between the dielectric functions for a-Si:H/void and a-Si:H/SiO_2 mixtures, the two layers are difficult to be distinguished. As a consequence, the effect of the surface layers on the optical properties is eliminated in the

analysis and the true dielectric function of the bulk film can be determined (Dawson *et al.*, 1992).

Alternatively, the correct dielectric function for a given bulk thin film can be determined by choosing the microstructural parameters, such as bulk layer and roughness layer thicknesses, that minimize artifacts in the inverted (ε_1, ε_2) spectra. These artifacts can originate from interference fringes or from the substrate optical response when the incorrect microstructural parameters are chosen (Aspnes *et al.*, 1984).

Finally, when analyzing RTSE data, one can take advantage of the available (ψ, Δ) spectra as a function of time to determine both the microstructural parameters and the dielectric function of the film material in a self-consistent approach that uses both the mathematical inversion and LRA. This approach is described in the next section.

2.4.3 Global $\bar{\sigma}$-minimization method for RTSE data analysis

In most thin film deposition processes, the dielectric function of the resulting film depends on the deposition conditions. For this reason, a complete analysis of the RTSE spectra [$\psi(E,t)$, $\Delta(E,t)$] must provide (i) time (t)-independent parameters as a function of photon energy, i.e., the dielectric function spectra of the film, and (ii) photon energy (E)-independent parameters as a function of time, i.e., the time evolution of the microstructural parameters such as bulk layer and surface roughness layer thicknesses, material composition, etc. For this purpose, a minimization method combining mathematical inversion and least-squares regression analysis (LRA) has been developed (An *et al.*, 1990). A refinement of this method is described in the following paragraphs. First, however, a brief description of substrate analysis is required.

The substrate must be characterized prior to the deposition. For the case of crystalline silicon (c-Si), spectra in (ψ, Δ) at room temperature are measured and the thickness of the native oxide (SiO_2) layer is determined by using the known dielectric functions of c-Si and SiO_2. After the substrate is heated to the deposition temperature, new (ψ, Δ) spectra are collected, and the true dielectric function of the substrate is obtained by means of mathematical inversion. In this procedure, it is assumed that the

thickness and dielectric function of the oxide layer remain constant upon heating, which is reasonable for the range of temperatures explored in this research (T<300°C).

In the first step of the analysis of data collected during film growth a suitable optical model must be chosen. Figure 2.6 depicts a two-layer optical model used in the analysis of bulk film growth on a smooth substrate such as c-Si. In this model, the variable microstructural parameters of the film include the bulk layer thickness d_b and the surface roughness layer thickness d_s. The bulk layer material is characterized by its dielectric function ε, and the dielectric response of the roughness layer is determined by the Bruggeman EMA assuming a mixture of (bulk material)/ambient with volume fractions of 0.5/0.5. Previous studies have found that in the initial stages of growth, prior to the formation of a bulk layer, a one-layer model is sufficient to describe the nucleation regime (An *et al.*, 1990; Li *et al.*, 1992). In this case, the variable microstructural parameters include the height of the layer and the volume fraction of the material within the layer. It was found that as the film becomes continuous, the void volume fraction stabilizes near 0.5 and this layer is incorporated as the surface roughness layer (An 1992b).

Figure 2.7 presents a schematic of the global $\overline{\sigma}$-minimization method. This method assumes that the dielectric function of the bulk layer is independent of thickness over a time regime ($t_0 \le t \le t_f$) around $t = t_i$. Mathematical inversion is used to determine a dielectric function for the bulk film (ε_1, ε_2) from the (ψ, Δ) spectra at $t=t_i$, assuming trial values for the structural parameters (d_b, d_s). The trial (ε_1, ε_2) is then used as a reference dielectric function for the bulk film in the LRA of the (ψ, Δ) spectra for ($t_0 \le t \le t_f$), in order to obtain the time evolution of (d_b, d_s) as well as the time evolution of the unbiased estimator σ. Finally, the average of σ over time is calculated as

$$\overline{\sigma} = \frac{1}{M}\sum_{j=1}^{M}\sigma_j, \tag{2.43}$$

where σ_j is the unbiased estimator for the LRA of the jth pair of spectra. The average is performed from spectra 1 to M, corresponding to $t=t_0$ and $t=t_f$, respectively. Usually, the

time t_i is chosen to correspond to a d_b value of approximately 200Å, and the time range is chosen to correspond to 100 Å ≤ d_b ≤ 300Å.

The above procedure is repeated for N_g^2 different pairs of trials (d_b, d_s) values over a square grid. (N_g is the size of the grid.) If reasonable values for the grid ranges are used (e.g., d_b can chosen based on the estimated growth rate), then $\overline{\sigma}$ is a continuous, well-behaved function of (d_b, d_s) and its minimum can be identified. Subsequent refined grid iterations are performed until either the size of the steps in (d_b, d_s) is less than a given value and/or the minimum in $\overline{\sigma}$ is not reduced further relative to the previous grid iteration. Therefore, the pair of (d_b, d_s) values that yield the minimum $\overline{\sigma}$ corresponds to the correct values at $t=t_i$. An example of one grid iteration with $N_g=7$ for the deposition of an a-Si:H film is depicted in Fig 2.8.

In summary, the results of this method include (i) the bulk dielectric function of the film at $t=t_i$, (ε_1, ε_2), obtained by mathematical inversion; and the time evolution of the microstructural parameters and the LRA unbiased estimator, {$d_b(t)$, $d_s(t)$, $\sigma(t)$} for $t_0 \leq t \leq t_f$. Furthermore, once (ε_1, ε_2) is found, the LRA can be extended to the full deposition data set (i.e., the full range in time), as long as the values of $\sigma(t)$ remain low. This indicates that the assumption of a homogeneous bulk layer holds and a single (ε_{b1}, ε_{b2}) spectra can describe the bulk film. Figure 2.9 present an example of such results for an amorphous silicon film deposition.

The main improvements on the $\overline{\sigma}$-minimization method described above included the introduction of the grid approach and the combination of mathematical inversion and LRA in a single computer program. As a result, a large area in the structural parameter space can be scanned in a short time. In fact, more complex optical models can also be applied routinely that include more than two structural parameters, e.g., the volume fraction of film material filling an underlying rough substrate can also be used as a free parameter (Rovira *et al.*, 1999). Furthermore, in the analysis of multilayer structures (e.g., a complete solar cell deposition), this method can be applied successively for each layer by incorporating the previously analyzed layer in the substrate structure (Koh *et al.*, 1995). Finally, the same approach is valid for deposition of films that are

inhomogeneous through the depth of the film. In this case, the film is analyzed as being composed of series of discrete stacked layers having different optical properties (Ferlauto *et al.*, 2000a).

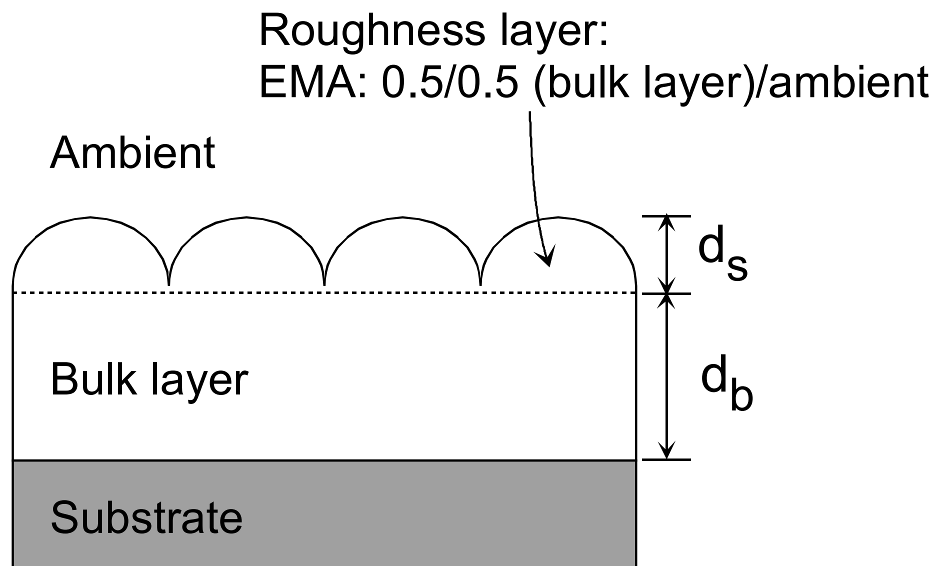

Figure 2.6 Representation of the optical model used in the analysis of thin film growth. This model includes two layers with variable thicknesses: a bulk layer with thickness d_b, and surface roughness layer with thickness d_s. The dielectric function of the roughness layer is determined by the EMA assuming an equal mixture of film material and void [f_v(void) =0.5].

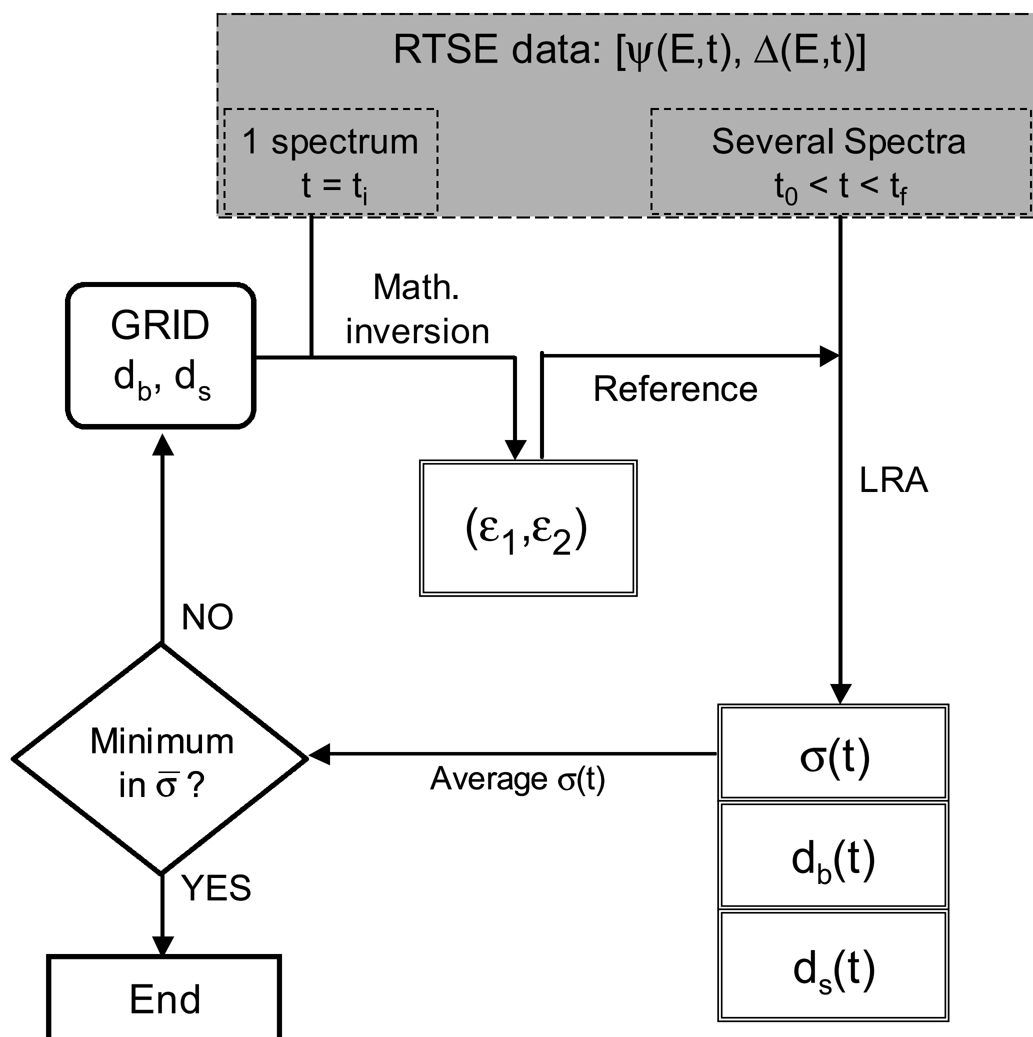

Figure 2.7 Flow chart of the global $\overline{\sigma}$-minimization method for RTSE data analysis.

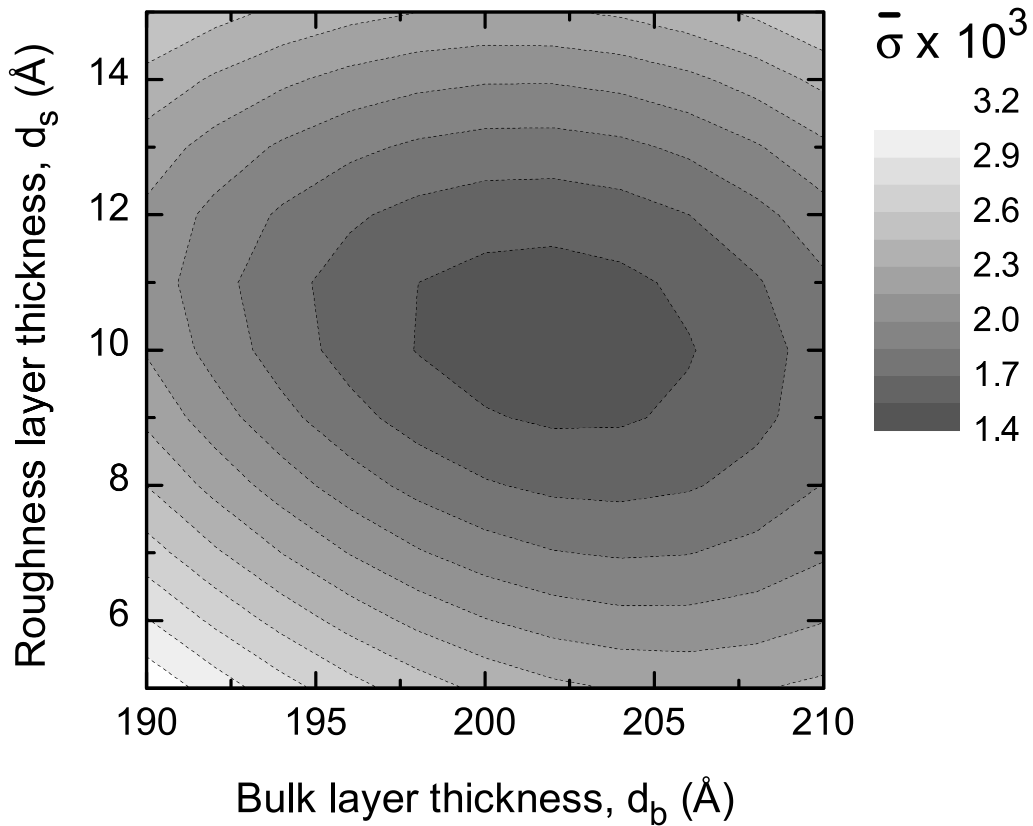

Figure 2.8 Time-averaged unbiased estimator in the LRA ($\overline{\sigma}$) versus the two trial microstructural parameters – the bulk layer (d_b) and roughness layer (d_s) thicknesses – for an a-Si:H deposition. The minimum in $\overline{\sigma}$ defines the correct values of (d_b, d_s) at a given time $t=t_i$.

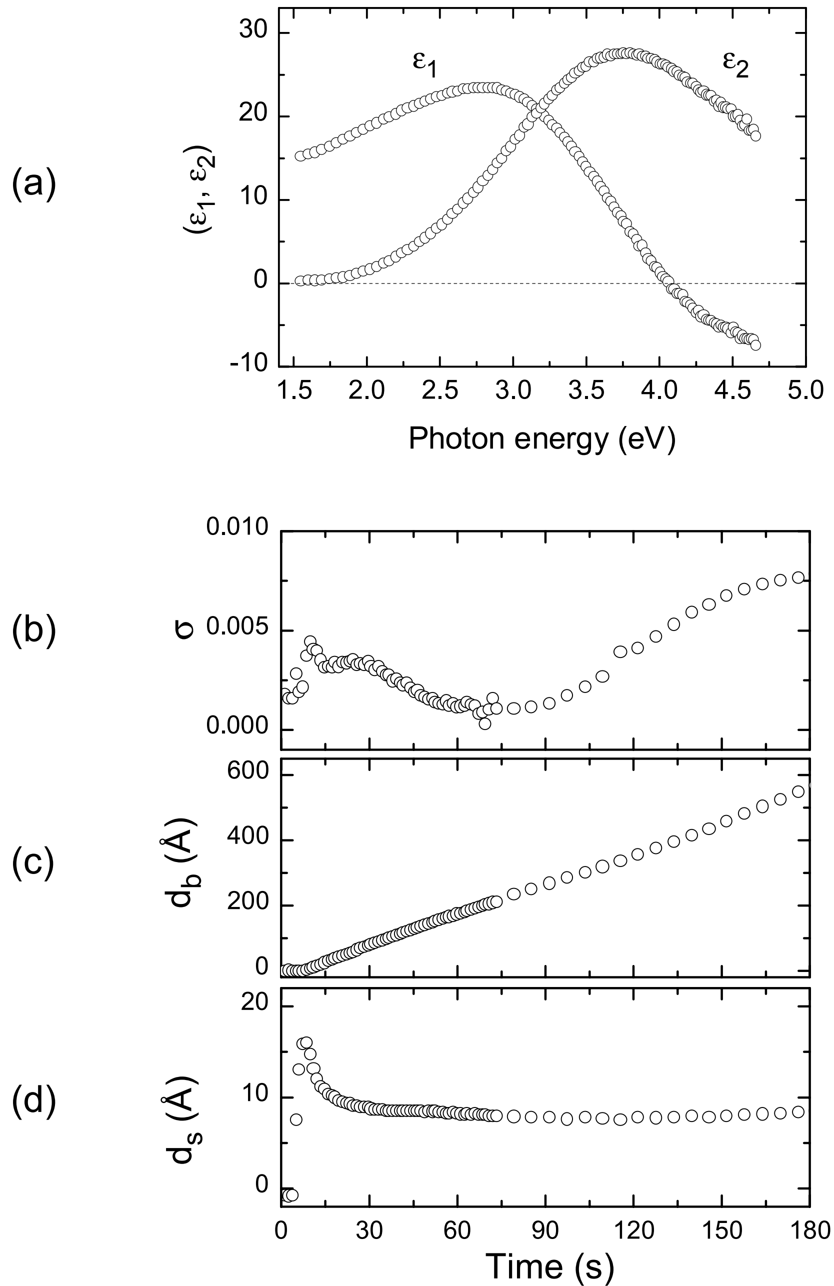

Figure 2.9 Example of the results of the $\overline{\sigma}$-minimization method: (a) real and imaginary parts of the dielectric function (ε_1, ε_2) for an a-Si:H film at a given time $t=t_i$, obtained from mathematical inversion from the values of (d_b, d_s); time evolution of (b) the unbiased estimator σ, (c) the bulk layer thickness d_b, and (d) the roughness layer thickness d_s, all obtained from the LRA by using the (ε_1, ε_2) spectra obtained in (a).

CHAPTER 3

MICROSTRUCTRAL EVOLUTION

IN Si:H THIN FILM GROWTH

3.1 INTRODUCTION

Extensive research over the past three decades has generated a basic understanding of the structural, electronic, and optical characteristics of a-Si:H films (Street, 1991). This research has supported the development of a number of a-Si:H-based large-area devices (Kanicki, 1991). This research has also revealed, however, that a-Si:H material properties and device performance depend sensitively on the fabrication methods and deposition conditions (Tanaka, 1989; Luft and Tsuo, 1993; Bruno *et al.*, 1995). Over the more recent years, as the deposition and device technologies have matured, the focus of a-Si:H research has shifted from studies of basic material properties to studies capable of providing more *direct* information about the deposition and film growth processes that impact materials and devices.

Such studies include three distinct approaches: (i) in situ characterization of the plasma chemistry, that allows correlations to be established between the gas-phase/plasma processes and the material/device properties (Bruno *et al.*, 1995; Matsuda, 1998); (ii) ex situ and static in situ characterization of the surfaces of the films, including the surface morphology by scanning probe techniques (Ikuta *et al.*, 1994; Ikuta *et al.*, 1996; Tanenbaum *et al.*, 1997; Flewitt *et al.*, 1999; Herion, 1999; Ross *et al.*, 2000); and the surface hydrogen bonding by infrared spectroscopy techniques (Toyoshima *et al.*, 1991); (iii) dynamic in situ (or real time) characterization of the films, using optical techniques such as spectroscopic ellipsometry (Collins *et al.*, 2000) and infrared

spectroscopy (Fujiwara *et al.*, 1999b). Such techniques can provide information on the evolution of surface and bulk film microstructure, optical properties, and H-bonding configurations. The detailed relationships between growth processes and material/device properties provided by such studies have helped in further optimization of devices.

As an example, recent studies have revealed that, in plasma enhanced chemical vapor deposition (PECVD) of a-Si:H films, moderate H_2-dilution of the source gases results in improved material/device properties (Lee *et al.*, 1996; Rech *et al.*, 1996; Tsu *et al.*, 1997). In addition, when very high levels of H_2-dilution are employed the formation of μc-Si:H films is favored. In fact, as will be addressed in detail in Chapter 4, a-Si:H films deposited under conditions close to the boundary between a-Si:H and μc-Si:H microcrystalline silicon (μc-Si:H) growth exhibit optimum electronic properties that lead to improved device performance (Koh *et al.*, 1999a). Interestingly, μc-Si:H films deposited under conditions close to the same boundary, but on the μc-Si:H side, also present improved properties (Vetterl *et al.*, 2000).

This chapter is devoted to a detailed discussion of the microstructural evolution of plasma-enhanced chemically-vapor-deposited of Si:H films, as revealed primarily from real time spectroscopic ellipsometry (RTSE) measurements and analyses. First, however a brief description of the deposition processes is given in Sec. 3.2. Then an overview of the main features of the microstructural evolution as observed from RTSE analyses is provided in Sec. 3.4. The experimental results and analyses described in this chapter are separated into two sections. In Sec. 3.5, the results of a detailed investigation are presented concerning the microstructural evolution in the amorphous film growth regime. The RTSE analyses are complemented by atomic force microscopy (AFM) measurements as described in Sec. 3.5.2, and the results from both techniques are compared to theoretical simulations of film growth. In Sec 3.6, the results of a detailed investigation are presented concerning the microstructural evolution of Si:H deposition whereby the amorphous–to–microcrystalline phase transition is observed with increasing film thickness. The RTSE analyses performed in this growth regime are also complemented by AFM measurements as described in Sec. 3.6.1. A phenomenological growth model is

proposed in Sec. 3.6.2 that attempts to interpret the RTSE results in terms of simple geometric parameters. Finally in Sec. 3.6.3, a more sophisticated RTSE analysis is presented.

3.2 DEPOSITION PROCESSES OF Si:H FILMS

The deposition of Si:H films by plasma techniques can be separated into three interlinked processes as depicted in Fig. 3.1, viz., (i) gas phase/plasma processes, (ii) surface processes, and (iii) subsurface processes. These three processes will be described briefly in the next paragraphs; and detailed reviews can be found in the literature (Tanaka, 1989; Abelson, 1993; Bruno *et al.*, 1995).

(i) *Gas-phase processes*:

The primary processes occurring in the gas-phase involve the electron impact-induced dissociation of SiH_4 (or another Si-bearing gas) that generates neutral radicals (SiH_n, n=0,1,…3), as well as excited and ionic species. The primary reactions are controlled by the deposition parameters such as the gas flows, the partial pressures, and the plasma excitation power and frequency. In secondary processes, the reactive species generated in the plasma undergo different types of reactions, mainly with SiH_4 and H_2 molecules (the most abundant species). The secondary reactions are important because on the one hand they provide the beneficial effect of consuming the high reactivity radicals such as SiH_2, thus increasing the relative concentration of low reactivity radicals such as SiH_3 (Matsuda, 1998). On the other hand, under high plasma power and/or pressure conditions, secondary processes lead to detrimental cascade insertion reactions of reactive SiH_2 with SiH_4. As a result, higher silanes build up in the plasma and lead to the formation of polymeric particles (Takai *et al.*, 2000).

The plasma processes have been characterized extensively by using several different techniques (Bruno *et al.*, 1995; Matsuda, 1998). Thus, the concentrations of the plasma species under typical conditions that yield high electronic quality a-Si:H are

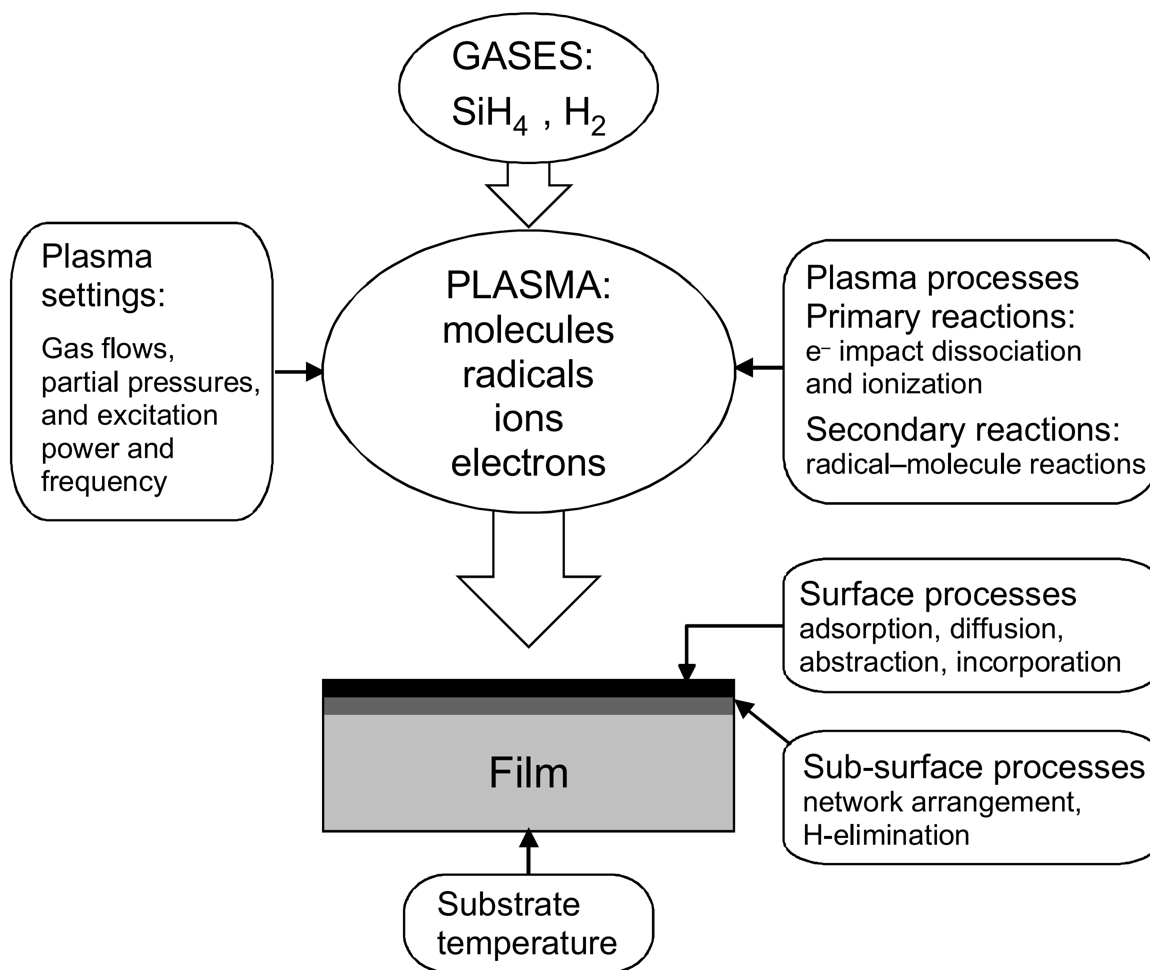

Figure 3.1 Schematic diagram of the processes in Si:H plasma-enhanced chemical vapor deposition, including (i) gas phase/plasma processes, (ii) surface processes, and (iii) sub-surface processes.

reasonably well established. A summary of these concentrations is given in Fig. 3.2, which is based on a review by Matsuda (Matsuda, 1998)

(ii) *Surface processes*

The schematic diagram of Fig. 3.3 depicts the principal processes believed to occur in the near-surface region of a-Si:H during growth, based on proposals by different authors (Matsuda and Tanaka, 1986; Perrin *et al.*, 1989; Matsuda *et al.*, 1990), as reviewed recently by Robertson (Robertson, 2000b). In situ infrared measurements have shown that for substrate temperatures T<300°C, the growing surface is passivated by H atoms (Toyoshima *et al.*, 1991). For the deposition of high electronic quality material

deposition conditions the flux of Si-containing species is believed to be dominated by SiH_3 (Gallagher, 1988; Matsuda, 1998). Unlike the highly reactive SiH_2 and SiH radicals that insert directly into the passivated surface at their impact sites, SiH_3 radicals have a low reactivity and are not readily incorporated into the film. SiH_3 adsorbs in a weakly-physisorbed state, which allows this radical to hop along the surface sampling numerous sites until it either (i) abstracts a surface H, desorbing as SiH_4 and forming one dangling-bond (DB), or (ii) finds a DB and incorporates into the film. In other words, a-Si:H growth is believed to be a two step process, whereby a DB must be created first as a result of surface H abstraction by SiH_3 (or H) so that a second diffusing SiH_3 can incorporate into the film (Doughty *et al.*, 1990). The surface reactions can be quantified in terms of a reaction probability β which is the sum of the probabilities for incorporation (s) and desorption (γ). Thus, β is given by $\beta=(1-r)=(s+\gamma)$, where r is the probability that the radical reflects without reacting (Perrin *et al.*, 1998). Several studies have determined that, for conditions leading to high electronic quality a-Si:H, $\beta \sim 0.2$–0.3 (Doughty *et al.*, 1990; Matsuda *et al.*, 1990), and is independent of temperature from 25°C to 400°C. In addition, the incorporation probability has been estimated to be $s \sim 0.1$ (Matsuda and Goto, 1990; Matsuda *et al.*, 1990). In fact, β was found to increase to higher values if the ion bombardment is increased ($\beta=0.59$), or if the flux of the reactive radicals SiH_2 and SiH at the film surface is increased ($\beta \sim 1$) (Abelson, 1993). The smooth surfaces and good conformal coverage associated with high electronic quality a-Si:H

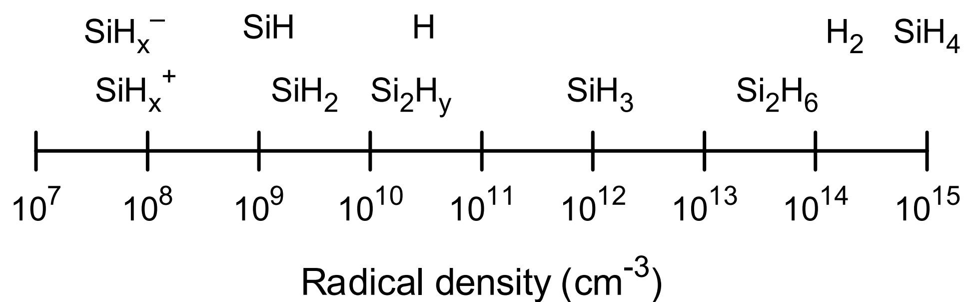

Figure 3.2 Schematic diagram of the concentrations of different radicals in the plasma during PECVD of electronic quality a-Si:H; adapted from (Matsuda, 1998).

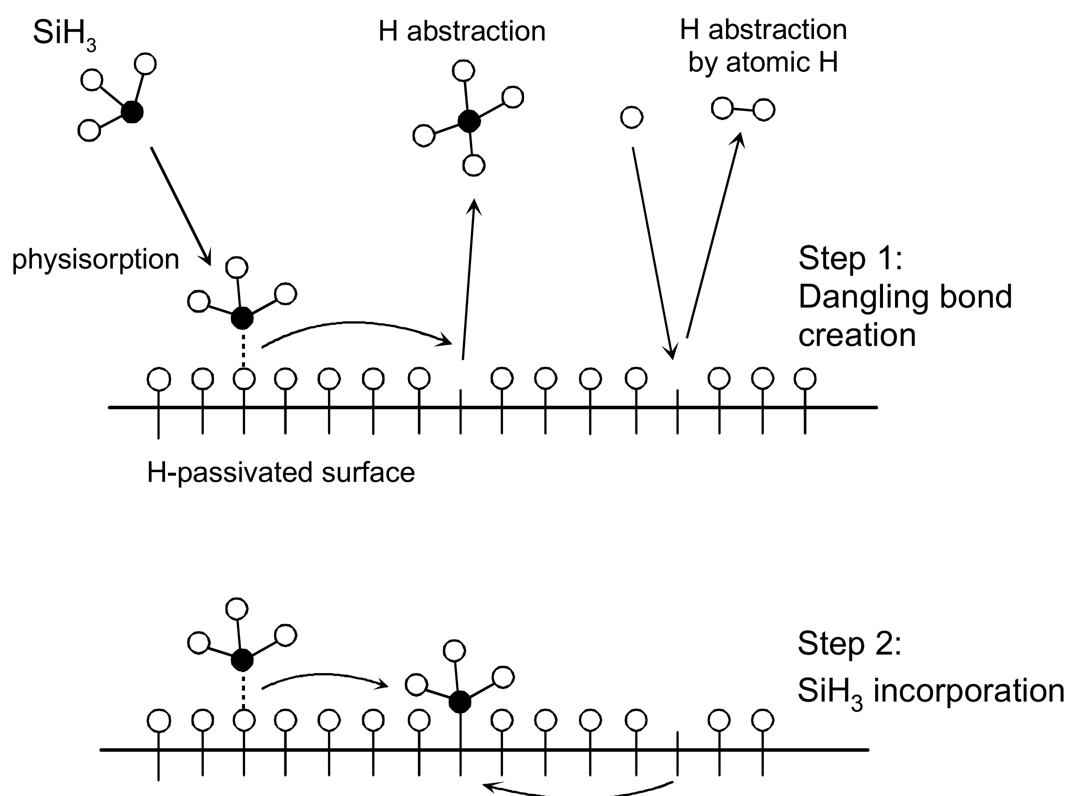

Figure 3.3 Schematic of the surface processes occurring during a-Si:H growth by PECVD; adapted from (Robertson, 2000).

films have been attributed to the low values of β and s, whereas the surface roughening and columnar-like morphologies associated with non-optimum a-Si:H films have been attributed to high values, which are typical of PVD-like growth (Tsai *et al.*, 1986).

(iii) *Sub-surface processes*

The final step in film growth is the conversion of the surface layer, consisting predominantly of Si-H bonds, into the bulk film network, consisting predominantly of Si-Si bonds. In fact, the surface layer has H-content >50 at.%, whereas the bulk film has a H-content of 5–30 at.%, and therefore H-elimination processes must occur. Different mechanisms have been proposed to describe the H-elimination processes and account for the final network configuration and density of defects. Shimizu and coworkers proposed the concept of "chemical annealing" whereby excited plasma species interact with the top few monolayers to promote H-elimination and the formation of a stable network with a low density of weak bonds (Shirai *et al.*, 1991). In more recent studies, Robertson demonstrated by thermodynamic equilibrium arguments that the H chemical potential gradient from the growing film into the plasma causes the expulsion of H from the a-Si:H sub-surface. At low temperatures (T_s<300°C), limitations on H-elimination via activated diffusion, lead to the formation of weak Si-Si bonds in the near surface that are trapped in the resulting bulk film and lead to dangling-bonds defects. Furthermore, it was proposed that athermal processes such as ion bombardment and atomic H in-diffusion from the plasma are important for the facilitation of H-elimination and the passivation of weak-bonds, respectively, both effects occurring at low temperatures (Robertson, 2000a).

In spite of extensive research, several questions regarding a-Si:H film growth mechanisms and their effects on the final film properties remain unsettled. One example, is the mechanism of dangling bond (DB) formation in the bulk a-Si:H film. Ganguly and Matsuda have proposed that the DBs in the bulk film originate from the burial of DBs originally on the surface. Thus, the bulk density of DBs is ultimately determined by the surface reactions [as described briefly above under (ii)] (Ganguly and Matsuda, 1993). On the other hand, Robertson has argued that the bulk DB density is determined by the weak Si-Si bond density, which, in turn is controlled by the sub-surface processes of H-

elimination (Robertson, 2000a). Another controversial issue involves the detailed mechanisms of the surface processes. Although surface diffusion processes are generally agreed to be fundamental to the growth of electronic-quality a-Si:H, it is still not clear what species are diffusing and what mechanisms control this diffusion. This issue will be discussed further in Sec. 3.5.

3.3 EXPERIMENTAL DETAILS

This Chapter presents results from real time spectroscopic ellipsometry measurements (RTSE) and atomic force microscopy (AFM) measurements of Si:H films deposited by rf plasma-enhanced chemical vapor deposition on c-Si and a-Si:H substrates with different H_2-dilution ratios R=[H_2]/[SiH_4]. The details of each deposition will be given as the results are presented. Two different instruments were used for the AFM measurements (Multimode^{TM} SPM and Dimension 3100, both manufactured by Digital Instruments). The measurements were performed in the tapping mode using a standard c-Si cantilever.

3.4 OVERVIEW OF MICROSTRUCTURAL EVOLUTION IN Si:H GROWTH

Figures 3.4 and 3.5 show the evolution of the surface roughness layer thickness (d_s) versus the bulk layer thickness (d_b) as deduced from RTSE measurements of Si:H films deposited on c-Si substrates. Results for films deposited with H_2-dilution ratios R varying from 0 to 40 are shown. The fixed deposition parameters include the rf plasma power which was set at P=0.08 W/cm^2 and the substrate temperature which was set at T=200ºC. Further details of the deposition conditions are given in Chapter 4. Figures 3.4 and 3.5 provide representative examples of the most important features of the microstructural evolution observed during Si:H film growth. An overview of these features (each one designated by a Roman numeral from I to VII) is given next.

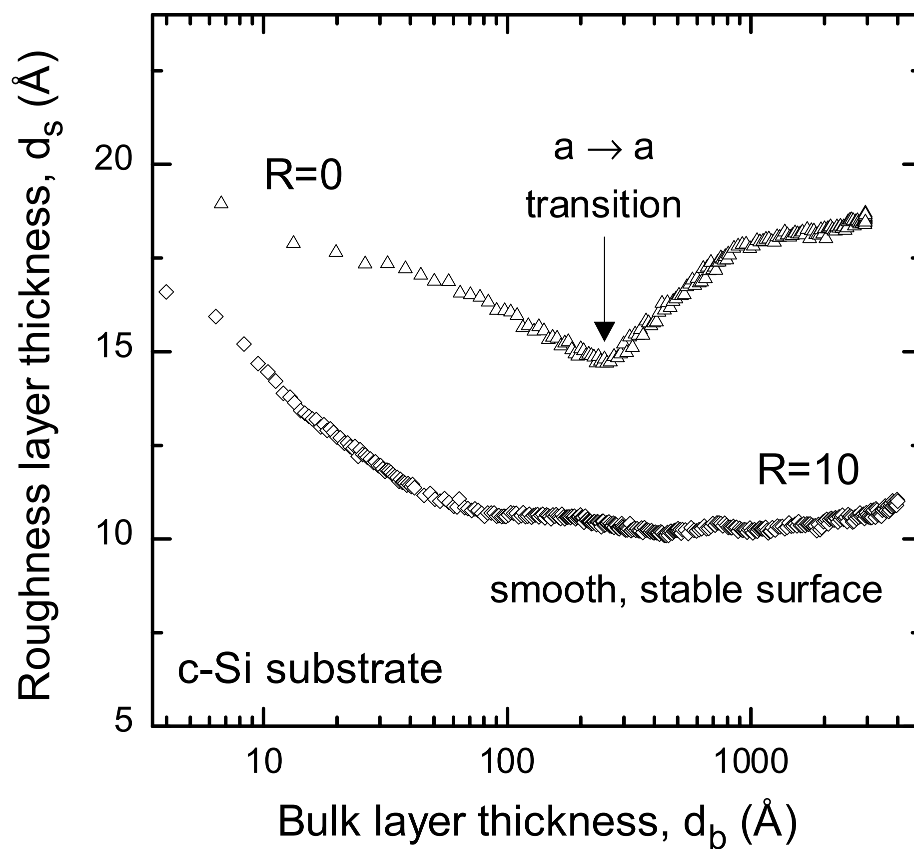

Figure 3.4 Surface roughness layer thickness (d_s) versus bulk layer thickness (d_b) for the deposition of a-Si:H films on c-Si substrates at 200°C with H_2-dilution ratios of R=0 and 10.

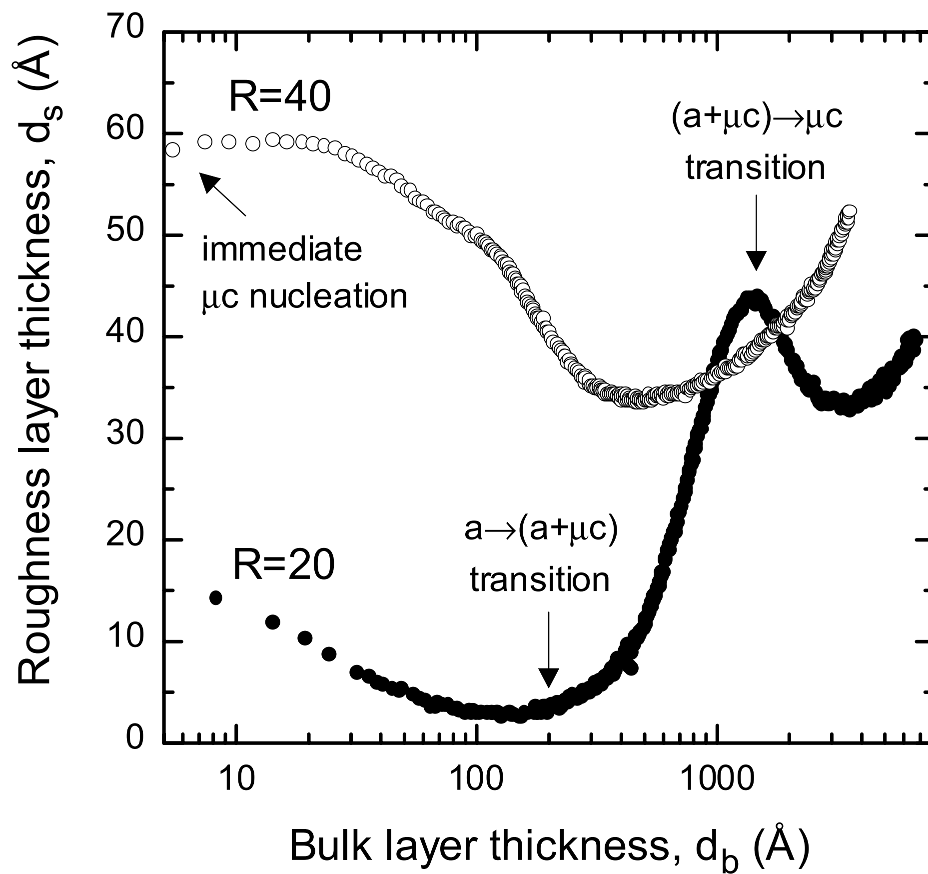

Figure 3.5 Surface roughness layer thickness (d_s) versus bulk layer thickness (d_b) for the deposition of Si:H films on c-Si substrates at 200°C with H_2-dilution ratios of R=20 and 40.

I. Nucleation

The initial stages of a-Si:H film growth on atomically-smooth substrates have been thoroughly described in previous studies. Initially, clusters composed of Si and H atoms nucleate on the substrate. The shape and density of these clusters was found to be dependent on both the substrate nature and the deposition conditions (Collins and Yang, 1989; An *et al.*, 1990; Li *et al.*, 1992). The clusters or islands increase in size with time until they make contact, covering most of the substrate area, and then coalesce to form a continuous film. In this process, the residual clustering gives rise to a surface roughness layer as the bulk layer starts to grow. The height of the islands in the nucleation stage and the surface roughness layer thickness in the bulk film growth stage are described by one parameter d_s that can be obtained in the RSTE analysis (An *et al.*, 1990; Li *et al.*, 1992). The value of d_s increases with time in the nucleation regime as the clusters increase in size, and it reaches a maximum at the cluster contact time. In typical a-Si:H depositions, the peak in d_s ranges from 15 to 20 Å, which can be associated with nucleation densities on the order of 10^{12}-10^{13} cm^{-2} using simple geometrical models (Li *et al.*, 1992). The peak value in d_s is weakly dependent on the substrate temperature, but more strongly dependent on parameters such as plasma power and pressure. This observation suggests that the nucleation behavior is controlled by defects in the substrate that act as nucleation centers. Such defects can be generated by ion bombardment or they can be passivated or eliminated by atomic H exposure or etching, respectively (Li *et al.*, 1992; Ikuta *et al.*, 1996). Although the details of the nucleation regime are not presented in this study, it is important to remark that for atomically-smooth substrates such as c-Si wafers, the nucleation behavior will establish the starting surface microstructure from which the bulk film microstructure will ultimately develop.

II. Coalescence of initial amorphous nuclei

The coalescence of nucleation-induced microstructure is observed as a surface smoothening effect during a-Si:H film growth in the first ~100 Å of bulk layer thickness. Such an effect can be observed for the R=0 and 10 depositions in Fig. 3.4 as well as for the R=20 film in Fig 3.5. For these three depositions, the films nucleate on the c-Si

substrate as a-Si:H clusters. The smoothening is believed to originate from a surface diffusion mechanism (see Sec. 3.4). The magnitude of the surface smoothening can be characterized by $\Delta d_s = d_s(2.5\ \text{Å}) - d_s(100\ \text{Å})$ [where $d_s(x)$ is the value of d_s when d_b=x]. Previous studies have shown that the a-Si:H films with the largest Δd_s exhibit the best electronic performance for applications as i-layers in solar cells – as long as the films remain amorphous throughout the deposition (Li *et al.*, 1992; Lu *et al.*, 1994).

III. Coalescence of initial microcrystalline nuclei

An even larger surface smoothening effect can be observed upon microstructural coalescence of clusters that nucleate directly on the substrate as microcrystalline silicon (μc-Si:H). This larger effect can be observed for the R=40 deposition of Fig. 3.5. In this case, the much larger d_s value of ~60 Å at the onset of bulk layer growth is due to a lower initial nucleation density compared to that of the a-Si:H films. The mechanisms that control amorphous and microcrystalline cluster coalescence are likely to be different (surface diffusion vs. competitive space filling, respectively).

IV. Amorphous stable surface regime

Under a narrowly-defined set of deposition conditions (specifically, for R=10 in Fig. 3.4), the a-Si:H surface remains smooth and stable with <1 Å change in the roughness layer thickness from the end of coalescence throughout the growth of a thick film, e.g., from 100 to 4000 Å in the example of Fig. 3.4. When the stable surface regime is present, it is found to occur at an R value just prior to the amorphous–to–(mixed-phase microcrystalline) transition. Under these conditions, the highest performance and stability materials for solar cells are obtained as will be shown in Chapter 4.

V. Amorphous roughening transition (a→a)

For deposition conditions different from the optimum ones associated with the stable surface regime (i.e., R=10 in Fig. 3.4) an onset of roughening is observed at a well-defined d_b value. This onset identifies the amorphous roughening transition as can be observed for the R=0 deposition of Fig. 3.4. In fact for R=0, the stable smooth surface

regime is not observed, i.e., the surface evolution makes a transition from a smoothening regime (indicating coalescence behavior) to a roughening regime, but without reaching stable, low d_s values. The growing film is amorphous on both sides of this transition as determined from the dielectric function of the film extracted at different thicknesses. A shift in the a→a roughening transition to lower d_b (as occurs with decreasing R for $0 \leq R \leq 10$) can be attributed to a reduction in the surface diffusion length scale of the adsorbed radicals that form the film. Possibly other effects may also establish the position of this transition as will be discussed in greater detail in Sec. 3.4. Correlations with solar cell measurements have shown that the shift in the a→a roughening transition to lower d_b is associated with reductions in performance and stability of solar cell having of i-layers prepared under the corresponding conditions (see Chapter 4).

VI. Amorphous–to–mixed-phase microcrystalline transition [a→(a+μc)] and mixed-phase (a+μc)-Si:H growth regime

In the intermediate H_2-dilution regime ($10<R<40$), a different type of roughening transition is observed in which crystallites nucleate from the growing amorphous phase. Because the crystallite nucleation density is usually low (10^9-10^{11} cm^{-2}) (Ferlauto *et al.*, 2000b; Fujiwara *et al.*, 2001b), the crystalline protrusions generate a roughness layer that increases rapidly in thickness with d_b due to preferential growth of the crystalline phase. Thus, the onset of roughening identifies a transition to mixed-phase (a+μc)-Si:H film growth regime. For the example in Fig. 3.5 with R=20, this transition occurs at d_b=200 Å. During the mixed-phase (a+μc)-Si:H growth regime, the crystallites increase in size and density with increasing thickness until they make contact. In this case, the changes in the microstructure after the roughening transition are accompanied by changes in the film optical properties, in contrast to the case of the amorphous roughening transition. Details on the evolution in the optical properties will be given Sec. 3.6.

VII. (Mixed-phase)–to–(single-phase-microcrystalline) transition [(a+μc)→μc]

For thin films that have already undergone an a→(a+μc) transition, a second transition is possible that occurs at even greater bulk layer thicknesses. In this transition, the crystalline protrusions that extend above the surface make contact, leading to a coalescence process with continued film growth. This process is manifested in the data as a transition from surface roughening to smoothening. Once the crystallites have coalesced to cover the growing film surface completely, single-phase μc-Si:H growth proceeds with a resumption of surface roughening. An example of such a transition is evident in Fig. 3.5 for the film deposited with R=20 at a bulk layer thickness of d_b=1450 Å.

The thicknesses at which the a→(a+μc) and (a+μc)→μc transitions occur reflect the nucleation and preferential growth mechanisms of the μc-Si:H phase. The details of the a→(a+μc) and (a+μc)→μc transitions will be the subject of Sec. 3.5. Here, it is important to emphasize that one should avoid crossing the a→(a+μc) transition for optimum a-Si:H i-layer preparation as will be discussed in Chapter 4. A schematic cross-sectional view of a film that nucleates as a-Si:H and undergoes the a→(a+μc) and (a+μc)→μc transitions as a function of accumulated thickness is shown in Fig. 3.6.

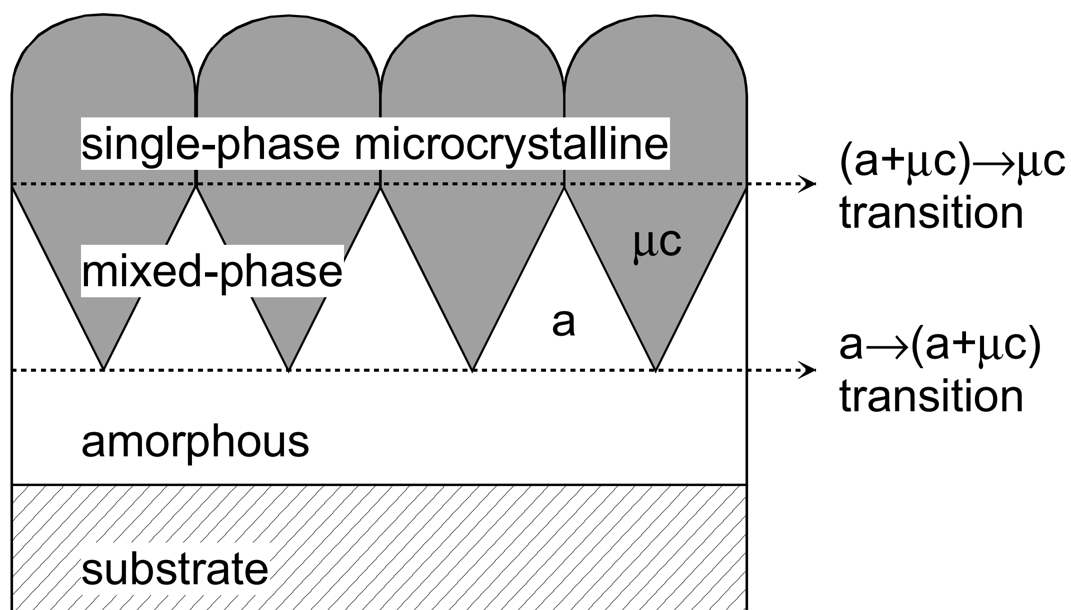

Figure 3.6 Schematic diagram of the cross-section of a Si:H film. This diagram depicts the Si:H phase evolution with thickness, beginning with an a-Si:H growth regime at the substrate interface followed by an intermediate mixed-phase (a+μc)-Si:H growth regime, and finally a single-phase μc-Si:H growth regime.

3.5 MICROSTRUCTURAL EVOLUTION IN THE AMORPHOUS GROWTH REGIME

In this Section, the features of surface roughness evolution observed in the growth of Si:H films in the *amorphous regime* are investigated. In order to understand these features, one must first consider the basic mechanisms of film growth.

3.5.1 General treatment of thin film growth

Thin film growth is an inherently non-equilibrium process, whereby material in the vapor phase is incorporated into the solid film. As a result, the surface can be viewed as a dynamic interface between the vapor and solid phases. In general, different mechanisms are involved in thin film growth and these are mainly controlled by the substrate temperature, film bombardment, and surface chemistry (Messier *et al.*, 1984). In spite of the diverse nature of these mechanisms, the morphological evolution of the surface during growth can be viewed as the result of a simple competition between surface roughening and relaxation/smoothening processes (Yang *et al.*, 1993). Surface roughening can occur due to random fluctuations in the flux of film-forming species (Kardar *et al.*, 1986; Kardar, 2000), or to limited diffusion of the gas phase species specifically in chemical vapor deposition (CVD) processes (Palmer and Gordon, 1988). In addition, roughening can originate from such local effects as the preferential enhancement of surface features due to shadowing (Mazor *et al.*, 1988). On the other hand, relaxation processes are usually related to mechanisms of material transport on the surface and thus are effective on the local scale. The most important relaxation process is the surface diffusion of the adsorbed film-forming radicals; however, other effects such as low energy ion bombardment can also facilitate surface relaxation. Therefore, thin film growth can exhibit different surface evolutionary characteristics depending on the degree of surface relaxation. At one extreme, deposition processes in which the surface relaxation is small or non-existent, such as random or ballistic processes (whereby the particles impinge at normal incidence on the surface with little or no surface mobility)

lead to rough surfaces. For the corresponding processes in which relaxation mechanisms are dominant, layer-by-layer growth can occur that results in atomically-smooth surfaces (Kardar, 2000).

The approaches for modeling the surface evolution of thin films can be divided in two categories. (i) In discrete models, one attempts to study the dynamics of surface evolution by considering the atomic-scale mechanisms. This approach is usually applied in numerical simulations of film growth. (ii) In continuum models, one applies a continuum equation of interface motion in order to characterize the average features of the surface evolution. In particular, the dynamics of the surface height function is described by a differential equation that may contain non-linear terms. A review of some of these equations is provided elsewhere (Kardar, 2000). In addition, the concept of dynamic scaling, originally proposed by Family and Vicsek (Family and Vicsek, 1985), has been extensively applied to characterize the surface morphology and evolution in terms of universal scaling exponents (Family and Vicsek, 1991).

Continuum models have been applied to describe both PVD (Mazor *et al.*, 1988) and CVD film growth processes (Palmer and Gordon, 1988; Bales *et al.*, 1989; Thiart *et al.*, 2000). In such studies, the dynamics of the surface roughness morphology was investigated by means of linear stability analysis. In this analysis, the surface roughness is considered to be a perturbation from a perfectly flat surface (or a perturbation from a straight line profile in a one dimensional simulation). In general, the time evolution of the amplitude A(k, t) of a surface perturbation with a given spatial frequency k ($k=2\pi/\lambda$, where λ is the spatial wavelength in the in-plane direction) can be described as

$$A(k,t) \propto \exp[\omega(k)\, t] , \tag{3.1}$$

where ω is a stability parameter that depends on the growth mechanisms and ultimately on the deposition conditions. The parameter ω can be described in simple terms as a polynomial function of k (Williams *et al.*, 1995) according to

$$\omega(k) = \sum_m a_m k^m , \tag{3.2}$$

where the coefficients a_m are obtained from physical quantities that depend on the deposition parameters. The polynomial order and relative magnitude of each term determine which physical mechanisms impact the evolutionary development of the surface and over what in-plane spatial scales this development occurs.

In the surface diffusion mechanism, the current that transports material from protrusions to depressions on the surface is related to the gradient of the chemical potential $\nabla\mu$. The chemical potential, in turn, is proportional to the local surface height curvature $\nabla^2 h$. As a result, surface diffusion leads to 4th order term in $\omega(k)$ with a_4 being negative (Kardar *et al.*, 1986; Mazor *et al.*, 1988). The k^4 dependence of the surface diffusion indicates that it is an effective smoothening mechanism at short lengths scales but its efficacy decays very rapidly for larger scales. Terms of order greater than 4 are usually either not present or can be neglected entirely. On the other hand, roughening mechanisms usually generate lower order terms ($m<4$) and exhibit positive a_m values. For example, Mazor et al. showed that for PVD processes, the finite atomic size effect is associated with a 2nd order term (Mazor *et al.*, 1988), whereas Palmer and Gordon showed that for CVD processes the limited diffusion of species in the gas phase is associated with a 1st order term (Palmer and Gordon, 1988). The sign of the stability parameter $\omega(k)$ determines whether the amplitude of the perturbation grows with time ($\omega>0$) or dampens with time ($\omega<0$).

Such analyses is useful because they can describe the time evolution of surface roughness in different film growth regimes. For example, in the case of a-Si:H deposition on flat c-Si surfaces, the nucleation-induced morphology can be described as an initial surface perturbation and the subsequent surface roughness evolution can be described in terms of the impact of this perturbation. The application of such an approach will be presented in the next section.

3.5.2 AFM study and comparison with RTSE measurements

Figure 3.7 depicts a typical series of series of AFM images obtained for a-Si:H films deposited with R=0 on c-Si substrates to different thicknesses. The film thicknesses determined by RTSE measurements are as follows: (a) 4 Å, (b) 240 Å, (c) 780 Å, (d) 1900 Å, and (e) 5200 Å. All images cover the same area of 500×500 nm^2, and the gray scales correspond to surface height ranges from 15 Å in (a) to 120 Å in (e). The surface topography for all thicknesses consists of mounds and valleys typical of amorphous films. Two aspects must be considered in the analysis of such images, namely, the variations in the surface heights and the variations in the in-plane scales of the surface morphology. The film surface can be represented as the function $z(\mathbf{r})$, where $\mathbf{r}=(x, y)$ is the vector defining the position in the x-y plane normal to the growth direction. The height variations in the surface can be quantified by the root-mean-square (RMS) roughness d_{rms} defined as

$$d_{rms} = \langle [z(\mathbf{r}) - \langle z(\mathbf{r}) \rangle]^2 \rangle^{1/2} , \qquad (3.3)$$

where the angular brackets denote an average over the entire image area. In a previous study it was reported that, for thick a-Si:H films, a linear relationship is observed between d_{rms} from AFM and d_s from RTSE given by $d_s = 1.5d_{rms} + 4$ Å (Koh *et al.*, 1996). Thus, in order to provide a better comparison between the AFM and RTSE results, a "corrected" RMS value $d_{c,rms}$ can be calculated from the measured value d_{rms} using

$$d_{c,rms} = 1.5d_{rms} + 4 \text{ Å}. \qquad (3.4)$$

Figure 3.8 presents the evolution of the surface roughness layer thickness d_s vs. the bulk layer thickness d_b as determined from RTSE analysis (solid squares), together with $d_{c,rms}$ obtained from the AFM images presented in Fig. 3.7 (open circles). The corrected RMS roughness $d_{c,rms}$ increases continuously with increasing thickness in contrast to d_s which shows smoothening and roughening regimes as described in Sec 3.4. The lack of a one-to-one correlation between d_s and $d_{c,rms}$ can be attributed in part to the fact that AFM images can be described as a convolution of the surface features and the probe geometry (Griffith and Grigg, 1993). Typical AFM probes have an apex radius of

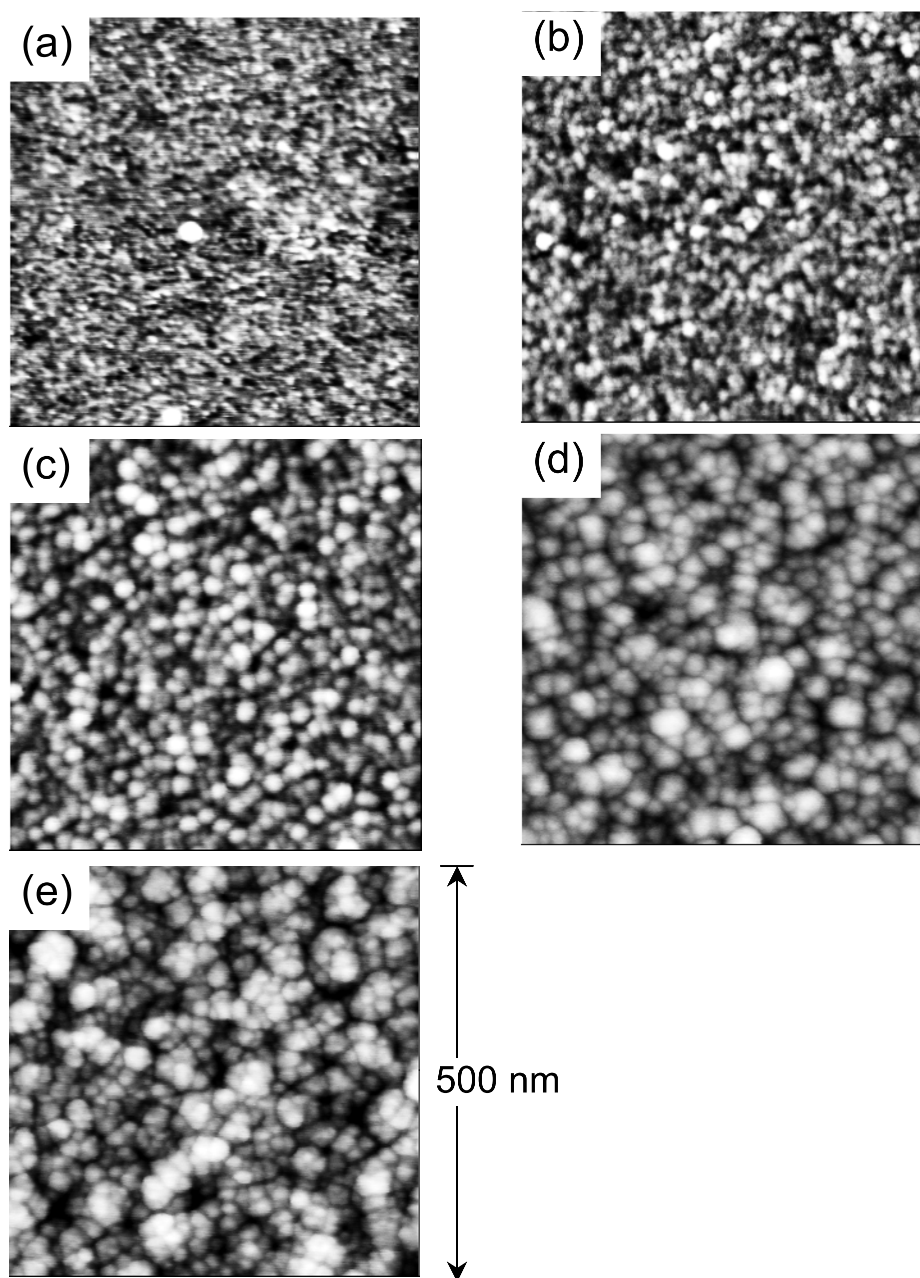

Figure 3.7 Series of AFM images of a-Si:H films deposited with a H_2-dilution ratio of R=0, a plasma power of P=0.08W/cm^2, and a substrate temperature T=200ºC. Each image corresponds to a film deposited to a different thickness including (a) ~4 Å, (b) 240 Å, (c) 780 Å, (d) 1900 Å, and (e) 5200 Å. All images have the same dimensions of 500×500 nm^2. The full-scale ranges for the surface heights (i.e., the gray scale) are (a) 15 Å, (b) 20 Å, (c) 50 Å, (d) 100 Å, and (e) 120 Å.

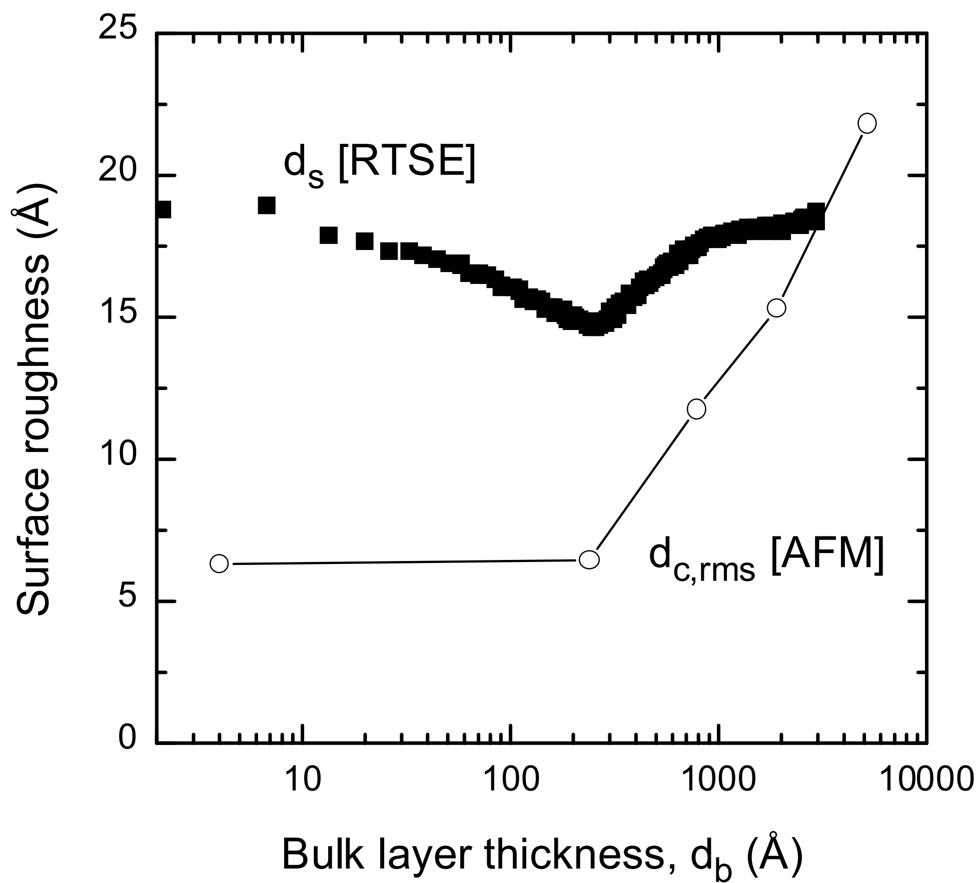

Figure 3.8 Values for the surface roughness layer thickness versus bulk layer thickness d_b, including the roughness d_s (filled squares), obtained from RTSE, and the corrected RMS roughness $d_{c,rms}$ (open circles), obtained from the AFM images of Fig. 3.7.

curvature of 50–100 Å, and thus for surfaces having features with small in-plane scales (i.e., high frequency surface modulations), the measured $d_{c,rms}$ value is lower than the correct value. This effect can be enhanced by the native oxide (present in ex-situ AFM studies, but absent in RTSE studies) that can smoothen the surface features during its formation. These observations highlight the limitations of the AFM technique for precise characterization of surfaces with small in-plane scales and/or large aspect ratios, as has been pointed out elsewhere (Griffith and Grigg, 1993).

The unique information that AFM images can provide (but RTSE cannot) is the distribution of in-plane scales for the surface roughness features (within the limitations just described). In Fig. 3.7, it can be seen clearly that the size of the mounds increases with increasing thickness. A quantitative method for assessing the in-plane scales of the surface roughness is by calculating a height-to-height correlation function G(ρ), which is defined as (Family and Vicsek, 1985; Yang *et al.*, 1993)

$$G(\rho) = \left\langle [z(\mathbf{r}+\boldsymbol{\rho}) - z(\mathbf{r})]^2 \right\rangle_r , \tag{3.5}$$

where the average is performed over all the **r**=(x, y) points within a given area. Hence, G(ρ) is a measure of the relative height fluctuations on the surface. As an example, Fig. 3.9 shows a plot of G(ρ) (symbols) derived from AFM images of the surface corresponding to the a-Si:H film of Fig 3.7(d). In the small scale regime ($\rho<100$ Å), G(ρ) increases with increasing ρ according to a power law such that $G(\rho) \propto \rho^{2\alpha}$. Thus as ρ becomes larger, the surface features become uncorrelated and G(ρ) tends to saturate at (or oscillate about) a constant value in the large scale regime ($\rho>300$ Å). It can be shown that this constant value is equal to $2d_{rms}^2$ (Yang *et al.*, 1993). The cross-over between the two asymptotic behaviors of G(ρ) defines a surface correlation length ξ. The value of ξ can be calculated by expressing G(ρ) according to the following phenomenological scaling function (Yang *et al.*, 1993)

$$G(\rho) = 2d_{rms}^2 \left\{1 - \exp[-(\rho/\xi)^{2\alpha}]\right\}. \tag{3.6}$$

Here, α is the static scaling exponent that defines self-affine fractal surface morphologies (Family and Vicsek, 1985; Yang *et al.*, 1993). The solid line in Fig. 3.9 corresponds to a

fit of the experimental $G(\rho)$ using the function of Eq. 3.6. Such a fit can thus provide the average correlation length ξ, which is a quantitative measure of the average in-plane size of the surface roughness features.

Fig 3.10(b) shows the correlation length ξ determined using the method described in the previous paragraph plotted versus the bulk layer thickness d_b. Here, the effects of the probe tip size and the native-oxide layer may lead to values of ξ to be larger than the correct values. Thus, the measured values in Fig. 3.10(b) should be considered upper limits for ξ. In view of this uncertainty, the value of ξ=50 Å just after nuclei contact (d_b~4 Å) shows reasonable agreement with the value of 36 Å, which would be expected if the initial a-Si:H clusters exhibit a hemispherical shape with a height of 18 Å. In Fig. 3.10(b), it can be seen that ξ increases with increasing thickness, as was noted from a visual inspection of the AFM images. Similar behavior has been observed previously in in-situ scanning tunneling microscopy studies of a-Si:H films (Ikuta *et al.*, 1994; Tanenbaum *et al.*, 1997), and the values reported for the in-plane scales agree reasonably well with those obtained here. The important feature in Fig. 3.10 is the steeper increase in ξ observed in the vicinity of the thickness corresponding to the a→a transition thickness as deduced from the RTSE analysis (d_b~250 Å). This correlation suggests that the roughening transition observed in d_s, which is a measure of the roughness scale in the direction *normal* to the substrate plane, is related to a transition in the correlation length that is a measure of the roughness in the direction *parallel* to the substrate plane.

We can resort to a simple model proposed by Mazor et al. (Mazor *et al.*, 1988) described in the previous section in order to understand the roughness evolution regimes in a-Si:H films. In this model, the expression for ω is given by

$$\omega(k) = \delta J k^2 - D_e k^4 , \qquad (3.7)$$

where $k=2\pi/\lambda$, J is the deposition rate, δ is the atomic radius, and D_e is a term proportional to the surface diffusivity. In Eq. 3.7, ω is positive for surface height perturbations with wavelength λ greater than a critical value of λ_0. In this case, λ_0 is the surface diffusion length defined by $\lambda_0 = (4\pi^2 D_e / \delta J)^{1/2}$. Figure 3.11 shows a plot of ω

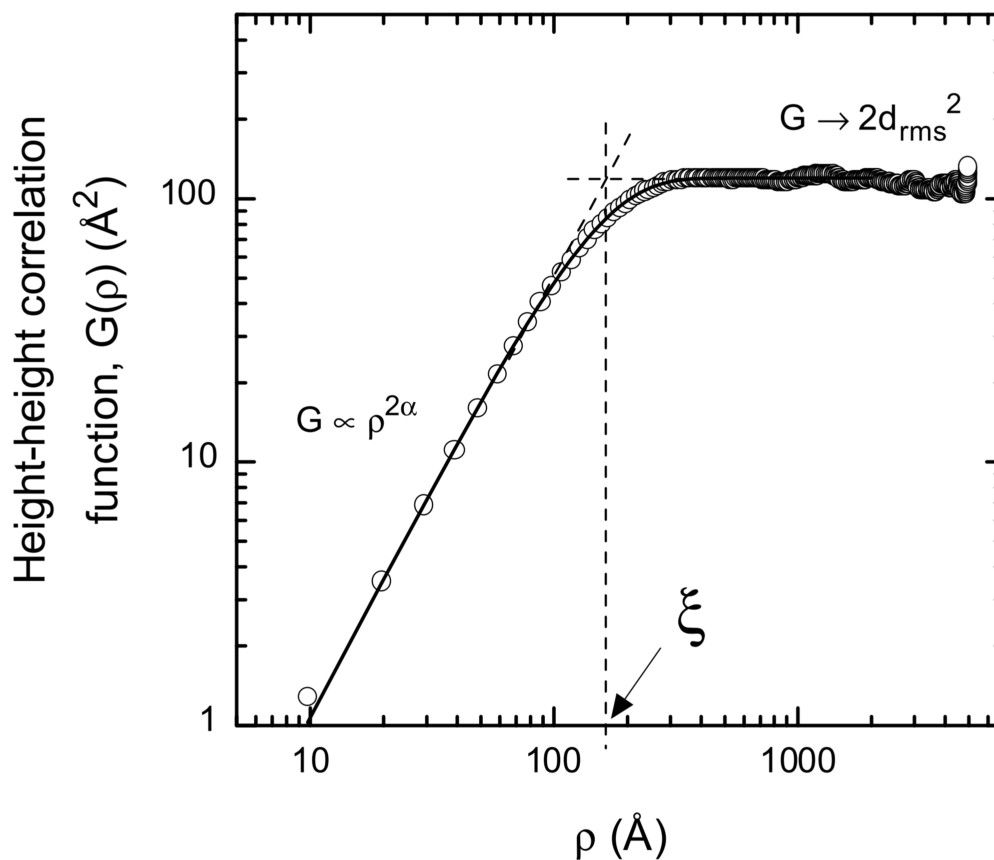

Figure 3.9 Height-height correlation function G(ρ) versus the in-plane length scale ρ. The experimental results for the surface of the R=0 a-Si:H film at a thickness of 1900 Å [see Fig. 3.7(d)] are shown as open circles. These experimental results are deduced from Eq. 3.5. The solid lines correspond to a fit based on Eq. 3.6, and the best fit parameter ξ defines the correlation length.

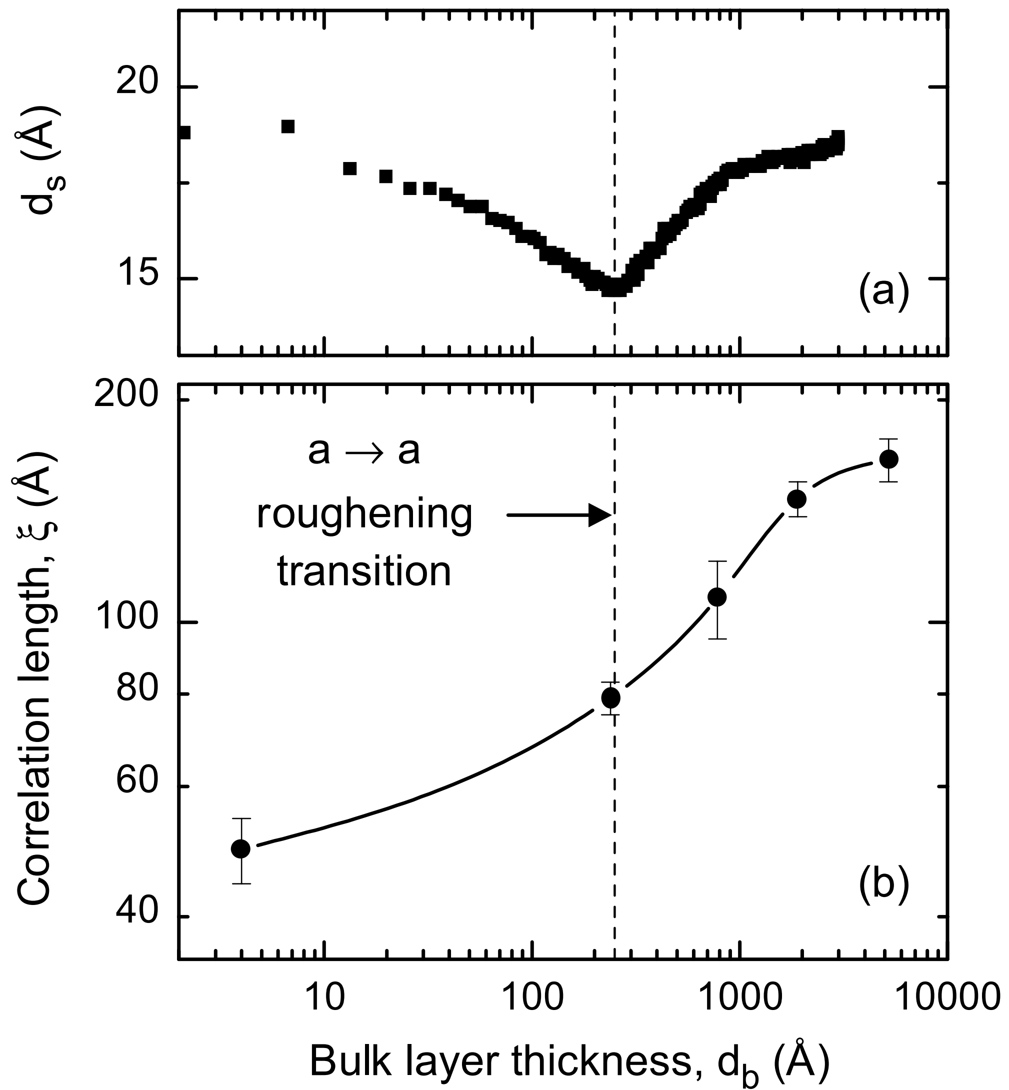

Figure 3.10 (a) Surface roughness layer thickness d_s (from RTSE) and (b) surface roughness in-plane correlation length ξ (from AFM) versus the bulk layer thickness d_b for the R=0 a-Si:H film series of Fig. 3.7.

versus the in-plane wavelength λ of the surface perturbations for four different values of λ_0. Similar relationships can be found in more complicated models for thin film growth by CVD, whereby a critical wavelength λ_0 exists that separates roughness features that will decay over time ($\lambda<\lambda_0$) from those that will increase over time ($\lambda>\lambda_0$). This critical wavelength is in fact a sensitive function of the deposition conditions (Palmer and Gordon, 1988; Bales *et al.*, 1989; Thiart *et al.*, 2000).

An example of the results for the time evolution of a hypothetical one-dimensional surface profile calculated from the model of Mazor et al. (Mazor *et al.*, 1988) is presented in Fig. 3.12. In Fig. 3.12(a), the solid line represents a surface profile obtained from the sum of three sinusoidal perturbations with spatial wavelengths of λ_i = (32, 64, 128) Å for i=(1, 2, 3), respectively, having amplitudes A_i = (5, 1, 1) Å for i=(1, 2, 3), respectively. Such a profile is intended to simulate qualitatively the surface morphology of a-Si:H after the initial nucleation regime. The time evolution of the profile can be calculated using Eqs. 3.1 and 3.7, where J=1 Å/s and δ=3 Å. Figure 3.12(b) shows the calculated value of d_{rms} for the profile plotted versus time using different values for the surface diffusion length λ_0 in Eq. 3.7.

First, the predicted roughness evolution corresponding to the largest diffusion length λ_0=100 Å will considered [solid line in Fig. 3.12(b)]. Three regimes similar to those observed in the RTSE analysis of a-Si:H film growth can be observed. In the initial stages, d_{rms} decreases rapidly due to the dampening of the features having wavelengths smaller than λ_0. In fact, this effect was proposed to be responsible not only for the smoothening of the nucleation-induced surface roughness in the initial stages of a-Si:H growth on c-Si substrates (Li *et al.*, 1992) but also for the smoothening of substrate-induced surface roughness when growth occurs on substrates having a well defined morphology (Collins and Yang, 1989). The smoothening regime is followed by a long period when the surface is relatively stable and d_{rms} is constant. This regime resembles the stable surface regime described in Sec. 3.4. With increasing time, the surface perturbations having wavelengths larger than λ_0 become dominant and because their amplitudes increase with time (ω>0), d_{rms} is observed to increase at the longest times. As

a result, a clear "roughening transition" is predicted. In Fig. 3.12(a), the profile for λ_0=100 Å and t=500 s (dashed line) shows how the surface is dominated by the large scale features after the roughening transition. In summary, this model qualitatively reproduces the behavior observed in the combined RTSE and AFM results presented in this section.

Next, the effects of variations in the surface diffusion length λ_0 will be considered as shown in Fig 3.12(b). The first observation is that, as λ_0 is increased from 40 to 100 Å, the initial decrease in d_{rms} shifts to shorter times. As a result, the RMS roughness at a given time (or film thickness) decreases. Second, the time (or film thickness) at which d_{rms} begins to increase, i.e., the roughening transition thickness, increases with increasing λ_0. For very large λ_0, d_{rms} tends to remain stable up to very large film thicknesses, giving rise to a smooth, stable surface regime.

The results of such simulations strongly suggest that two of the quantities describing the microstructural evolution of a-Si:H films as deduced in RTSE measurements, namely, the magnitude of the surface smoothening in the coalescence process and the position of the amorphous roughening transition (a→a), can be used as indicators of the relative surface diffusion scale of the adsorbed radicals on the growing film under different deposition conditions. As a result, these two quantities also provide insights into the a-Si:H material quality owing to the positive impact that surface diffusion exerts on the properties of the resulting a-Si:H films.

3.5.3 Discussion and Summary

From the RTSE and AFM results presented above, different regimes have been identified that describe the surface roughness evolution of a-Si:H films deposited on c-Si substrates. Based on a simple continuum model, it was proposed that the evolution of the surface roughness layer thickness as a function of the bulk layer thickness is a consequence of the evolution of surface features having different in-plane scales. The latter behavior is controlled by various physical processes that are dependent, in turn, on the deposition conditions. Among such physical processes, surface diffusion is believed

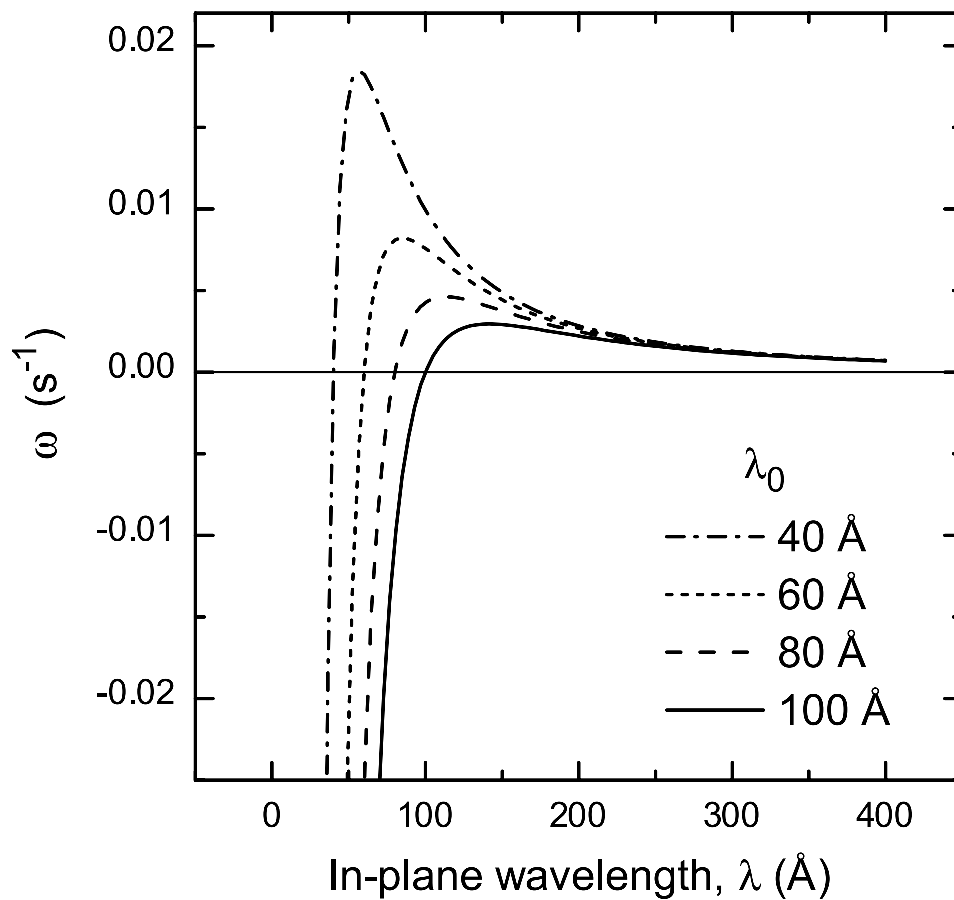

Figure 3.11 Stability parameter (ω) versus the in-plane wavelength (λ) of the surface perturbations. The values for ω are calculated from Eq. 3.7, by assuming a deposition rate of J=1 Å/s, an atomic radius of δ=3 Å, and different values for the surface diffusion length λ_0 (40–100 Å). The diffusion length λ_0 corresponds to a root of Eq. 3.7 and separates the perturbations that will grow with time ($\omega>0$) from those that will decay with time ($\omega<0$).

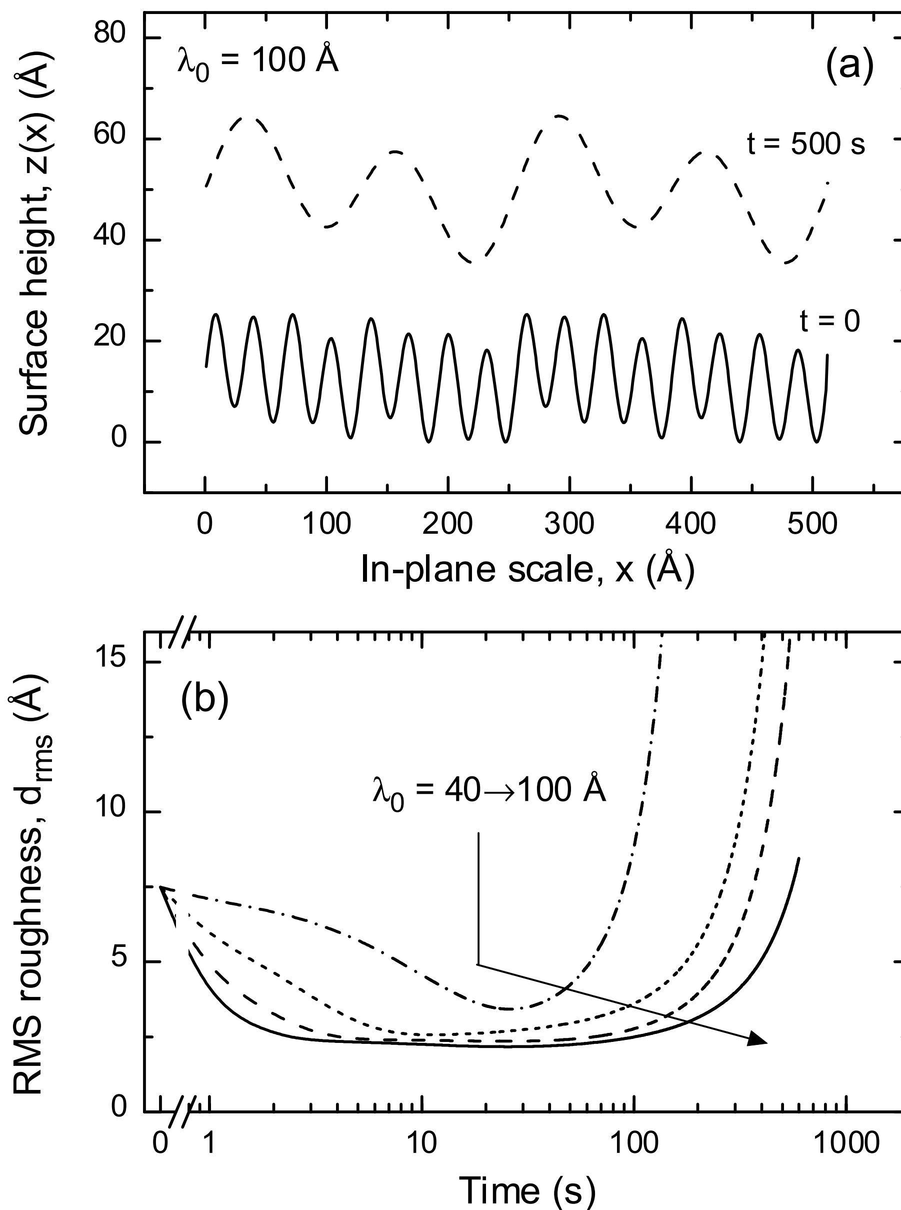

Figure 3.12 (a) One dimensional profiles of the surface height function z(x) simulating the surface roughness on an a-Si:H film. The solid line corresponds to the initial profile (t=0), and the dashed line corresponds to the same profile after 500 s of simulated evolution, obtained by using the values for ω determined in Fig. 3.11 (with λ_0=100 Å). (b) Evolution of the RMS roughness d_{rms} versus time starting from the initial profile in (a) assuming different values of λ_0. The time evolution of such a profile is calculated from Eqs. 3.1 and 3.7.

to be the key to overcoming the inherent roughening mechanisms and to generating smooth, stable surfaces.

The importance of surface diffusion processes in a-Si:H growth has been long recognized. Yet the details of the surface diffusion mechanisms and their role in film growth are controversial. In the surface reaction model proposed by Perrin et al. and Matsuda et al. (Perrin *et al.*, 1989; Matsuda *et al.*, 1990) described in Sec. 3.2, the diffusion of the physisorbed SiH_3 on the H-passivated surface is critical to the formation of smooth surfaces and to the generation of low defect densities in the bulk a-Si:H (Ganguly and Matsuda, 1993). However, several studies based on scanning probe microscopy and numerical simulations have suggested that SiH_3 diffusion is just one part of a more complicated picture. Doughty et al. proposed that the "valley filling" mechanisms that generate smooth surfaces is actually accomplished by the diffusion of dangling bonds (DB's) to surface valleys where they can be shared among several Si atoms (Doughty *et al.*, 1990). Along a similar line of research, Flewitt et al. proposed that the creation of DB's in kink-like or step-like sites is favored (Flewitt *et al.*, 1999). A growth model based on the thermally activated diffusion of "reactive sites" was also described by Smets et al. to simulate the time evolution of the surface roughness on a-Si:H film growth (Smets *et al.*, 2000). From a different perspective, Maeda et al. have suggested that SiH_3 does not need to find a DB in order to incorporate into the film but instead may react with SiH_n complexes on the surface (Maeda *et al.*, 1995).

Such studies suggest that the surface bonding and morphology of a-Si:H are in fact interlinked. Such a relationship has been evidenced in a number infrared absorption and reflection spectroscopy experiments. Such experiments have shown that the H-passivated surface includes different hydrides of silicon (SiH_n), and that the relative concentrations of these hydrides depend on the substrate temperature and the H_2-dilution ratio (Toyoshima *et al.*, 1991; Marra *et al.*, 1998). They have also shown that the concentration of SiH and SiH_2 on the surface evolves with time in proportion to the surface roughness layer thickness as determined by RTSE (Fujiwara *et al.*, 1999b). Moreover, in a combined topographic and spectroscopic STM study by Herion, it was demonstrated that the different hydrides are not evenly distributed on the a-Si:H surface.

In fact, prominent hills are covered by monohydrides and/or adsorbed H, whereas valley regions are rich in the higher hydrides (SiH_2, SiH_3) (Herion, 1999).

In conclusion, it is likely that the surface roughness evolution on a-Si:H films results from a combination of mechanisms. On the one hand, the reactivity of the species impinging on the film surface is important to the extent that low reactivity, high mobility radicals are necessary for the production of smooth, compact and low-defect-density films. On the other hand, because radical incorporation into a "reactive site" is a necessary step in film formation, the creation and/or diffusion of such reactive sites may also be important. Finally, the surface and sub-surface mechanisms that lead to H-elimination also establish the bonding configurations in the surface layer, which in turn can affect the diffusion of the radicals as well as the creation and diffusion of reactive sites. One can speculate that the smooth, stable surface regime observed in a-Si:H growth (e.g. for the R=10 film in Fig. 3.3) results from a combination of the high mobility of SiH_3 radicals impinging on the surface and the efficient dehydrogenation and network relaxation in the surface and sub-surface regions (e.g., due to the high H flux impinging on the surface as a result of the H_2-dilution). This in turn is expected to facilitate the diffusion of both the Si-containing adsorbed radicals and the reactive sites for radical attachment.

3.6 DETAILS OF THE AMORPHOUS TO MICROCRYSTALLINE TRANSITION

In this Section, the presentation of results and the discussion will focus on the features of microstructural evolution associated with the development of the μc-Si:H phase in Si:H films. The RTSE measurements of such films reveal that when nucleation occurs on the substrate as a-Si:H, the amorphous–to–microcrystalline transition is characterized by two regimes in the surface roughness evolution. First, a rapid increase in the surface roughness is observed that can be associated with the nucleation of crystallites from the amorphous phase and their preferential growth. Second, a peak and subsequent decrease in the surface roughness layer thickness is observed that can be associated with coalescence of the μc-Si:H phase, which completely dominates over the a-Si:H phase by that point.

The evolution of the surface roughness layer thickness for such films was obtained through analyses based on the global $\overline{\sigma}$-minimization method with a two-layer optical model, as described in detail in Sec. 2.4.3. An example of the results of such an analysis is presented in Fig. 3.13. Figure 3.13(a) shows the evolution of the roughness layer thickness d_s versus the bulk layer thickness d_b, while Fig. 3.13(b) shows the evolution of the unbiased estimator σ obtained in the least-squares analysis. It is clear that the increase in d_s for d_b>200 Å, reflecting the development of the μc-Si:H phase, is associated with a significant increase in σ. This indicates that the simple two-layer optical model is insufficient to fully describe the optical and microstructural evolution of such films.

The description of the amorphous–to–microcrystalline transition in Si:H films is a very complex problem because both the microstructure and the optical properties change continuously and significantly with thickness as the film evolves from the amorphous to the microcrystalline phase. In order to overcome these difficulties, different strategies will be presented in the next sections that attempt to provide a more complete picture of this evolutionary process. First in Sec 3.6.1, AFM measurements are presented that

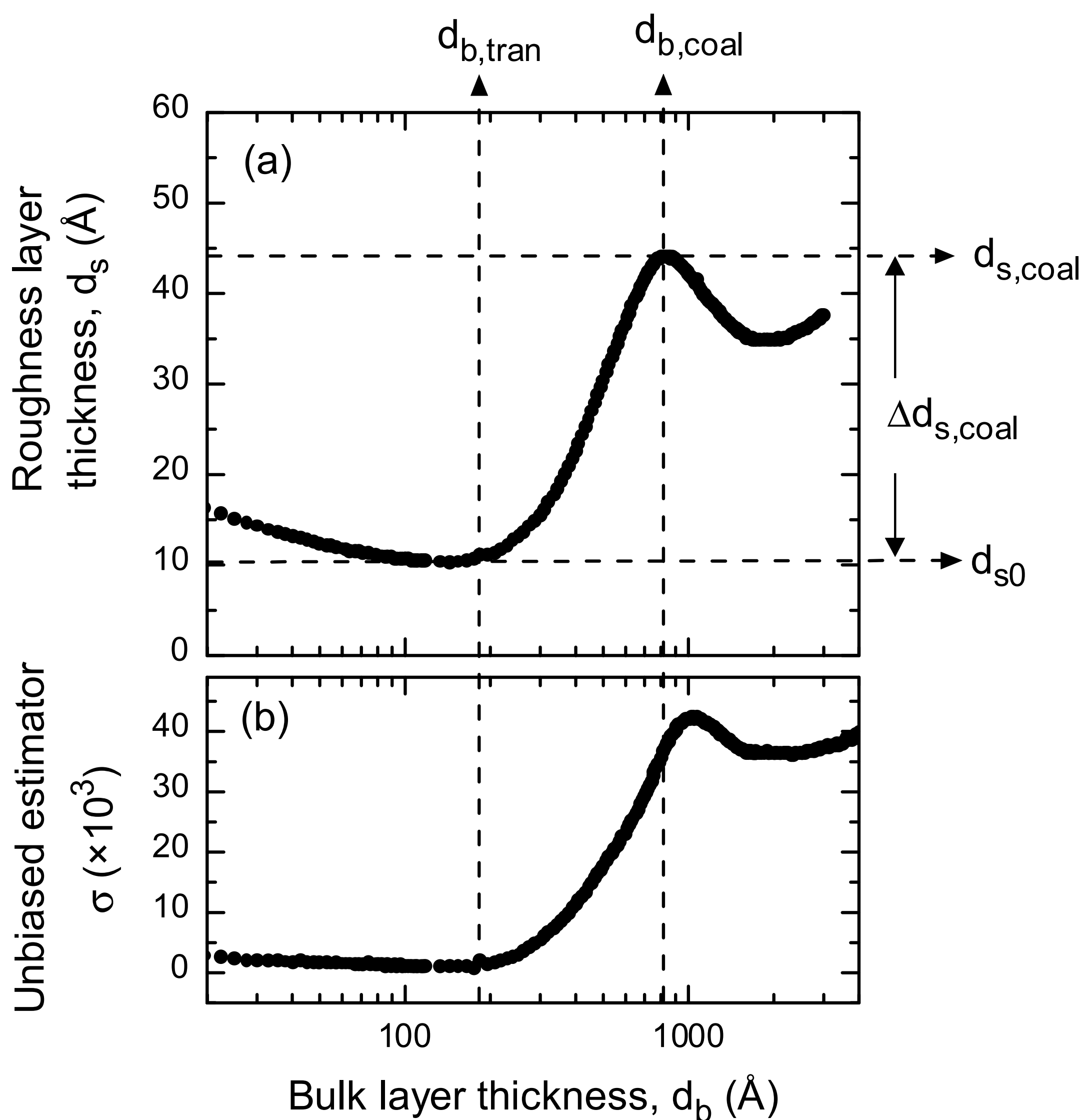

Figure 3.13 Results from RTSE analysis using a two-layer optical model for a Si:H film deposition in which the amorphous–to–microcrystalline transition is observed. The results are plotted versus the bulk layer thickness d_b and include (a) the surface roughness layer thickness d_s and (b) the unbiased estimator σ of the mean square deviation obtained in the least-squares regression analysis. The relevant thicknesses that can be deduced from the analysis are identified by the arrows in (a).

provide a direct characterization of the morphology of the evolving Si:H film surface. In addition, a comparison between the AFM and RTSE results clarify the optical model used for the interpretation of the RSTE results. In Sec. 3.6.2, a phenomenological model for the crystallites growth in the mixed-phase (a+μc)-Si:H deposition regime is proposed. This growth model attempts to provide a simple, universal description of the RTSE results from a number of Si:H depositions. Finally in Sec. 3.6.3, a more elaborate self-consistent analysis of the RTSE measurements based on a "virtual interface" approach is presented. This approach provides a more detailed description of the evolution of the microstructure and optical properties during the amorphous–to–microcrystalline transition.

3.6.1 AFM study and comparison with RTSE measurements

Figure 3.14 presents a series of typical AFM images obtained in this case from the surface of Si:H films deposited to different thicknesses under fixed conditions on R=0 a-Si:H thin film substrates. The fixed conditions include a H_2-dilution ratio of R=20, a rf plasma power of P=0.08 W/cm^2, and a substrate temperature of T=200°C. The film thicknesses as determined by RTSE measurements are (a) 430 Å, (b) 880 Å, (c) 2050 Å, and (d) 3500 Å. All images cover the same area of 2×2 μm^2, and the gray scales indicating the surface heights correspond to full scale ranges of (a, b) 500 Å, (c) 1000 Å, and (d) 2000 Å. In such images the crystallites can be discerned from the amorphous matrix as protuberances on the surface. The amorphous phase has RMS roughness values of 5-10 Å, whereas the crystallites exhibit heights of a few hundred Å. These images reveal that as the Si:H film evolves with thickness in the mixed-phase (a+μc)-Si:H growth regime, the density of the crystalline nuclei and also the size of these nuclei increase.

The AFM images of Fig. 3.14 can provide quantitative information on the evolution of the μc-Si:H phase in the mixed-phase (a+μc)-Si:H growth regime. First the corrected RMS roughness $d_{c,rms}$ can be determined according to Eqs. 3.3 and 3.4. In addition, the number of crystallites within each image and the area covered by these

crystallites can be determined. Thus, values for the crystalline nuclei density and the fractional area coverage by μc-Si:H can be estimated. Such estimates are performed using an average over 2–4 images taken at different positions on the film surface. The limitations on these estimates are established at one extreme by the maximum roughness of the amorphous matrix (~10 Å), which makes it impossible to discern crystallites having heights less than this dimension. At the other extreme, for large film thicknesses the crystallites begin to coalesce, and the number of individual crystallites are undercounted.

In Fig. 3.15, the AFM and RTSE results for the Si:H films of Fig. 3.14 are plotted versus the bulk layer thickness d_b as determined by RTSE. These results include: (a) the surface area fraction covered by the μc-Si:H phase A[μc-Si:H]; (b) the crystalline nuclei density N_d; and (c) $d_{c,rms}$ from AFM as defined by Eq. 3.4 (filled squares) along with d_s from RTSE (open circles). First, Fig. 3.15(a) shows that the μc-Si:H fractional area coverage A[μc-Si:H] is ~1% at the thickness corresponding to the a→(a+μc) transition as identified by RTSE (d_b~900 Å). As a result, it is suggested that ~0.5% coverage defines the detection limit of RTSE. Second, Figs. 3.15(b-c) show that the roughening onset in d_s that identifies the a→(a+μc) transition thickness, as determined by RTSE, matches an abrupt increase in the crystalline nuclei density, as determined by AFM. These results corroborate the interpretation of the RTSE data for determination of the phase boundary.

Figure 3.15(c) also demonstrates that the values for the surface roughness thickness obtained from RTSE (d_s) and AFM ($d_{c,rms}$) do not scale as reported previously for homogeneous surfaces of thick a-Si:H and μc-Si:H films (Koh *et al.*, 1996). This observation can be explained by the inhomogeneous nature of the surface in the mixed-phase regime. The surface height distributions the mixed-phase regime deviate from a random (normal) distribution (in which case the RMS roughness corresponds to the standard deviation). This is evidenced in Fig. 3.16 by plots of the bearing ratios of the height distributions for the surfaces corresponding to the AFM images in Fig. 3.14 with d_b values of (a) 880 Å, (b) 2050 Å, and (c) 3500 Å. For a normal distribution, the bearing ratio is an s-shaped curve, as in the case of Fig 3.16(a) which corresponds to the

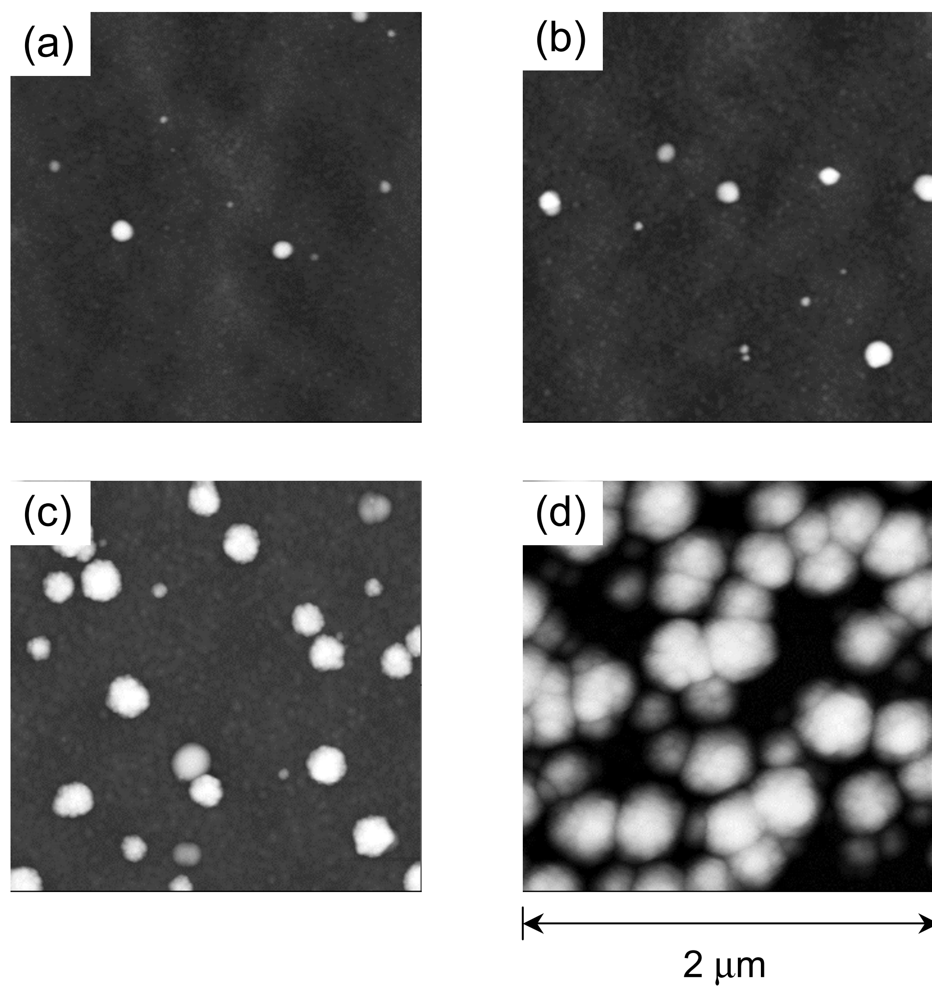

Figure 3.14 Series of AFM images for R=20 Si:H films deposited on 500 Å R=0 a-Si:H substrates. The fixed conditions included a H_2-dilution ratio of R=20, a plasma power of P=0.08 W/cm^2, and a substrate temperature of T=200ºC. Each image corresponds to a film deposited with a different thickness including (a) 430 Å, (b) 880 Å, (c) 2050 Å, and (d) 3500 Å. All images have the same area of 2×2 μm^2. The full scale range for the surface height distributions (i.e., the gray scales) are (a) 500 Å, (b) 500 Å, (c) 1000 Å, and (d) 2000 Å.

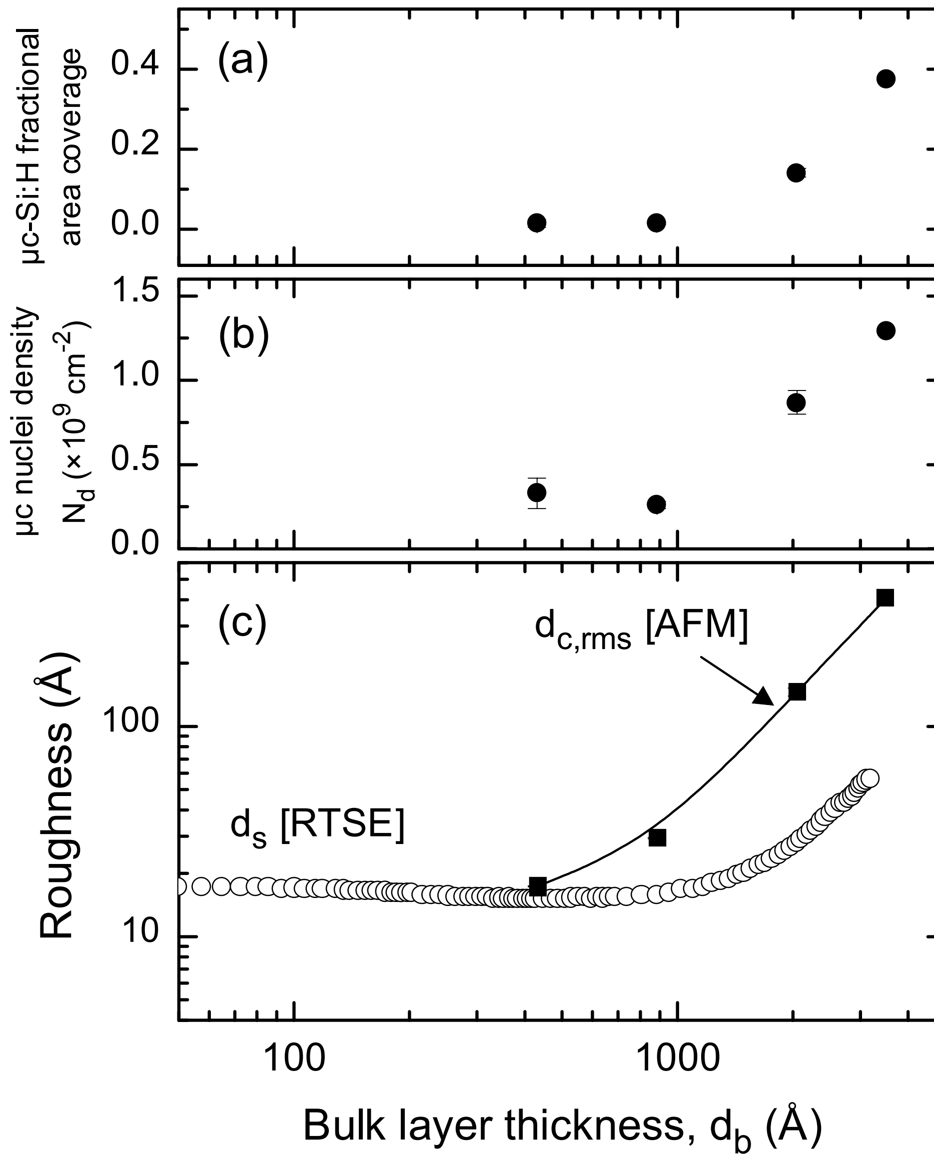

Figure 3.15 Combined RTSE and AFM results for the R=20 Si:H film series of Fig. 3.14 plotted versus bulk layer thickness d_b. The results include (a) μc-Si:H fractional surface area coverage from AFM, (b) μc-Si:H nuclei density from AFM, and (c) roughness layer thickness d_s from RTSE (obtained from the 3500 Å Si:H deposition) and corrected RMS roughness $d_{c,rms}$ from AFM.

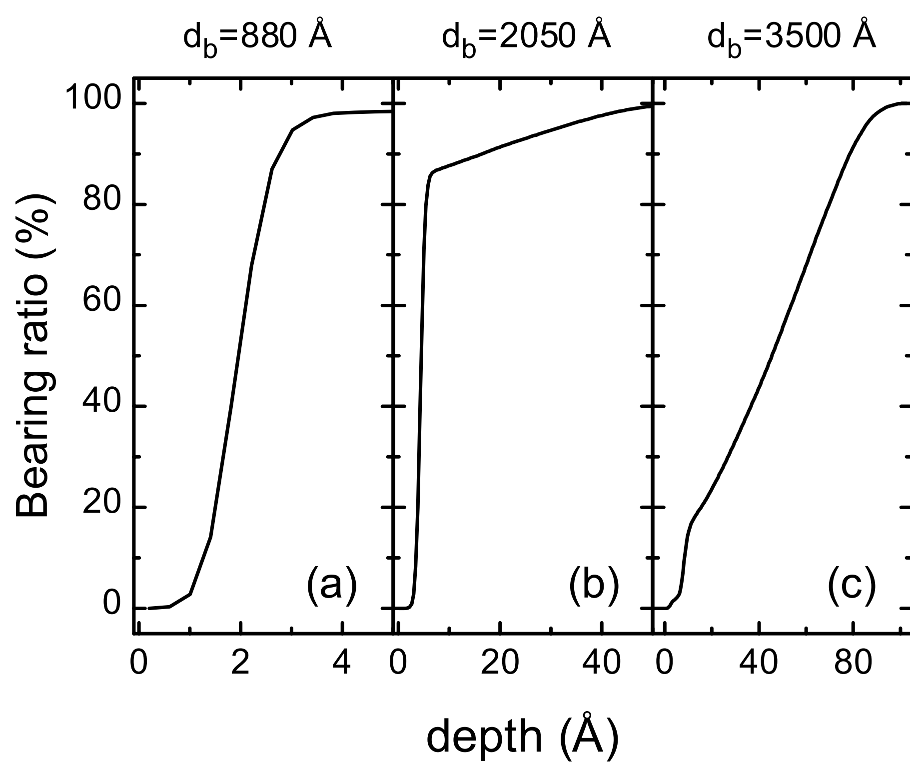

Figure 3.16 Bearing ratios of the surface height distributions obtained from the AFM images for the R=20 Si:H film series of Figs. 3.14 and 3.15.

homogeneous surface of the a-Si:H matrix. The deviations from the s-shape in Figs. 3.16(b-c) indicate that the surfaces are inhomogeneous due to the presence of the crystallite protrusions on the surface of the Si:H films in the mixed-phase growth regime. Such a complex distribution in the volume fraction of Si:H material within the roughness layer is not accounted for in the simple optical model of roughness adopted in the RTSE analysis. Finally, the presence of a low density of crystallites observed in the amorphous regime [Fig. 3.14(a) and 3.15(b)] may be attributed to crystallite nucleation at defect sites on the substrate surface.

3.6.2 Phenomenological model

The results of the previous section, in conjunction with those obtained in other studies using scanning probe microscopies (STM and AFM) and transmission electron microscopy (TEM) (Houben *et al.*, 1998; Ross *et al.*, 2000; Fujiwara *et al.*, 2001b), demonstrate that the μc-Si:H grains in the mixed-phase (a+μc)-Si:H growth regime evolve according to a cone-like geometry. Here, a phenomenological growth model is proposed based on such a geometry in order to analyze RTSE results for a number of Si:H depositions, in which both the a→(a+μc) transition and the (a+μc)→μc transition are observed.

Figure 3.17 depicts a schematic diagram of such model, including (a) a cross-sectional view and (b) a top view. The assumptions of this model are as follows. First, the crystalline nuclei consist of spherically capped cones with a fixed cone angle θ with respect to the substrate normal. Second, all crystallites nucleate at the same bulk layer thickness denoted $d_{b,tr0}$, with a nucleation density of N_d. Although these assumptions may oversimplify complicated statistical processes, they suffice to provide a physically reasonable model with a minimum number of free parameters.

In order to apply this geometric model to the RTSE data analysis results, one must develop relationships between the geometric parameters of the model and the parameters that are readily extracted in the RTSE analysis. Various parameters of importance can be extracted directly from the evolution of the surface roughness layer thickness (d_s) versus

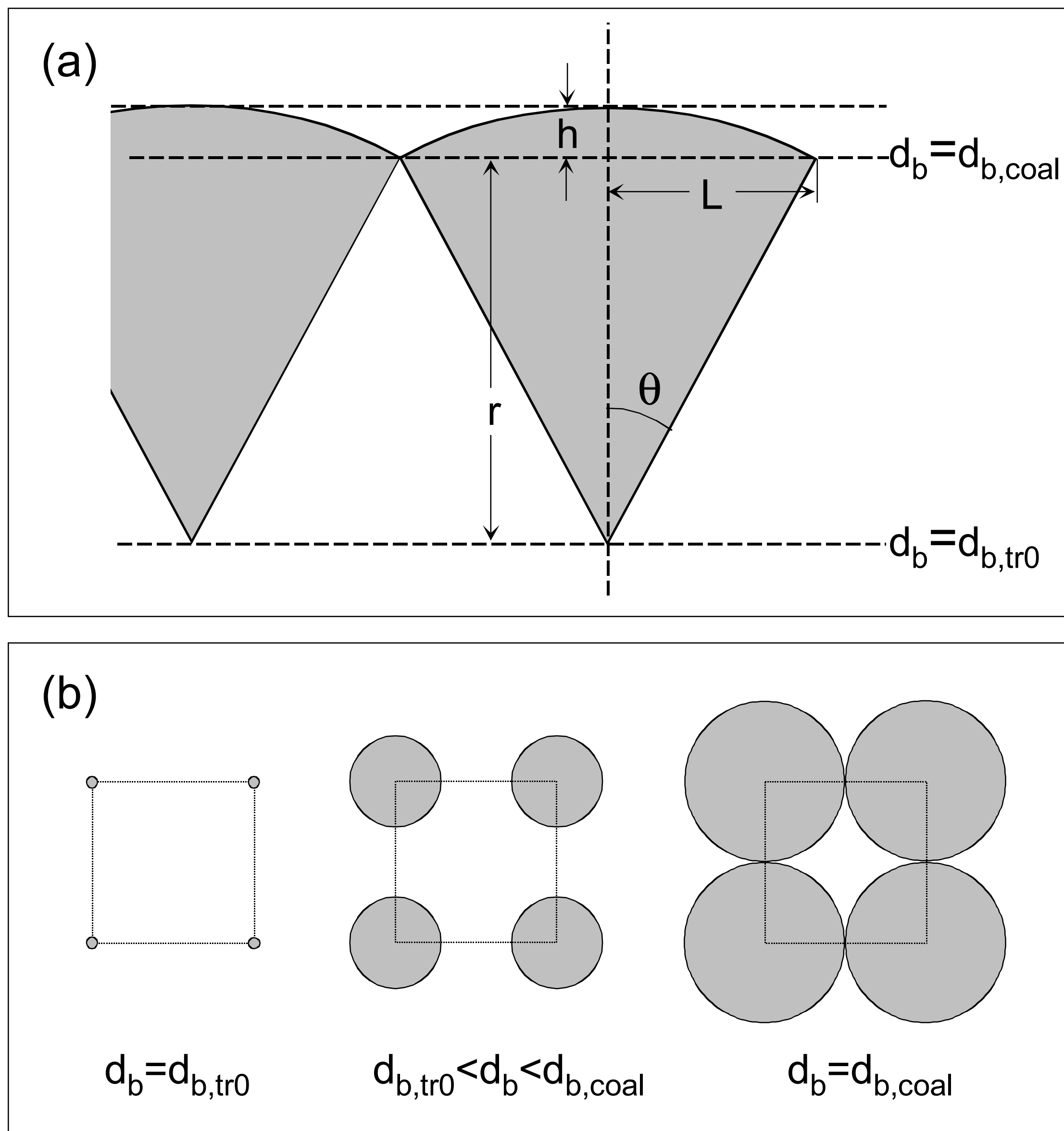

Figure 3.17 Schematic diagrams of the cone growth model that describes the evolution of the microcrystalline phase in the mixed-phase (a+μc)-Si:H growth regime, including (a) a cross-sectional view and (b) a top view.

the bulk layer thickness (d_b) during Si:H growth as obtained in the RTSE analysis. First, the bulk layer thickness corresponding to the a→(a+μc) transition is denoted $d_{b,tran}$ and is defined as the d_b value at which d_s increases by ~1 Å from its baseline value for the amorphous layer. This baseline or minimum value of d_s in the a-Si:H growth regime is denoted d_{s0}. Second, the pair of (d_b, d_s) values at the (a+μc)→μc transition (where the peak in d_s is observed) is denoted ($d_{b,coal}$, $d_{s,coal}$). Figure 3.13 provides an example of the determination of the values of $d_{b,tran}$, d_{s0}, $d_{b,coal}$, and $d_{s,coal}$. The two unknown geometric parameters of the growth model, N_d and θ, can in principle be determined from the measured parameters from the RTSE analysis. In the next paragraphs, different functional relations are derived to obtain an optimal solution for this problem.

First, it is necessary to develop several some geometric relationships. The height of each cone cap h and the radius of the cap base L in Fig. 3.17 can be calculated from the cone height r and the cone angle θ as

$$h = r\frac{1-\cos\theta}{\cos\theta}, \quad (3.8a)$$

$$L = r\tan\theta. \quad (3.8b)$$

The volume V_i of each cap and the area A_i covered by each cap can be calculated from h and L. Thus, they can also be expressed using Eqs. 3.8 as functions of r and θ according to:

$$V_i(r,\theta) = f_{Vi}(\theta)r^3 , \quad (3.9a)$$

$$A_i = f_{Ai}(\theta)r^2 , \quad (3.9b)$$

where the functions $f_{Vi}(\theta)$ and $f_{Ai}(\theta)$ exhibit the following form

$$f_{Vi}(\theta) = \frac{\pi}{6}\frac{1-\cos\theta}{\cos\theta}\left[3\tan^2\theta + \left(\frac{1-\cos\theta}{\cos\theta}\right)^2\right] \quad (3.10a)$$

$$f_{Ai}(\theta) = \pi\tan^2\theta. \quad (3.10b)$$

Therefore, the total volume V_{TOT} of cone caps per unit area and the fractional area coverage A_{TOT} of the caps are given by:

$$V_{TOT} = N_d V_i = N_d f_{Vi}(\theta) r^3 \ , \tag{3.11a}$$

$$A_{TOT} = N_d A_i = N_d f_{Ai}(\theta) r^2 . \tag{3.11b}$$

Finally, the height of the cones r at the bulk layer thickness d_b is given in terms of the RTSE analysis results and $d_{b,tr0}$ by $r = d_b - d_{b,tr0}$.

Next, the geometric aspects of the a→(a+μc) transition will be considered. The cone model predicts that in the initial stages of the mixed-phase (a+μc)-Si:H growth regime the crystalline nuclei are widely separated, and the total volume per unit area V_{TOT} of the cone caps varies according to the cube of the cone height (Eq. 3.11a). However, the volume fraction of material within the surface roughness layer is fixed for simplicity at 0.5 in the RTSE analysis. As a result, it is not valid simply to equate $\Delta d_s = d_s - d_{s0}$, the roughness increase relative to the baseline, with the cap height h. Instead, the effective thickness or Si:H volume per unit area in the roughness layer as deduced from the RTSE analysis is equated to the total volume per unit area V_{TOT} for the cone caps according to:

$$0.5 k_{EMA} \Delta d_s = V_{TOT} = N_d f_{Vi}(\theta) (d_b - d_{b,tr0})^3 \ . \tag{3.12}$$

Here k_{EMA} is a proportionality constant to account for the possibility that the EMA exhibits a different sensitivity to very small volume fractions of Si:H in the roughness layer. Equation 3.12 explains the rapid increase in the surface roughness layer thickness d_s with increasing bulk layer thickness d_b as observed in the RTSE results (see Fig. 3.13). In fact, Eq. 3.12 can be used to fit the evolution of d_s versus d_b according to the expression

$$\Delta d_s = d_s - d_{s0} = \begin{cases} 0 & d_b < d_{b,tr0} \\ a\,(d_b - d_{b,tr0})^3 & d_b > d_{b,tr0} \end{cases} , \tag{3.13}$$

where $a \equiv 2 N_d f_{Vi} / k_{EMA}$ and $d_{b,tr0}$ are the free parameters. An example of such an approach is shown in Fig. 3.18. A relatively good fit to the experimental data is observed in Fig. 3.18, suggesting that the interpretation of the initial stages of the mixed-phase growth regime is valid. Analyses of several Si:H depositions, however, have revealed

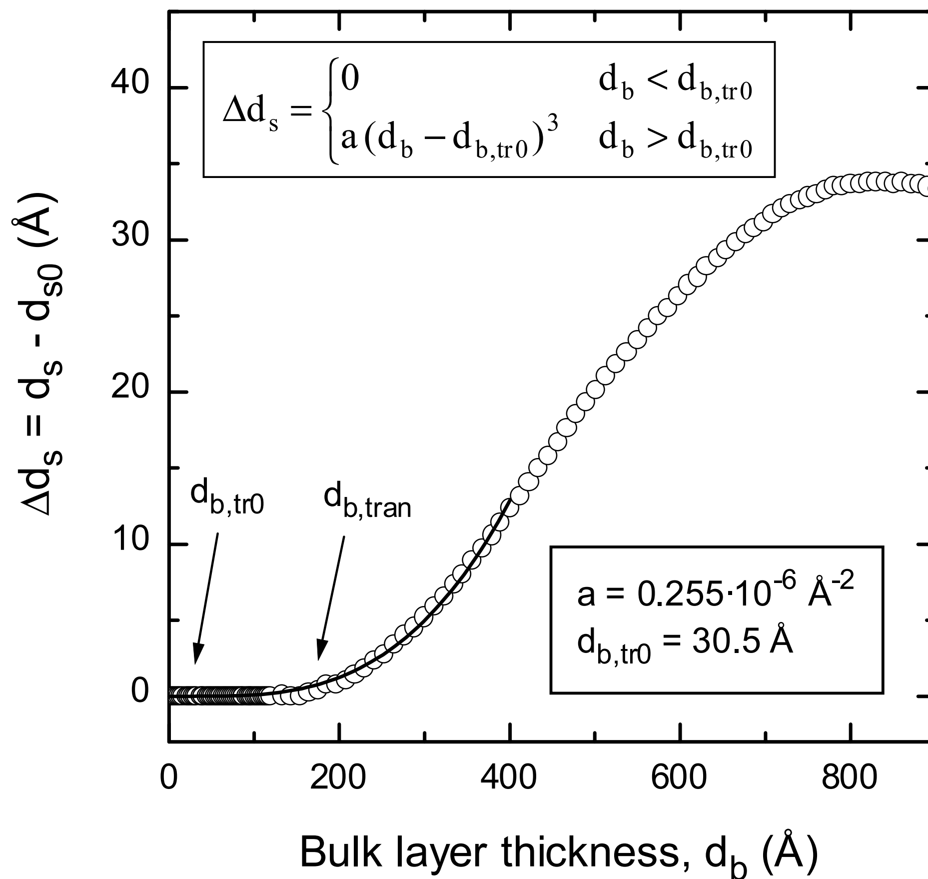

Figure 3.18 Increase in the surface roughness layer thickness Δd_s versus bulk layer thickness d_b as deduced from RTSE (open circles). The onset of roughening in Δd_s in the initial stages of the mixed-phase growth regime can be fit according to Eq. 3.13 (solid line). The values for the best fit parameters a and $d_{b,tr0}$ are listed within the plot.

that $d_{b,tr0}$ can assume unphysical negative values, and that the best-fit values of a and $d_{b,tr0}$ in Eq. 3.13 are strongly correlated. The unphysical values may result because the cone growth model assumes that the height and radius of the cap increase continuously from zero with a linear dependence on the cone height. In contrast, the actual crystalline nuclei may initially form with a finite radius and initially increase in size non-linearly with thickness. Another complication is the fact that when the crystalline nuclei are small their protuberances cannot be differentiated from the mounds that form the roughness layer of the a-Si:H matrix. Such observations indicate that $d_{b,tr0}$, i.e., the thickness at which the crystallites start to nucleate cannot be established unequivocally on the basis of Eq. 3.13. Therefore, in order to proceed, it is assumed for simplicity in the model that $d_{b,tr0}$ (the bulk layer thickness at the apexes of the cones in Fig. 3.17) equals $d_{b,tran}$ (the a→(μ+c) transition thickness as detected by RTSE). This approach is supported by the RTSE-AFM correlation of Fig. 3.15 and the consistent results for N_d and θ deduced for several different Si:H depositions as described in the following paragraphs.

Next, the geometric aspects of the (a+μc)→μc transition will be considered. At the coalescence thickness $d_{b,coal}$ the μc-Si:H cones begin to make contact, and the fractional area coverage of the caps should equal a constant K near unity, depending on the initial distribution of the crystalline nuclei (e.g., for a hexagonal lattice, K=0.907; for a square lattice as in Fig. 3.17, K=0.785). Thus, by equating A_{TOT} to K, the following relationship is obtained:

$$N_d f_{Ai}(\theta)(d_{b,coal} - d_{b,tr0})^2 = K. \qquad (3.14)$$

In addition at $d_{b,coal}$, the Si:H volume fraction within the surface roughness layer is assumed to be 0.5 in the RTSE analysis. Thus, the total volume of the cone caps per unit area V_{TOT} can be equated to the effective thickness of the surface roughness layer thickness at coalescence, $d_{s,coal}$ according to

$$0.5\Delta d_{s,coal} = V_{TOT} = N_d f_{Vi}(\theta)(d_{b,coal} - d_{b,tr0})^3, \qquad (3.15)$$

where $\Delta d_{s,coal}$ is the difference between $d_{s,coal}$ and the baseline d_{s0}, i.e., $\Delta d_{s,coal} = d_s(d_{b,coal}) - d_{s0}$ (see Fig. 3.13). In contrast to Eq. 3.12, a factor k_{EMA} is not required in Eq. 3.15 because the assumed and actual values of the Si:H volume fraction in the roughness layer are expected to be similar, i.e., near 0.5. The value of $\Delta d_{s,coal}$ in Eq. 3.15 exhibits a relatively large uncertainty since it is derived from the two-layer optical model that fails to provide a good fit to the experimental (ψ, Δ) spectra in the (a+μc)-Si:H and μc-Si:H growth regimes [see Fig. 3.13(b)].

Equations 3.14 and 3.15 can be rewritten to provide the nucleation density

$$N_d = \frac{K}{f_{Ai}(\theta)(d_{b,coal} - d_{b,tr0})^2} , \tag{3.16}$$

$$N_d = \frac{0.5\,\Delta d_{s,coal}}{f_{Vi}(\theta)(d_{b,coal} - d_{b,tr0})^3} . \tag{3.17}$$

By eliminating N_d from Eqs. 3.16 and 3.17, the following expression for θ can be found:

$$\frac{f_{Vi}(\theta)}{f_{Ai}(\theta)} = \frac{0.5\,\Delta d_{s,coal}}{K}(d_{b,coal} - d_{b,tr})^{-1} . \tag{3.18}$$

After extensive manipulation of Eq. 3.18, the following third order equation in $\cos\theta$ is obtained

$$\cos^3\theta - \frac{X+6}{X+2}\cos\theta + \frac{4}{X+2} = 0, \tag{3.19}$$

where

$$X = \frac{3\,\Delta d_{s,coal}}{K(d_{b,coal} - d_{b,tr})}. \tag{3.20}$$

The three roots of Eq. 3.19 can be determined, and only one root assumes a value between 0 and 1. Thus, θ can be estimated unambiguously from the experimentally-defined values of $d_{b,tran}$, d_{s0}, $d_{s,coal}$, and $d_{b,coal}$. Once θ is determined, N_d can be determined from Eq. 3.16 or Eq. 3.17.

Figure 3.19 presents results for (a) the cone angle θ and (b) the nuclei density N_d plotted as a function of the observed a→(a+μc) transition thickness $d_{b,tran}$ as deduced

from RTSE for a number of Si:H films deposited under different conditions (open circles). In Fig. 3.19(a), it can be seen that the values for θ all lie in between 10 and 20° with an average value of 15°, whereas in Fig. 3.19(b), the nucleation density N_d varies by three order of magnitudes, decreasing with increasing $d_{b,tran}$.

In Figs. 3.19(a-b), results estimated from the AFM images of Fig. 3.14 are included as well (solid circles). The cone angle is determined from the film thicknesses and the radii of the largest crystallites in Fig. 3.14(a) and 3.14(d), assuming a linear relation between radius and thickness. In addition, the nucleation density is estimated from Fig. 3.14(c), just after the a→(a+μc) transition. These direct measurements are consistent with the trends among the different samples as obtained from RTSE analyses using the cone model. For films in which the a→(a+μc) transition is observed at a thickness greater than 750 Å, however, delamination occurs before the (a+μc)→μc transition can be observed. As a result, no direct comparisons can be made between the AFM values of θ and N_d from Fig. 3.14 and the corresponding RTSE values for samples deposited under the same conditions.

Figures 3.19(a-b) also include results extracted from a study reported by Fujiwara et al. in which the crystallite nucleation regime was investigated by a combination of RTSE, AFM and cross-sectional transmission electron microscopy (TEM) (Fujiwara *et al.*, 2001b). The solid triangles in Fig. 3.19 correspond to values obtained directly from (a) TEM for θ, and (b) AFM for N_d; and the solid squares correspond to the values for N_d and θ obtained from an application of the cone model to the RTSE results (d_s vs. d_b) published by Fujiwara et al. Very good agreement is observed between both the direct measurement results of N_d and θ by AFM and TEM, respectively, by Fujiwara et al. (Fujiwara *et al.*, 2001b) and the corresponding results predicted by the cone growth model applied to their RTSE data. This suggests that the parameters obtained in the RTSE analysis can be correlated with simple geometrical parameters that describe the microstructural evolution in the mixed-phase (a+μc)-Si:H growth regime.

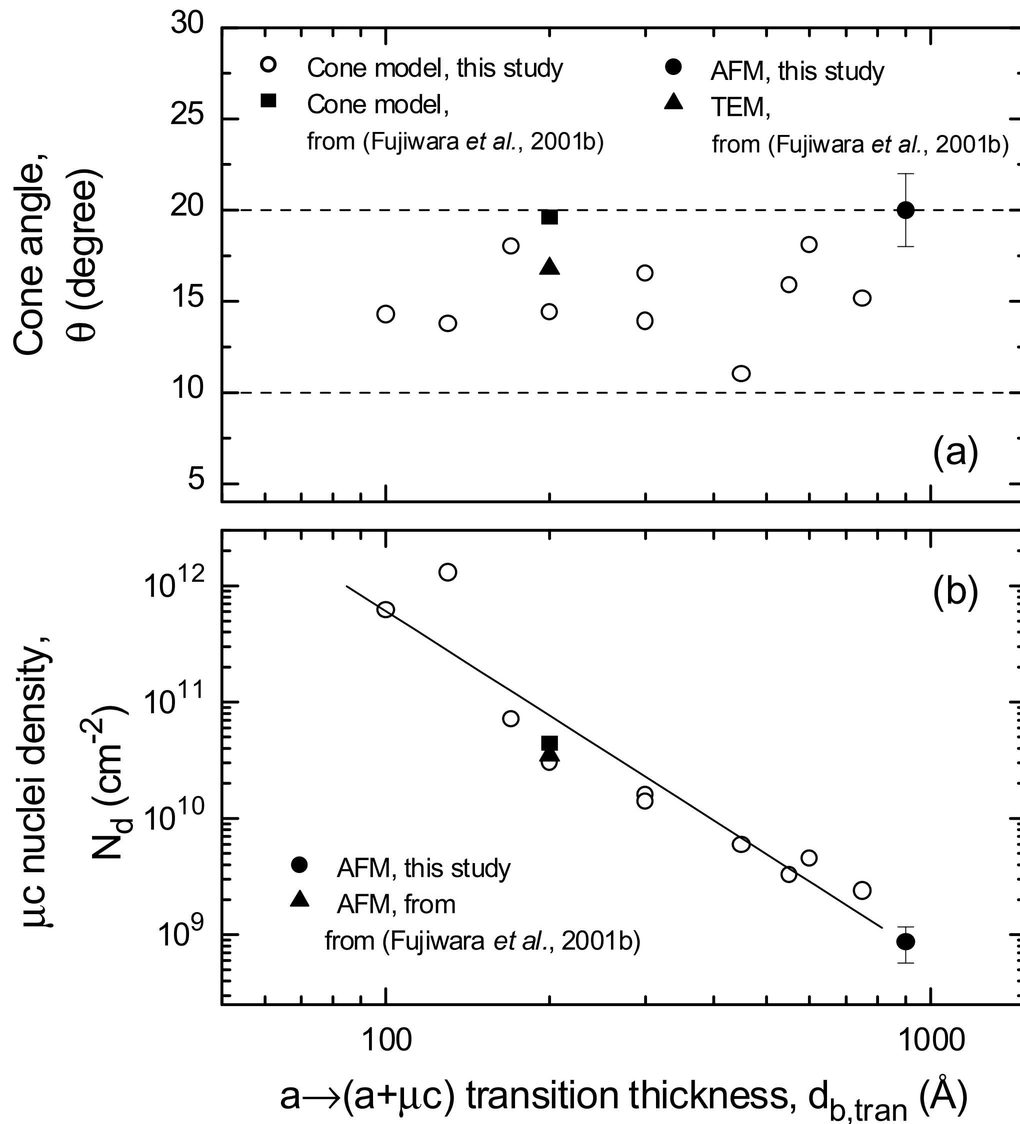

Figure 3.19 (a) Cone angle θ and (b) nucleation density N_d versus the a→(a+μc) transition thickness $d_{b,tran}$ for several Si:H films deposited under different conditions. The values for θ and N_d (open circles) are deduced by the cone growth model as described in the text. Values extracted from AFM study of Fig. 3.14 (solid circles), as well as from the RTSE, AFM and TEM study presented elsewhere (solid squares and triangles) (Fujiwara *et al.*, 2001b) are also included for comparison.

3.6.3 Virtual interface analysis

As discussed so far in this section, the complexity of the amorphous–to–microcrystalline transition requires more sophisticated approaches for RTSE analysis than the one based on the two-layer optical model. Ideally, a complete analysis should be able to provide the microstructural evolution of the Si:H film as well as the thickness evolution of the dielectric function in the mixed-phase (a+μc)-Si:H and single-phase μc-Si:H growth regimes. The microstructural parameters may include the bulk layer thickness, the volume fraction of μc-Si:H in the bulk layer, the surface roughness layer thickness, and the volume fractions of a-Si:H, μc-Si:H, and void in the surface layer.

One approach to solve this problem is to consider the film as a series of discrete stacked layers and perform the $\overline{\sigma}$-minimization routine for each layer, as described in Sec 2.4.3. In this way, the evolution of the dielectric function can be obtained in a step-wise manner. This approach has been used elsewhere to obtain the dielectric functions of the a-Si:H, mixed-phase (a+μc)-Si:H, and single-phase μc-Si:H films in the three stages of a single Si:H deposition (Ferlauto *et al.*, 2000a). Fujiwara et al. applied the same approach to describe the evolution of the microstructural and optical properties in the mixed-phase (a+μc)-Si:H growth regime (Fujiwara *et al.*, 2001b). The discrete, stacked-layer approach has its limitations, however. First it is susceptible to cumulative errors generated by stacking many layers and performing a numerical inversion of the RTSE data for each layer. Second, because of the complexity of the stacked layer model, the surface roughness layer must still be described as a 0.5/0.5 Si:H/void volume fraction mixture. The latter leads to surface roughness layer dielectric functions with unphysically high amplitudes (based on expectations from AFM images) and consequently low surface roughness layer thicknesses d_s, as can be seen in Fig. 3.15(c) for the two-layer model and also noted by Fujiwara et al. for the stacked-layer model (Fujiwara *et al.*, 2001b). Here, a self-consistent alternative approach is proposed based on a so-called 'virtual interface analysis' to be described in next paragraphs.

Aspnes was the first to propose a method for the analysis of real time ellipsometric data of complex graded thin-film structures based on a three-medium

optical model for the growing film. This model incorporated an ambient/outerlayer interface and an outerlayer/pseudosubstrate virtual interface (Aspnes, 1993). Such a method was used to provide information on the dielectric function of the outerlayer, eliminating the contribution of the underlying film structure to the experimental data. Later, this method was expanded to incorporate a surface roughness layer on top of the outerlayer in the optical model. The expanded virtual interface analysis permitted the determination of gradients in the volume fraction of voids in PECVD of a-Si:H (Kim and Collins, 1995), and gradients in the binary alloy composition x in PECVD of a-$Si_{1-x}C_x$:H films (Fujiwara *et al.*, 1997). The four-medium optical model used in these analyses consists of (i) the ambient, (ii) a surface roughness layer, usually [0.5/0.5 outerlayer/void] (iii) an outerlayer with dielectric function ε_o, and (iv) the pseudosubstrate with dielectric function $\langle\varepsilon\rangle$.

A schematic diagram of the corresponding four-medium optical model used in this study is depicted in Fig. 3.20. This model will be applied to obtain the volume fractions of μc-Si:H and a-Si:H versus bulk layer thickness in the mixed-phase regime by means of least-squares regression analysis of the experimental (ψ, Δ) spectra versus time. Thus, in this case, the dielectric function ε_o of the outerlayer is calculated from the EMA assuming a mixture of μc-Si:H and a-Si:H materials [$f_{\mu c}/(1-f_{\mu c})$ μc-Si:H/a-Si:H], whereby the volume fraction of the μc-Si:H phase $f_{\mu c}$ is a free parameter to be determined in the analysis. The dielectric function of the surface roughness is calculated as usual from the EMA assuming a fixed [0.5/0.5 outerlayer/voids] mixture, and its thickness d_s is also a free parameter. The dielectric function of the a-Si:H phase ε_a can be deduced from the standard two-layer optical model as applied to an analysis of the film growth in the amorphous regime. The deposition rate is assumed to be constant, since excellent linearity is observed in the time evolution of d_b as obtained in a least-squares regression analysis using the two-layer model and the dielectric function ε_a, obtained in the a-Si:H growth regime. In this previous model, however, the large values of the unbiased estimator (see Fig. 3.13) lead to significant uncertainties in the values of the surface roughness layer thickness in the mixed-phase regime and at $d_{b,coal}$. As a result, significant

uncertainties also exist in the dielectric function of the μc-Si:H phase $\varepsilon_{\mu c}$, which is extracted by inversion of the (ψ, Δ) spectra collected near the (a+μc)→μc transition where d_b=$d_{b,coal}$.

In order to eliminate these uncertainties, a self-consistent routine is applied that is based on the same principles as the $\overline{\sigma}$-minimization routine described in Sec. 2.4. In this new routine, the surface roughness layer thickness $d_{s,coal}$ at $d_{b,coal}$ is the only 'global' free parameter. This thickness is used to determine $\varepsilon_{\mu c}$ by exact inversion, which in turn will be used as the reference dielectric function of the μc-Si:H phase in the least-squares regression analysis using the four-medium virtual interface model of Fig. 3.20. This iteration is repeated for several guesses of $d_{s,coal}$ and a minimum in $\overline{\sigma}$ can be found as demonstrated in Fig. 3.21. As a result, the dielectric function of the μc-Si:H phase $\varepsilon_{\mu c}$ and the time evolution of the microstructural parameters d_s and $f_{\mu c}$ can be determined using the choice of $d_{s,coal}$ that minimizes $\overline{\sigma}$ (86 Å in this case). Finally, $\varepsilon_{\mu c}$ can also be used to determine the evolution of d_s in the single-phase μc-Si:H regime [after the a→(a+μc) transition] by applying a two-medium model of ambient/(semi-infinite film). The final results of such an analysis are given in Figs. 3.22 and 3.23. This overall procedure will be designated the virtual interface (or VI) analysis from here onward.

Figure 3.22 depicts the microstructural parameters deduced from the VI analysis versus the bulk layer thickness d_b for a Si:H film deposited on a c-Si substrate with a H_2-dilution ratio of R=40, a plasma power of P=0.83 W/cm^2, and substrate temperature of T=260ºC. The values for d_b as a function of time were deduced previously in the simplified analysis using the two-layer model. The best fit deposition rate obtained from the observed linear slope of d_b vs. time is 2.84 Å/s and is fixed in the VI analysis. The results in Fig. 3.22 include (a) the volume fraction $f_{\mu c}$ in the outerlayer, (b) the surface roughness layer thickness d_s, and (c) the unbiased estimator σ of the VI least-squares regression analysis . The results in Fig. 3.22(a) are compared to the function for $f_{\mu c}$ predicted by the cone model (solid line), and in Figs. 3.12(b) and 3.12(c), the VI analysis results are compared to those for d_s and σ obtained by the two-layer analysis (solid symbols).

First, in Fig. 3.22(c) it is observed that the values for σ obtained in the VI analysis are much lower ($<1\times10^{-2}$) than those obtained in the standard two-layer analysis. This indicates that a much improved description of the (a+μc)-Si:H and μc-Si:H growth regimes is obtained from the VI analysis. Next, it is worth noting that $f_{\mu c}$ determined in the VI analysis for the outerlayer of thickness d_o (in this case, d_o~6 Å) is in fact a snapshot of the average fractional area of the surface covered by μc-Si:H. The evolution of $f_{\mu c}$ from the VI analysis shows an inflection near d_b~1000 Å where $f_{\mu c}$~0.5. This may indicate a threshold thickness demarcating a regime wherein the crystallites are well separated from a regime wherein the growth of each crystallite is influenced by the presence of its neighbors (e.g., when the "radical capture areas" around the crystallites at the surface begin to overlap). The differences in the $f_{\mu c}$ values predicted by the cone growth model and the those measured in the VI analyses indicates that a more sophisticated growth model may be necessary, in particular one including statistical distribution of crystallites nucleation sites rather than sites arranged geometrically in a two-dimensional array (Fejfar *et al.*, 2001). The surface roughness evolution d_s determined in the VI analysis shows the same behavior as that from the two-layer model, but the values are larger because $d_{s,coal}$, the value of the surface roughness layer thickness at coalescence, was found to be larger in the $\overline{\sigma}$-minimization procedure. Here it is worth noting that the material fraction within the surface roughness layer in the VI analysis is fixed at 0.5, as in the simpler two-layer analysis. Attempts to vary this parameter did not allow convergence of the $\overline{\sigma}$-minimization routine. This suggests limitations on the EMA in its ability to describe the optical properties of the surface roughness on the mixed-phase films. These limitations may occur for two reasons. First the average in-plane separation of the crystallites (100 Å for a $N_d=10^{12}$ cm^{-2} and 3000 Å for $N_d=10^{9}$ cm^{-2}) extends above the limit of validity of the EMA. The EMA is believed to be valid for microstructural scales less than about 1/10 the wavelength of the probe light (Aspnes, 1982). Second, in the initial stages of the mixed-phase regime, the volume fraction of μc-Si:H in the surface roughness layer is very small, and the EMA has yet to be test under these circumstances.

Before turning to the optical properties in the different growth regimes, it is useful to reassess the impact of the new value of $d_{s,coal}$ from Fig. 3.22 on the computation of N_d and θ from Eqs. 3.16 (or 3.17) and 3.19, respectively. Using the $\Delta d_{s,coal}$ value of 55 Å from the two-layer analysis yields (N_d, θ)=(1.6×10^{10} cm^{-2}, 13.9°), whereas the new value of $\Delta d_{s,coal}$=77 Å from the VI analysis yields (N_d, θ)=(1.1×10^{10} cm^{-2}, 16.4°). It is concluded that the two-layer analysis provides sufficiently accurate results for estimates of the nucleation density and cone angle within the cone growth model. In any case, the two-layer analysis is expected to consistently underestimate $d_{s,coal}$ so the trends observed in Fig. 3.19 are expected to be unchanged when all N_d and θ values are obtained from VI analyses results.

Finally, Fig. 3.23 depicts the spectra in the dielectric function for the Si:H film of Fig 3.22 in the a-Si:H growth regime (ε_a) at a thickness d_b~200 Å (squares) and in the single-phase μc-Si:H growth regime ($\varepsilon_{\mu c}$) at a thickness d_b~2200 Å (circles). The dielectric function of the film at any intermediate thickness in the mixed-phase (a+μc)-Si:H growth regime can be deduced by the EMA by using the best fit $f_{\mu c}$.

3.6.4 Discussion and Summary

First, the nucleation mechanisms of the μc-Si:H phase will be discussed. The RTSE analysis of Si:H films deposited on c-Si substrates with different H_2-dilution ratios R as presented in Sec. 3.4 show that the a→(a+μc) transition thickness decreases with increasing R. The same trend is observed for different deposition conditions and substrates, as will be presented in Chapters 4 and 5. In addition, the AFM measurements presented in Sec. 3.6.1 suggest that RTSE is sensitive to a minimum of ~0.5% area fraction coverage of the μc-Si:H phase and that the a→(a+μc) transition thickness as detected by RTSE is associated with a rapid increase in the nucleation density of the crystallites. These observations suggest that the μc-Si:H nucleation results from gradual modifications in the structure of a-Si:H phase with thickness such that above a certain threshold μc-Si:H nucleation is favored. In addition, such modifications are facilitated by

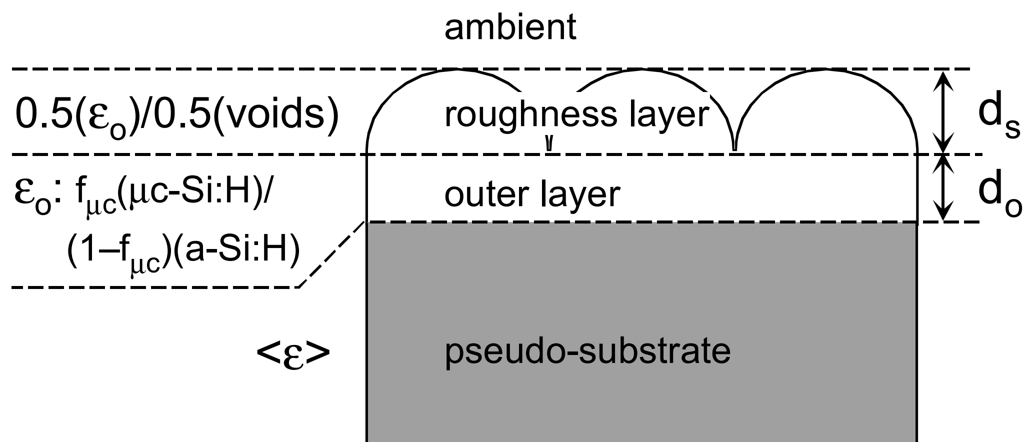

Figure 3.20 Schematic of the four-medium optical model used in the RTSE virtual interface (VI) analysis of the amorphous–to–microcrystalline transition in Si:H films. The free parameters in this model are (i) the volume fraction $f_{\mu c}$ of the μc-Si:H phase in the outerlayer of thickness d_o and (ii) the surface roughness layer thickness d_s.

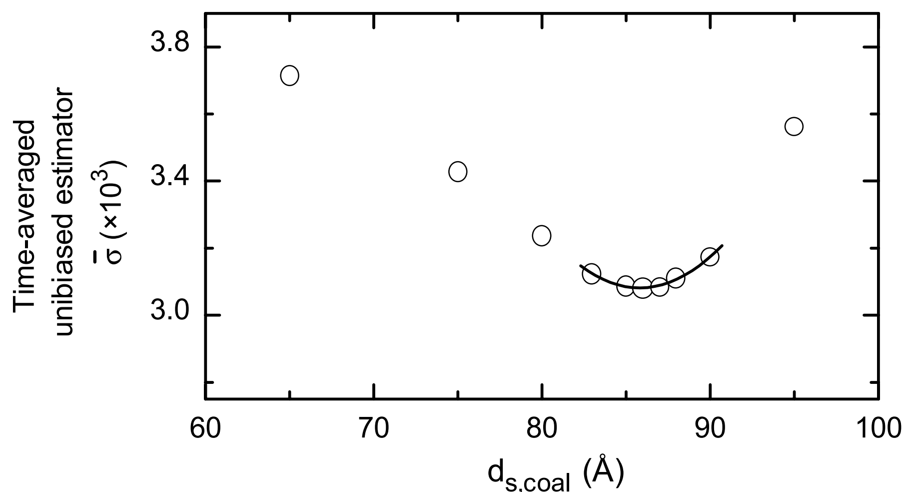

Figure 3.21 Time-averaged unbiased estimator $\overline{\sigma}$ versus the value of the surface roughness layer thickness $d_{s,coal}$ at the (a+μc)→μc transition thickness $d_{b,coal}$. The minimum in $\overline{\sigma}$ defines the value of $d_{s,coal}$ used to deduce the dielectric function $\varepsilon_{\mu c}$ of the μc-Si:H phase. This dielectric function is used in the least-squares regression analysis of the (ψ, Δ) spectra vs. time during the mixed-phase (a+μc)-Si:H growth regime.

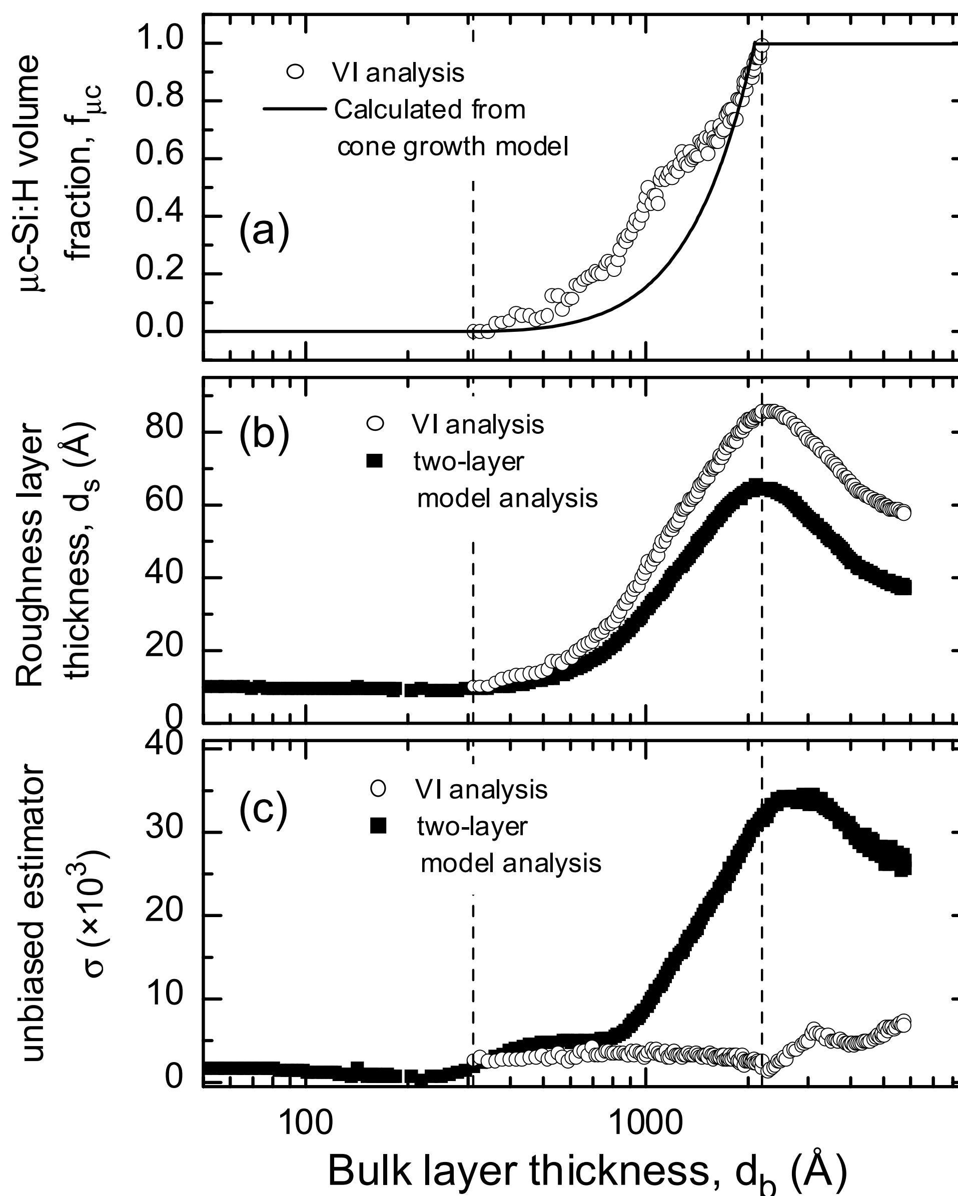

Figure 3.22 Results of the virtual interface (VI) analysis applied to RTSE data for a Si:H film as plotted versus the bulk layer thickness d_b (open circles). The results include (a) the microcrystalline volume fraction $f_{\mu c}$ in the outerlayer , (b) the surface roughness layer thickness d_s, and (c) the unbiased estimator σ. The results of the VI analysis are compared to (a) results predicted by the cone growth model of Sec. 3.6.2 (solid line), and (b, c) results obtained in the standard RTSE analysis using the two-layer model (solid squares).

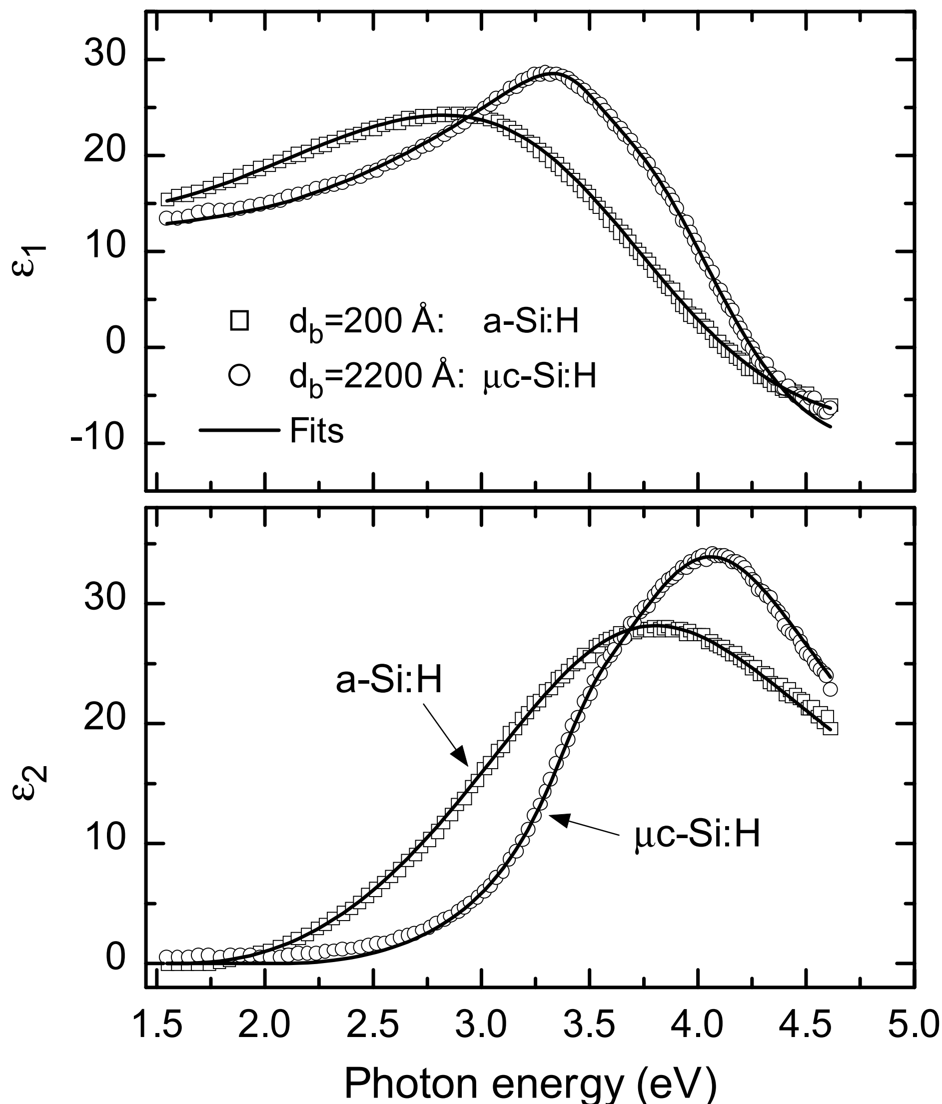

Figure 3.23 Dielectric function spectra (ε_1, ε_2) at different bulk layer thicknesses d_b for a Si:H film that undergoes the amorphous–to–microcrystalline transition. The squares represent the spectra in (ε_1, ε_2) at d_b=200 Å; here the film is in the a-Si:H growth regime. Such spectra are obtained in the standard RTSE analysis using the two-layer optical model. The circles represent the spectra in (ε_1, ε_2) at d_b=2200 Å; here the Si-H film is in the single-phase μc-Si:H growth regime immediately after the (a+μc)→μc transition. Such spectra are obtained from the virtual interface analysis, which is described in the text and in Figs. 3.22 and 3.23. The solid lines correspond to fits to the experimental spectra obtained by using the analytical expressions described in Chapter 6.

increases in the H_2-dilution ratio R. In a recent study that combined real time spectroscopic ellipsometry and infrared spectroscopy, Fujiwara et al. reported that the nucleation of the μc-Si:H phase is induced by the build-up in the concentration of a SiH_n (n=1~2) complex (with an infrared absorption peak at 1937 cm^{-1}) in a 2 monolayer (ML) thick a-Si:H subsurface region. It was proposed that such a complex is formed by the insertion of H into a strained Si-Si bond. The concentration of the SIH_n complexes was found to grow with increasing thickness, and the slope characterizing the SiH_n growth also was found to increase with increasing H_2-dilution ratio R. Furthermore, it was suggested that a threshold concentration of SiH_n complexes of ~7 at. % (assuming one H per complex), independent of R, is required for the nucleation of the μc-Si:H phase (Fujiwara *et al.*, 2000b). Such a concentration corresponds to an area density of $\sim 5\times10^{13}$ cm^{-2}, which is two orders of magnitude larger than the typical crystallite nucleation densities (see Fig. 3.19). Therefore, it is likely that clusters consisting of tens or hundreds of SiH_n complexes may act as nucleation sites for the μc-Si:H grains. These considerations also lend support to the results from the cone growth model presented in Fig. 3.19.

The next question to be addressed is how these SiH_n complexes are formed in the first place. One possible explanation is that the structural modifications in the a-Si:H incubation layer characterized by increases in the concentration of SiH_n complexes are induced ultimately by stress. It has been recognized for a long time that high electronic quality a-Si:H films exhibit high levels of compressive stress. An early study has shown that the compressive stress in a-Si:H films follows a positive correlation with the concentration of Si-H bonds in the film bulk (Hishikawa, 1987). In more recent work, it has been observed that Si:H films deposited at H_2-dilution levels R close to the (a→μc) boundary exhibit the highest compressive stress and a significant amount of unbonded H (Kroll *et al.*, 1996). In addition, it has been found that for a-Si:H deposited with moderate H_2-dilution (R=10), the intrinsic stress increases with increasing film thickness (Danesh *et al.*, 2001). The high compressive stress observed in a-Si:H deposited with H_2-dilution can then be attributed to H_2 molecules trapped in the a-Si:H network (Kroll *et al.*,

1996) and/or to the high concentration of Si-H bonds (as opposed to Si-H_2 bonds) in the film bulk (Hishikawa, 1987). Recently, it has been shown that the concentration of SiH_n complexes introduced within the 2 ML subsurface region of a-Si:H films by H_2-plasma treatment is proportional to the intrinsic stress in the films (Fujiwara *et al.*, 2001a). From the results of these studies, it is proposed here that two combined effects are responsible for the nucleation of the μc-Si:H phase from the a-Si:H phase. First. the intrinsic stress in the a-Si:H must be high so that the concentration of strained Si-Si bonds are also high. Second a high flux of atomic H from the plasma impinging onto the film is necessary. As a result, H diffusion into the subsurface and subsequent H insertion into the strained Si-Si bonds will create the conditions necessary for SiH_n complex formation which in turn leads to μc-Si:H nucleation.

Next, the evolution of the μc-Si:H phase in the mixed-phase (a+μc)-Si:H flm growth regime is addressed. The RTSE and AFM results presented here suggest that there is preferential growth of the μc-Si:H phase over the a-Si:H phase. As a result, the μc-Si:H grains increase in density and size with increasing thickness, resulting in the surface protrusions and roughening observed in the AFM and RTSE measurements, respectively. The same type of behavior has also been observed in previous AFM and TEM analyses of mixed-phase (a+μc)-Si:H films (Houben *et al.*, 1998; Ross *et al.*, 2000; Fujiwara *et al.*, 2001b). In addition, the proposed geometric growth model indicates that during the mixed-phase growth regime the μc-Si:H grains develop in a cone-like geometry. Furthermore, a relatively constant cone angle (15±5°) can be used to describe the RTSE data for a number of Si:H films. This angle is independent of the phase transition parameters deduced by RTSE [i.e., the bulk layer and surface roughness layer thicknesses at the a→(a+μc) and the (a+μc)→μc transitions], and thus it is independent of the deposition conditions, as well. The preferential growth of the μc-Si:H phase can be attributed to higher sticking coefficient of radicals on the surface of the crystalline phase than that on the surface of the amorphous phase. Alternatively, reactive sites such as dangling bonds may be more easily created or trapped on the surface of the crystalline phase. The resulting cone angle for the μc-Si:H grains can then be explained in terms of

a ratio between the growth rate in the direction normal to the substrate, i.e., the deposition rates, and the growth rate of the μc-Si:H grains in the in-plane direction. The in-plane growth rate for a given grain may be proportional to the radical-capture area around the grain and to the flux of radicals impinging on this area. Thus, the capture area is expected to be determined by the surface diffusion length of the radicals. The relatively constant cone angle deduced from the cone model may indicate that the variations in the surface diffusion length for the different Si:H depositions are not significant.

Finally, a self-consistent analysis was developed that allowed the determination of the evolution of the volume fraction for the μc-Si:H phase $f_{\mu c}$ during the mixed phase (a+μc)-Si:H growth regime, as well as the dielectric function of the same film in the a-Si:H (ε_a) and in the single-phase μc-Si:H ($\varepsilon_{\mu c}$) growth regimes. As a result, the dielectric function at any given thickness in the mixed-phase regime can be determined from ε_a, $\varepsilon_{\mu c}$, and $f_{\mu c}$ by applying the EMA approximation. Such an analysis can be adopted in future studies to determine quantitatively the evolution of the volume fraction of the μc-Si:H phase in the intrinsic Si:H layers employed in solar cells. In this way, the depth variation in the μc-Si:H content can be correlated with solar cell performance indicators. For example, it is now possible to compare the depth profile of the μc-Si:H volume fraction (and hence the dielectric function of the i-layer) with the depth profile of the mobility gap in the mixed-phase (a+μc)-Si:H growth regime. In a recent work, the characteristics of such profile in the μc-Si:H content has been shown to strongly affect the solar cell characteristics (Koval *et al.*, 2001).

CHAPTER 4

DEPOSITION PHASE DIAGRAMS FOR THE GUIDANCE OF SOLAR CELL OPTIMIZATION

4.1 INTRODUCTION

Several studies over the past twenty years have established that moderate H_2-dilution of the source gases used in plasma-enhanced chemical vapor deposition (PECVD) of amorphous silicon (a-Si:H) and its alloys at low temperatures (< 300°C) leads to improvements in the electronic quality of these materials (Guha *et al.*, 1981; Matsuda and Tanaka, 1987; Tanaka, 1989; Lee *et al.*, 1996; Okamoto *et al.*, 1996; Rech *et al.*, 1996). A-Si:H-based solar cells having intrinsic (i) layers prepared using this approach show improved performance and higher resistance to light-induced degradation (Bennett *et al.*, 1993; Yang *et al.*, 1994; Yang and Chen, 1994; Lee *et al.*, 1996; Okamoto *et al.*, 1996; Rech *et al.*, 1996; Tsu *et al.*, 1997; Koh *et al.*, 1998). It is generally believed that the use of H_2-dilution promotes the formation of an amorphous network with improved order, such that the density of defects that lead to light-induced degradation are reduced. However, the relationship between H_2-dilution and the film growth processes is complex and not yet completely understood. First, H_2-dilution affects the plasma chemistry and therefore determines the relative fluxes of silicon-containing radicals reaching the film surface (Tanaka, 1989; Takai *et al.*, 2000). Second, atomic H generated in the plasma interacts with the growing film affecting both surface and sub-surface (bulk) processes (Matsuda and Goto, 1990; Shirai *et al.*, 1991; Tsai *et al.*, 1991; Okamoto *et al.*, 1996).

If the H_2-dilution is increased well above the levels required to improve the electronic quality of a-Si:H materials and the performance of a-S:H-based solar cells, then microcrystalline Si:H (μc-Si:H) films are obtained even at the lowest temperatures used for a-Si:H PECVD (Kondo *et al.*, 2000; Vallat-Sauvain *et al.*, 2000; Vetterl *et al.*, 2000). In spite of the controversies over the mechanisms of low temperature (< 300°C) μc-Si:H growth (Matsuda, 1999), it is generally agreed that the presence of large amounts of atomic H reaching the substrate/film surface is fundamental for the nucleation and growth of the microcrystalline phase at the low temperatures. In fact, many groups have been using H_2-dilution as the most effective parameter in controlling the phase of Si:H films from amorphous to microcrystalline (Koh *et al.*, 1999a; Vallat-Sauvain *et al.*, 2000; Vetterl *et al.*, 2000).

In 1994, Lu et al. reported real time spectroscopic ellipsometry (RTSE) studies of amorphous silicon-carbon alloys (a-$Si_{1-x}C_x$:H) prepared as a function of the H_2-dilution ratio $R=[H_2]/\{[SiH_4]+[CH_4]\}$ and found that the highest electronic quality materials were obtained using the maximum R value before the formation of the microcrystalline silicon phase (Lu *et al.*, 1994). Later, this approach was successfully applied to the production of intrinsic a-Si:H layers in both n-i-p (Tsu *et al.*, 1997) and p-i-n (Koh *et al.*, 1998) solar cell configurations, resulting in devices with highest efficiency and stability under light-illumination. These achievements spurred a number of studies focused on the characterization of amorphous materials deposited near the onset of microcrystalline film formation. Studies using techniques such as X-ray diffraction, transmission electron microscopy (TEM), spectroscopic ellipsometry, and Raman spectroscopy revealed that these materials exhibit an improved network ordering (Tsu *et al.*, 1997; Guha *et al.*, 1999; Koh *et al.*, 1999a). In addition, it has been suggested that the improved resistance to light-induced degradation may, in fact, arise from the presence of small amounts volume fraction of nanocrystallites (Kamei *et al.*, 1999).

Recent RTSE studies have shown that the position of the amorphous-to-microcrystalline phase boundary versus the H_2-dilution level is sensitive to the nature of the substrate and that the Si:H films evolve from amorphous to microcrystalline as the film thickness is increased under certain H_2-dilution conditions (Koh *et al.*, 1999a).

These observations have made it clear that the conventional approach in which materials properties obtained by specialized thin film characterization techniques are correlated with the performance of the devices is in fact problematic because, in many cases, these characterization techniques require special substrates, and/or different thicknesses from the ones used in the actual devices. An additional complication is that the properties of these materials can be inhomogeneous in the growth direction, and many techniques that probe the carrier transport are based on measurements in the direction parallel to the film surface. In contrast, the transport in solar cells is in the transverse direction. More sophisticated approaches are needed that (i) probe the a-Si:H film properties in configuration as close as possible to the device configuration and (ii) account for the inhomogeneous, evolving properties of the films and layers in the device. As a result, RTSE is an ideal probe that can provide detailed insights into this complicated materials and device optimization problem.

In this Chapter, phase diagrams are presented that characterize rf plasma enhanced chemical vapor deposition (PECVD) of Si:H films on different substrates. The substrates utilized include: native-oxide covered crystalline Si wafers (c-Si), a-Si:H films, and μc-Si:H films. Because the surface of c-Si is smooth, it allows the maximum sensitivity to changes in the surface roughness of the overdeposited Si:H as detected by RTSE. On the other hand, a-Si:H and μc-Si:H film substrates are used to simulate i-layer deposition in the actual solar cell configuration. The phase diagrams are derived from real time spectroscopic ellipsometry (RTSE) measurements of the evolution of surface roughness on the Si:H films, as described in the previous chapter. In these diagrams, transitions lines are drawn that identify the bulk layer thicknesses (d_b) separating different film growth regimes as a function of the hydrogen-to-silane gas flow ratio $R=[H_2]/[SiH_4]$. The transitions detected by RTSE include (i) an onset of surface roughening from a stable surface regime such that the Si:H film is amorphous on both sides of the onset [denoted "a→a"]; (ii) an onset of surface roughening associated with the nucleation of Si microcrystals, leading to a mixed-phase growth regime [denoted "a→(a+μc)"], and (iii) an onset of surface smoothening associated with the coalescence of the microcrystals,

leading to a single-phase microcrystalline Si:H (μc-Si:H) growth regime [denoted "(a+μc)→μc"]. By comparing the phase diagram results with selected solar cell studies it will be shown how such diagrams can be applied to guide the fabrication of optimum thin film Si:H-based solar cell components.

The organization of this Chapter is as follows. Section 4.2 describes the experimental approach and, in particular, the details of the three different substrate structures. In addition, this section describes how the RTSE data analysis is modified for each structure. Section 4.3 presents the results and discussion for the phase diagrams obtained in studies of Si:H film growth on each of the three substrate structures. Finally, in Sec. 4.4, selected solar cell results are presented and discussed. These final results establish the usefulness of the phase diagrams in providing insights into optimization of the deposition processes for i-layer materials in p-i-n solar cells.

4.2 EXPERIMENTAL DETAILS

4.2.1 Deposition conditions

The Si:H films were deposited in a single-chamber system on three types of substrates at 200°C. The substrates included (i) c-Si with its native oxide intact; (ii) a newly-deposited 500-2000 Å thick a-Si:H film prepared using R=0, an rf power of 0.08 W/cm^2, and a total pressure of 0.07 Torr; and (iii) a newly-deposited 200 Å thick p-type μc-Si:H film, prepared on a-Si:H (R=0) at 200°C using gas flow ratios [SiH_4]:[BF_3]:[H_2] of 1:0.05:200 sccm, an rf power of 0.8 W/cm^2, and a total pressure of 0.9 Torr. The overdeposited Si:H films were prepared with H_2-dilution ratios R from 0 to 40, obtained by fixing the SiH_4 partial pressure at 0.07 Torr with a 5 sccm flow and increasing the H_2 flow from 0 to 200 sccm. This approach led to a variation in the total pressure from 0.07 Torr for R=0 to 0.9 Torr for R=40. For films with R>40, the H_2 flow was fixed at 200 sccm, and the SiH_4 flow was adjusted to obtain the desired R. In this case the total

pressure was in the range of 0.8-0.9 Torr. For the applied rf power flux of 0.08 W/cm^2, typical steady-state deposition rates were 1.3 Å/s for R=0, 0.5 for R=10, 0.2 Å/s for R=40, and 0.1 Å/s for R=80.

4.2.2 RTSE data analysis

The resulting Si films were measured by RTSE using multichannel ellipsometers in the rotating polarizer and rotating compensator configurations. The acquisition time for full spectra (1.5–4.5 eV) was typically 0.8-1.0 s, whereas the repetition time was set in the range of 3.5-60 s, depending on the deposition rate.

The basic analysis procedure for RTSE data has been described in Sec. 2.4. Here, specific details of the analysis for each of the three different substrates are described. For Si:H film growth on smooth, native-oxide-covered c-Si, a two layer model that includes bulk and surface roughness layers is appropriate, as long as the film does not cross the a→(a+μc) phase boundary versus thickness. For films that do cross this boundary, a complete analysis is much more complicated owing to the variations in the microstructure and optical properties with accumulated thickness. An example of such an analysis was presented in detail in Chapter 3. In order to obtain approximate results for the surface roughness evolution for such films (that allows one to identify the bulk layer thicknesses at which the phase transitions occur), the simpler two-layer model is suitable in which the best fit dielectric function of the initially-deposited a-Si:H bulk layer is used. For Si:H film growth on p-type μc-Si:H, a three layer model is necessary owing to the relatively thick (40-50 Å) roughness layer on the substrate film surface. The three layers include a bulk Si:H layer, a surface roughness layer, and an interface roughness layer whose voids are filled during initial Si film growth. Finally, for Si film growth on a-Si:H (R=0) substrates, a four layer model is used. In this case, the additional layer is a ~300 Å thick modified region at the near surface of the substrate film that results when atomic H from the H_2-rich plasma penetrates the underlying a-Si:H network, breaks a significant fraction of Si-Si bonds, and terminates the dangling bonds, leading to a change in the dielectric function of the substrate material.

4.3 DEPOSITION PHASE DIAGRAMS – THE SUBSTRATE EFFECT

4.3.1 c-Si substrate

The RTSE results for the microstructural evolution of Si:H films deposited on c-Si substrates with different H_2-dilution levels were presented in detail in Figs. 3.4 and 3.5 of Chapter 3. These results can be applied in the development of the extended phase diagram shown in Figure 4.1 The data points on this diagram correspond to the bulk layer thicknesses at which the phase transitions occurs, as deduced from the plots of the surface roughness layer thickness d_s versus bulk layer thickness d_b in Figs. 3.4 and 3.5 (wherein the transition positions are indicated by the arrows). Three transition lines connect the data points, including (i) the amorphous roughening transition [a→a] (dotted line), (ii) the amorphous–to–(mixed-phase) transition [a→(a+μc)] (solid line), and (iii) the (mixed-phase)–to–(single-phase-microcrystalline) transition [(a+μc)→μc] (dashed line).

In the low R region (R<10) of Fig. 4.1, it is notable that the bulk layer thickness at which the a→a transition occurs increases significantly with increasing R to the extent that at R=10 no roughening is detected even for d_b up to 4000 Å (as indicated by the upward pointing arrow). Based on the discussions provided in Chapter 3, the increase in the a→a transition thickness with increasing R can be attributed to the beneficial effects of H_2-dilution including (i) generation of high surface mobility SiH_3 radicals in the plasma, with limited contribution from SiH_n ($n \leq 2$) and higher silanes Si_mH_n ($m>1$) (Osborne *et al.*, 1996), (ii) enhanced surface H coverage with minimal surface dangling bond density (Ganguly and Matsuda, 1993), and (iii) effective sub-surface penetration of H that facilitates H elimination (Terakawa and Matsunami, 2000) and structural relaxation (Shirai *et al.*, 1991; Fujiwara *et al.*, 2000b).

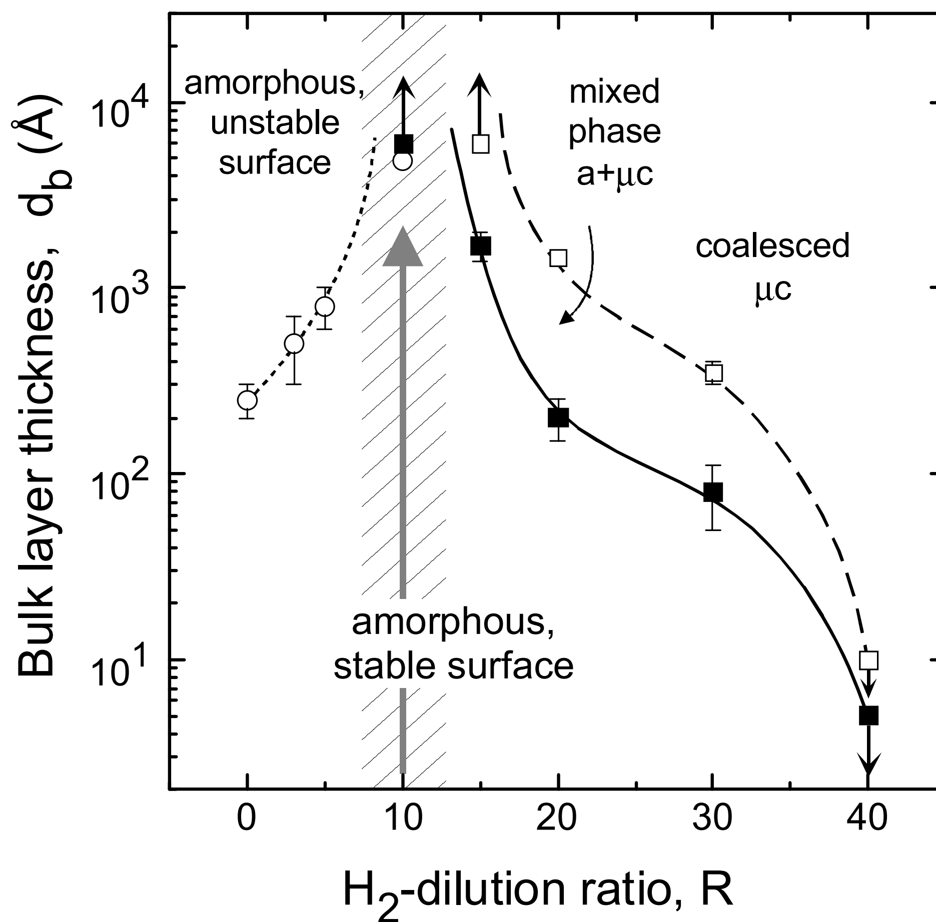

Figure 4.1 Evolutionary phase diagram for Si:H PECVD under standard low rf power conditions (0.08 W/cm^2) on c-Si substrates held at a temperature of 200°C.

In the intermediate H_2-dilution regime (10<R<40), a transition from amorphous to microcrystalline growth is observed as reported in Chapter 3. The a→(a+μc) boundary decreases in thickness continuously with increasing R from d_b~2000 Å for R=15 to d_b~75 Å for R=30. In addition, a parallel decreasing trend is observed for the (a+μc)→μc boundary over this range of R. For R≥40, however, crystallites nucleate immediately from the substrates as indicated by the downward arrow in Fig. 4.1

In Fig. 4.1, the dashed region centered at R=10 indicates the H_2-dilution ratio range yielding film growth characteristics that result in the best electronic quality for a-Si:H layers 4000 Å thick (i.e. layers that are amorphous throughout growth). These growth characteristics include: (i) a large amorphous smoothening effect for d_b<100 Å due to coalescence of nucleation-induced microstructure and (ii) a smooth, stable surface throughout growth, implying that the a→a transition occurs at a thickness greater than the film thickness at the end of the deposition. Most importantly, these characteristics occur at the maximum possible H_2-dilution ratio without crossing the a→(a+μc) boundary for a 4000 Å a-Si:H film. In Sec. 4.4, it will be shown how these characteristics and, in particular, the concept of maximum H_2-dilution can be used to guide the fabrication of optimum performance a-Si:H i-layers for solar cells.

4.3.2 a-Si:H substrate

Figure 4.2 depicts the evolution of d_s versus d_b for Si:H films deposited at selected H_2-dilution levels on a-Si:H (R=0) substrate films. In this case, the evolution of the surface roughness in the initial growth stages is controlled by the surface morphology of the substrates. As a result, the initial roughness at the first monolayer of bulk film growth is determined by the roughness on the underlying substrate film, which varies (10–30 Å) with the previous deposition history. A smoothening of the surface roughness (6-8 Å) is observed for all three depositions shown in Fig. 4.2, which is associated with the beneficial effects of these moderate to high H_2-dilution plasma conditions (R≥20). The key feature in Fig. 4.2, however, is the abrupt increase in the surface roughness layer thicknesses at a well defined d_b which identifies the a→(a+μc) transition. This transition

occurs near d_b = 3000, 300, and 30 Å for R=15, 30, and 80, respectively. In addition, the transition from the mixed-phase (a+μc) regime to a single-phase microcrystalline regime is also observed for some of the films deposited on a-Si:H substrate. As a result, the extended phase diagram for films deposited on a-Si:H (R=0) can be obtained, as depicted in Fig. 4.3. In the diagram the two transitions depicted are (i) the amorphous–to–(mixed-phase) transition [a→(a+μc)] (solid line), and (ii) the (mixed-phase)–to–(single-phase-microcrystalline) transition [(a+μc)→μc] (broken line). The open squares with upward pointing arrows in Fig. 4.3 indicate that the (a+μc)→μc transition occurs at a bulk layer thickness greater than this value. In addition, the a→a roughening transition is not included in Fig. 4.3 owing to the limitations of detecting small changes in d_s in the presence of substrate-induced roughness.

Here it is worth emphasizing the effect of the substrate. Figure 4.4 shows a comparison between the evolution of d_s for films deposited with R=40 on c-Si (open symbols) and R=0 a-Si:H substrates (solid symbols). The film deposited on c-Si nucleates immeditally as single-phase μc-Si:H, whereas the film deposited on the R=0 a-Si:H substrate nucleates as a-Si:H and undergoes the a→(a+μc) transition at d_b~200 Å. This effect will be discussed further in Sec. 4.3.4.

4.3.3 p-μc-Si:H substrate

In order to further explore the thickness and substrate dependence of the development of the μc-Si:H phase, p-type doped μc-Si:H substrate films were employed. Such substrates can be applied to simulate the process of i-layer deposition for the p-i-n solar cell in which the underlying p-type layer is μc-Si:H. In fact, because no significant differences are expected between single-phase n- or p-type μc-Si:H, the same substrates can also simulate i-layer deposition on μc-Si:H n-layers in the n-i-p solar cell configuration. The deposition conditions for the substrate film were optimized for the formation of single-phase, high-density μc-Si:H with a thickness of 200 Å (Ferlauto *et al.*, 1999; Koh *et al.*, 1999b).

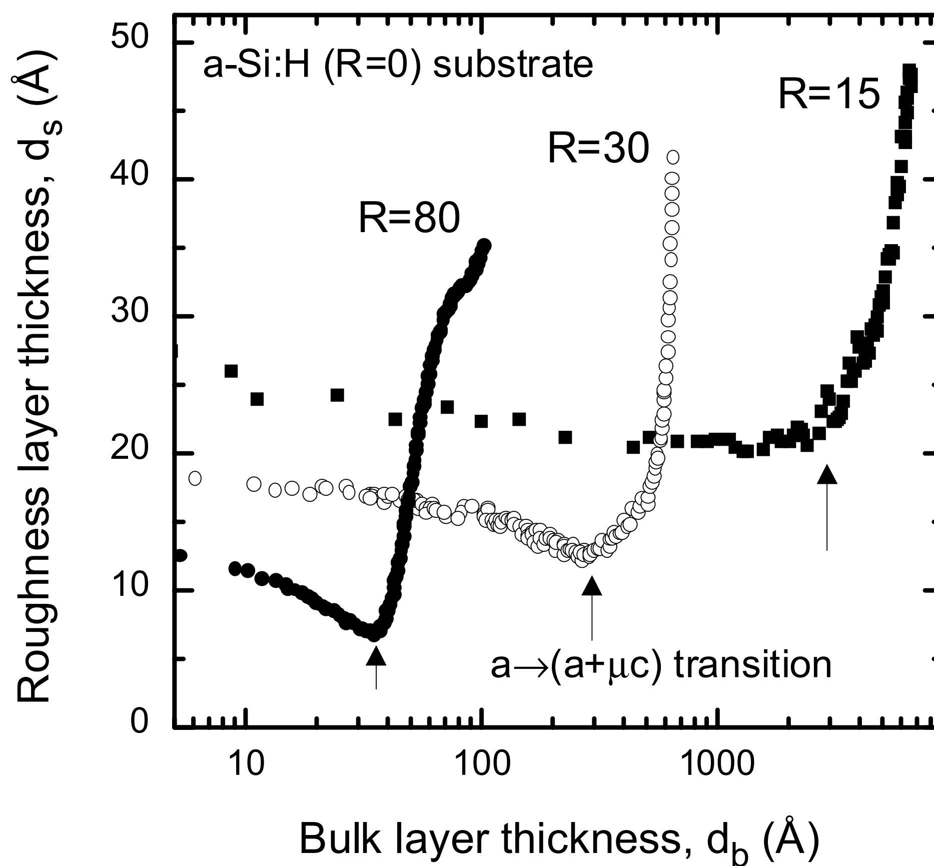

Figure 4.2 Roughness layer thickness (d_s) versus bulk layer thickness (d_b) for the deposition of Si:H films on R=0 a-Si:H substrates at 200°C using hydrogen dilution ratios of R=15, 30 and 80.

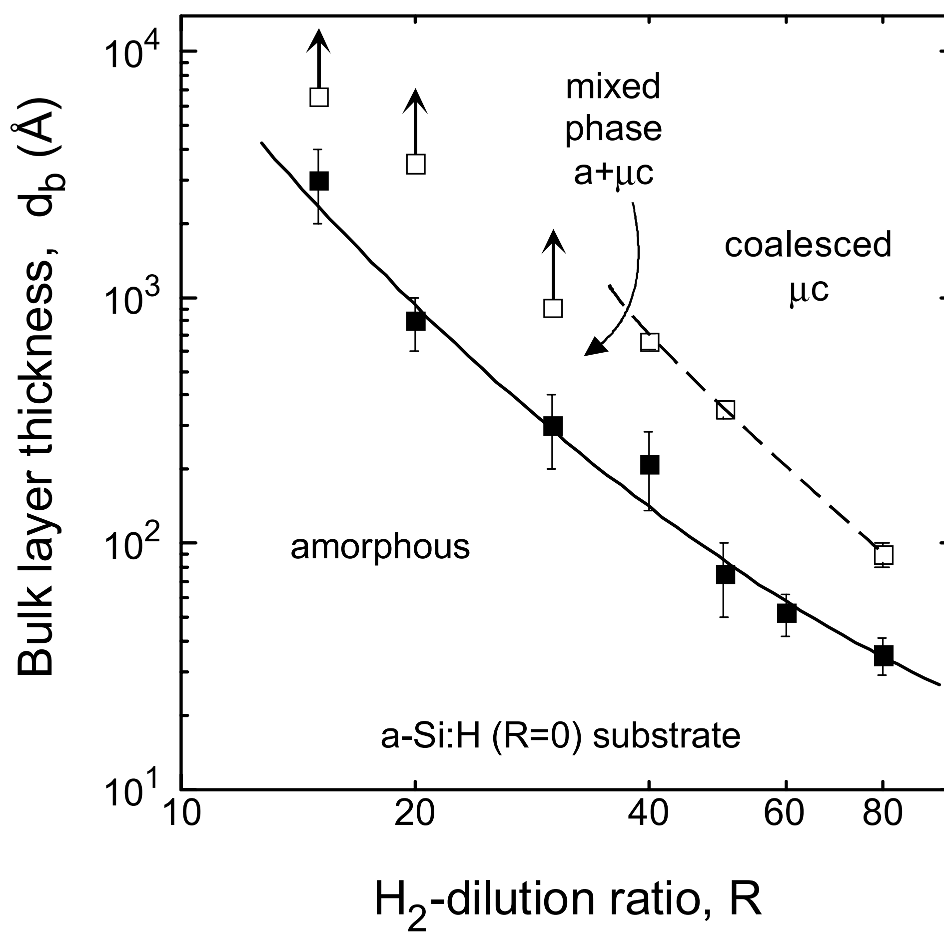

Figure 4.3 Evolutionary phase diagram for Si:H PECVD under standard low rf power conditions (0.08 W/cm^2) on R=0 a-Si:H substrates held at a temperature of 200°C.

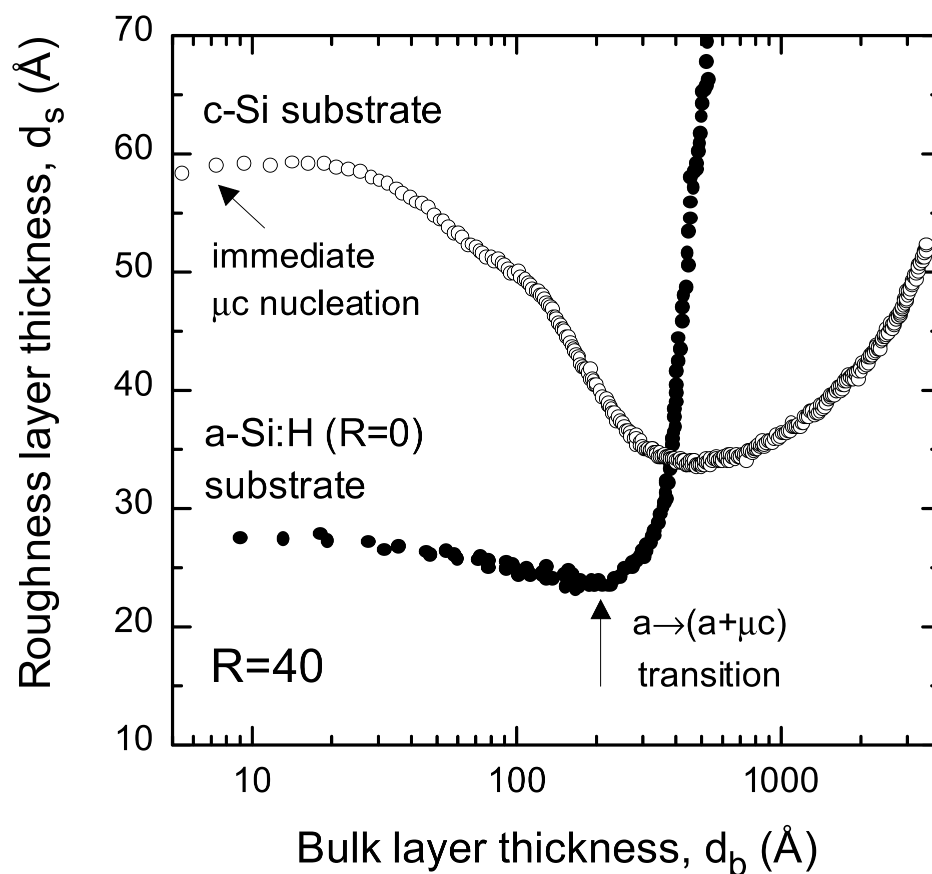

Figure 4.4 Comparison of the roughness layer thickness (d_s) versus bulk layer thickness (d_b) for deposition of Si:H films with R=40 on c-Si (open circles) and a-Si:H (R=0) (solid circles) substrates. The substrate temperature in both cases was 200°C.

Figure 4.5(a) shows the evolution of d_s vs. d_b for two selected R values (R=5 and 10) used in the growth of Si:H films on p-type μc-Si:H. As in the case of the a-Si:H substrate, the initial roughness is determined by the underlying p-layer. For R=5, the smoothening behavior observed throughout the growth of a 2000 Å film is consistent with a-Si:H growth, and this is corroborated by the spectrum in the imaginary part of the dielectric function (ε_2) obtained at d_b~180Å, depicted in Fig. 4.5(b) (solid lines). In contrast, for R=10 the surface exhibits a long-term roughening trend that is consistent with the continued development of the μc-Si:H phase. The smoothening trend observed in the first 300 Å of bulk layer thickness, however, can be attributed a mixed-phase initial growth regime or to the formation of a finer-grained μc-Si:H film that is able to fill the valleys present in the surface morphology of the underlying p-layer. The spectrum in ε_2 shown in Fig. 4.5(b) is consistent with a fine-grained μc-Si:H. Therefore, because the substrate is single-phase μc-Si:H and there is no convincing evidence of a reversion to the mixed-phase (a+μc) regime, only a single a→μc boundary is drawn on the phase diagram. In addition, this boundary appears to be independent of d_b and thus lies in a vertical strip between R=5 and R=10, as depicted in Fig. 4.6. This figure will be the subject of a more detailed discussion in the next section.

4.3.4 Comparison among substrates

As a summary of the results of the three previous sections, Fig. 4.6 presents superimposed simplified phase diagrams for the Si:H films deposited on the three different types of substrates. In Fig. 4.6, the a→(a+μc) transition is plotted in the R-d_b plane for each of the three types of the substrates. For R=0 a-Si:H substrates, the a→(a+μc) boundary (solid line) varies continuously from d_b~3000 Å for R=15 to d_b~30 Å for R=80. For oxide-covered c-Si substrates, the a→(a+μc) boundary (dashed line) varies from d_b~2000 Å for R=15 to d_b~75 Å for R=30; immediate nucleation of μc-Si:H occurs on c-Si for R≥40. Finally, for μc-Si:H p-layer substrates, overlying Si films prepared with R≤5 remain amorphous from d_b~50 Å throughout deposition to d_b~3000 Å,

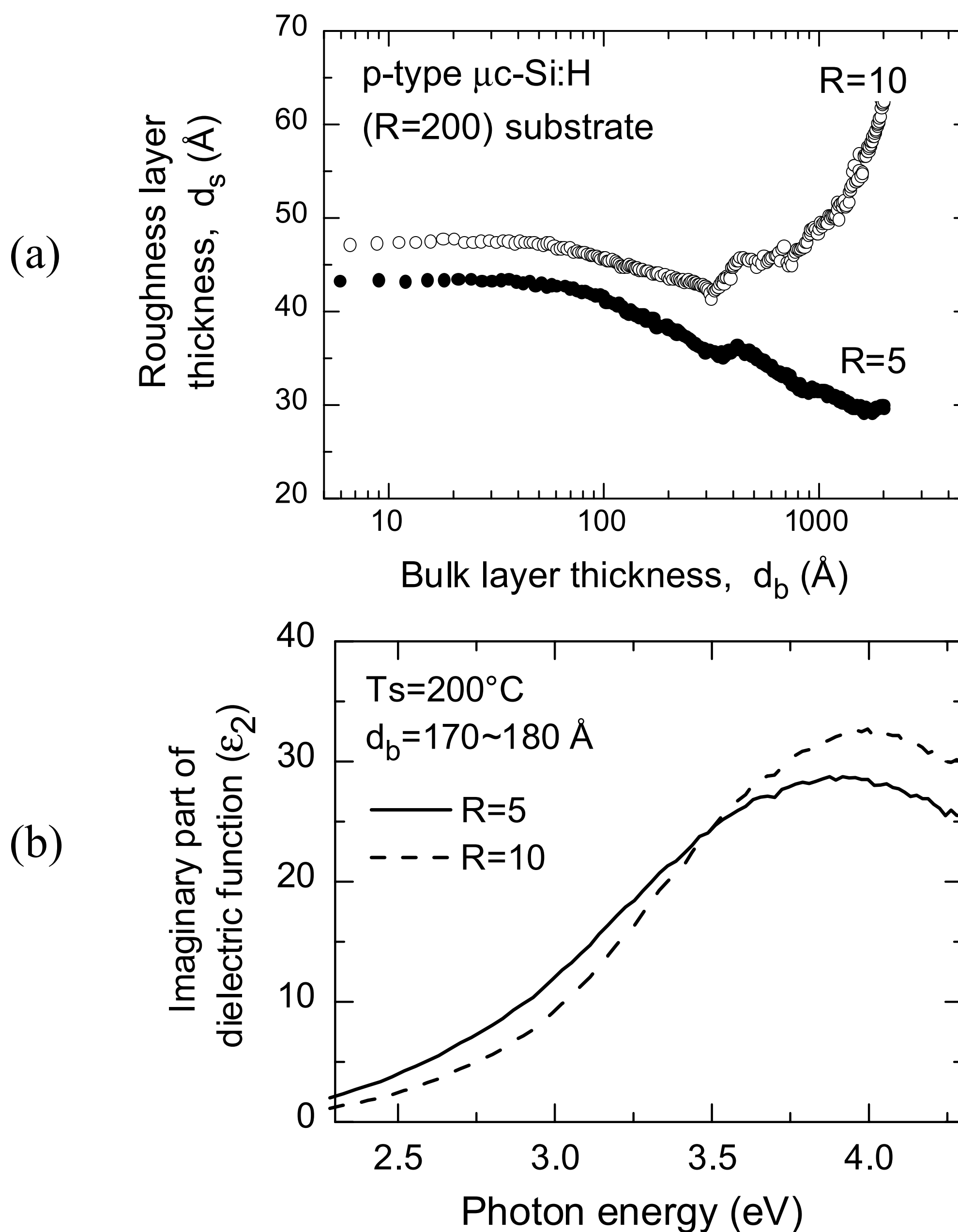

Figure 4.5 In (a) the roughness layer thickness (d_s) is plotted versus bulk layer thickness (d_b) for the deposition of Si:H films on p-type μc-Si:H substrates. Results for depositions with H_2-dilution ratios of R=5 and 10 are shown for comparison. In (b) the imaginary parts of the dielectric functions (at 200°C) for thicknesses of d_b~170-180Å are presented for the same two films.

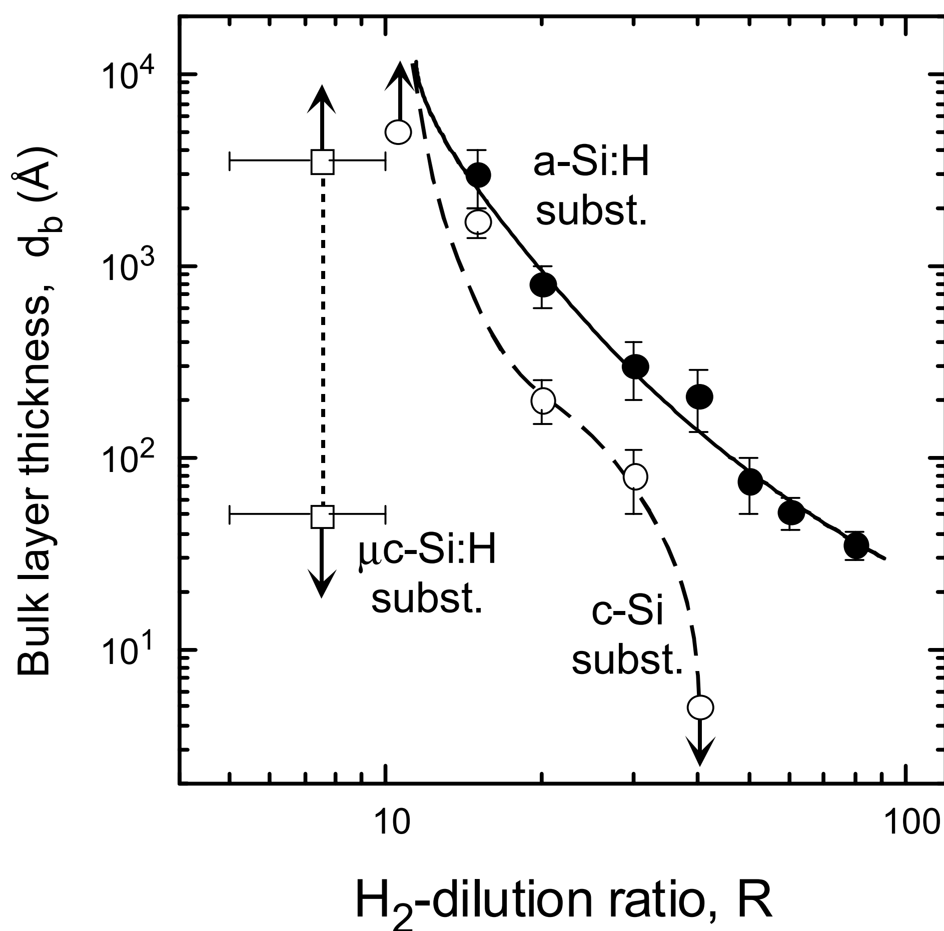

Figure 4.6 Simplified phase diagrams in the plane of versus R and d_b for the PECVD of Si:H films on different substrates; the data values and connecting lines represent the a→(a+μc) transitions for the a-Si:H and c-Si substrates, and the a→μc direct transition for the μc-Si:H substrate.

whereas films prepared with R≥10 appear to be single-phase μc-Si:H over this range. Thus, the a→μc boundary (dotted line) for this substrate lies between R=5 and 10 for 50<d_b<3000 Å. For d_b<50 Å, it is more difficult to distinguish the phase owing to the ~50 Å thick roughness on the p-type μc-Si:H substrates.

The results in Figure 4.6 show that Si microcrystals do not nucleate immediately from R=0 a-Si:H surfaces even for R values up to 80. This behavior is in contrast to oxide-covered c-Si and p-type μc-Si:H surfaces on which immediate nucleation (or localized epitaxy) occurs for R=40 and 10, respectively. Thus, the a-Si:H substrates suppress μc-Si:H formation by imposing their structure on the growing film. On the other hand, an opposite effect is observed for μc-Si:H substrates, i.e., μc-Si:H substrates favor the development of the μc-Si:H phase for the over-deposited films as compared to oxide-covered c-Si and freshly-deposited a-Si:H substrates. In this case, a similar explanation is possible, namely, that film grow occurs epitaxially at least locally, whereby the crystalline network of the substrate continues to propagates across the interface to the over-deposited film.

Next, the discussion will focus on how the phase diagrams of Fig. 4.6 can provide insights into solar cell optimization. First, we consider solar cells in the p-i-n configuration with μc-Si:H p-layers. In this case, the phase boundary for the R=200 p-type μc-Si:H substrate in Fig. 4.6 is relevant for guiding i-layer fabrication. As a result, one must firsts initiate the i-layer deposition with a low R value (R≤5) to prevent propagation of microcrystallinity across the p/i interface, and then increase R to ensure the highest quality i-layer material in the bulk film. Similar considerations apply for solar cell fabrication in the n-i-p configuration having a μc-Si:H n-layer. For cells in the p-i-n configuration having amorphous p-layers, the phase boundary for the R=0 a-Si:H substrate in Fig. 4.6 is relevant for guiding i-layer deposition. In this case, higher cell performance can be obtained by initiating i-layer deposition at the p/i interface with a high R value, and then reducing R for the bulk i-layer in order to avoid microcrystal development. This places material with the highest overall quality and widest optical gap adjacent to the p/i interface, where it is most effective at enhancing solar cell

performance. As will be shown in the next section, for a 4000-Å-thick i-layer prepared in two steps of 200 and 3800 Å, optimum cell performance in both annealed and fully light-soaked states has been obtained using two-step R values of 40 and 10, respectively (Koh *et al.*, 1998). This result is consistent with the concept of maintaining deposition as close as possible to the a→(a+μc) boundary, but on the amorphous side versus thickness.

It is important to discuss the implications of the deposition phase diagrams of Fig. 4.6 for the correlation of materials properties with solar cell performance. First, the thickness dependence of the a→(a+μc) boundary can lead to inconsistencies when correlating materials and device properties. For a 2000 Å-thick i layer of a solar cell, for example, R=15 is expected to yield high performance as this is the maximum value sustainable while remaining below the a→(a+μc) transition. If 5000-Å-thick R=15 films are prepared on either amorphous layers or c-Si substrates for materials analysis, however, such layers will exhibit a structure varying from a-Si:H in the first ~2500 Å to mixed-phase (a+μc) in the next ~2500 Å. Second, the substrate dependence of the phase boundary can lead to similar inconsistencies. For a 1000-Å-thick i-layer used in a multijunction solar cell, for example, R=18 is expected to yield high performance. If 1000-Å-thick R=18 films are prepared on c-Si substrates, however, only the first ~500 Å of the film will be amorphous, whereas the remaining ~500 Å will be in the mixed-phase regime.

Thus, the phase diagrams demonstrate that to obtain valid (materials properties)–(device performance) correlations, the material properties must be obtained from depositions on similar substrates with similar thicknesses as those for devices. This fact also demonstrates the need to consider the effects of texturing of the conducting oxide and back reflector used in p-i-n and n-i-p solar cell production. Because the texture exhibits a large in-plane scale ≥1000 Å and the a-Si:H i-layers appear to conformally cover such surfaces, we expect that the texture has little effect on the deposition phase diagram; however, future studies are needed to verify this expectation.

Finally, we note that for R≤10 in Fig. 4.6, the a→(a+μc) phase boundary for the c-Si and a-Si:H substrates nearly overlap, and occur at bulk layer thicknesses greater than

~5000 Å. As a result, for this range of R, insights into material and solar cell optimization can be obtained in studies using c-Si substrate in spite of the fact that such structures differ from the device configuration. Thus, the a→a roughening transition observed for $0 \leq R \leq 10$ on the extended phase diagram of Fig. 4.1 and the stable surface regime near R=10 are both relevant for directing materials and devices fabrication.

4.4 GUIDANCE FOR SOLAR CELL OPTIMIZATION

Next, a comparison will be drawn between the phase diagrams obtained from RSTE studies presented in Sec. 4.3 and the performance trends for a-Si:H p-i-n solar cells as a function of i-layer H_2-dilution level and thickness.

The solar cells studied were fabricated in a multichamber system according to the following structure: [glass] / [specular SnO_2] / [250 Å a-$Si_{1-x}C_x$:H:B (p)] / [a-Si:H (i)] / [350 Å μc-Si:H:P (n)] / [1000 Å Cr (contact)]. The solar cell characteristics were measured before and after light-soaking with AM1.5 illumination at 25°C for ~100 hours. It should be recalled that the solar cell efficiency is the product of the open circuit voltage V_{oc}, short circuit current J_{sc}, and fill factor FF. Here, the $V_{oc} \times FF$ product is used as a measure of solar cell performance since J_{sc} depends on characteristics that are unrelated to material quality such as the SnO_2 texturing and back contact reflectance. In contrast, V_{oc} and FF are very sensitive to the energy distribution of defects within the band gap of the i-layer material near the p/i interface and in the bulk, respectively.

Figure 4.7 provides the results for (a) V_{oc} and (b) FF measured in the annealed state for p-i-n solar cells prepared by using two approaches. In the first approach, a one-step i-layer is deposited to a thickness of 4000 Å with a fixed H_2-dilution ratio R. In the second approach, the i-layer is deposited in two steps. First, an initial intrinsic layer is deposited at the p/i interface to a thickness of 100–200 Å, using a relatively high H_2-dilution level ($20 \leq R \leq 80$). In the second step, the remaining i-layer is deposited to a total thickness of 4000 Å using R=10. In Fig. 4.7, the V_{oc} and FF values are plotted as a function of the bulk i-layer R for solar cells with one-step i-layers (open symbols) and as

function of the p/i interface layer R for cells with two-step i-layers (solid symbols). Among cells with a one-step i-layer, R=10 yields the best overall performance in annealed and degraded states. By incorporating 100–200 Å i-layers with higher H_2-dilution adjacent to the p-layer, further improvement predominantly in V_{oc} is obtained. In this case, the optimum is observed for an interface layer with R=40.

These results can be interpreted in the light of the phase diagram for Si:H film deposition on a-Si:H (R=0) substrates of Fig. 4.3. First we address the one-step i-layer deposition process. In this case, its helpful to envision a horizontal line across the phase diagram corresponding to the i-layer thickness of 4000 Å. This line crosses the a→(a+μc) transition at R~12, the maximum possible R value for a 4000 Å thick a-Si:H i-layer. In Fig. 4.7(b), the relatively constant annealed state FF for R≤10 suggests that these i-layers have similar bulk defect densities in the annealed states, a result confirmed by electron spin resonance (ESR) measurements. The sharp decrease in the annealed state FF for R=15 is attributed to the nucleation and growth of the microcrystalline inclusions within the top ~1000 Å of the i-layer. Such nucleation characterizes the transition to the mixed-phase growth regime. An inspection of the phase diagram of Fig. 4.3 indicates that at R=15 the a→(a+μc) transition is detected near d_b~3000 Å, and the (a+μc)→μc transition occurs at i-layer thicknesses larger than 6500 Å. In Fig. 4.7(a), the annealed state V_{oc} values increase with increasing i-layer R from R=0 to 10 and remain relatively constant thereafter. The increase in V_{oc} may be due to a combination of effects including a widening of the i-layer band gap, a narrowing of the band tails that produces a widening of the i-layer mobility gap, and a reduction in the defect density near the p/i interface. The near constant value of V_{oc} versus R for i-layers with R≥10 may result from the balancing of two effects: (i) an increase in V_{oc} due to the mechanisms of the previous sentence and (ii) a decrease in V_{oc} due to microcrystallinity in an increasing fraction of the bulk i-layer.

The results for solar cells with two-step i-layers cells can be explained by the phase diagram of Fig. 4.3 by envisioning a horizontal line across the diagram corresponding to the interface i-layer layer thickness of 200Å. In Fig. 4.7(a) (solid

circles), the decrease in V_{oc} for R>40 is attributed to the incorporation of crystallites within the interface i-layer with possible contributions due to crystallites propagating deeper into the bulk. For example at R=40, the a→(a+μc) transition occurs when d_b~200 Å, whereas for R=60 this transition occurs when d_b~75 Å. The increase in V_{oc} values with increasing R for 20≤R<40 in Fig. 4.7(a) can be attributed to an increase in ordering near the p/i interface as well as a widening of the optical gap there. In contrast in Fig. 4.7(b) (solid circles), the relatively constant annealed-state FF values for 20≤R<40 are attributed to the fact that this parameter is controlled by the bulk i-layer which is prepared with R=10 in all cases. The rapid decrease of the FF for R≥60 may result form a propagation of the crystalline phase from the interface i-layer to the bulk i-layer in accordance with the phase boundary in Fig. 4.6 for the p-type μc-Si:H substrate film.

Perhaps the most important result from Fig. 4.7(b) is the light-induced degradation behavior. Figure 4.7(b) also includes the FF values as measured after light-soaking with AM1.5 illumination at 25°C for ~100 hours. Here the beneficial effect of the H_2-dilution in reducing the light-induced degradation is clear. For the one-step i-layers with R≤10 (open squares), the degraded-state FF increases significantly with increasing H_2-dilution ratio. This behavior can be understood in terms of the phase diagram for Si:H films deposited on c-Si of Fig. 4.1. In this diagram, the transition of interest is the a→a transition. The increase in the a→a transition thickness with increasing R correlates with the increase in the degraded state FF, i.e., with the reduction in the light-induced degradation. In fact, a peak in the degraded-state V_{oc}×FF product is observed for the i-layers deposited with R=10, corresponding to the conditions whereby a smooth, stable surface is observed throughout the growth of a 4000 Å film. On the other hand, the slight improvement observed in the degraded-state FF when the p/i interface R is increased from 10 to 40 can be attributed to a substrate-dependent effect on the bulk i-layer. The ordering in the R=10 bulk i-layer appears to be improved when it is fabricated on R=20 and 40 interface layers.

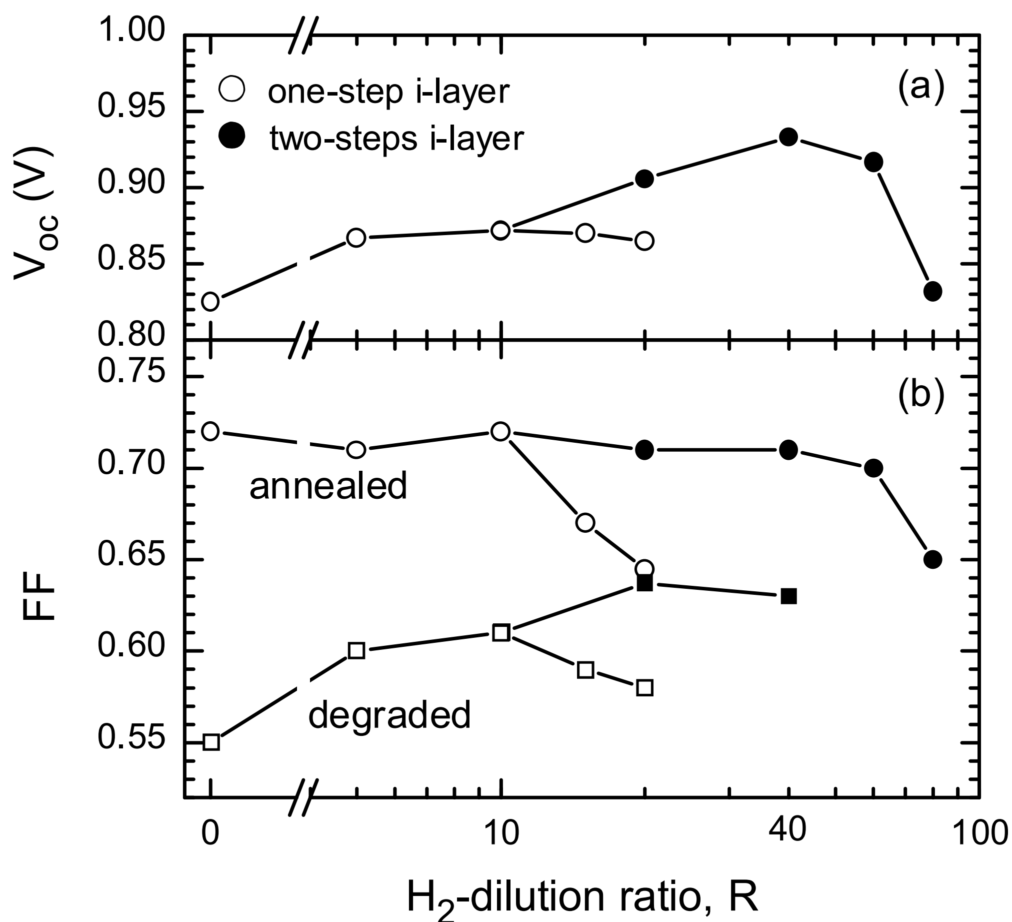

Figure 4.7 (a) Open circuit voltage (V_{oc}) and (b) fill factor (FF) for a-Si:H p-i-n solar cells prepared at 200°C, plotted as a function of the bulk i-layer H_2-dilution ratio R for one-step i-layers (open symbols) and as a function of the p/i interface layer R value for two-step i-layers (closed symbols). The thickness of the p/i interface layers was 200 Å for 20≤R≤40 and 100Å for 60≤R≤80. The total i-layer thickness was fixed at 4000 Å for all cells. In (b) results are shown for the annealed-state FF (circles) and the 100 h AM1.5 degraded-state FF (squares).

In order to further elucidate the thickness dependence of the i-layer microstructure and its effect on the solar cell performance, solar cells having i-layers prepared with different H_2-dilution ratio and thicknesses were studied. Here the focus is on the annealed-state FF, which is the parameter most sensitive to the changes in the bulk i-layer properties. Figure 4.8 presents a plot of annealed-state FF versus i-layer thickness for solar cells having i-layers deposited with R=0 (squares), 10 (circles) and 20 (triangles). For the two cases in which the i-layer is completely amorphous for thicknesses up to 4000 Å, i.e., R=0 and 10, a slight decrease in FF with increasing thickness is observed. This decrease is due to the changes in the electric field distribution and carrier collection with i-layer thickness. For the R=20 i-layer, however, a much larger decrease in the annealed-state FF with increasing thickness is observed that must have a different origin. Again, an inspection of the phase diagram of Fig. 4.3 can help to explain this result. For R=20 Si:H films deposited on a-Si:H substrates, the a→(μ+c) transition is observed at d_b ~800-900 Å, and the mixed-phase (a+μc)-Si:H growth regime extends to at least d_b=3500Å. Therefore, the decrease in FF with the increase in thickness for R=20 in Fig. 4.8 correlates with the increase in the volume fraction of the μc-Si:H phase with increasing thickness in the mixed-phase regime. Such correlation is further supported by the combined RTSE and AFM study of Sec. 3.6.1. Recent studies based on measurements and simulations of the solar cell dark and light J×V characteristics have investigated this effect (Koval *et al.*, 2001). These recent studies have shown that the decrease in FF for i-layers in the mixed phase regime can be attributed to the increase in photocarrier recombination in the μc-Si:H regions in the i-layer. In addition, the higher photocarrier densities generated in the μc-Si:H region of the i-layer lead to an electric field collapse in that region occurring because current continuity must be maintained across the entire i-layer. As a consequence, most of the voltage drop occurs across the amorphous region close to the p-layer. The weaker average field across the i-layer results in an anomalous inflection point in the light J×V characteristics that generates the reduction in FF (Koval *et al.*, 2001).

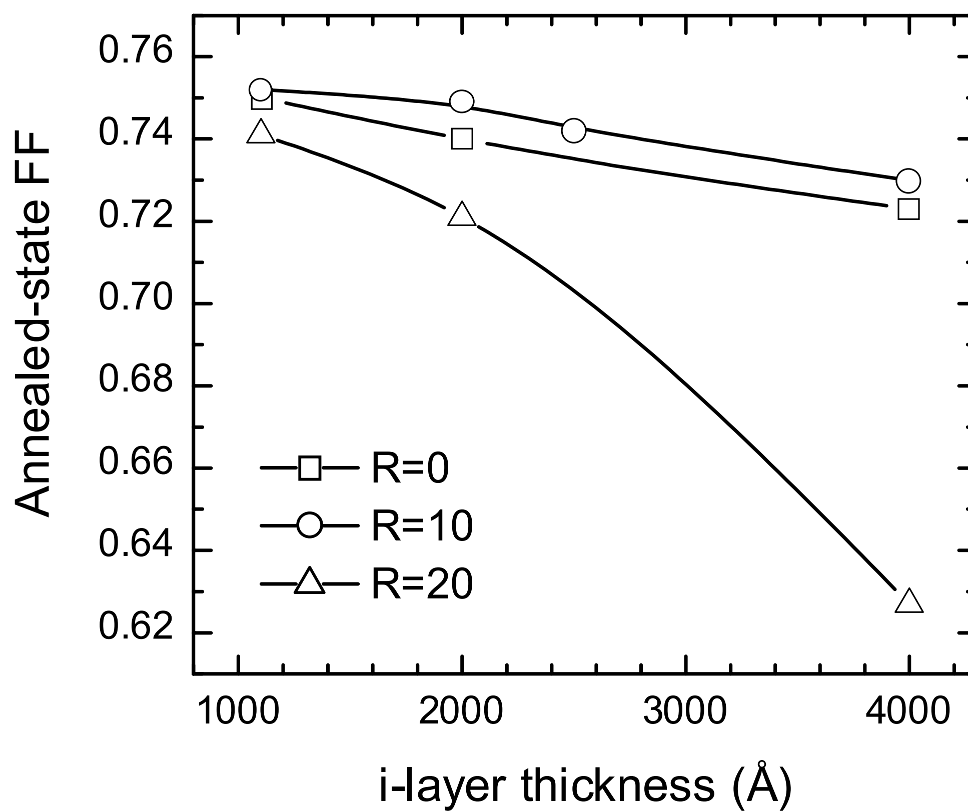

Figure 4.8 (a) Annealed-state fill factor (FF) plotted as a function of the bulk i-layer thickness for p-i-n solar cells having i-layer prepared with H_2-dilution ratios of R=0 (squares), R=10 (circles), and R=20 (triangles).

4.5 SUMMARY

Real time spectroscopic ellipsometry (RTSE) measurements of the surface roughness evolution in Si:H films have been applied to develop phase diagrams that provide guidance for a-Si:H film optimization for incorporation in high performance, high stability solar cells. The deposition phase diagram characterizes the Si:H PECVD process over very wide ranges of bulk layer thickness and H_2-dilution ratio $R=[H_2]/[SiH_4]$ used in the gas phase. The H_2-dilution ratio is chosen over other possible parameters such as substrate temperature or plasma power owing to its unique role in controlling not only the phase of the Si:H film (amorphous vs. microcrystalline) but also its stability against light-induced degradation.

Three key observations concerning the deposition phase diagrams have been made that are relevant for the optimization of a-Si:H-based solar cells. (i) The H_2-dilution ratio at which the amorphous-to-(mixed-phase) [a→(a+μc)] transition occurs is a sensitive function of the substrate material. (ii) For a given substrate material, the H_2-dilution ratio at which the a→(a+μc) transition occurs depends sensitively on the accumulated thickness d_b. (iii) For films that are amorphous, a surface that remains smooth and stable throughout i-layer deposition (i.e. an amorphous roughening transition at a bulk layer thickness greater than 4000 Å) indicates optimum electronic quality.

The first two observations demonstrate that correlations between film characteristics and solar cell performance for a-Si:H prepared in the optimum growth regime near the a→(a+μc) boundary must be established using films deposited to similar thicknesses and on similar substrates as in the devices. In fact, such correlations that employ the deposition phase diagram in conjunction with performance analyses of a-Si:H-based p-i-n solar cells with i-layers prepared in one and two steps at different R values have yielded guiding principles for optimum cell fabrication. These correlations have revealed that the optimum devices are obtained in processes in which the value of R is maintained as high as possible to take advantage of favorable plasma conditions while avoiding the transition to microcrystallinity as a function of film thickness.

CHAPTER 5

APPROACHES FOR HIGH RATE DEPOSITION OF INTRINSIC LAYER a-Si:H

5.1 INTRODUCTION

A thin-film photovoltaic (PV) technology based on hydrogenated amorphous silicon (a-Si:H) has proven to be one of the most important for the fabrication of low-cost, large-area PV modules with high conversion efficiency (Guha *et al.*, 2000). This PV technology contributes to ~20% of the total market worldwide. However, further reductions in fabrication costs are required in order for PV technology in general to become competitive with current fossil-fuels technology for large-scale energy production. In the case of the a-Si:H PV technology, one key issue in lowering the costs is to increase the throughput of the fabrication machines by increasing the deposition rates of the thin film solar cell components, especially for the intrinsic (i) absorber layers, which must be deposited to thicknesses of ~1000–4000 Å.

As has been described in the previous chapters, intrinsic a-Si:H and its alloys used in state-of-the-art commercial solar cells are produced mainly by either dc or rf PECVD and with H_2-dilution of the source gases. As a result, the typical deposition rates for the i-layers are low (~1 Å/s) and different approaches are being pursued in attempts to increase the i-layer deposition rates while maintaining a high level of performance for the resulting solar cells. Several new deposition methods have been developed that can potentially produce high electronic quality materials at increased rates. These methods include PECVD but at higher excitation frequencies in the vhf (50-100 MHz) (Curtins *et al.*, 1987) and microwave (2.45 GHz) (Guha *et al.*, 1995) ranges, hot-wire CVD (Mahan

et al., 1991), expanding thermal plasma CVD (Kessels *et al.*, 2001), etc. In many cases, promising results for solar cells produced on the research scale have been obtained. The transfer to a manufacturing scale, however, usually adds several complexities. For example in vhf-PECVD, the utilization of higher frequencies (50–100 MHz) for the plasma excitation leads to problems of non-uniformity over large deposition areas. As a consequence, a more effective short-term approach is to further explore the current dc and rf PECVD fabrication methods.

Higher deposition rates in rf PECVD can be achieved by increasing the plasma power and/or increasing the gas pressure. In general, however, these conditions have been observed to produce materials with lower electronic quality and solar cells with overall poorer performance. Early studies that investigated such effects on the properties of rf PECVD a-Si:H films have shown that high power and high pressure conditions lead to films with high porosity (low density) (Andújar *et al.*, 1991), larger fractions of SiH_2 bonding units in the film (Lucovsky *et al.*, 1979), rough surfaces, and/or columnar microstructure (Tsai *et al.*, 1986). These characteristics have been attributed to the enhanced generation of species in the plasma that have low surface mobility, including reactive SiH_n ($n<3$) or higher silanes Si_mH_n ($m>1$), and thus are detrimental to the film growth processes (Tanaka, 1989).

More recent studies have focused on the identification of the specific plasma species and reactions that are dominant in processes that yield elevated rates (Takagi *et al.*, 1999; Takai *et al.*, 2000). These studies have proposed that for optimized a-Si:H growth the concentration of SiH_2 radicals relative to the desirable SiH_3 radicals in the plasma must be reduced. A reduction in the concentration of SiH_2 is important because it is very reactive and (i) exhibits low mobility on the growing film surface and (ii) favors the formation of higher silanes in the plasma through successive insertion reactions (e.g. $SiH_2 + SiH_4 = Si_2H_6$). Different approaches that can be applied to reduce the relative concentration of SiH_2 include (i) decreasing the electron temperature, (ii) increasing the H_2-dilution level, and (iii) decreasing the SiH_4 partial pressure while increasing the SiH_4 gas flow rate (in order to avoid SiH_4 gas depletion). A detailed description of these concepts can be found elsewhere (Matsuda, 1998; Takagi *et al.*, 1999; Takai *et al.*, 2000).

In addition, recent studies exploring a combination of high-pressure and high H_2-dilution conditions have suggested that this combination can produce high electronic quality a-Si:H (Oversluizen and Lodders, 1998) and μc-Si:H (Guo *et al.*, 1998; Kondo *et al.*, 2000) films at elevated rates.

Finally, it is important to note that even though the plasma characteristics for high-rate depositions have been well characterized and controlled in various ways, there are only few detailed studies of the film growth processes and resulting film obtained under these conditions. Most of the detailed studies performed to date have focused on the optimum, low rate conditions. Therefore, an understanding of the growth processes under the high-rate conditions is fundamental for guiding the optimization of high rate rf PECVD processes for solar cell production.

In this chapter, the framework developed in Chapters 3 and 4 for the study of Si:H film growth based on the deposition phase diagrams is applied to the fabrication of Si:H films under conditions that yield higher deposition rates. Such conditions entail increases in the rf plasma power and the total gas pressure in order to increase the rates, as well as variations in the H_2-dilution ratio and substrate temperature in attempts to optimize the electronic quality of the a-Si:H at the higher rates. RTSE measurements of the surface roughness evolution of Si:H films in different deposition series are used to develop phase diagrams. In each series, all deposition parameters are fixed except for one. Usually the hydrogen-to-silane ratio, R, is varied in order to control the phase from amorphous to mixed-phase and single-phase microcrystalline Si:H. In addition, for some more limited deposition series, the H_2-dilution ratio R is fixed and another parameter such as the plasma power or the total pressure is varied. In this way, the effect of these other parameters on the film growth processes can be assessed directly.

The organization of this Chapter is as follows. Section 5.2 presents details on the depositions conditions. Sections 5.3–5.5 present results and discussion concerning the effects of different PECVD parameters on the Si:H film growth processes as deduced from the RTSE measurements results. The parameters varied include the rf plasma power (Sec. 5.3), the substrate temperature (Sec. 5.4), and the gas pressure (Sec. 5.5). In Sec. 5.6, a summary with a comparison among the different approaches is presented.

5.2 EXPERIMENTAL DETAILS

The Si:H films were prepared in a PECVD reactor having an rf diode parallel-plate electrode configuration with an electrode spacing of 1.9 cm. The substrates were native oxide-covered c-Si wafers. Four series of Si:H depositions were analyzed, each covering a wide range in the H_2-dilution R. For the first and second deposition series, the plasma power fluxes were fixed at 0.08 W/cm^2 and 0.83 W/cm^2, respectively. In both series, the substrate temperature was 200°C; in addition the SiH_4 flow was fixed at 5 sccm while the H_2 flow ranged from 0 to 200 in order to establish the desired R from 0 to 40. The SiH_4 partial pressure was maintained approximately constant at 0.05 ± 0.02 Torr, resulting in a variation in the total pressure from 0.07 Torr at R=0 to 0.9 Torr at R=40. The conditions for the third series were the same as those of the second high-power series except that the substrate temperature was fixed at 260° C. In the fourth series, the plasma power was fixed at the intermediate value of 0.34 W/cm^2. Furthermore, the total pressure was fixed at 4.0 Torr, resulting in a variation in the SiH_4 partial pressure from 0.3 Torr at R=10 to 0.01 Torr at R=100. Table 5.1 lists the relevant deposition conditions together with the range of deposition rates. Additional results obtained by varying other parameters besides R are presented to highlight the effects of these other PECVD parameters. The deposition conditions used to obtain these results will be described in the text when the results are presented.

Table 5.1: Summary of the conditions for four deposition series. For each series the minimum and maximum hydrogen-to-silane gas flow ratios R=[H_2]:[SiH_4] are shown, along with the corresponding total and silane (partial) pressures and the measured deposition rates. Note that for series IV the total pressure is kept constant at 4.0 Torr, in contrast to the other three series for which the silane partial pressure is kept relatively constant at (0.05 ± 0.02) Torr. The entries in bold are the values differing from those of the standard series I.

Series	T (°C)	P (W/cm^2)	R=[H_2]:[SiH_4] (sccm: sccm)	p_{tot} (Torr)	p_{silane} (Torr)	Dep. rate (Å/s)
I	200	0.08	0 = 0:5 (min) 40 = 200:5 (max)	0.07 0.90	0.07 0.03	1.2 0.2
II	200	**0.83**	0 = 0:5 (min) 40 = 200:5 (max)	0.07 0.90	0.07 0.03	7.9 2.0
III	**260**	**0.83**	0 = 0:5 (min) 20 = 100:5 (max)	0.07 0.50	0.07 0.03	7.7 2.8
IV	200	**0.34**	10 = 100:10 (min) 100 = 200:2 (max)	**4.00**	0.3 0.01	7.9 2.1

5.3 EFFECT OF PLASMA POWER AT LOW TEMPERATURE

Figure 5.1 depicts the evolution of the surface roughness layer thickness (d_s) versus the bulk layer thickness (d_b) for selected Si:H films of the high power series (series II of Table 5.1). For different H_2-dilution ratios R in Fig. 5.1, the different growth regimes characterized in detail in Chapter 3 are clearly present. In Fig. 5.1(a), the films deposited with low R (R=0 and R=10) are amorphous throughout the growth and the amorphous roughening transition (a→a) is observed at 30 Å for R=0 and 500 Å for R=10. In Fig. 5.1(b), the onset of roughening associated with amorphous–to–(mixed-phase) [a→(a+μc)] transition is observed at d_b=800 Å for R=20. For R=40, an [a→(a+μc)] transition is observed for d_b=170 Å and a (mixed-phase)–to–(single-phase) microcrystalline transition [(a+μc)→μc] is observed at d_b=850 Å. In order to assess the effect of the plasma power on the film growth, the evolution of d_s versus d_b for the films of the low power series (P=0.08 W/cm^2) and the high power series (P=0.83 W/cm^2) will be compared in the following paragraphs. The results for the low power series have been presented previously in Secs. 3.4 and 4.2.

Figure 5.2 provides a comparison of the evolution of d_s versus d_b for Si:H films deposited with R=10 using low (solid circles) and high (open squares) rf plasma power levels. First, it is worth noting that the surface smoothening during coalescence decreases with increasing power in the initial 100–200 Å of film growth. The surface smoothening can be quantified by calculating the difference (Δd_s) between the d_s value at d_b=100 Å and the d_s value at nuclei contact (d_b~2.5 Å), [$\Delta d_s = d_s(2.5\text{ Å}) - d_s(100\text{ Å})$]. Figure 5.3 provides the values for d_s(2.5 Å) (squares) and Δd_s (triangles) versus H_2-dilution R for the films of the low power series (solid symbols) and the high power series (open symbols). Figure 5.3 shows that the reduction in the surface smoothening (Δd_s) with increased power observed for R=10 in Fig. 5.2 in fact occurs for all values of R throughout the regime in which a-Si:H nucleates. Returning to Fig. 5.2, it is observed that the stable-surface behavior obtained at P=0.08 W/cm^2 and R=10 – whereby no a→a transition is detected up to d_b=4000 Å – is lost with the increase in plasma power. In

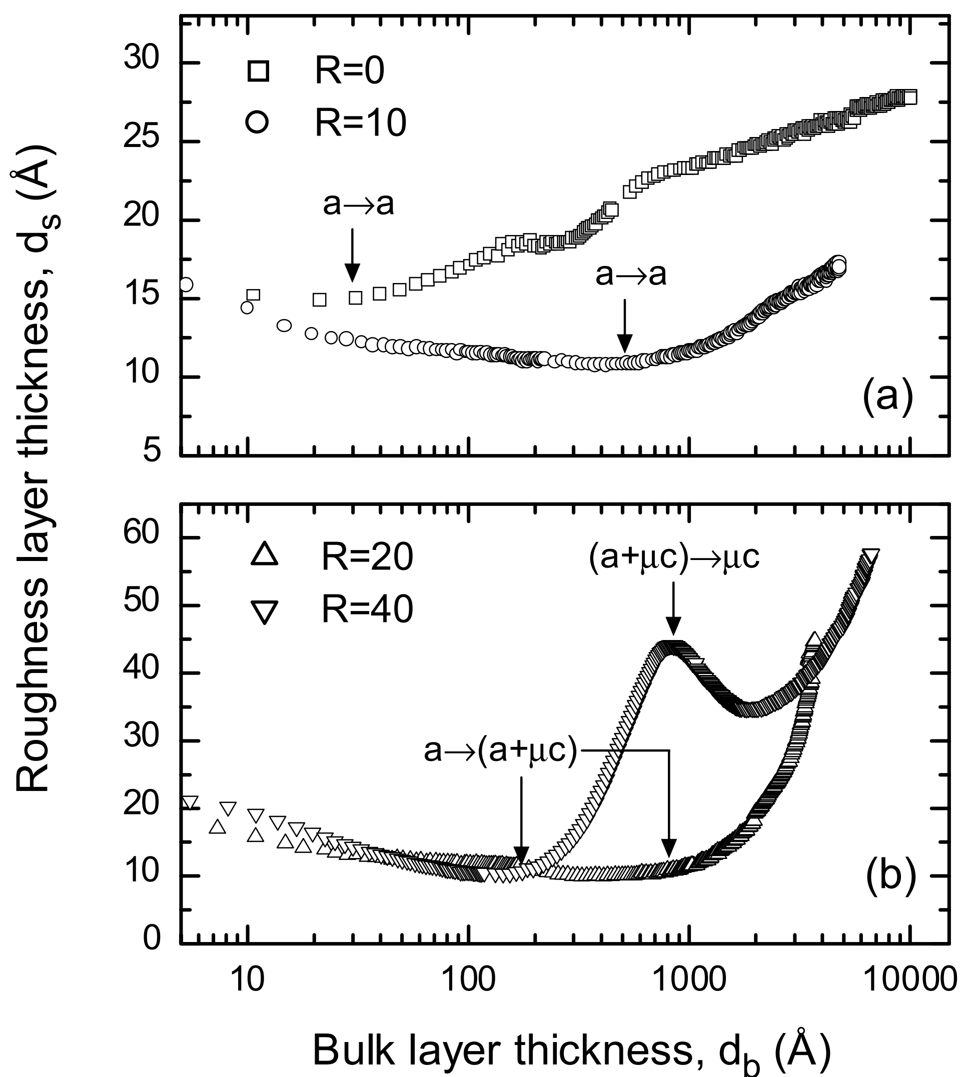

Figure 5.1 Roughness layer thickness d_s vs. bulk layer thickness d_b for the deposition of Si:H films on c-Si with H_2-dilution ratios of (a) R=0 and 10; and (b) R=20 and 40. The fixed deposition conditions include a rf plasma power of P=0.83 W/cm^2 and a substrate temperature of T=200°C.

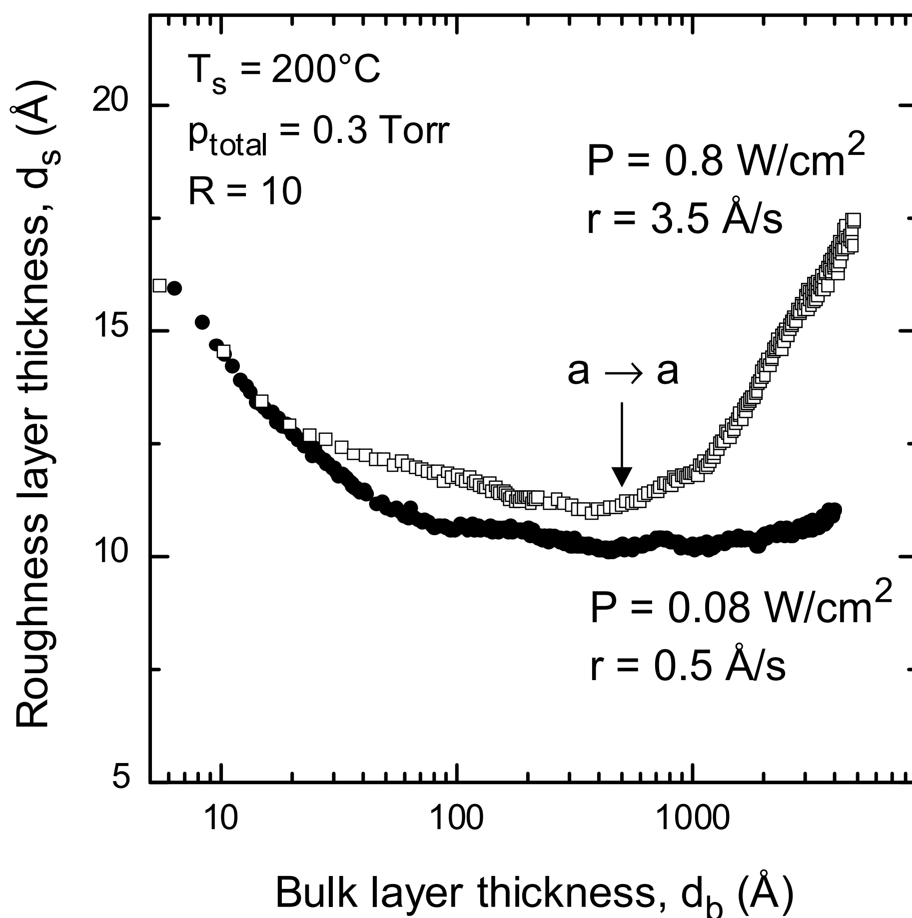

Figure 5.2 Surface roughness layer thickness d_s vs. bulk layer thickness d_b for a-Si:H films deposited on c-Si with fixed T=200°C and R=10, but at different rf power levels of P=0.08 W/cm^2 (solid circles) and 0.83 W/cm^2 (open squares). For the higher P film, an amorphous-to-amorphous surface roughening transition (a→a) occurs near d_b=500 Å (arrow), whereas for the lower P film, any such transition must occur for d_b>4000 Å.

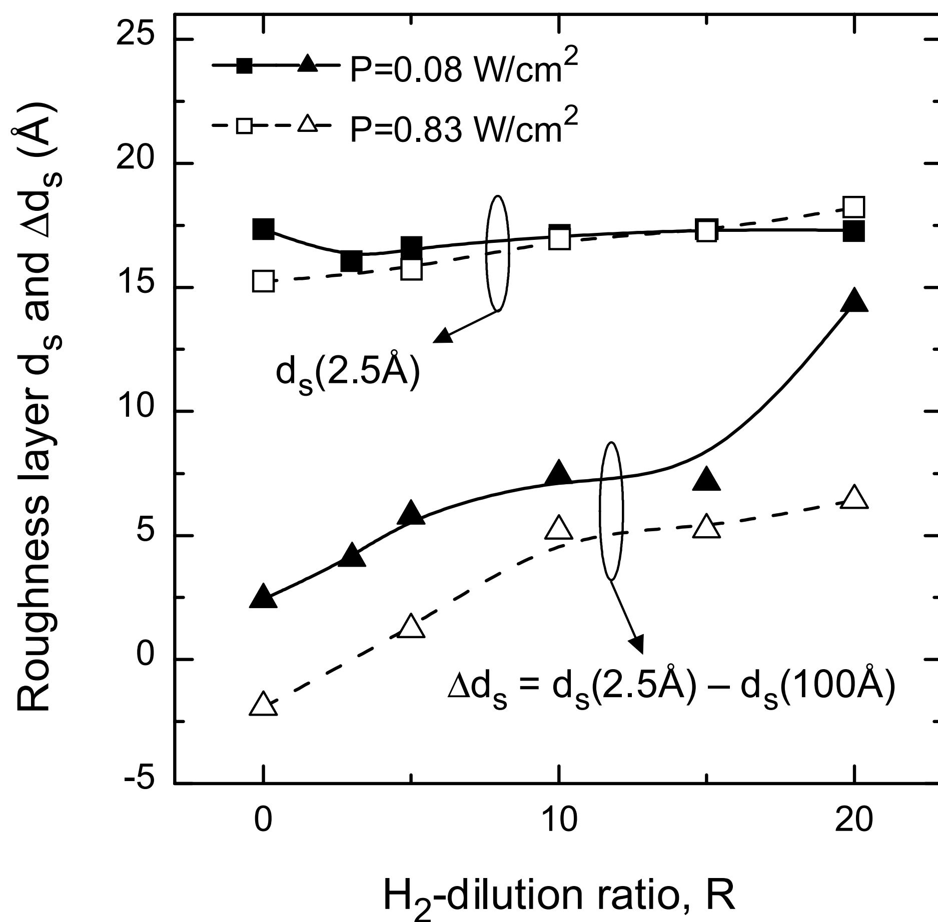

Figure 5.3 Values of the surface roughness layer thickness d_s at nuclei contact d_s(2.5 Å) (squares) and the smoothening magnitude Δd_s due to nuclei coalescence in the first 100 Å bulk layer growth (triangles) both plotted versus the H_2-dilution ratio R for Si:H films of the low power series with P=0.08 W/cm^2 (series I – solid symbols and solid lines) and the high power series with P=0.83 W/cm^2 (series II – open symbols and dashed lines).

fact, for the high power deposition with R=10, the a→a transition decreases significantly to d_b=500Å. Furthermore, results for stepwise increases in the rf plasma power starting from 0.08 W/cm^2 (not shown) reveal that the amorphous roughening transition first appears above the highest d_b of 4000 Å and then shifts monotonically to lower d_b with increasing power.

The reduction in Δd_s and the shift in the a→a roughening transition to lower d_b with increasing rf plasma power can both be attributed to a reduction in the diffusion length of either the adsorbed radicals on the a-Si:H surface or the reactive sites for radical attachment, as discussed in Chapter 3. This may be explained by (i) enhanced ion bombardment of the surface that generates reactive sites for immobilization of diffusing radicals (Perrin, 1995); (ii) enhanced generation of plasma species with shorter surface diffusion length, either SiH_n (n<3) owing to SiH_4 depletion in the plasma, or higher silanes Si_mH_n (m>1) owing to radical-radical reactions in the plasma (Matsuda, 1998); or (iii) reduced concentration of beneficial H radicals relative to reactive SiH_n (n≤3) radicals reaching the surface at the higher rf plasma power.

Figure 5.4 depicts a comparison of the surface roughness evolution for low and high rf plasma power depositions with T=200°C and R=40. Here, it is evident that the immediate μc-Si:H nucleation and subsequent nuclei coalescence that occurs on the c-Si substrate at a power of P=0.08 W/cm^2 is suppressed with the increase in power to 0.83 W/cm^2. At the higher rf power, an amorphous phase evolves first from the substrate, followed by an a→(a+μc) transition at d_b=170 Å, and then an (a+μc)→μc transition at d_b=850 Å. In spite of the differences in the structural evolution, the final single-phase μc-Si:H films prepared at low and high power levels exhibit similar roughness layer thicknesses and roughening rates at the end of the depositions. The changes in the nucleation behavior as the rf power is increased are likely to be explained by a shift in the PECVD process from one in which atomic H etching of initial nuclei is dominant (at low power) (Tsai, 1989) to one in which amorphous film growth is promoted with insufficient etching to generate microcrystallites on the substrate (at high power). Such behavior supports explanation (iii) of the previous paragraph.

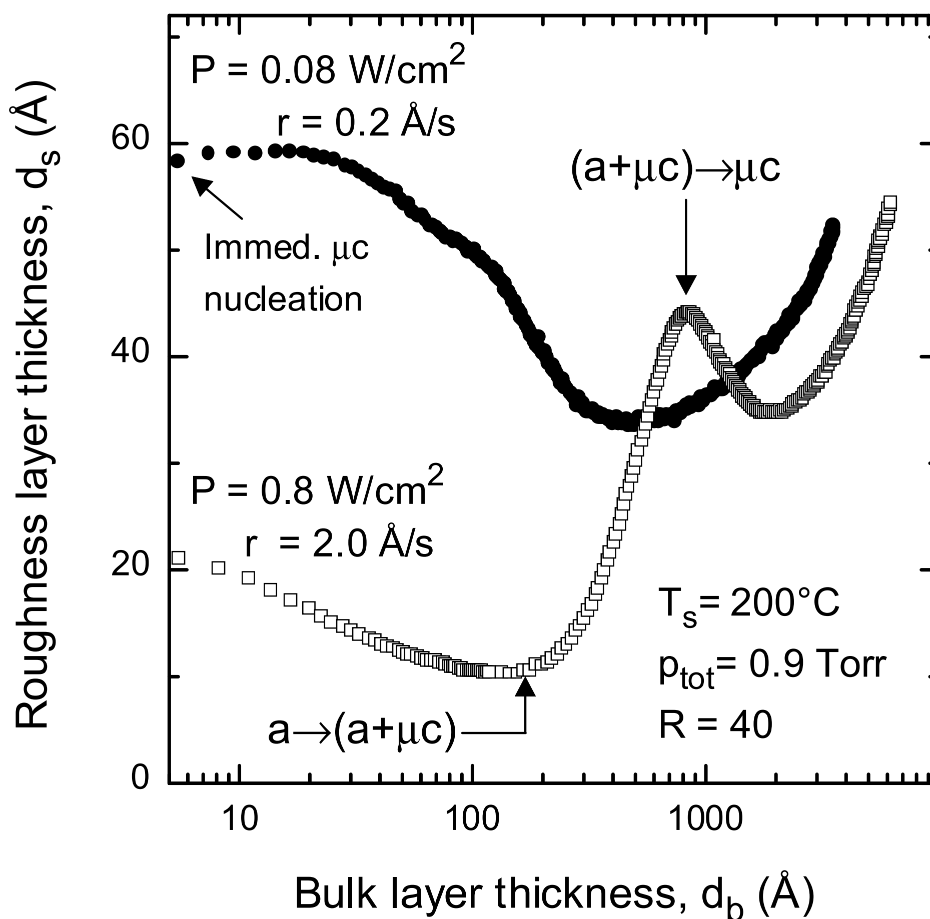

Figure 5.4 Surface roughness layer thickness d_s vs. bulk layer thickness d_b for Si:H films prepared on c-Si with fixed T=200°C and R=40, but different rf power levels of P=0.08 W/cm^2 (solid circles) and 0.83 W/cm^2 (open squares). For the lower P film, μc-Si:H nucleates immediately from the substrate, whereas for the higher P film, an amorphous–to–(mixed-phase) transition [a→(a+μc)] occurs near d_b=170 Å, and a (mixed-phase)–(single-phase) microcrystalline transition [(a+μc)→μc] occurs near 850 Å.

The results from Figs. 5.2 and 5.4, along with those obtained at other R values, provide the two overlapping extended phase diagrams of Fig. 5.5. In this figure, the boundaries corresponding to the a→a transitions (dashed lines) and the a→(a+μc) transitions (solid lines) are plotted for the two series of Si:H depositions with rf plasma power levels of 0.08 W/cm^2 (circles) and 0.83 W/cm^2 (squares). The effects of plasma power on the transition lines are clear. First, with the increase in P, the a→a transition is shifted to lower d_b by an order of magnitude or more, irrespective of R. Second, at moderately high R (R≥20), the a→(a+μc) transition is shifted to higher d_b, apparently owing to the suppression of H etching (e.g., for R=40) or owing to the higher rate growth kinetics at high plasma power (e.g., for R=20). Finally, a reversal of this second effect appears to occur at intermediate R (R=15). For this latter film, the very smooth surface obtained at low power may suppress crystallite nucleation from the amorphous phase, whereas the tendency toward roughening at higher power due to the a→a transition may promote this nucleation process.

Finally, it is important to note that the narrow window for smooth, stable-surface deposition, observed for (R=10, P=0.08 W/cm^2) just prior to the onset of the a→(a+μc) transition (see also Fig 4.1), closes with the increase in rf plasma power. This result suggest that increases in the growth rate obtained simply by increasing the rf plasma power will lead to deterioration of the material quality. This observation is confirmed by the solar cell results to be presented and discussed next.

Figure 5.6 depicts results for the fill factor (FF) of solar cells having i-layers deposited with R=10 and different rf plasma powers levels (P= 0.06 to 0.78 W/cm^2, circles). Also shown is the FF for one cell having an i-layer deposited with R=0 at the lowest power (P=0.06 W/cm^2, squares). The solar cell configuration in these studies is the same as that described in Sec 4.4. The substrate temperature for all cells was 200 °C, and the i-layer thickness is 4000 Å. In Fig. 5.6, the FFs in both the annealed (solid symbols) and degraded states (open symbols) are plotted versus the i-layer deposition rate. This plot emphasizes the differences obtained for the solar cell performance in the annealed and degraded states for i-layers prepared with similar growth rates but under

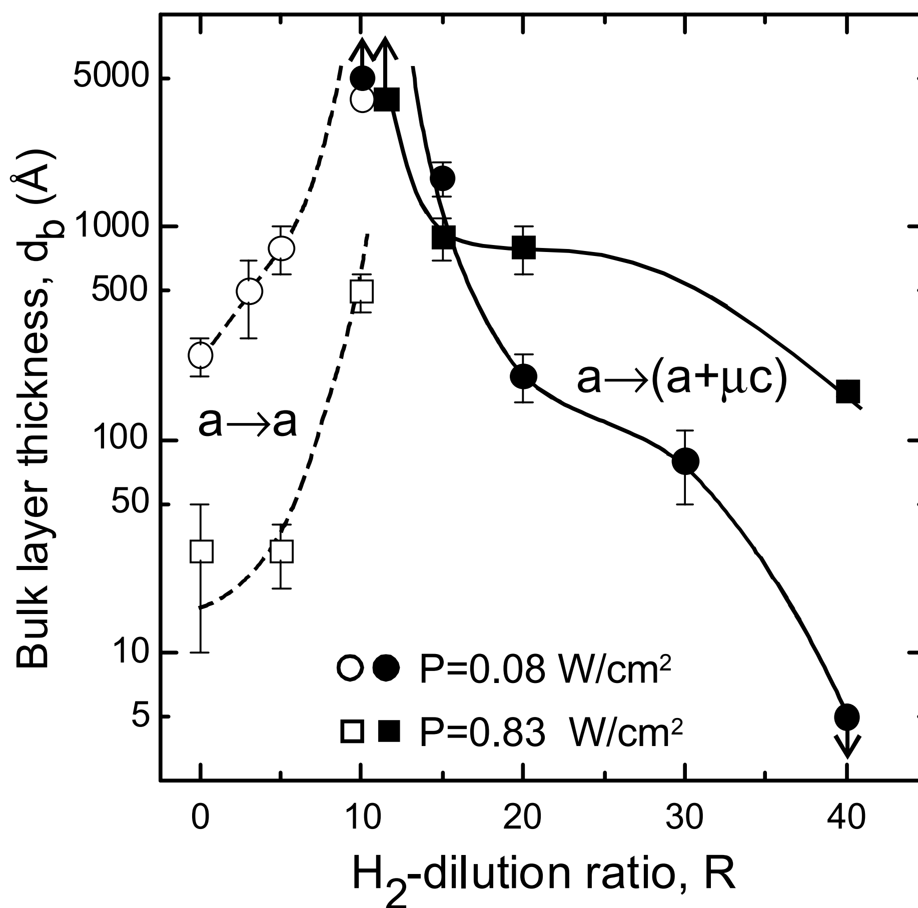

Figure 5.5 Comparison between the phase diagrams for Si:H film deposition on c-Si at 200°C and two different rf powers levels: 0.08 W/cm^2 (series I - circles) and 0.83 W/cm^2 (series II - squares). The open symbols and broken lines indicate amorphous-to-amorphous roughening transitions [a→a], and the solid symbols and solid lines indicate amorphous-to-(mixed-phase-microcrystalline) [a→(a+μc)] transitions. The (up, down) arrows indicate that the transitions occur (above, below) the indicated thicknesses.

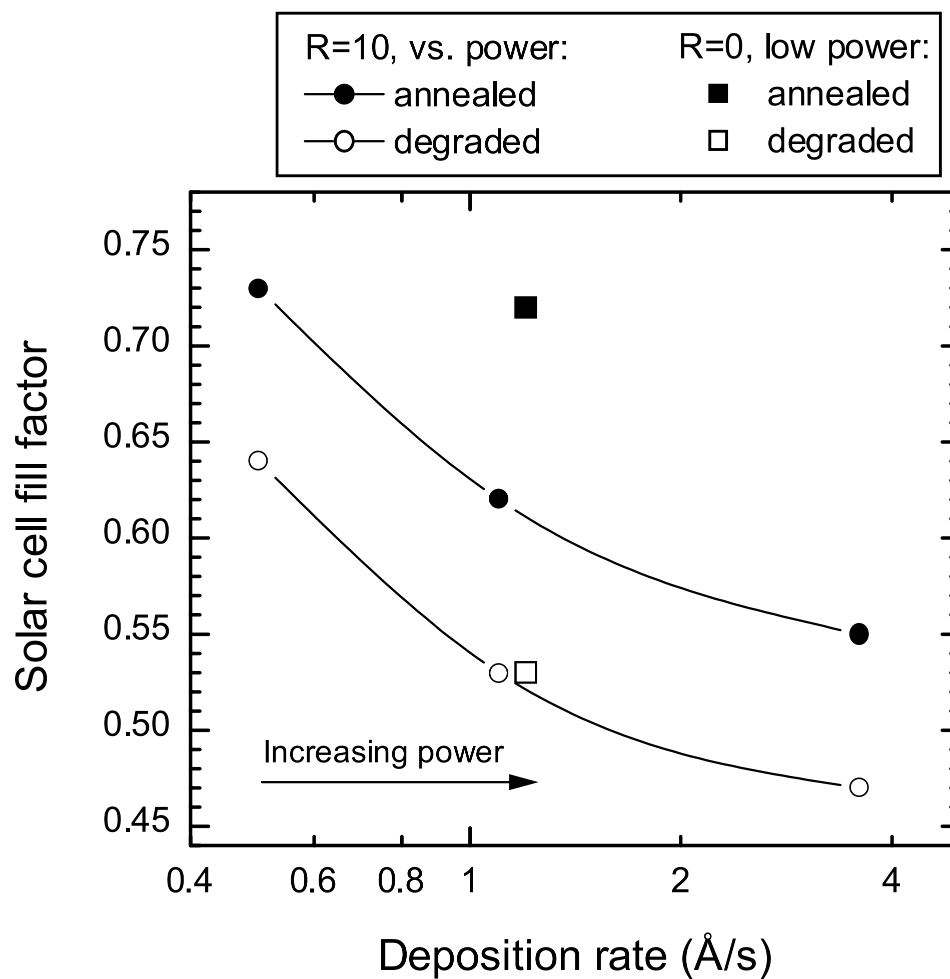

Figure 5.6 Annealed state (solid symbols) and degraded state (open symbols) fill factors versus i-layer deposition rate for solar cells having 4000 Å i-layers deposited at R=10 with different rf plasma power levels (circles), and at R=0 with the lowest plasma power (squares).

different conditions. These results suggest that for the solar cells incorporating i-layers deposited at different plasma power levels with R=10, the defect density in the bulk i-layer increases monotonically with the plasma power density. Interestingly, the light-induced degradation characteristics are not significantly dependent on the plasma power density under R=10 H_2-dilution conditions. The differing roles of the defects that control the annealed FF and its degradation must be explored in future studies.

5.4 EFFECT OF TEMPERATURE AT HIGH PLASMA POWER

Figure 5.7 depicts the evolution of the surface roughness layer thickness (d_s) versus the bulk layer thickness (d_b) for selected Si:H films from series III of Table 5.1. In this series the rf plasma power was fixed at the same value as for series II (P=0.83 W/cm^2) but the substrate temperature was increases to T=260°C. In Fig. 5.7, different growth regimes can be observed for the films deposited with different H_2-dilution levels, analogous to the regimes observed in Fig. 5.1. Here, in order to assess the effect of the substrate temperature on the high plasma power film growth process, comparisons between the evolution of d_s versus d_b for the films of the low temperature series (T=200°C) and the high temperature series (T=260°C) will be presented in the following paragraphs.

Figure 5.8 provides a comparison of the evolution of d_s versus d_b for Si:H films deposited with substrate temperatures of 200°C (open squares) and 260°C (solid circles) using R=0 and a plasma power of 0.83 W/cm^2. Although the a-Si:H nucleation densities are similar for the two temperatures, an enhancement in the surface smoothening during nuclei coalescence is observed at the higher temperature. This behavior is evidenced in Fig. 5.9, where the values of d_s(2.5 Å) and Δd_s are plotted versus H_2-dilution ratio for depositions at the two temperatures. The increase in Δd_s with increased T is observed for all R values throughout the regime in which a-Si:H nucleates, and this increase is more pronounced at low R values. For example at R=0 (as depicted in Fig. 5.8), the film deposited at low T exhibits a negative Δd_s, which means that the smoothening regime is

very short and the surface starts to roughen even at a very low d_b (e.g., d_b<100 Å). This is in contrast the film deposited at T=260°C whereby the smoothening regime extends to larger d_b, resulting in Δd_s~5 Å. As a consequence of the enhanced smoothening during a-Si:H coalescence, the amorphous roughening transition shifts to larger d_b at the higher temperature. These observations are consistent with an expected increase in the surface diffusion length of adsorbed radicals (or the sites for radical attachment) at the higher substrate temperature, as has been proposed in similar previous studies based on the assumption of thermally activated diffusion (Li *et al.*, 1992).

Figure 5.10 provides a comparison of the evolution of d_s versus d_b for Si:H films deposited with substrate temperatures of 200°C (open squares) and 260°C (solid circles) using R=10 and a plasma power of 0.83 W/cm^2. In this case, the increase in the temperature leads to the appearance of an a→(a+µc) transition near d_b=700 Å (indicated by an arrow). The latter transition is established not only from the roughness evolution, but also from the changes in the dielectric function of the film (not shown). This effect can also be attributed to a higher nucleation rate of microcrystallites from the amorphous phase at the higher temperature.

The results from Figs. 5.7, 5.8 and 5.10 are incorporated into the phase diagrams superimposed in Fig. 5.11. It is clear from Fig. 5.11 that the increase in T leads to a modest reversal of the effects of high plasma power to the extent that the amorphous roughening transition now shifts back to higher d_b. On the other hand, the increase in T shifts the a→(a+µc) transition to lower R. The net result is that for the region of R just below the a→(a+µc) transition where optimum electronic material and solar cell performance are expected (in this case R~7.5), the a→a roughening transition still occurs at a relatively small thickness (d_b~350 Å). In other words, the stable-surface condition observed for the low power series in the narrow R region of R just below the a→(a+µc) transition (as depicted in Fig 4.1), which was lost upon increasing the plasma power, is not regained upon increasing the substrate temperature at the elevated power.

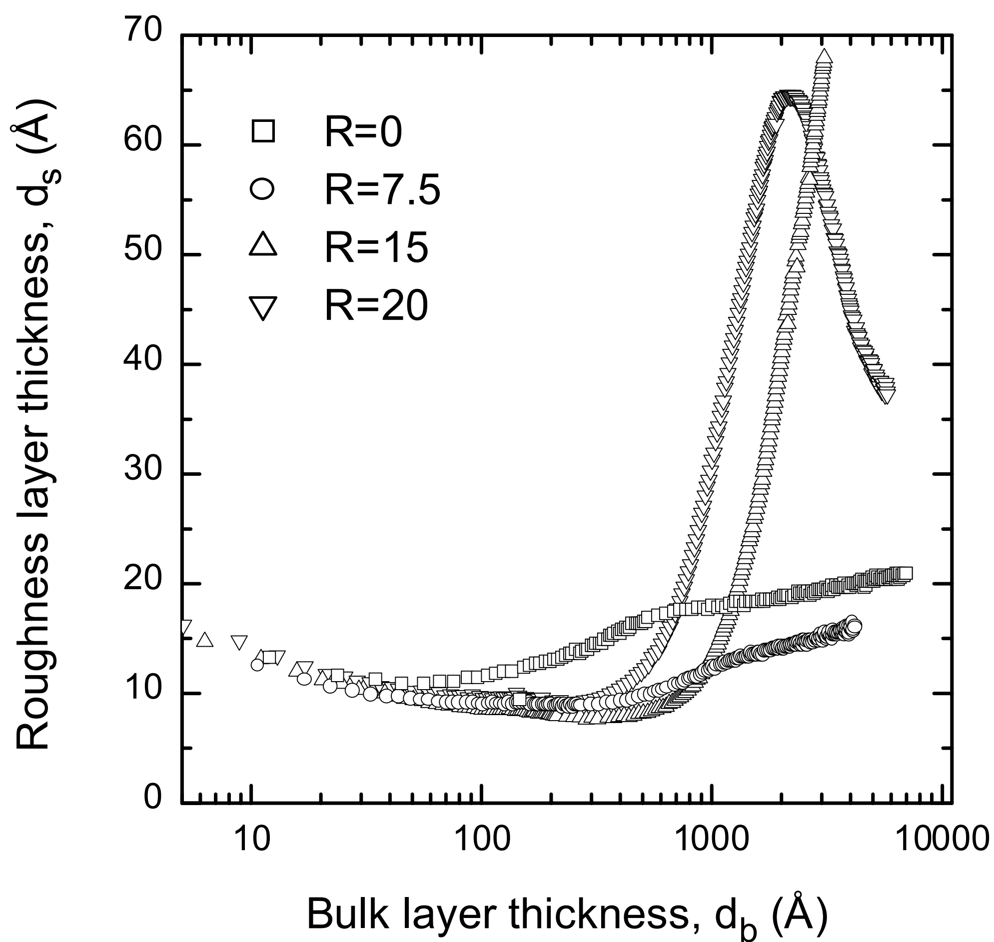

Figure 5.7 Roughness layer thickness (d_s) versus bulk layer thickness (d_b) for deposition of Si:H films on c-Si substrates with H_2-dilution ratios of R=0, R=7.5, R=15, and R=20. The fixed deposition conditions include a rf plasma power of P=0.83 W/cm^2; and a substrate temperature of T=260°C.

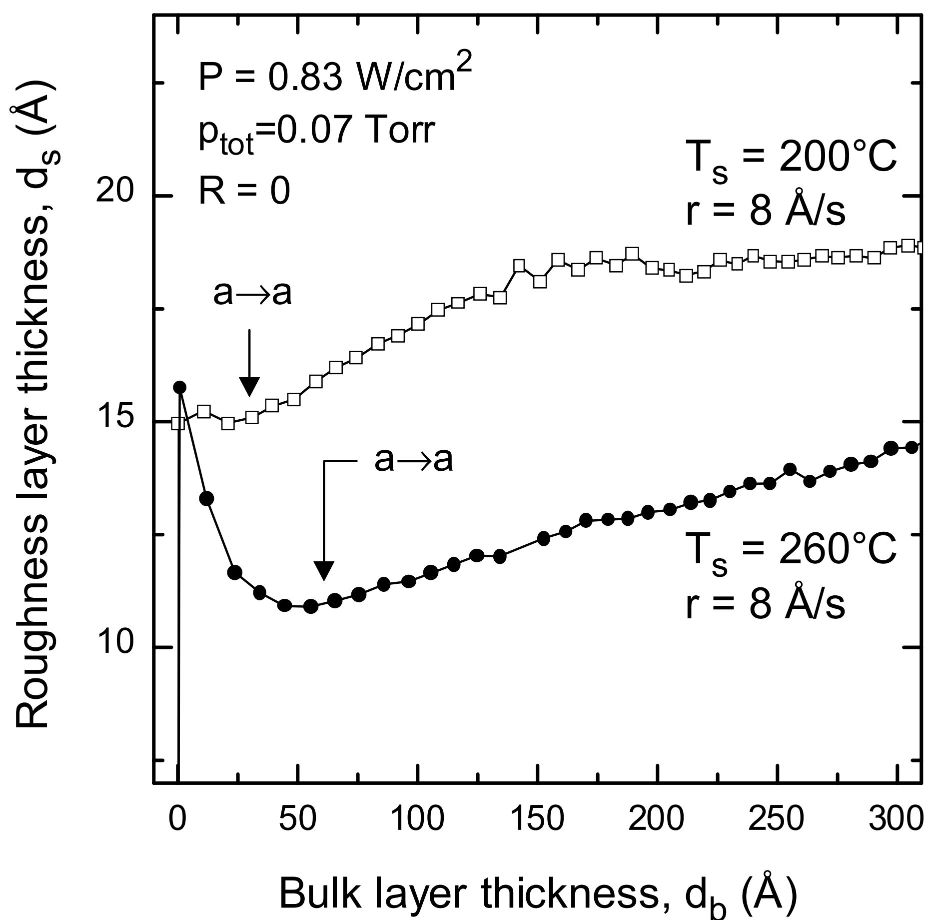

Figure 5.8 Roughness layer thickness d_s vs. bulk layer thickness d_b for a-Si:H films deposited on c-Si with fixed R=0 and P=0.83 W/cm^2, but different substrate temperatures of T=200°C and 260°C. For the T=200°C film, amorphous phase surface roughening begins immediately, whereas for the T=260°C film, the a→a roughening transition occurs near d_b=60 Å.

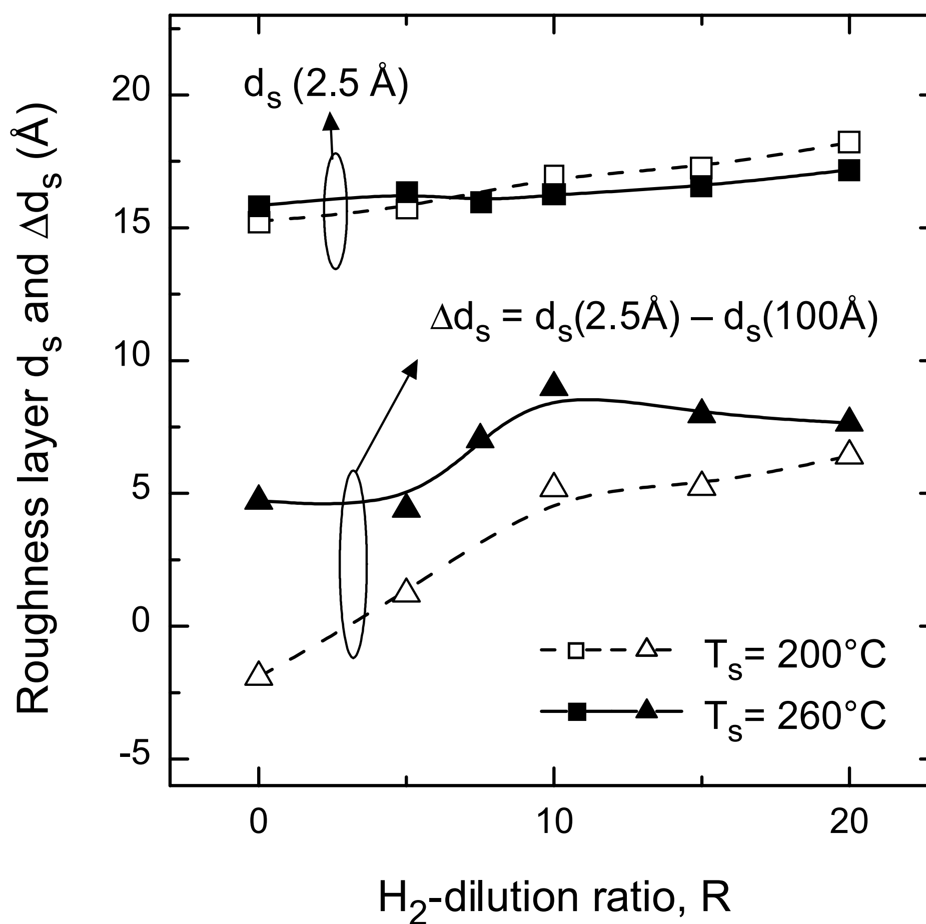

Figure 5.9 Values of the surface roughness layer thickness d_s at nuclei contact d_s(2.5 Å) (squares), and the smoothening magnitude Δd_s due to nuclei coalescence in the first 100 Å of bulk layer growth (triangles) both plotted versus the H_2-dilution ratio R for Si:H films deposited with a plasma power of P=0.83 W/cm^2 and at two different substrate temperatures of T=200°C (series II – open symbols and dashed line) and 260°C (series III – solid symbols and solid line).

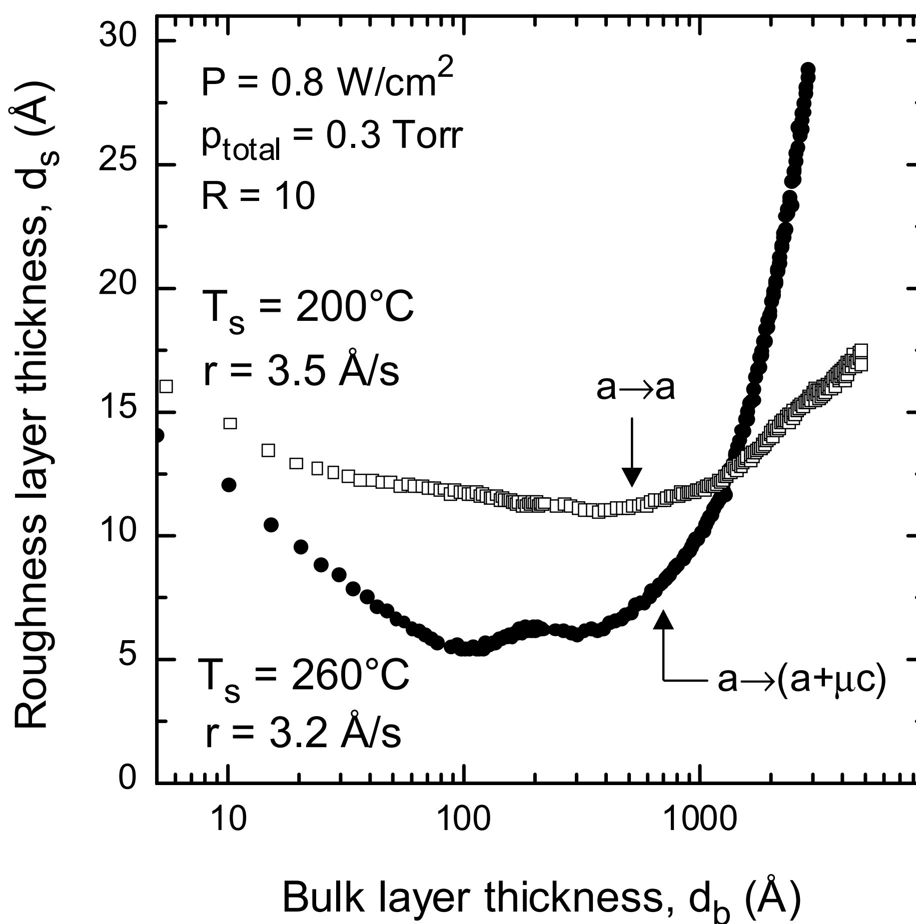

Figure 5.10 Surface roughness layer thickness d_s vs. bulk layer thickness d_b for Si:H films deposited on c-Si with fixed R=10 and P=0.8 W/cm^2, but different substrate temperatures of T=200°C and 260°C. For the T=200°C film, the a→a roughening transition occurs near d_b=500 Å, whereas for the T=260°C film, the a→(a+μc) roughening transition occurs near d_b=700 Å.

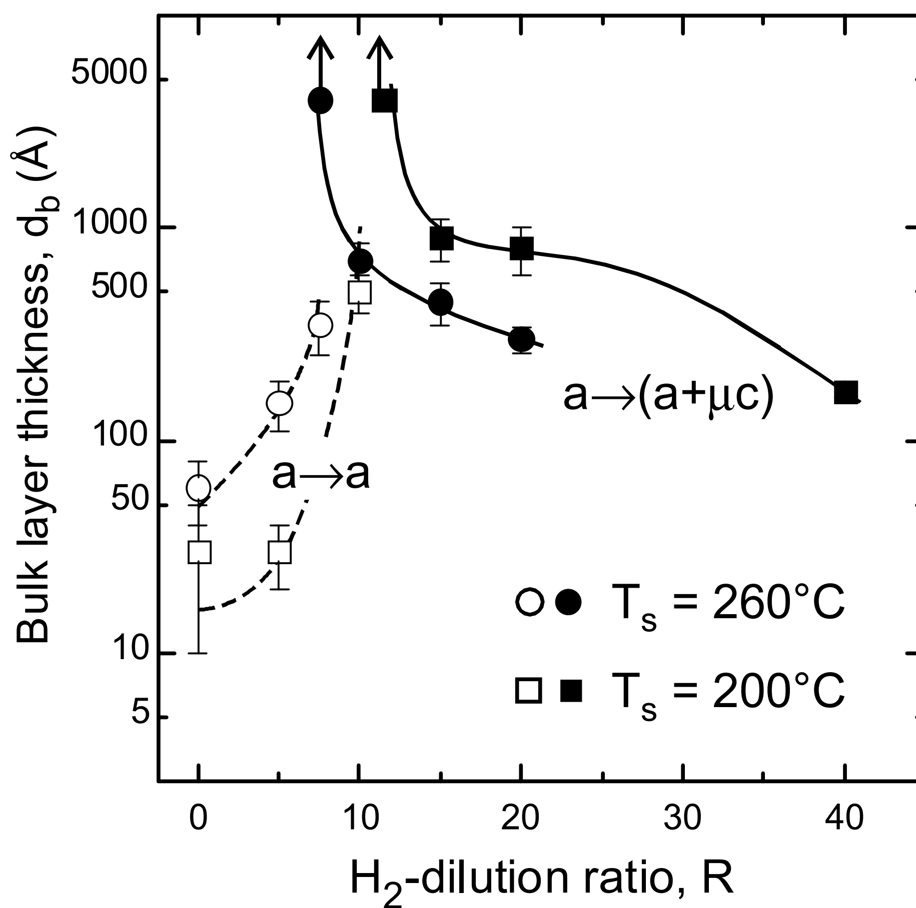

Figure 5.11 Comparison between the phase diagrams for Si:H film deposition on c-Si at P=0.83 W/cm^2 and two different substrate temperatures: T=200°C (series II - squares) and 260°C (series III - circles). The open symbols and broken lines indicate the amorphous-to-amorphous roughening transitions [a→a], and the solid symbols and solid lines indicate the amorphous-to-(mixed-phase-microcrystalline) transitions [a→(a+μc)]. The up arrows indicate that the transition occurs above the indicated thicknesses.

In summary, the increase in substrate temperature leads to weakly beneficial effects on film growth processes due to enhanced diffusion at the film surface as described in the previous paragraphs. However, the modest increase in temperature explored here is insufficient to counterbalance the deleterious effects arising from the modifications of the distribution of plasma species generated by the increased rf power. Therefore, for the high plasma power ($P=0.83$ W/cm^2) and relatively low temperature ($T<300$°C) conditions studied so far, it is likely that the final Si:H film properties will be controlled mainly by the plasma chemistry characteristics as established by the elevated power level, as discussed in the previous section. It is possible that further increases in T above 300°C may exert a more pronounced beneficial effect on film growth at elevated rates as has been reported elsewhere (Takagi *et al.*, 1999). Such a range of T would be of limited value for the deposition of a-Si:H i-layers in p-i-n solar cells, however, where the maximum substrate temperature is limited to 250-300 °C. Future studies are needed to assess the effect of the substrate temperature on the solar cell performance and stability.

5.5 EFFECT OF PRESSURE

An alternative approach often applied to increase the deposition rates in rf PECVD of Si:H films is to increase the process pressure. This enhances the probability of the SiH_4 dissociation reactions that produce the film-forming radicals. Figure 5.12 shows the deposition rate versus the total gas pressure for Si:H films deposited with R=10 (squares) and R=40 (circles) at a fixed plasma power of 0.34 W/cm^2. For R=10, the sharp increase in deposition rate for p_{tot}~1.5 Torr is an indication of a plasma transition from the so called α-regime to the γ'-regime. This transition has been observed in several previous studies (Perrin *et al.*, 1988; Andújar *et al.*, 1991; Perrin, 1995; Oversluizen and Lodders, 1998) and is attributed to the build-up of particles in the plasma with increased pressure. Electron attachment to the particles makes the plasma more resistive, driving the transition from the capacitive (α) to the resistive (γ') regime. As a result, an electric field builds up in the plasma bulk that accelerates the electrons to

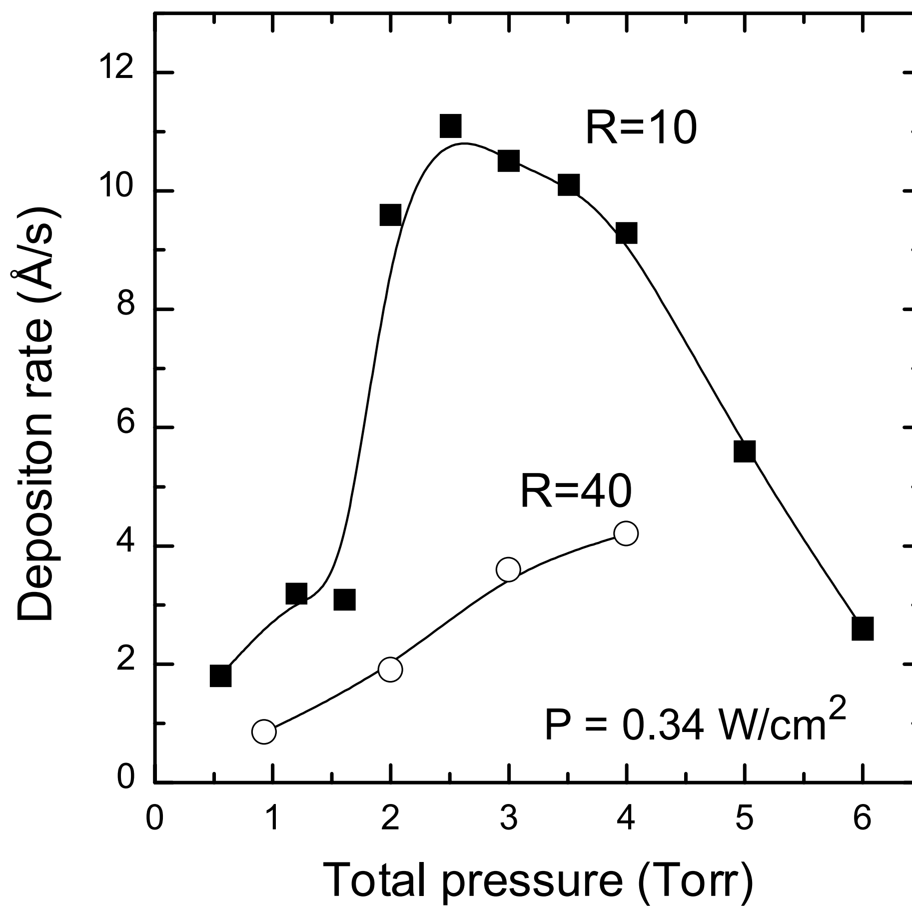

Figure 5.12 Deposition rate versus total gas pressure (p_{tot}) for Si:H films prepared with R=10 (squares) and R=40 (circles). The fixed deposition conditions include a rf plasma power of P=0.34 W/cm^2 and a substrate temperature of T=200°C.

higher kinetic energies. This mechanism described as "Joule heating" (Perrin, 1995) promotes more efficient power transfer in the γ'-regime so that the growth rates are higher in this regime. For high H_2-dilution, however, the α–γ' transition is not as abrupt and is shifted to higher pressures, as can be seen for the case of R=40 in Fig. 5.12. This behavior has been observed elsewhere (Oversluizen and Lodders, 1998), and suggests that the H_2-dilution is effective in arresting the formation of higher-order silanes that build up to form large particles. Moreover, the reduction in deposition rate for R=10 and p_{tot}>2.5 Torr in Fig. 5.12, can be attributed to a reduction in the generation of film-forming SiH_n (n≤3) radicals due to a reduction in the electron temperature at higher pressure (Guo *et al.*, 1998).

Next, in order to investigate the effects of total gas pressure in light of the observations made in the previous paragraph, comparisons will be presented among Si:H depositions performed at selected H_2-dilution levels and at different pressures. Figure 5.13 depicts the evolution of the surface roughness layer thickness (d_s) versus the bulk layer thickness (d_b) for Si:H films deposited using fixed values of R=10 and P=0.34 W/cm^2 with total pressures of p_{tot}=0.3 Torr (squares) and 4.0 Torr (circles). It can be seen that the increase in pressure leads to a strong shift in the a→a transition to lower d_b. This can be attributed to (i) increased concentrations of higher silanes due to the increase in the SiH_4 partial pressure (Matsuda, 1998; Oversluizen and Lodders, 1998), but possibly also to (ii) enhanced kinetic limitations on the surface processes due to the much higher deposition rate for p_{tot}=4.0 Torr (r=9 Å/s) .

Figure 5.14 depicts a similar plot for films deposited using fixed values of R=40 and P=0.34 W/cm^2, but with four different pressures over the range 0.9≤p_{tot}≤4 Torr. In this case, it is clear that the effect of pressure is to suppress the formation of the microcrystalline phase for a fixed H_2-dilution ratio. Similar results have been obtained elsewhere (Roschek *et al.*, 2000). For example in Fig.5.14, a→(a+μc) transitions can be observed at d_b~130 Å for p_{tot}=0.9 Torr (squares) and at d_b=500 Å for p_{tot}=2.0 Torr. In contrast, films deposited with p_{tot}≥3.0 Torr are amorphous throughout the growth. For the latter films, the a→a roughening transition is observed at d_b~2700 Å for p_{tot}=3.0 Torr

and at d_b~2100 Å for p_{tot}=4.0 Torr. These results demonstrate that the total gas pressure can be used as an effective parameter to control the phase of Si:H films. In fact in other research groups, the pressure is being used for control and optimization of the Si:H phase in solar cells incorporating intrinsic μc-Si:H layers (Kondo *et al.*, 2000; Roschek *et al.*, 2000).

The results of Fig. 5.14 can be applied to the development of a phase diagram as a function of bulk layer thickness d_b and total gas pressure p_{tot}. Such a diagram is depicted in Fig. 5.15, and includes three transition lines that describe (i) the a→a transition (short-dashed line), (ii) the a→(a+μc) transition (solid line), and (iii) the (a+μc)→μc transition (dashed line). The fact that the pressure is an effective parameter in controlling the phase of the film, as illustrated in Figs. 5.14 and 5.15, can be generally understood in terms of the pressure dependence of the ratio of the flux of SiH_n ($n \leq 3$) film-forming radicals to that of atomic hydrogen H reaching the substrate. As the total pressure is increased, H is scavenged by SiH_4 in secondary reactions of the type

$$SiH_4 + H \rightarrow SiH_3 + H_2 \, . \qquad (5.1)$$

This effect has been confirmed by Guo and Lin using optical emission spectroscopy measurements (Guo and Lin, 2000). Hence, with the increase in pressure the SiH_n/H ratio is increased which causes a suppression of the microcrystalline phase. Such an explanation is further supported by the results of Figs. 5.16 and 5.17.

Figures 5.16 and 5.17 depict the evolution of d_s versus d_b for Si:H films deposited using different H_2-dilution ratios R, but with fixed values of P=0.34 W/cm^2, T=200°C and p_{tot}=4.0 Torr (series IV of Table 5.1). Figure 5.16 shows results for $10 \leq R \leq 60$, while Fig. 5.17 shows results for $60 \leq R \leq 100$. Here, the effect of H_2-dilution on the growth of a-Si:H films at high pressure for is evidenced. In Fig. 5.16, for R=10 (the same data set as in Fig. 5.13 – circles), the d_s evolution reveals characteristics of poor quality material, as reflected in the small a→a transition thickness (d_b~100 Å). However, when the H_2-dilution is increased to R=60, the a→a transition shifts significantly to much larger thicknesses. In addition, the formation of the μc-Si:H phase is shifted dramatically to larger R as evidenced in Fig. 5.17, where the a→(a+μc) transition is observed only for

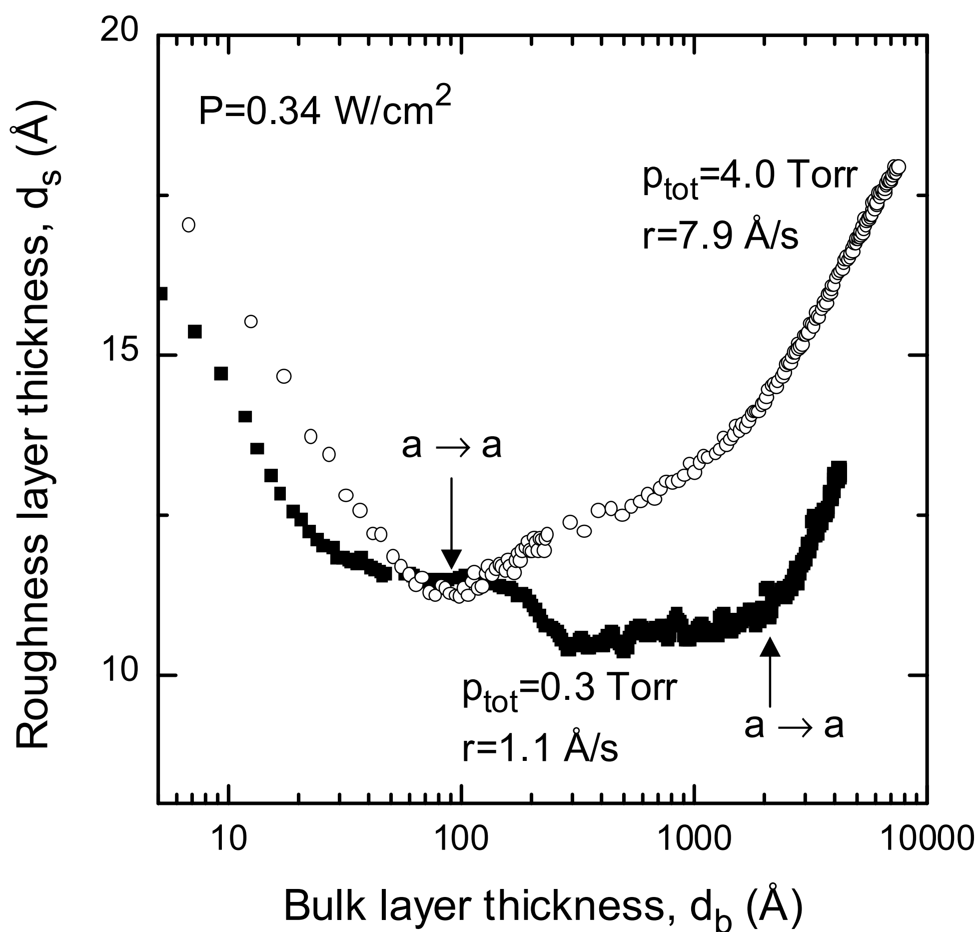

Figure 5.13 Surface roughness layer thickness (d_s) versus bulk layer thickness (d_b) for the deposition of Si:H films on c-Si substrate using R=10 and with total pressured of p_{tot}=0.3 (solid squares) and p_{tot}=4.0 Torr (open circles). The fixed deposition conditions include a rf plasma power of P=0.34 W/cm^2 and a substrate temperature of T=200°C.

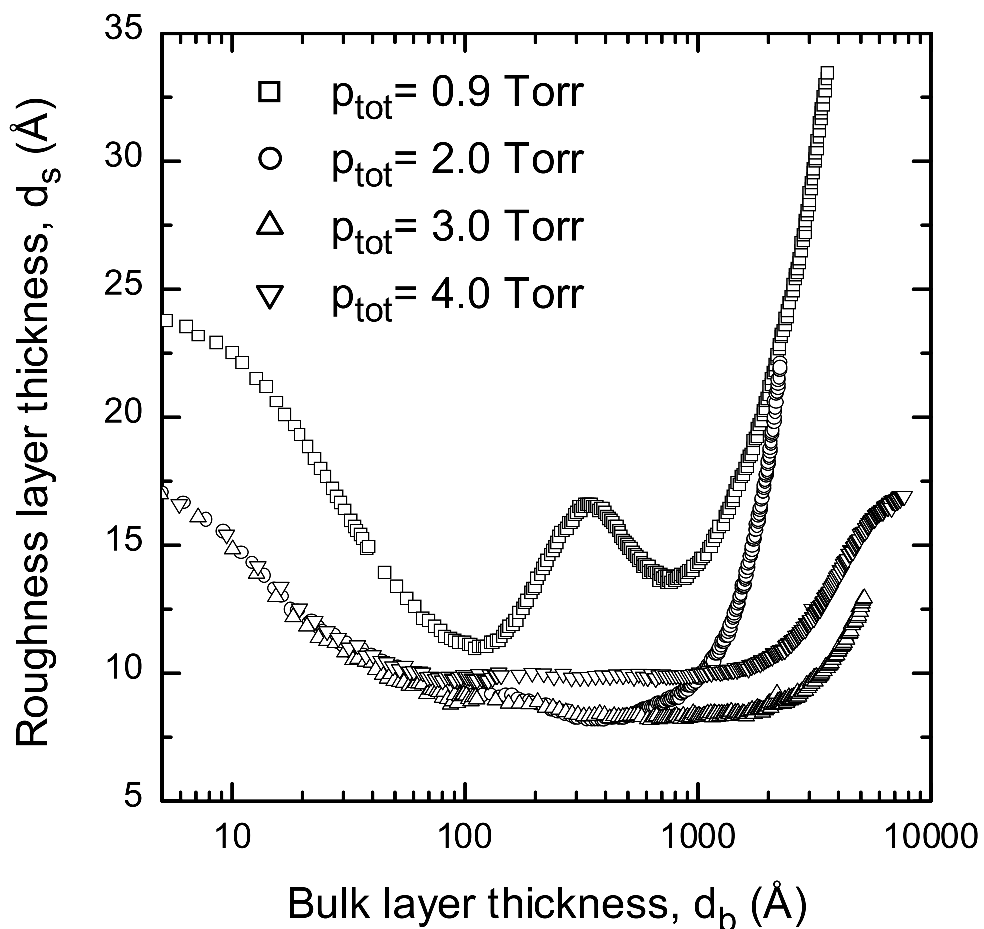

Figure 5.14 Surface roughness layer thickness (d_s) versus bulk layer thickness (d_b) for the deposition of Si:H films on c-Si substrates with R=40 and with total pressures ranging from 0.9 to 4.0 Torr. The fixed deposition conditions include a plasma power of P=0.34 W/cm^2 and a substrate temperature of T=200°C.

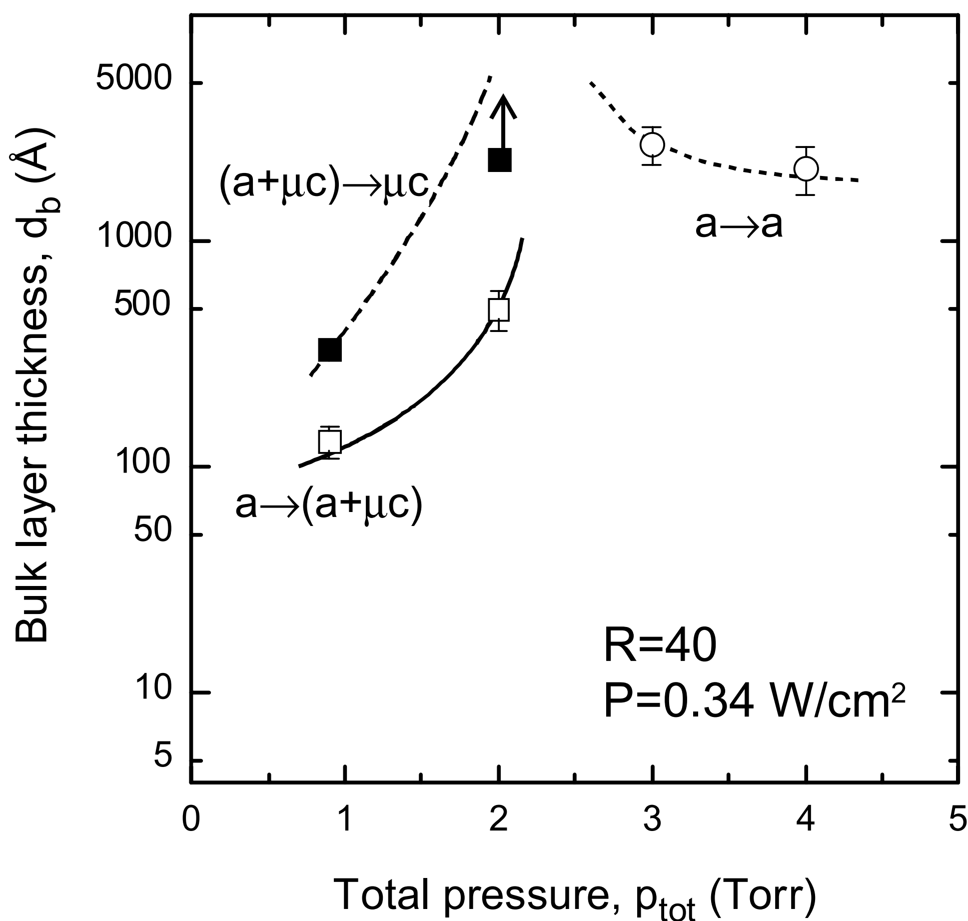

Figure 5.15 Extended phase diagram for Si:H film deposition on c-Si with R=40, P=0.34 W/cm^2, and T=200°C. Note that in this case the phase diagram is plotted in the parameter space of the bulk layer thickness and total gas pressure (d_b-p_{tot}). The open circles and dotted line indicate the amorphous roughening transitions [a→a], the open squares and solid line indicate the amorphous-to-(mixed-phase-microcrystalline) transition [a→(a+μc)], and the solid squares and dashed line indicate the (mixed-phase)–(single-phase) microcrystalline transition [(a+μc)→μc].

$R \geq 80$. Further insights into the growth processes and the improved quality of Si:H films deposited at high pressure can be obtained from a more detailed analysis of the RTSE results for the depositions of Figs. 5.16 and 5.17, as presented in Figs. 5.18 and 5.19.

Figure 5.18 summarizes the characteristics of the initial stages of film growth. Here the values for d_s(2.5 Å) (squares) and Δd_s (circles) are presented versus the H_2-dilution R for the Si:H films of the high-pressure series deduced from the plots of Figs. 5.16 and 5.17. The value d_s(2.5 Å) is constant for $R<60$, and then continuously increases with increasing R for $R \geq 60$. This increase reflects a decrease in the nucleation density of the a-Si:H clusters on the c-Si substrate, probably due to the etching effect of atomic H at high R. The magnitude of surface smoothening, characterized by the value of Δd_s, increases with increasing R, reflecting the beneficial effects of the H_2-dilution on the surface diffusion of the adsorbed radicals.

Figure 5.19 presents results deduced from analyses of the 200°C dielectric functions obtained at 200 Å for the Si:H film series deposited at high pressure. In Fig. 5.19(a), the relative void volume fraction f_v[void] is plotted versus the H_2-dilution ratio. The quantity f_v[void] is obtained by fitting the (ε_1, ε_2) spectra for each of the different films assuming a mixture of a dense reference material and voids in the Bruggeman effective medium approximation. In this case, the (ε_1, ε_2) spectra of the reference material is obtained from RTSE measurements of the a-Si:H deposition under optimized conditions (R=10, P=0.08 W/cm^2, T=200°C, p_{tot}=0.3 Torr). It is clear that for all H_2-dilution ratios $R \geq 20$, the f_v[void] in Fig. 5.19(a) is nearly constant with $0.03 \leq f_v[\text{void}] \leq 0.05$, indicating that the films are relatively compact. For R=10, the high value of $f_v[\text{void}] \sim 0.1$ indicates that these conditions lead to much lower density films. Figure 5.19(b) also presents the values for the optical band gap as a function of the H_2-dilution ratio. The values indicated by the squares are obtained by the extrapolation method as described in detail in Chapter 6, whereas those indicated by the circles are obtained from fits to the (ε_1, ε_2) spectra using parameterized equations that are also described in detail in Chapter 6. The behavior of the gap versus R can be separated into three regimes. First, as R is increased from 10 to 20, the gap decreases, probably due to a reduction in the

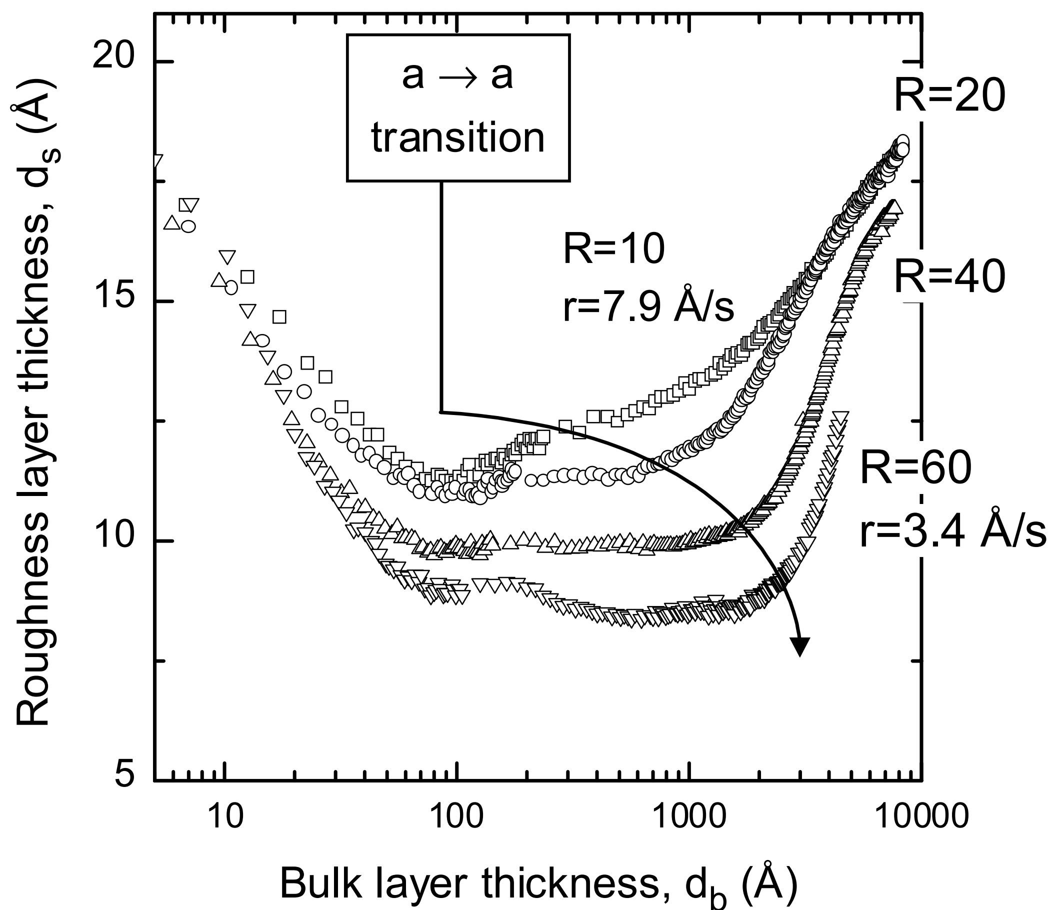

Figure 5.16 Surface roughness layer thickness (d_s) versus bulk layer thickness (d_b) for deposition of a-Si:H films on c-Si substrates with H_2-dilution ratios of R=10, 20, 40, and 60. The fixed deposition conditions include a rf plasma power of P=0.34 W/cm^2, a total pressure of p_{tot}=4.0 Torr; and a substrate temperature of T=200°C.

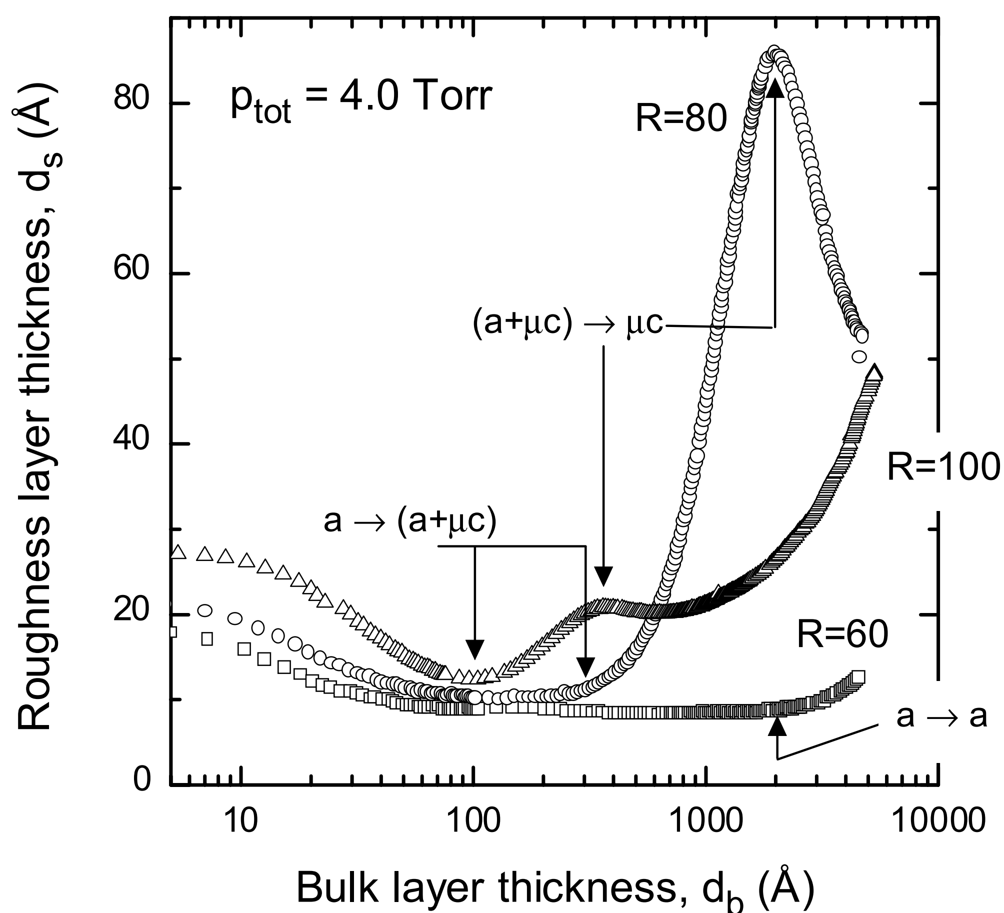

Figure 5.17 Surface roughness layer thickness (d_s) versus bulk layer thickness (d_b) for deposition of Si:H films on c-Si substrates with H_2-dilution ratios of R=60, 80 and 100. The fixed deposition conditions include a rf plasma power of P=0.34 W/cm^2, a total pressure of p_{tot}=4.0 Torr; and a substrate temperature of T=200°C.

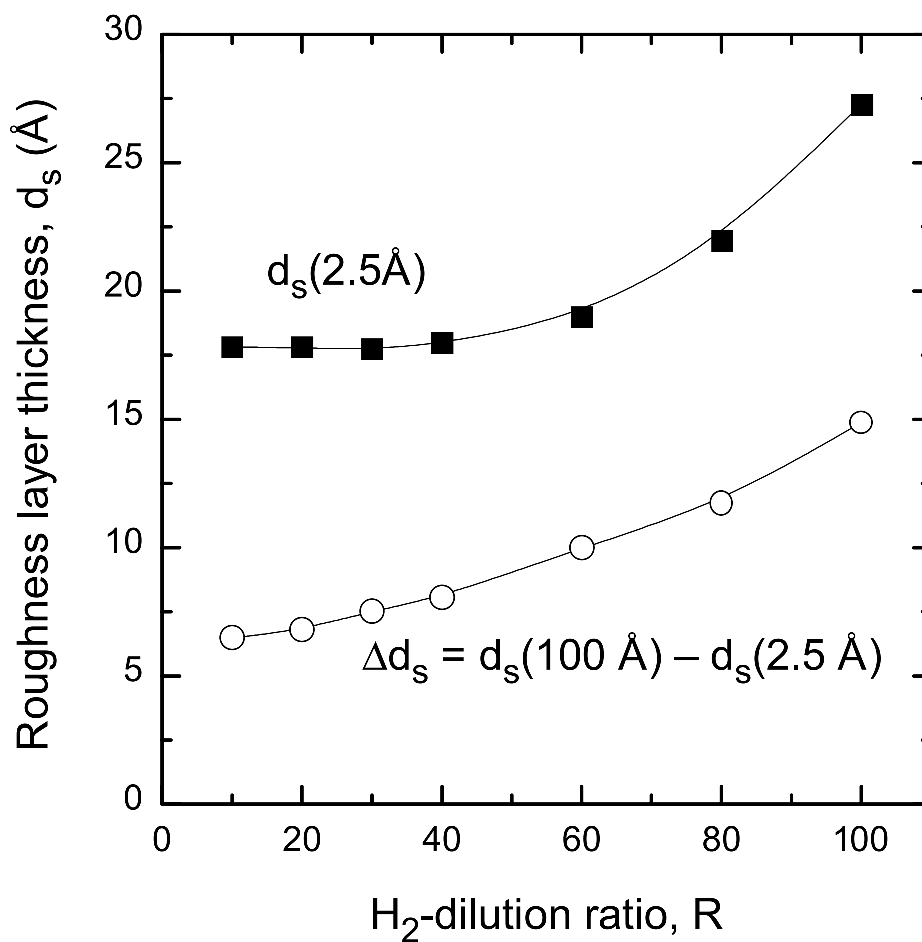

Figure 5.18 Values of the surface roughness layer thickness d_s at nuclei contact d_s(2.5 Å) (solid squares), and smoothening magnitude Δd_s due to nuclei coalescence in the first 100 Å of bulk layer growth (open circles) both plotted versus the H_2-dilution ratio R for Si:H films deposited with a plasma power of P=0.34 W/cm^2, a substrate temperature of T=200°C, and a total pressure of p_{tot}=4.0 Torr.

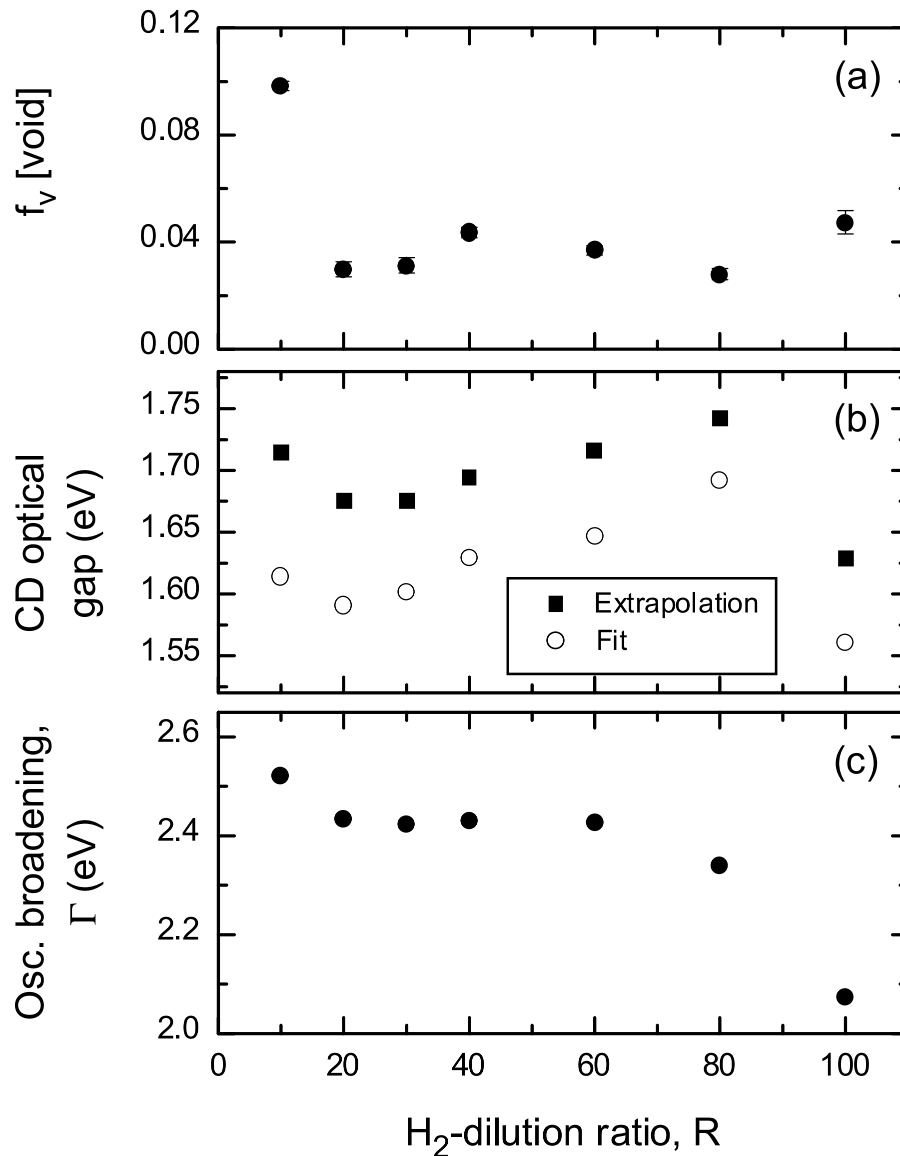

Figure 5.19 Parameters obtained from the analysis of the dielectric functions versus H_2-dilution ratio R, for the Si:H films of series IV. The plasma power was P=0.34 W/cm^2; the substrate temperature was T=200°C; and the total pressure was p_{tot}=4.0 Torr. In (a) the relative void volume fraction f_v [voids] is plotted. In (b) the optical band gap obtained by the extrapolation method (solid squares) and from fits to a parameterized equation (open circles) are shown. (See Chapter 6 for a detailed description of these two methods.) In (c) the Lorentz oscillator broadening parameter Γ obtained from fits to the same parameterized equation is provided. (See again Chapter 6 for detailed description.)

content of SiH_2 bonding configurations in the film. Second, from R=20 to 60 the gap increases monotonically with increasing H_2-dilution, as observed previously (Koh *et al.*, 1999a). Third, for R=100 the gap is reduced significantly due to the presence of the μc-Si:H phase in the film at 200Å, The presence of this phase is reflected in the (ε_1, ε_2) spectra through the appearance of an absorption tail in the low energy region of ε_2. Finally, Fig. 5.19(c) shows the best-fit parameter Γ corresponding to the Lorenz oscillator width obtained from the same fits to the (ε_1, ε_2) spectra. The parameter Γ is believed to be affected by the network disorder such that low Γ values correspond to higher ordering (Ferlauto *et al.*, 2000a). (A detailed discussion appears in Sec. 6.4.) Again three regimes can be observed in Fig. 5.19(c). First, for R=10 Γ is the highest and its value decreases to a relatively constant value of ~2.43 for 20≤R≤60. For R≥80, Γ decreases further indicating the increased ordering associated with the mixed-phase regime.

In Fig. 5.20, the phase diagrams for the Si:H films of series II and IV of Table 5.1 are compared. The plasma power in series IV was lower (P=0.34 W/cm^2) and the total pressure was higher (p_{tot}=4.0 Torr); however, the a-Si:H deposition rates near the a→(a+μc) boundaries (R=10 and R=60 for series II and IV) are comparable (3.5 and 3.4 Å/s, respectively). The increase in pressure leads to a substantial change in the phase diagram with a significant shift of the a→(a+μc) transition to much higher R. The shift in the a→(a+μc) transition opens up a wide range in the H_2-dilution ratio (20≤R≤60) whereby the films remain amorphous throughout the growth of thick films (~5000 Å). Furthermore, the a→a transition occurs at much larger thickness near the onset of the a→(a+μc) transition for the high pressure series (d_b~2900 Å for R=60) in comparison with the low pressure series (d_b~500 Å for R=10).

From the results of Figs. 5.18, 5.19 and 5.20, the effects of increasing the total gas pressure can be proposed as follows. (i) For R=10, the formation of higher silanes inherent in high-pressure deposition leads to film growth characteristics indicating poor material quality including a low bulk density, a reduced surface smoothening effect during nuclei coalescence, and a large a→a roughening transition thickness. (ii) By increasing the H_2-dilution ratio above R=10, the additional H_2 in the plasma inhibits the

formation of detrimental higher silanes (Takai *et al.*, 2000), and thus the film growth characteristics indicating high material quality are least partially regained. These include a reduced void volume fraction, a large surface smoothening effect during nuclei coalescence, a large a→a transition thickness, and a reduced broadening parameter Γ. (iii) The improved a-Si:H material quality is made possible by a shift in the a→(a+μc) transition to much larger R (R>60). This effect can be explained by an increased probability at higher pressures for the reaction given in Eq. 5.1. This reaction reduces the flux ratio of atomic H to SiH_n ($n \leq 3$) radicals reaching the surface.

Finally, the fact that at high pressure and intermediate R ($20 \leq R \leq 60$), the a-Si:H films exhibit a smooth, stable surface and a high degree of ordering can be explained not only by a reduction in the higher silanes content of the plasma, but also by a reduction in the energy of the ions bombarding the film surface. It is well known that ion bombardment may have either beneficial or deleterious effects on the growth and final properties of thin films, depending on the ion kinetic energy (Perrin, 1995; Messier *et al.*, 1990). It has been proposed that relatively low energy (on the order of 10 eV), "soft" ion bombardment promotes film densification and produces good electronic quality material (Cabarrocas *et al.*, 1991; Ganguly and Matsuda, 1996). However, more energetic ions can create localized defects and dangling bonds in the near-surface region of the film, reducing the surface diffusion length of adsorbed radicals. At high pressure, the ion energy is limited due to a reduction in the mean free path of the ions, and therefore the detrimental effects of the ion bombardment can be suppressed. In fact, recent studies have demonstrated that increasing the pressure is an effective way to increase the growth rates while limiting the detrimental effects of ion-bombardment for μc-Si:H film growth (Kondo *et al.*, 2000; Roschek *et al.*, 2000; Rech *et al.*, 2001).

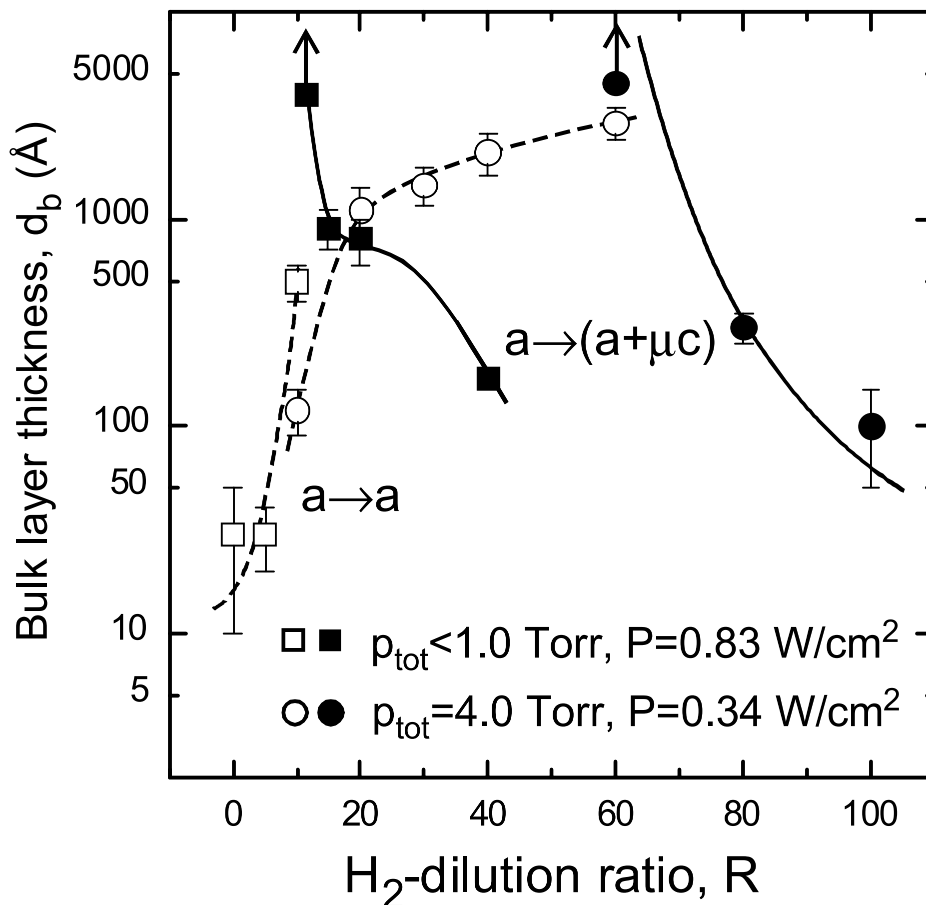

Figure 5.20 Comparison between the phase diagrams for Si:H film deposition on c-Si substrates using P=0.83 W/cm^2 and p_{tot}<1.0 Torr (series II – squares), and using P=0.34 W/cm^2 and p_{tot}=4.0 Torr (series IV – circles). The open symbols and broken lines indicate the amorphous roughening transition [a→a], and the solid symbols and solid lines indicate the amorphous-to-(mixed-phase-microcrystalline) transition [a→(a+μc)]. The up arrows indicate that the transition occurs above the indicated thicknesses.

5.6 SUMMARY

Real time spectroscopic ellipsometry has been applied in the study of rf PECVD processes that produce a-Si:H films with elevated deposition rates. The effects of rf plasma power, substrate temperature, and total gas pressure on Si:H film growth processes were investigated by means of extended phase diagrams plotted in the plane of the bulk layer thickness and the H_2-dilution ratio. The information provided by the phase diagrams was complemented by analyses of the surface smoothening during coalescence and optical properties of the Si:H films. The results obtained for low rate deposition in Chapter 3 have suggested that optimum a-Si:H i-layer deposition is performed in the amorphous regime with maximum possible H_2-dilution while avoiding the amorphous-to-(mixed-phase) microcrystalline transition. Further optimization requires the largest possible thickness for the amorphous roughening transition, thus ensuring growth with a stable surface throughout i-layer deposition.

Based on the above principles, the results of Secs. 5.3 and 5.4 have demonstrated that increases in the rf power alone are highly detrimental to a-Si:H electronic quality, and that modest increases in substrate temperature do not lead to a significant recovery of the film quality. These findings can be attributed to the fact that detrimental plasma effects such as higher silane production and ion bombardment dominate over any beneficial surface and sub-surface effects provided by the moderate H_2-dilution and increased substrate temperature. Furthermore, the $a \rightarrow (a+\mu c)$ transition is found to shift to lower R with increasing T, limiting the ability to apply H_2-dilution for materials improvement in processes at elevated T.

In overall contrast, the results of Sec. 5.5 have revealed that increases in the total pressure lead to dramatic changes in the phase diagrams. First, the $a \rightarrow (a+\mu c)$ transition is shifted to much larger R with increased pressure. In fact, it was demonstrated that the pressure can be used, just like the H_2-dilution ratio, as a parameter to control the phase of Si:H films from amorphous to mixed-phase and single-phase microcrystalline. Second, the combination of high pressure and intermediate H_2-dilution ($20 \leq R \leq 60$) conditions reverses the detrimental plasma effects such as high Si_mH_n ($m>1$) production and ion

bombardment. As a consequence the window within which a smooth stable surface is observed throughout thick layer growth is partially recovered. These observations suggest that the gas pressure can be used effectively, together with the H_2-dilution ratio, in the optimization of a-Si:H film deposition at higher rates.

Finally, the conclusions of the two previous paragraph are evidenced in Fig. 5.21, whereby the evolution of the roughness layer thickness d_s versus bulk layer thickness d_b is plotted for selected a-Si:H films of each series deposited under nominally “optimum conditions”, defined as the maximum H_2-dilution possible without crossing the a→(a+μc) transition for a 4000 Å film. It should be emphasized that for all films of Fig. 5.21 the deposition rates are higher than 3 Å/s, except for the R=10 film of series I (in which case the rate is 0.5 Å/s).

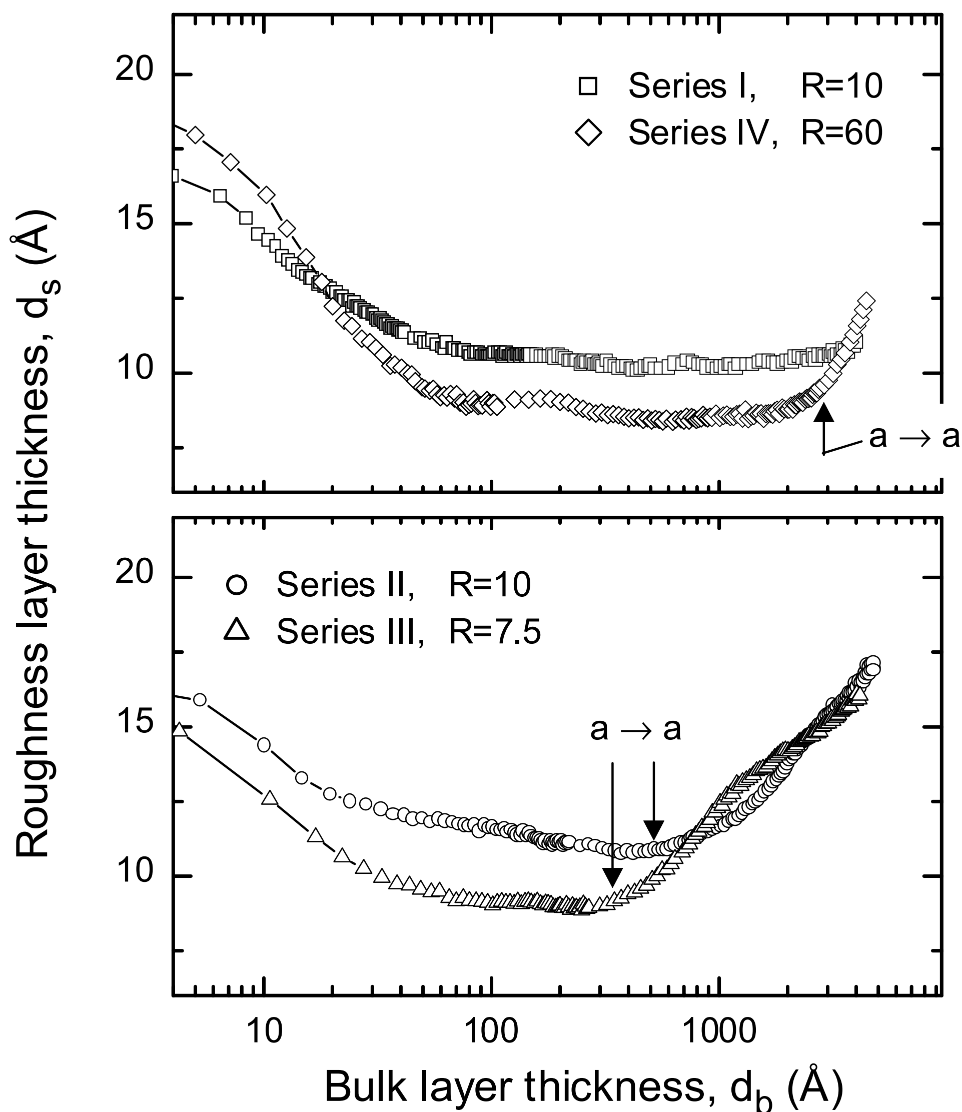

Figure 5.21 Surface roughness layer thickness (d_s) vs. bulk layer thickness (d_b) for one selected film of each of the four series described in the text. The films were deposited under nominally "optimum conditions" for each series, i.e., with maximum H_2-dilution possible without crossing the a→(a+μc) transition for a 4000 Å a-Si:H film. The R value for each film is provided; other conditions are listed in Table 5.1.

CHAPTER 6

OPTICAL PROPERTIES OF

a-Si:H BASED SOLAR CELL MATERIALS

6.1 INTRODUCTION

Over the past two decades, amorphous silicon (a-Si:H) photovoltaics technology has become a very complex and sophisticated thin film technology. Improvements in both the quality of the component materials and in the overall design of the devices have led to a steady increase in the conversion efficiency, as well as a decrease in the production costs. As a result, this technology is very competitive in the photovoltaics market (Guha *et al.*, 2000). Nowadays, state-of-the-art solar cells are fabricated in the multijunction configuration, where two or three p-i-n junctions are stacked in the same device. The optical band gap of each active layer material is chosen so that each junction provides maximum photon collection in a different part of the solar spectrum, and the overall collection is improved as compared to single-junction devices (Yang *et al.*, 1997; Guha *et al.*, 2000). Furthermore, textured layers and back-reflector layers are incorporated to generate multiple light passes through the active layers and thus increase their effective absorbance (Schropp and Zeman, 1998). As a result, state-of-the-art solar cell devices consist of a stack with several layers of different materials as depicted in Fig 6.1. The complexity of such structures imposes difficulties in the optimization of these devices when attempted by simple empirical variations of the materials properties and device configuration. Therefore, computer programs that simulate the optical and/or the electronic characteristics of solar cells have been developed in attempts to provide guidance for further improvements in the device performance (Schropp and Zeman, 1998; Sopori *et al.*, 1999).

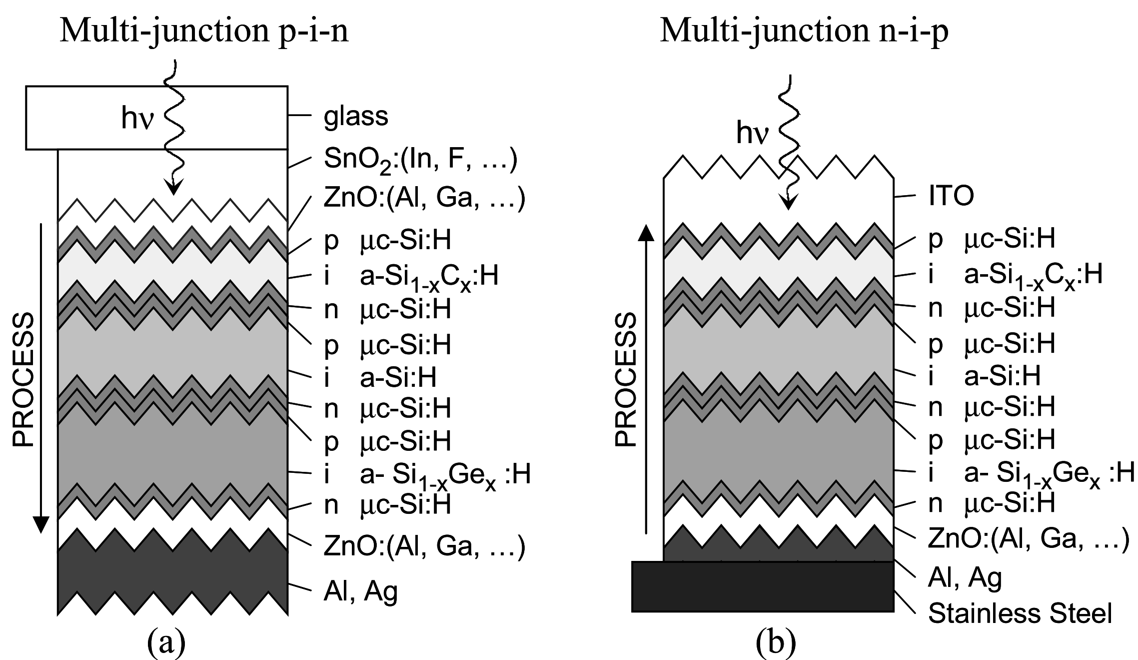

Figure 6.1 Multijunction a-Si:H-based solar cell structures based in the p-i-n and n-i-p configurations. In these hypothetical structures, a-$Si_{1-x}C_x$:H, a-Si:H, and a-$Si_{1-x}Ge_x$:H are used as the wide-gap, mid-gap, and narrow-gap components, respectively. In addition, all contact layers are assumed to be μc-Si:H:(B,P).

Any useful simulation must fulfill the following requirements: (i) utilization of accurate optical functions for the different component materials and (ii) incorporation of the different optical phenomena such as coherent and incoherent multiple reflections, modification of reflection and transmission coefficients by microscopically rough and chemically-mixed interface layers, and light scattering by macroscopically rough surface/interface layers. As outputs, the optical simulation program should predict the spectroscopic reflectance, absorbance, and transmission losses, and to determine the optical quantum efficiency associated with each active layer (Sopori *et al.*, 1999). Finally, the depth-profile of the photon generation rates, proportional to the amplitude-squared of the optical electromagnetic fields inside the device, must be calculated in order to serve as inputs for computer programs that model the electronic characteristics of the solar cells.

The development of a computer program that fulfills the above requirements is being carried out at Penn State (Ferreira *et al.*, 2001). The focus of this chapter is the determination of an input database that defines the spectra in the optical properties, e.g., (n, logα) or (ε_1, ε_2), for (a-Si:H)-based solar cell component materials. For this purpose, new analytical expressions have been developed to describe the optical spectra of amorphous and microcrystalline semiconductors based on a minimum number of physically meaningful parameters (Ferlauto *et al.*, 2000a). Such expressions have two-fold utility. First, they can be applied in the analysis of optical spectra determined experimentally by techniques such as transmission and reflection (T&R) spectroscopy and spectroscopic ellipsometry (SE), wherein physical parameters such as optical gaps can be obtained by means of least-squares regression analysis. Second, by using these expressions to characterize a set of representative materials, simple formulas can be derived that describe the best-fit parameters as a function of one or more key parameters such as the optical band gap and void fraction. In this manner, one can retrieve the optical properties of a given material by specifying one ore more parameters.

In Sec. 6.2, the development of a new analytical expression to describe the optical functions of amorphous semiconductors is presented. In addition, expressions for microcrystalline semiconductors based on the same theoretical framework are included.

Section 6.3 describes the experimental approach used in the determination of the optical functions of a-Si:H and its alloys, based on a combination of three measurement techniques. The results are presented in Sec. 6.4 along with the implementation of the optical database for such materials. Section 6.5 describes how the optical functions of other component materials of (a-Si:H)-based solar cells can be measured and analyzed. These materials include (i) doped microcrystalline Si:H layers, (ii) transparent conducting oxides, specifically SnO_2 and ZnO, that are used as contacts and in back-reflector layers, and (iii) metals. Finally in Sec. 6.6, an example of the application of the optical properties database established thus far is presented.

6.2 THEORY OF OPTICAL PROPERTIES OF AMORPHOUS AND MICROCRYSTALLINE SEMICONDUCTORS

The imaginary part of the dielectric function $\varepsilon_2(E)$ of non-crystalline semiconductors can be generally described as

$$\varepsilon_2(E) = G(E) \cdot \sum_{j=1}^{N} L_j(E), \qquad (6.1)$$

where L_j represent lineshape functions corresponding to interband transitions, and G(E) describes the shape of ε_2 near the absorption onset (Jellison and Modine, 1996) and below it as well. The real part of the dielectric function ε_1 can be obtained as a Kramers-Kronig transformation of $\varepsilon_2(E)$, given by:

$$\varepsilon_1(E) = \varepsilon_{1\infty} + \frac{2}{\pi} \sum_{j=1}^{N} P \int_0^{\infty} \frac{E' G(E') L_j(E')}{E'^2 - E^2} dE'. \qquad (6.2)$$

In this equation, P denotes the principal values of the integrals and $\varepsilon_{1\infty} \geq 1$ accounts for transitions above the upper energy limit of measurement and not included in the sum in Eq. 6.1 (Collins and Vedam, 1995).

Jellison and Modine were the first to propose the above approach for the parameterization of the optical functions of amorphous materials (Jellison and Modine,

1996). They used one Lorenz oscillator lineshape function for the interband transitions given by

$$L_1(E) = \frac{A_1 E_{01} \Gamma_1 E}{(E_{01}{}^2 - E^2)^2 + \Gamma_1{}^2 E^2} \ , \tag{6.3}$$

where (A_j, E_{0j}, Γ_j) are the oscillator strength, resonance energy, and broadening parameter for the jth transition (j=1, in this case). Furthermore, they derived the gap function from the Tauc Law in which ε_2 is described as $\varepsilon_2 \propto (E-E_G)^2/E^2$ in the vicinity of the gap (Cody, 1984) , resulting in:

$$G(E) = \begin{cases} 0, & \text{for } E < E_G \quad (6.4a) \\ \dfrac{(E-E_G)^2}{E^2}, & \text{for } E \geq E_G \quad (6.4b) \end{cases}$$

where G(E) is forced to 0 for energies lower than optical band gap. The so called "Tauc-Lorentz" expression yields improved fits to ellipsometric data on a-Si:H in comparison to previous expressions (Jellison and Modine, 1996) and is now widely used for the parameterization of the optical properties of amorphous semiconductors. In spite of its success, the Tauc-Lorenz approach has a number of limitations. It was demonstrated by Cody that the shape of the absorption onset for a-Si:H is more closely consistent with a formula based on the assumption of parabolic band density of states and a constant dipole matrix element, rather than a constant momentum matrix element, as is assumed in the Tauc Law formula. As a result, the following relationship can be applied: $\varepsilon_2 \propto (E-E_G)^2$; rather than $\varepsilon_2 \propto (E-E_G)^2/E^2$ as given in the Tauc Law (Cody, 1984). In fact, it was found that for narrow gap a-$Si_{1-x}Ge_x$ alloys the Tauc-Lorenz formula did not provide good fits. Furthermore, unphysical values for $\varepsilon_{1\infty}$ ($\varepsilon_{1\infty} < 1$) are obtained for these alloys (Ferlauto *et al.*, 2000a). In addition, it is well known that the absorption coefficient $\alpha(E)$ exhibits Urbach behavior, i.e., it decays exponentially below a certain energy with a characteristic rate defined by the Urbach energy (Cody, 1984). This may occur due to electronic transitions to and from localized disordered states.

To account for the above observations, a simple piece-wise expression for the gap function is proposed, given by

$$G(E) = \begin{cases} \dfrac{E_1}{E}\exp\dfrac{(E-E_T)}{E_U}, & \text{for } E < E_G \quad (6.5a) \\ \dfrac{(E-E_G)^2}{E_P^2+(E-E_G)^2}, & \text{for } E \geq E_G \quad (6.5b) \end{cases}$$

where E_T is a transition energy below which the Urbach behavior is observed, and E_1 is defined such that $\varepsilon_2(E)$ is continuous at $E=E_T$. In addition, E_P defines another transition energy, given by E_P+E_G, that separates the Cody optical gap behavior $[E<(E_P+E_G)]$ from the Lorentz oscillator behavior $[E>(E_P+E_G)]$. Specifically, if $E \approx E_G$ [so that $(E–E_G) \ll E_P$], then $G(E) \rightarrow [(E–E_G)/E_P]^2$, whereas if $E \gg (E_P+E_G)$ [so that $(E–E_G) \gg E_P$] then $G(E) \rightarrow 1$, as required for the Kramers-Kronig integration (Ferlauto *et al.*, 2000a).

For microcrystalline silicon, the interband transitions can be described in terms of a sum of two Lorenz oscillator lineshape functions, that simulate the E_1 and E_2 transitions of the Si crystallites near 3.4 eV and 4.2 eV, and thus N=2 in Eq. 6.1 (Ferlauto *et al.*, 2000a). In this case, $\varepsilon_2(E)$ in the vicinity of the gap is described by the expression $\varepsilon_2 \propto (E–E_G)^2/E^2$, which can be obtained as an approximation to the absorption onset for an indirect gap semiconductor (Collins and Vedam, 1995). In fact, a similar expression has also been observed to describe the absorption onset of a collection of Si quantum dots (Wilson *et al.*, 1993). Therefore, an expression for the gap function for nanocrystalline and microcrystalline silicon is given by:

$$G(E) = \begin{cases} 0, & \text{for } E < E_G \quad (6.6a) \\ \dfrac{(E-E_G)^2}{E^2}, & \text{for } E \geq E_G \quad (6.6b) \end{cases}$$

Note that this expression is the same as the one derived from the Tauc Law for amorphous semiconductors.

The determination of $\varepsilon_1(E)$ from the Kramers-Kronig integration of $\varepsilon_2(E)$ given in Eq. 6.2 is quite long and tedious; thus, it is presented separately in the Appendix. In the Appendix, $\varepsilon_1(E)$ is determined for different combinations of the Urbach expression (Eq. 6.5a), the Cody expression (Eq. 6.5b), and the Tauc expression (Eq. 6.4b or 6.6b).

6.3 EXPERIMENTAL APPROACH FOR THE OPTICAL CHARACTERIZATION OF a-Si:H AND ITS ALLOYS

The decay of irradiance in a light beam over one optical pass through a layer at normal incidence obeys the expression $I/I_0=\exp(-\alpha d)$, where α is the absorption coefficient and d is the layer thickness (Collins and Vedam, 1995). For the (a-Si:H)-based absorber layers, d is on the order of 50-500 nm. For this range of thickness, the range of α for which 1% to 99% absorbance occurs in a single pass varies from $\sim10^2$ cm^{-1} (for $I/I_0=0.99$ and d=500 nm) to $\sim10^6$ cm^{-1} (for $I/I_0=0.01$ and d=50 nm). Thus, multiple techniques are required in order to span the required range of α for a given absorber layer. In this study, a unique combination of dual-beam photoconductivity (DBPC), transmission and reflection spectroscopy (T&R), and spectroscopic ellipsometry (SE) was employed in order to extract α over the range from ~10 cm^{-1}, where the Urbach tail begins, to $\sim2\text{x}10^6$ cm^{-1}, where the absorption coefficient α saturates near the optical wavelength of λ=300 nm (Dawson *et al.*, 1992). In addition to measuring the absorption coefficient spectra denoted $\alpha(\lambda)$, which control the absorbances of each of the layers, it is important to measure the index of refraction spectra $n(\lambda)$, as well. Both parts of the optical properties, n and α, can be combined to establish the complex dielectric function according to $\varepsilon = \varepsilon_1 + i\varepsilon_2 = (n + ik)^2$, where $k = \alpha\lambda/4\pi$ is the extinction coefficient (Collins and Vedam, 1995). DBPC cannot provide the index of refraction; however, $n(\lambda)$ can be deduced over the full range of semi-transparency by T&R spectroscopy. In addition, over the range where the film is more strongly absorbing or opaque, SE can provide the complex dielectric function, and hence $n(\lambda)$.

Each of the three measurement techniques applied here has advantages and disadvantages for the determination of the optical properties of a-Si:H-based materials (Dawson *et al.*, 1992; Collins and Vedam, 1995). The advantage of DBPC is its ability to deduce very low values of α (10^{-2}-10^{3} cm^{-1}); however, its disadvantage is that α is determined only on a relative scale. As a result, DBPC measurements must be normalized to the results for α obtained by T&R spectroscopy (Jiao *et al.*, 1998). The advantage of T&R spectroscopy is its ability to deduce α over the intermediate range ($5x10^{2}$ to $5x10^{4}$ cm^{-1}) with relative immunity to film overlayers such as oxides and microscopic surface roughness. Its disadvantage is a susceptibility to errors due to macroscopic surface roughness that scatters light from the specular beam. The advantage of SE is its ability to deduce high values of α ($>10^{4}$ cm^{-1}) with relative immunity to macroscopic roughness. One disadvantage is that SE, as a reflection measurement, provides k and α with linear sensitivity. Thus, the accuracy is ~0.01 in k or $\sim 2.5\times 10^{3}$ cm^{-1} in α (assuming λ=500 nm). Another disadvantage of SE is a susceptibility to errors due to film overlayers, such as surface roughness and oxide layers, that must be taken into account in the analysis. The effect of surface overlayers can be estimated and eliminated by comparing $\alpha(\lambda)$ from T&R and $\alpha(\lambda)$ from SE and ensuring that they match in their region of overlap, as described in Sec. 2.4.

6.4 RESULTS FOR AMORPHOUS SILICON AND ALLOYS

In this study, the combination of techniques described in the previous Section was used to measure *ex situ* the optical spectra of thin-film samples of amorphous silicon (a-Si:H) and its alloys with Ge (a-$Si_{1-x}Ge_x$:H) and C (a-$Si_{1-x}C_x$:H) at room temperature over the spectral range from ~1.2 eV to 5.0 eV. The optical properties of these materials depend on the deposition conditions, the film thickness, and the underlying substrate film structure. The samples were deposited on glass substrates under selected conditions that yield optimum i-layer material defined as leading to optimum solar cell performance and stability against light-induced degradation. Specifically, for the deposition conditions

used here, the highest possible H_2-dilution of the source gases was applied while maintaining the amorphous phase through the deposition thus avoiding the transition to microcrystallinity; see Chapter 4 (Lu *et al.*, 1994; Koh *et al.*, 1998). It should be kept in mind that a somewhat higher H_2-dilution ratio may be optimal for the i-layer deposition in the solar cell configuration when thinner layers are deposited on (a-Si:H)-based doped layers. In contrast, a lower H_2-dilution ratio may be optimal when the i-layers are deposited on μc-Si:H doped layers. In this case, the μc-Si:H substrate induces local epitaxial growth that must be suppressed by reducing the H_2-dilution ratio (Koh *et al.*, 1999a). The a-$Si_{1-x}Ge_x$:H samples were prepared at the University of Toledo in Prof X. Deng's group, the source gases used were Si_2H_6 and GeH_4. The a-Si:H and a-$Si_{1-x}C_x$:H samples were prepared at Penn State by rf PECVD and at BP-Solarex by dc PECVD using SiH_4 and CH_4.

Figure 6.2, 6.3, and 6.4 show the optical properties of selected samples of a-$Si_{1-x}Ge_x$:H, a-Si:H, and a-$Si_{1-x}C_x$:H, respectively. The experimental results are plotted in terms of spectra in (ε_1, ε_2) (upper panels), as well as spectra the index of refraction (n) and the absorption coefficient (α) on a logarithmic scale (lower panels). Under optimal circumstances, the data obtained from the three techniques (DBPC, T&R and SE) can be spliced together to obtain (ε_1, ε_2) [or (n, k)] spectra over the full range without gaps. In some cases, however, limitations exist. For example, for the a-$Si_{1-x}Ge_x$:H sample (Fig. 6.2), it was not possible to obtain an overlap between the DBPC and T&R measurements. However, since the DBPC measurement is a relative one, the normalization constant can be obtained by comparing the DBPC curve to an extrapolated curve generated by the expressions in Eqs. 6.1 and 6.5. In this extrapolation, E_U is determined directly from the exponential slope of the DBPC spectra and the other parameters are obtained from fits to the T&R and SE data alone. This procedure is similar to the approach outlined previously (Jiao *et al.*, 1998), that has been supported using independent measures of α by photothermal deflection spectroscopy. In addition, for the a-$Si_{1-x}C_x$:H sample in Fig 6.4, index of refraction measurements by T&R were unavailable. The fits to the experimental data of Fig 6.4-6.6 are based on the Urbach-Cody-Lorentz expression, with

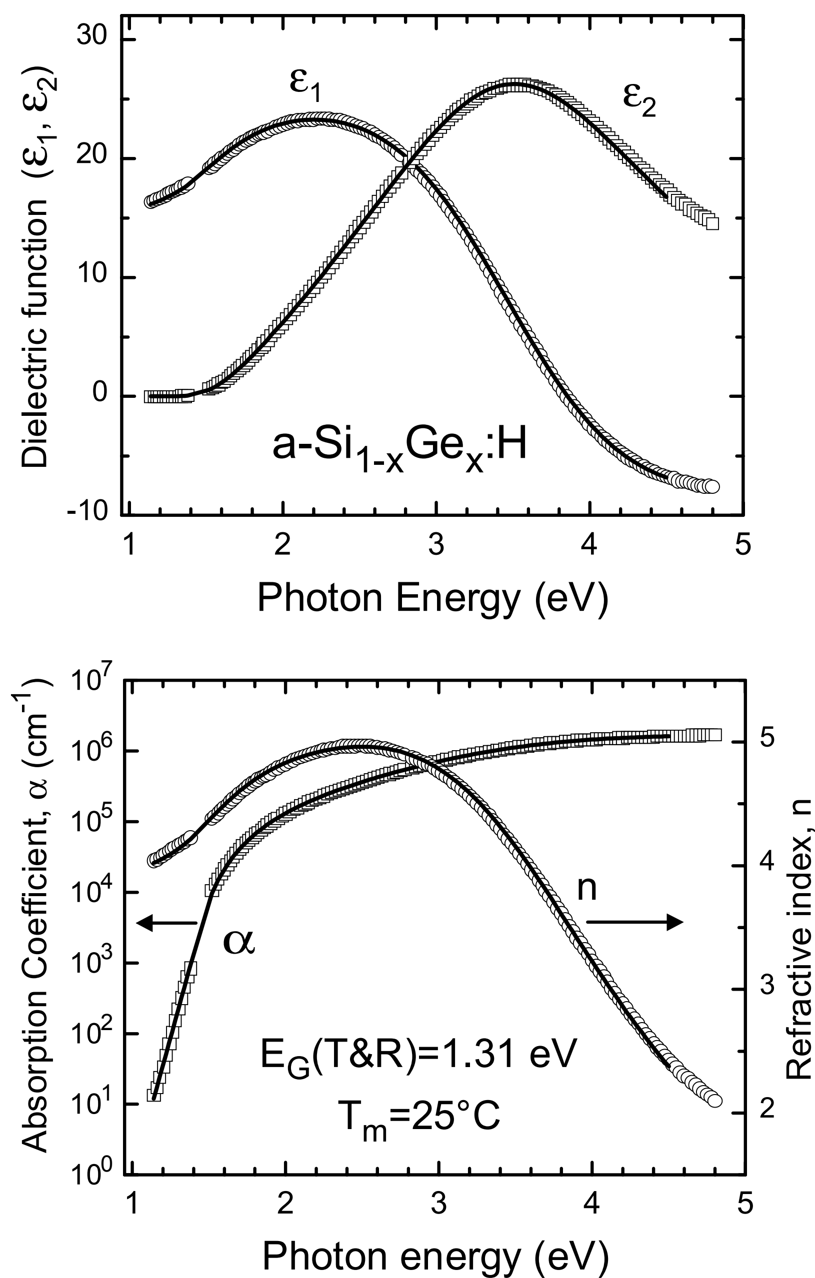

Figure 6.2 Optical properties of a-$Si_{1-x}Ge_x$:H expressed as (ε_1, ε_2) (top) and (n, logα) (bottom) versus photon energy (open symbols). These results were obtained ex-situ at room temperature by combining DBPC, T&R, and SE measurements. The solid lines are fits to the data using a seven parameter optical model including Urbach sub-gap, Cody near-gap, and Lorentz above-gap contributions.

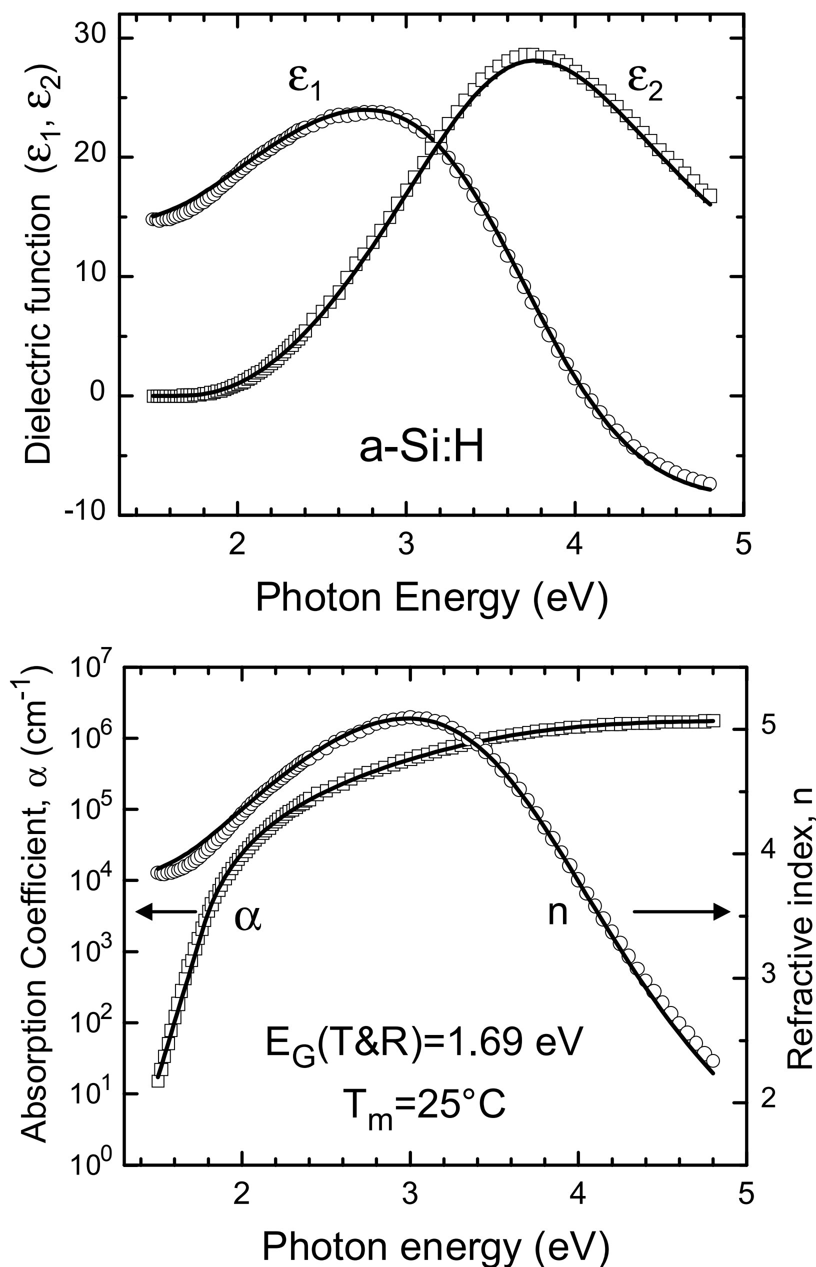

Figure 6.3 Optical properties of a-Si:H expressed as (ε_1, ε_2) (top) and (n, logα) (bottom) versus photon energy (open symbols). These results were obtained ex-situ at room temperature by combining DBPC, T&R, and SE measurements. The solid lines are fits to the data using a seven parameter optical model including Urbach sub-gap, Cody near-gap, and Lorentz above-gap contributions.

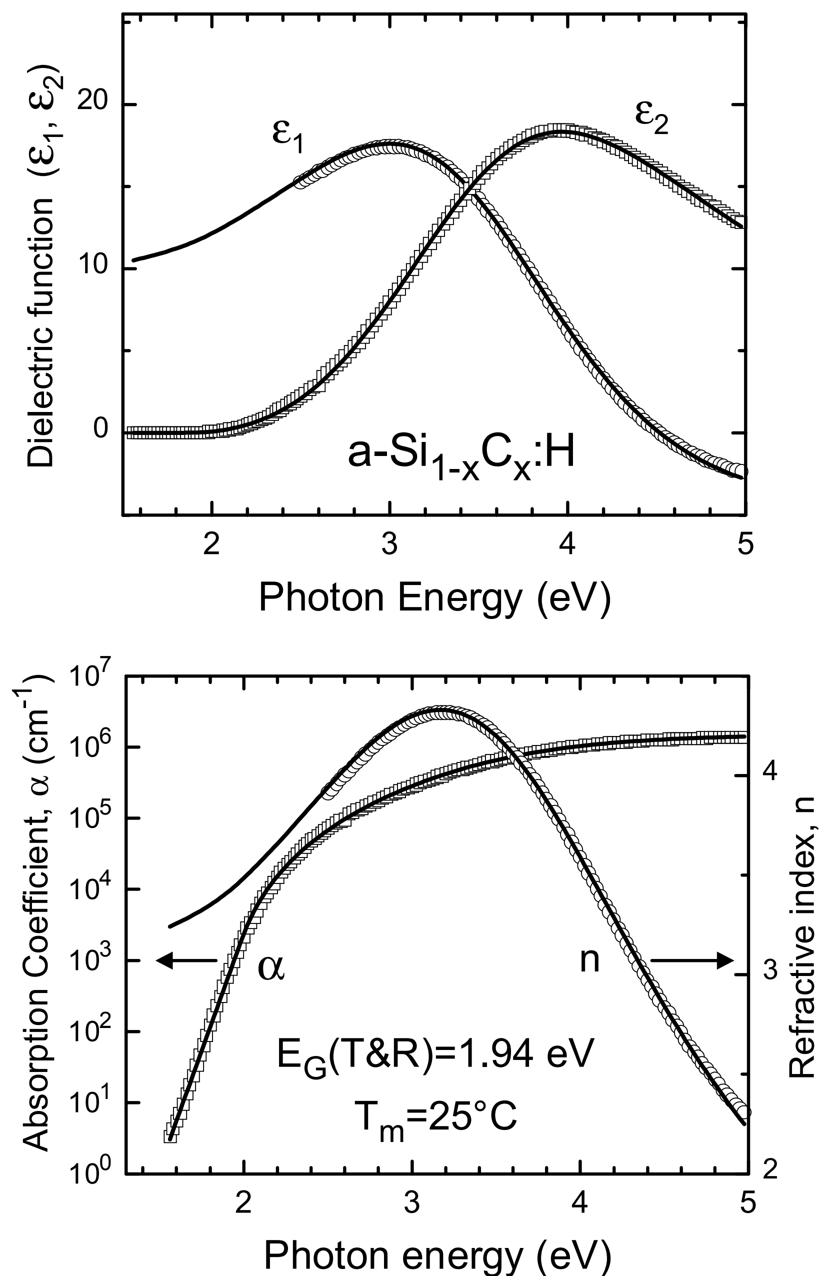

Figure 6.4 Optical properties of a-$Si_{1-x}C_x$:H expressed as (ε_1, ε_2) (top) and (n, logα) (bottom) versus photon energy (open symbols). These results were obtained ex-situ at room temperature by combining DBPC, T&R, and SE measurements. The solid lines are fits to the data using a seven parameter optical model including Urbach sub-gap, Cody near-gap, and Lorentz above-gap contributions.

seven free-parameters ($\varepsilon_{1\infty}$ is fixed at unity) and are included in the figures as the solid lines. High quality fits to the experimental are evidenced for all samples. The fits to the incomplete data sets suggest that, because the optical model is consistent with Kramers-Kronig relations, interpolation and extrapolations of the model will be valid throughout the regimes where data are unavailable.

Generally, in order to classify the optical properties of an amorphous semiconductor relevant for the design of solar cells, one quotes a nominal value of the optical gap that is easily accessible from T&R measurements. The nominal value of the optical gap is obtained most often from T&R data using the Tauc plot, i.e., a plot of $(\alpha nE)^{1/2}$ versus E, which is extrapolated linearly to the abscissa to obtain E_G(T&R) (Cody, 1984; Collins and Vedam, 1995). Such an approach is based on the assumption of parabolic valence and conduction band densities of states and a constant momentum matrix element. However, it is well known that such plots show significant curvature and that this approach leads to values of E_G(T&R) that depend on the range of available α values. Cody recommended an alternate plot of $(\alpha n/E)^{1/2}$ versus E, based on the assumptions of parabolic bands and a constant dipole matrix element (Cody, 1984; Collins and Vedam, 1995). This expression provides a larger linear region a and weaker dependence of E_G(T&R) on the range of available α. Figure 6.5 demonstrates the determination of E_G values by the Cody method for the three samples of Figs. 6.2-6.4.

Figure 6.6 and 6.7 present the seven parameters obtained in the best fits to data such as those of Fig. 6.2-6.4, in correlation with optical gap E_G(T&R), obtained according to the method of Fig. 6.5 (solid circles). Each point on these plots correspond to a different sample ranging from a-$Si_{1-x}Ge_x$:H with E_G(T&R)=1.31 eV to a-$Si_{1-x}C_x$:H with E_G(T&R)=1.94 eV. Figures 6.6(a-c) includes the three Lorentz oscillator parameters (A_1, E_{01}, Γ_1), respectively, and Figs. 6.7(a-d) include the two gap function parameters (E_G, E_P) and the two Urbach tail parameters (E_U, E_T), respectively (solid circles). In Fig 6.7(c), E_U values are also shown as deduced directly from an independent linear fit of the low energy logα spectra (open circles).

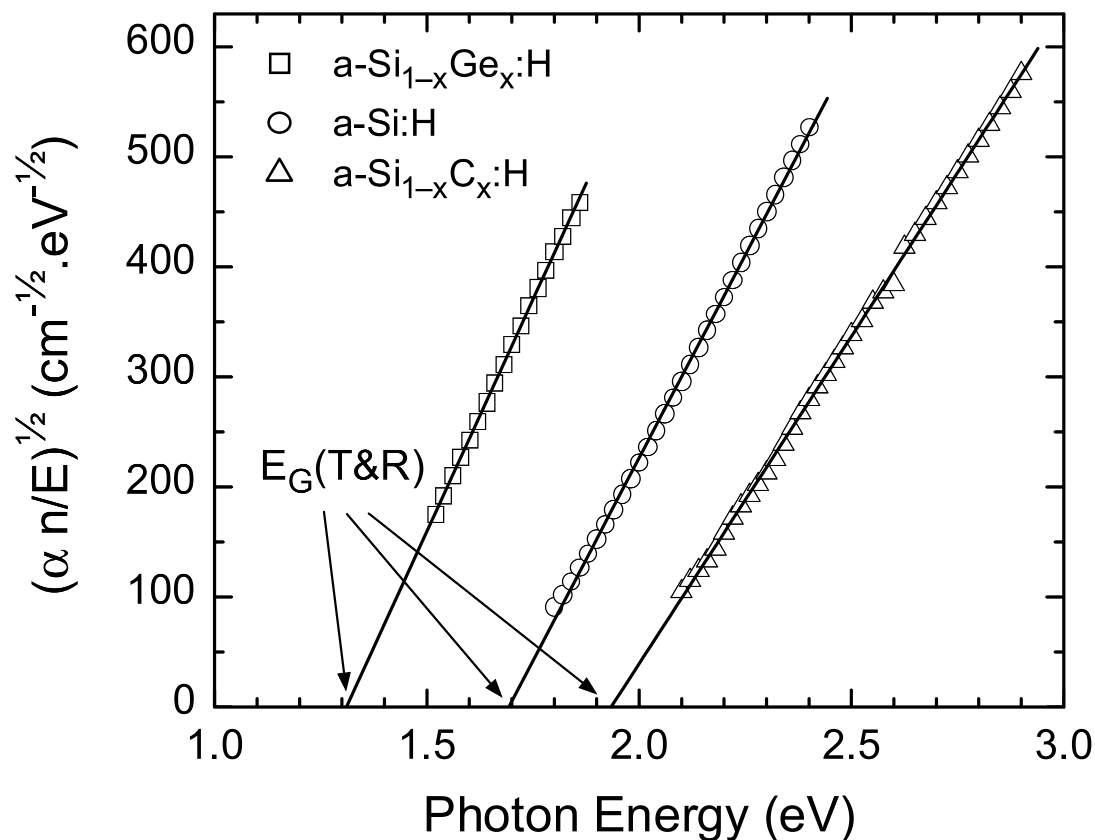

Figure 6.5 Determination of E_G from T&R data alone via the method proposed by Cody for the three samples of Figs. 6.2-6.4. This analysis assumes parabolic valence and conduction band densities of states, a constant dipole matrix element versus photon energy, and no states below the parabolic band edges. Room temperature gap values of 1.31, 1.69, and 1.94 eV are obtained for the a-$Si_{1-x}Ge_x$:H, a-Si:H, and a-$Si_{1-x}C_x$:H, respectively.

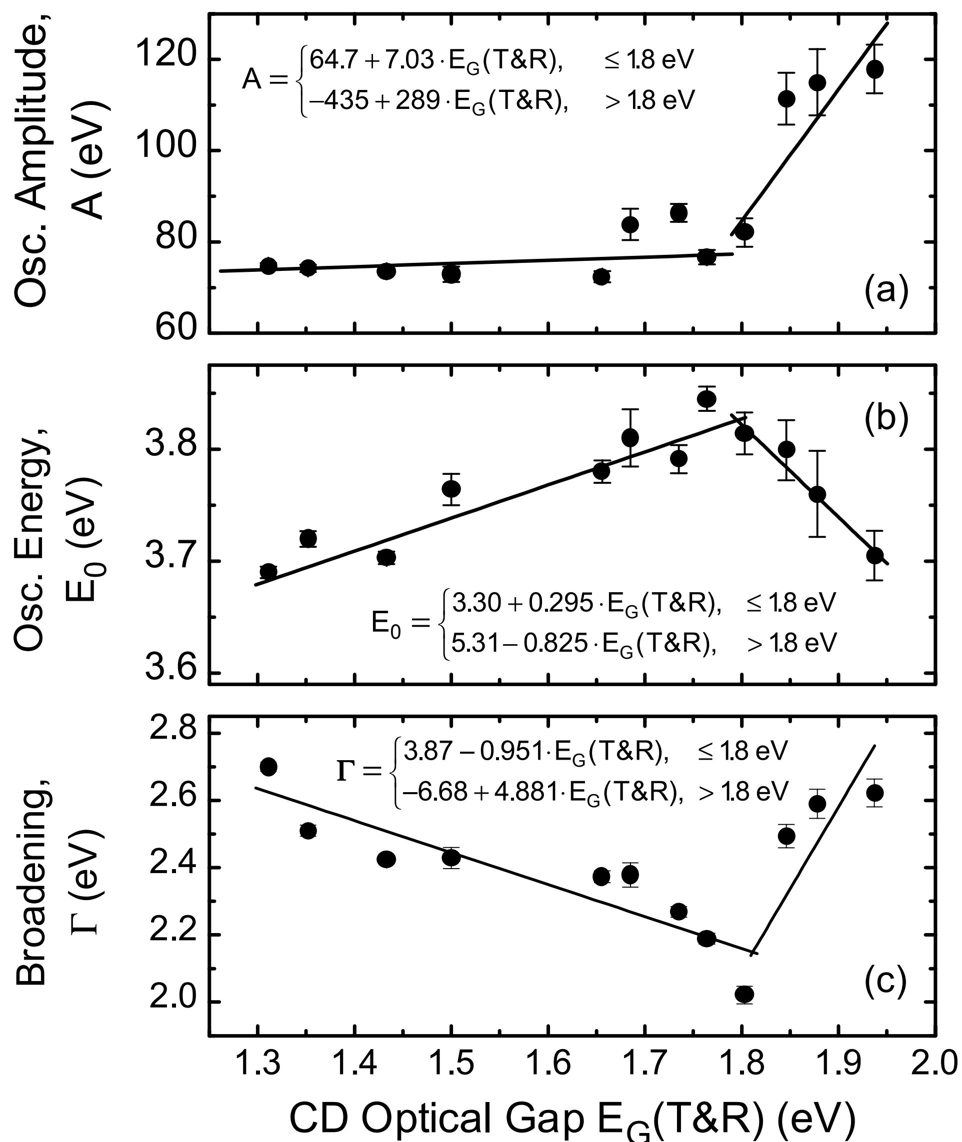

Figure 6.6 Free parameters of the Lorentz oscillator (A_{1b}, E_{01}, Γ_{1b}) in the analytical expression for the dielectric function, obtained in the best fits to data such as those of Figs. 6.2-6.4.. The results are plotted versus the optical gap E_G(T&R), obtained according to the method of Fig. 6.5. Results from 12 different photovoltaic-quality a-Si:H, a-$Si_{1-x}Ge_x$:H, and a-$Si_{1-x}C_x$:H materials are correlated, yielding the piecewise linear functions shown.

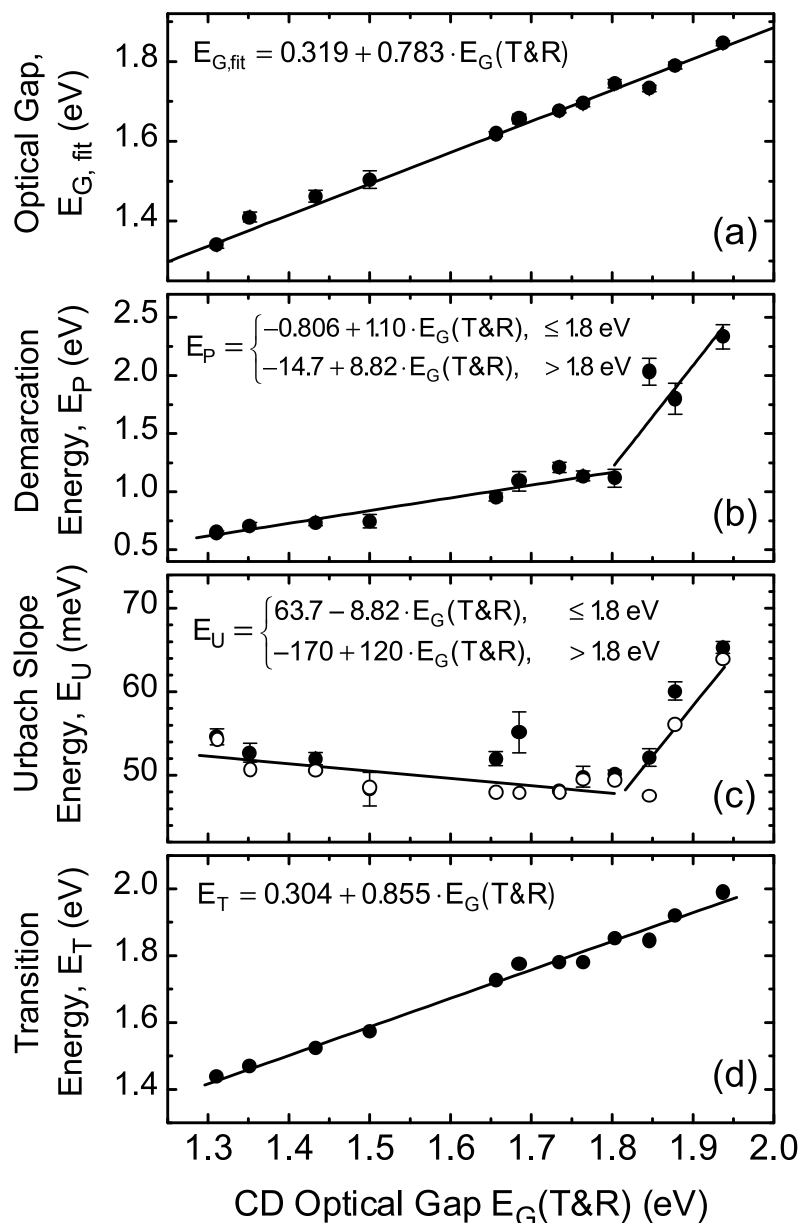

Figure 6.7 Free parameters of the gap function G(E) {(E_U, E_T), (E_G, E_P)} in the analytical expression for the dielectric function, obtained in the best fits to data such as those of Figs. 6.2-6.4. The results are plotted versus the optical gap E_G(T&R), obtained according to the method of Fig. 6.5. Results from 12 different photovoltaic-quality a-Si:H, a-$Si_{1-x}Ge_x$:H, and a-$Si_{1-x}C_x$:H materials are correlated, yielding the piecewise linear functions shown.

Among the parameters in Fig. 6.6 and 6.7, the transition energy between the Urbach tail and the parabolic region, E_T, shows the closest correlation with the extrapolated gap, E_G(T&R). In fact, the former parameter can be fit using a single linear expression over the full set of samples. The linearity of E_T versus the extrapolated gap reflects the requirement that the first derivative of $\varepsilon_2(E)$ be continuous from the Urbach tail to the parabolic region. If we neglect (i) the photon energy dependence of the Lorentz oscillator factor in this transition region, and (ii) terms in E_u^2 compared to E^2 and E_G^2, then the condition for continuity of the derivative of $\varepsilon_2(E)$ becomes $E_T=E_G+2E_U$. As a result of this relationship, E_T can be fixed at E_G+2E_U and the total number of free parameters can be reduced to six. It should be noted that the same relationship also holds if G(E) from the Tauc expression is used. A second parameter that can be fit using a single linear relationship is the fitted Cody gap in Fig. 6.7(a). Ideally, the fitted and extrapolated (T&R) gaps should be identical; however, the former includes the curvature associated with the Lorentz oscillator, and this effect leads to systematic variations between the two values. In addition, fluctuations occur owing to the difficulty of fitting the full spectral range simultaneously with a relatively small number of parameters. The same effect is responsible for the scatter in the best-fit values of the Urbach tail slope E_U as shown in Fig 6.7(c) (solid circles). In this case, the determinations of E_U directly from exponential slope from the DBPC data (open circles) provide values that are more accurate.

In general, well defined linear correlations are obtained between the best-fit parameters and E_G(T&R) for two distinct ranges in E_G(T&R). One range corresponds to the a-$Si_{1-x}Ge_x$:H and a-Si:H samples [E_G(T&R)$\leq$1.8 eV], and the other to the a-$Si_{1-x}C_x$:H samples [E_G(T&R)>1.8 eV]. The linear fits relating the parameters to E_G(T&R) are shown in Figs. 6.6 and 6.7, along with the corresponding expressions. These expressions are important because they can provide the full optical spectra (n, logα) in the visible region for an amorphous semiconductor of any arbitrary gap as determined from T&R data. The procedure is to (i) specify E_G(T&R), (ii) substitute this value into the appropriate linear expression to deduce all seven parameters {(A_{1b}, E_{01}, Γ_{1b}), (E_U, E_T),

(E_G, E_P)}, and (iii) substitute the seven parameters into the appropriate analytical expressions for the dielectric functions, obtained in Sec. 6.2. Figure 6.8 shows some typical results of this three-step process for the determination of (n, logα) given E_G(T&R). This procedure can be easily incorporated into computer code that generates the input databases for optical modeling programs of multilayer devices, and can provide powerful predictive capabilities over approaches based on sample-to-sample measurements, and interpolations between tabulated sets.

In addition to the dominant effect of the optical gap, weaker effects on the optical functions generated by other factors such as the void volume fraction (or material density) and network disorder can also be incorporated. Finally, this study provides a framework from which future improvements can be made. The results of Fig 6.6-6.7 are representative of optimum a-Si:H alloys materials achieved through H_2-dilution, however a number of other possible variations can be explored. For example, the alloy content of the materials to be measured can be fixed and their H-content can be varied (e.g., by changing the H_2-dilution) in order to span a range in the optical gap. This approach could lead to a dual specification of materials based on optical gap and H-content.

In addition to providing an effective algorithm for generating a database of optical properties of amorphous semiconductors from a single specification of the extrapolated (T&R) optical gap, the parameter variations in Fig. 6.6 and 6.7 also provide informative insights into the effects of Ge and C alloying. One interesting effect is the increase in the Lorentz broadening parameter with alloying. The broadening parameter is expected to scale inversely with the lifetime of carriers excited deep into the conduction and valence bands. It is clear that the trends in Γ are similar to those in E_U, and both trends may arise from the enhanced bond length, bond angle, and chemical disorder that occur with alloying. Evidently, the incorporation of small amounts of C is much more detrimental to the ordering than small amounts of Ge. The most highly ordered material from both standpoints is a-Si:H with an extrapolated gap of 1.8 eV, prepared by rf PECVD using a [H_2]/[SiH_4] gas flow ratio of 10, the same conditions that provide smooth stable surfaces (as discussed in Chapters 3 and 4) and optimized solar cell performance.

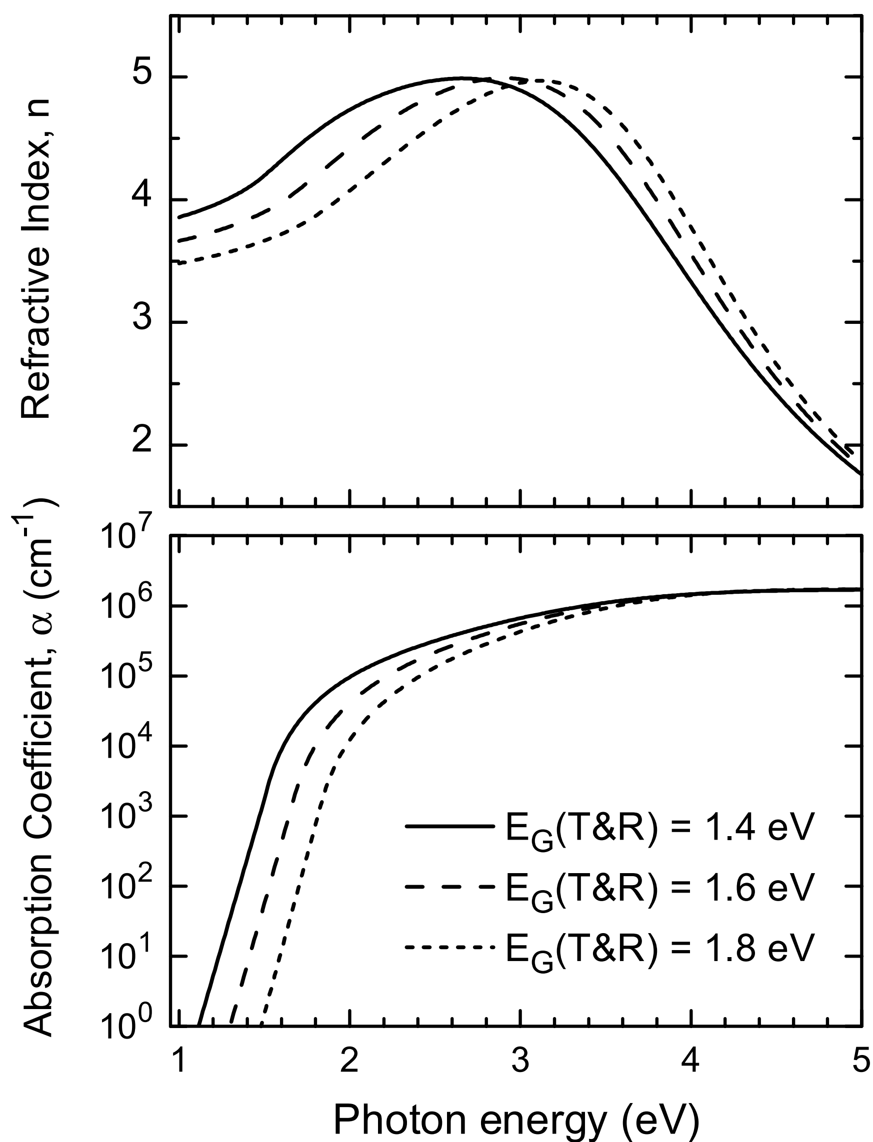

Figure 6.8 Room temperature optical properties (n, logα) for hypothetical a-Si:H alloys computed on the basis of a single specification of the optical band gap E_G(T&R) as determined from a conventional T&R measurement. These results were deduced from the relationships in Figs. 6.6 and 6.7 and from the analytical expression for the dielectric function.

6.5 OTHER COMPONENT MATERIALS

In this section, results are presented for the optical properties of the other component materials of (a-Si:H)-based multijunction solar cells. Although, these results were not obtained during the course of this thesis study, they are included here for completeness of the inputs used for the optical simulations of solar cell characteristics. In fact, as will be shown for each case, the analytical expressions presented in Sec. 6.2 can also be applied to describe the optical properties of most of these materials, provided some modifications are made in each case. Therefore, the basic approach is the same, i.e., to parameterize the optical properties of these materials using a minimum number of parameters that can be associated with physically meaningful quantities.

6.5.1 Microcrystalline silicon μc-Si:H doped layers

The microstructure and optical properties of μc-Si:H layers are extremely sensitive to the deposition conditions (Koh *et al.*, 1999b) and the layer thickness (Ferlauto *et al.*, 2000a). In addition, the doped layers used in multijunction solar cells are very thin (~100 Å). Therefore, the only way to obtain reliable information about the optical properties of μc-Si:H doped layers is by RTSE analysis of the deposition of these layers in the actual solar cell configuration. From Fig. 6.1, it can be seen that μc-Si:H doped layers are deposited on different substrate structures, depending on the deposition order (i.e., superstrate p-i-n or substrate n-i-p solar cell configurations) and on the doping type (i.e., n- or p-type). Here, the focus is on results for a p-layer in the p-i-n configuration. Similar studies of μc-Si:H n-layers on different substrate structures (Ferlauto *et al.*, 1999), and μc-Si:H p-layers on a-Si:H substrates (n-i-p configuration) have been presented elsewhere (Koh *et al.*, 1999b).

Figure 6.9 presents the best-fit to the dielectric function obtained by RTSE analysis for a 180Å-thick μc-Si:H:B p-layer deposited on ZnO-coated Asahi-U type SnO_2 obtained by RTSE analysis, as described in detail previously (Rovira *et al.*, 2000b). In this case, the PECVD conditions were optimized for the deposition of a dense single-

phase μc-Si:H layer, by promoting the immediate nucleation of the μc-Si:H on the ZnO surface. The fit was obtained from the model described in Sec 6.2 with $\varepsilon_{1\infty}$ set to unity to yield a total of seven adjustable parameters. The results of Fig. 6.9 exhibit clear evidence of microcrystallinity with features near 3.4 eV and 4.2 eV, and a gradual absorption onset typical of indirect band-gap behavior. These results were obtained at the deposition temperature of 200°C and cannot be applied directly in the optical simulation program. In order to the extract the optical functions at room temperature, in situ SE measurements can be performed after the deposition during the cool down as described elsewhere (Ferlauto *et al.*, 2001). In this way, best-fit parameters at any temperature between 40°C and 200°C were determined, as well as the parameters extrapolated to room temperature. From these parameters, the optical properties at the different temperatures can be reconstructed.

Finally, recent studies of p-layer deposition in the n-i-p solar cell configuration have suggested that the p-layers that yield solar cells with the highest open-circuit voltage in fact are not single-phase μc-Si:H but rather are prepared in the "protocrystalline" regime, with high H_2-dilution prior to the onset of the nucleation of the μc-Si:H phase (Koval, 2001). In this case, the optical properties of such layers can be estimated using the same linear expressions obtained in Sec. 6.4 for amorphous layers, by extrapolating the expressions valid for the a-$Si_{1-x}Ge_x$:H and a-Si:H layers (for $E_G \leq 1.8$eV) to higher optical gaps (e.g., to E_G=2.0 eV) in order to account for the improved order (much lower Γ) in comparison to the a-$Si_{1-x}C_x$:H alloys (Ferlauto *et al.*, 2000a).

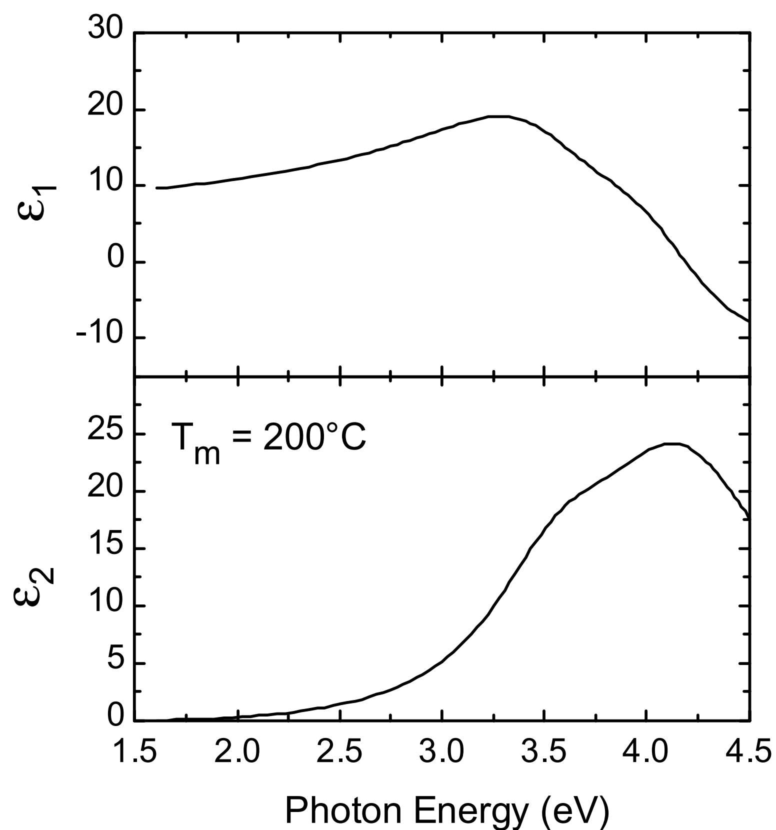

Figure 6.9 Dielectric function at 200°C for the μc-Si:H:B p-layer obtained in the actual device configuration (glass/SnO_2/ZnO/μc-Si:H) from an analysis of rotating-compensator RTSE data. Seven free parameters were used in the analytical expression for the dielectric function including near-gap Tauc behavior and two Lorentz oscillators.

6.5.2 Transparent conducting oxides (TCOs)

The optical properties of TCO materials can be separated into two contributions. In the low energy range, the absorption is generated by the intraband excitation of free electrons, which are introduced by degenerate doping. The intraband contribution to (ε_1, ε_2) can be described by a Drude expression given by (Collins and Vedam, 1995)

$$\varepsilon_{1,f} = 1 + \frac{A_f^2}{E^2 + \Gamma_f^2}, \qquad (6.7a)$$

$$\varepsilon_{2,f} = \frac{A_f^2 \Gamma_f}{E(E^2 + \Gamma_f^2)}. \qquad (6.7b)$$

Here, the two free parameters (A_f, Γ_f) are the Drude oscillator strength (proportional to the density of free-electrons) and the broadening parameter associated with free electron excitations. The second contribution to (ε_1, ε_2) is due to interband transitions, i.e., excitation of bound electrons, which generates absorption in the near-ultraviolet region of the spectrum.

The optical functions of TCOs can been determined by ex situ SE, however, two complications in the experimental determination of these results emerge. First, some TCO layers used in solar cells exhibit intentionally-produced macroscopic roughness (often called texture) that generates light-scattering. As a result, SE must be performed using a rotating-compensator configuration in order to separate out the effects of depolarization generated by multiple scattering (Rovira *et al.*, 1999). Second, since SE is based on a reflection measurement, the accuracy in the determination of the extinction coefficient is limited to k~0.01, and therefore additional transmission measurements are desirable for the determination of k with a higher accuracy.

Doped SnO_2 and Sn-doped In_2O_3 (ITO) are used most often as the contact layers in p-i-n and n-i-p configurations, respectively. For these materials, the absorption onset in the near-ultraviolet is weak, and a parameterized model based on the Tauc-Lorenz expression described in Sec. 6.2 provides a good description of the interband transitions. Figure 6.10 presents the optical properties (n, k) of an Asahi-U type SnO_2 film as

determined by rotating-compensator SE analysis (solid line). In this case, an analytical expression together with free microstructure parameters were used to fit the experimental (ψ, Δ) spectra directly (Rovira *et al.*, 1999). This analytical expression includes a contribution from interband transitions given by the Tauc-Lorenz expression with four free-parameters (presented in Sec. 6.2), along with an intraband contribution given by Eq. 6.7 with two free-parameters. (It should be noted that the constant parameter $\varepsilon_{1,f(\infty)} = 1$ in Eq. 6.7a for the latter contribution is replaced by the corresponding constant parameter of the interband contribution.) The broken line in Fig. 6.9 corresponds to results obtained from transmission spectroscopy (T), as described elsewhere (Rovira *et al.*, 1999). Even though there is reasonable agreement between the SE and T results, the minimum in k observed at $E \approx 2.5$ eV, corresponds to a single-pass absorbance loss of 10%, which is larger than has been reported in other studies (Schropp and Zeman, 1998). Further research is being carried out to establish more precise methods for the determination of k with higher accuracy for TCOs, especially for those that exhibit texture.

In the case of ZnO, a parameterized model has yet to be developed to describe the optical properties of polycrystalline thin films; thus, this is the goal of future research efforts. Any such model must account for a sharp absorption onset around at $E \approx 3.2$ eV associated with interband transitions. This onset exhibits extra doping-dependent features due to excitonic effects (Jin *et al.*, 1988; Jellison and Boatner, 1998). The low energy spectra, however, can be described in terms of the Drude free electron excitations as for SnO_2. Currently, ZnO films are measured on a sample-by-sample basis, in order to generate inputs for the optical simulation. As examples, Fig. 6.11(a) and Fig6.11(b) show the dielectric functions for two different ZnO films deposited by sputtering for applications as a back-reflecting spacer layer and as a thin protective layer on SnO_2, respectively. These results show significant differences, in particular, in the visibility of the band gap features and the magnitude of ε_2 below the band gap. The back-reflector layer of Fig. 6.11(a) shows sharp features near the band edge, and a low ε_2 value in the visible and infrared. This behavior is characteristic of a relatively low doping level

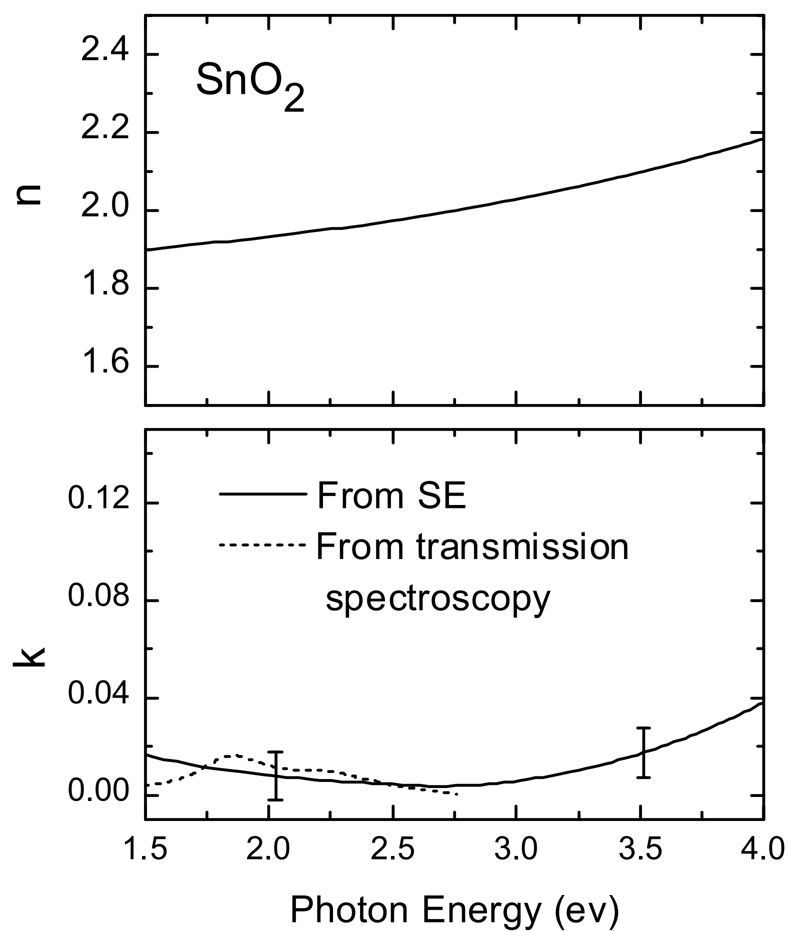

Figure 6.10 Index of refraction and extinction coefficient for an Asahi U-type textured SnO_2 film on glass measured at room temperature using rotating-compensator RTSE. The model applied for the optical properties includes the four-parameter interband Tauc-Lorentz contribution, along with the two-parameter intraband Drude contribution (solid lines). The broken line depicts results for the extinction coefficient extracted from transmission measurements.

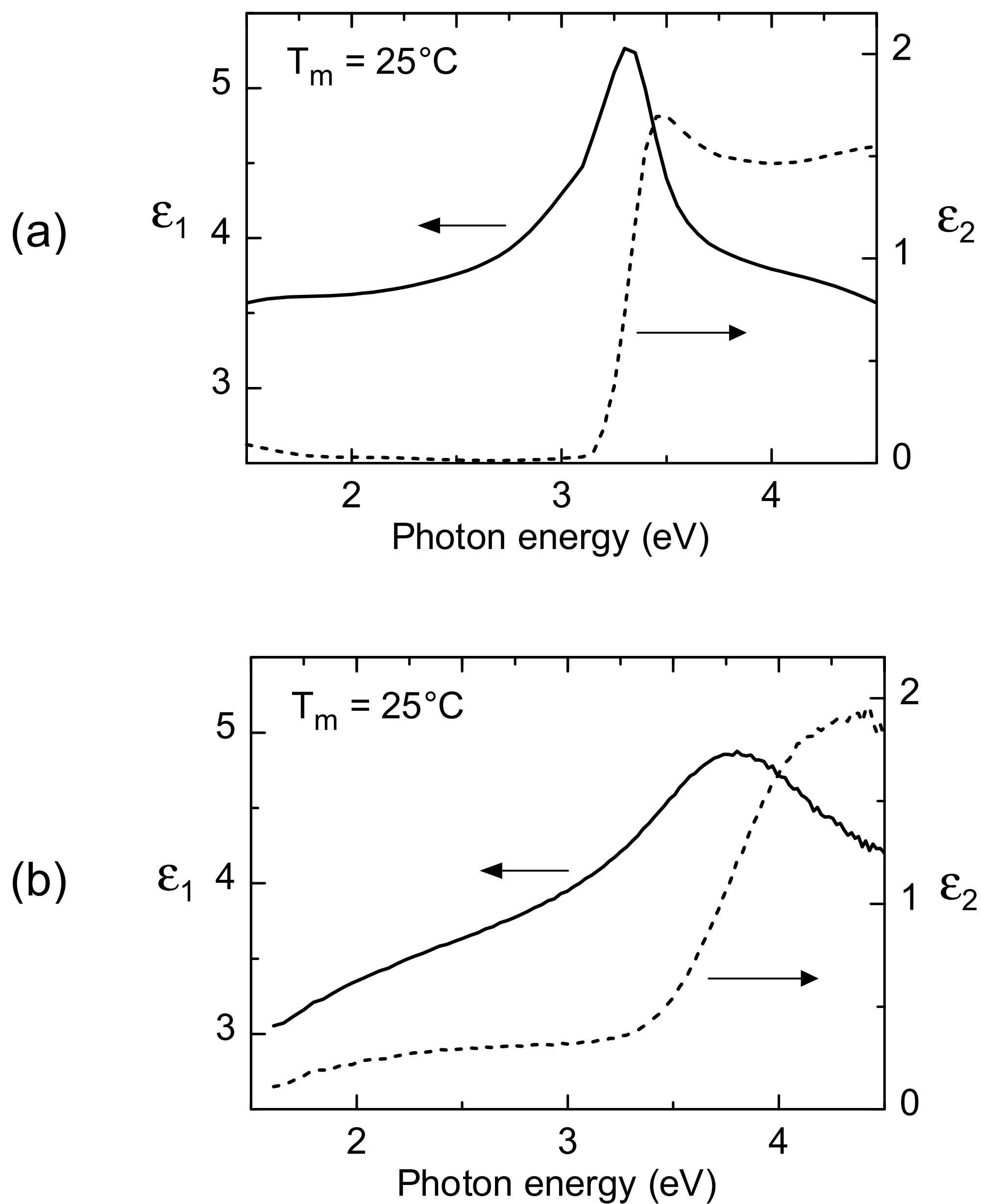

Figure 6.11 Dielectric functions of two different types of ZnO films used in a-Si:H-based solar cells: (a) a film used as the dielectric spacer layer in the back-reflector structure, and (b) a thinner film used as the protective layer on a glass/SnO_2 structure.

compared to the film of Fig. 6.11(b), for example. For the latter film, the band edge features are no longer visible, the band edge itself is significantly broadened, and the value of k below the gap is much larger. For both materials of Fig. 6.11, improvements in the optical properties can be made for their specific applications, for example, to reduce the k values to minimize parasitic absorbance losses in these layers.

6.5.3 Metals

Ag and Al are used most widely as back-reflector metals in the (a-Si:H)-based solar cell structure. These metals exhibit not only the Drude free electron behavior described by Eq. 6.7, but also interband transitions (Collins and Vedam, 1995). Ag provides the simplest situation since the interband transitions are due to the excitation of electrons from the d-band to the Fermi level, and these occur with an abrupt onset near 3.75 eV. Thus, these transitions are of little practical interest in this study since no appreciable photon flux in this range of energies reaches the back reflector. The interband transitions in Al are predominately due to electronic excitations that occur between parallel bands in the reciprocal space planes parallel to (200) and (111). An analytical expression describing these transitions was derived much earlier (Ashcroft and Sturm, 1971). In Al the interband feature of interest leads to a peak in ε_2 for E~1.5 eV, which is also associated with a minimum in the reflectance spectrum.

Figure 6.12(a) shows (ε_1, ε_2) of Ag measured at room temperature as reported elsewhere (Palik, 1985) (solid lines), along with its decomposition into intraband (dotted lines) and interband (dashed lines) components. For the intraband component, the Drude expression was used with variable amplitude and broadening parameters (as in Eq. 6.7), chosen to best fit the experimental data. For the interband component, however, no specific form was assumed. The Drude terms dominate below 2 eV with the exception of the constant ε_1 contribution given by $\varepsilon_{1\infty}-1 = 2.2$, that can be included as part of the constant $\varepsilon_{1,f(\infty)}$ term in Eq. 6.7 (increasing its value from unity to 3.2). This demonstrates that it is unnecessary to incorporate details of the d-band transitions into the optical properties of this material for solar cell modeling purposes. The best metals for back-

reflector applications exhibit the largest magnitude (i.e., the most negative) values for ε_1 and the lowest values for ε_2; this situation is favored when the broadening parameter Γ_f=h/($2\pi\tau_f$) in Eqs. 6.7 is minimized. Thus, if the relaxation time τ_f is very short, e.g., as in a small grain-size metallic film, then the reflectance is reduced due to dissipation via electron scattering in the metal. Figure 6.12(b) exhibits the dielectric functions of two different Ag films, one prepared by evaporation on glass at Penn State University (solid line) (Nguyen *et al.*, 1992) and the other prepared by sputtering onto stainless steel by United Solar (open points). The United Solar film exhibits a larger free electron contribution to ε_2, suggesting a smaller grain size in the material and higher parasitic absorption in the back-reflector.

Figure 6.13(a) shows the calculated dielectric function for Al at room temperature (solid lines), using the expressions derived earlier (Ashcroft and Sturm, 1971). Also included here is the decomposition of (ε_1, ε_2) into intraband (dotted lines) and interband (dashed lines) components. For the intraband component, the Drude expression was used with amplitude and broadening parameters deduced from best fits to experimental data [see, e.g., Fig. 6.13(b)]. For the interband component, two parallel-band transitions associated with the (200) and (111) reciprocal space planes were used with transition energies and broadening parameters also deduced from best fits to data. Figure 6.13(b) shows experimental results obtained earlier by rotating-polarizer RTSE during evaporation of Al (points) (Nguyen *et al.*, 1993), along with data reported much earlier (Shiles *et al.*, 1980). The advantage of the RTSE measurements is that they avoid distortion of the optical properties by oxide overlayers that form rapidly upon removing the sample from the vacuum chamber. The agreement between the RTSE and the reference data set is good and reveals the dominance of the (200) parallel band transitions centered near 1.5 eV, as in Fig. 6.13(a). As noted earlier, such transitions lead to a minimum in the reflectance spectrum at this energy due to the enhanced dissipation. A calculation of the reflectance at the interface between the spacer layer and the reflector

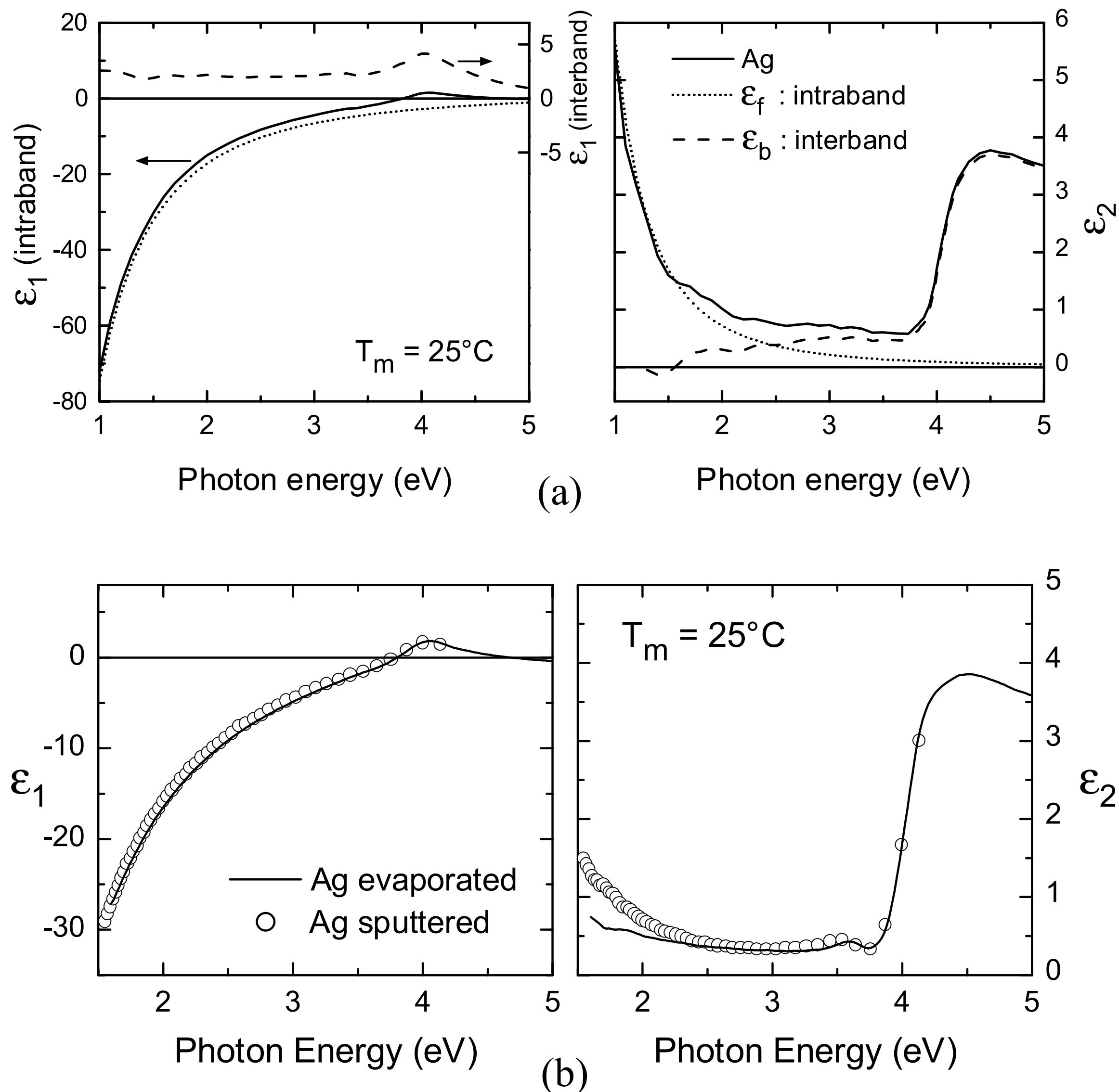

Figure 6.12 (a) Dielectric function of Ag measured at room temperature as reported by (Palik, 1985) (solid lines) demonstrating its decomposition into intraband (dotted lines) and interband (dashed lines) components. For the intraband component, the Drude expression was used with variable amplitude and broadening parameters, and for the interband component a tabular listing was deduced from the decomposition. (b) Room temperature dielectric functions of thin film Ag prepared by evaporation on glass (solid lines) and by magnetron sputtering on stainless steel (points), both obtained at room temperature by ex situ rotating-analyzer SE.

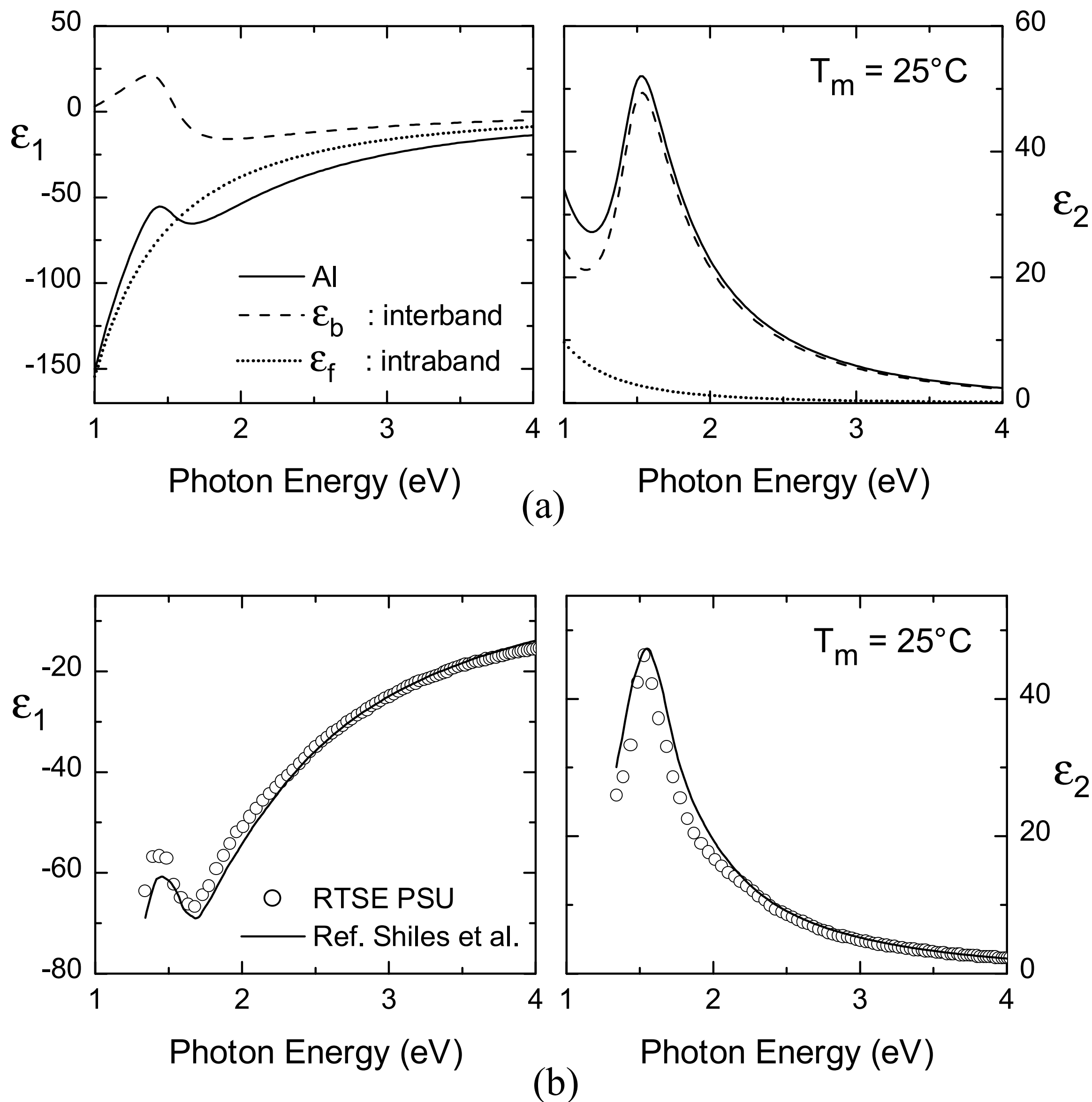

Figure 6.13 (a) Calculated dielectric function for Al at room temperature (solid lines), including a decomposition into intraband (dotted lines) and interband (dashed lines) components. (See text for details.) (b) Room temperature dielectric functions of thin film Al as reported in (Shiles *et al.*, 1980) (solid lines) and as obtained by rotating-polarizer RTSE during evaporation on a room-temperature silicon wafer substrate (points) (Nguyen *et al.*, 1993).

layer of the back-reflector structure yields R=0.83 at 750 nm for Al versus R=0.98 for Ag. This lower reflectance generates a significant absorbance loss at the ZnO/Al interface over the spectral range where it is least desired (750-1000 nm), and demonstrates the clear superiority of the ideal ZnO/Ag back-reflector structure over the ZnO/Al structure.

6.6 APPLICATIONS

In this section, the optical property database established thus far is applied to assess the impact of interface non-idealities on optical collection in single-junction a-Si:H-based solar cell structures. In the multilayer optical analysis used here, incoherent multiple reflections within the glass substrate and coherent reflections within all other layers are assumed in order to compute the optical characteristics of the solar cells. These characteristics include the absorbance for each layer and the reflectance for the entire structure. Because the Ag back-reflector incorporated into the solar cell structure is opaque, the spectral transmittance is zero. Thus, photon flux that is not absorbed in the a-Si:H i-layer will be absorbed in the other layers and lost, or reflected from the entire structure and lost. The basic solar cell structure consists of glass/SnO_2/p-i-n/ZnO/Ag, where the inputs include the SnO_2 optical properties from Fig. 6.10 (solid lines), the μc-Si:H p-layer optical properties from Fig 6.9 (modified for room temperature), the computed a-Si:H optical properties from Fig. 6.8 (with E_G=1.8 eV), the ZnO optical properties from Fig. 6.11(a), and the Ag optical properties from Fig. 6.12(b) (solid lines). Here, for simplicity, the ZnO protective layer is omitted, and the n-layer optical properties are assumed to be the same as those of the p-layer.

The upper panel of Fig. 6.14(a) shows the difference between the spectral absorbances in the i-layer (fractions of incident irradiance absorbed) for a solar cell structure with a 45 nm microscopic roughness layer at the SnO_2/p interface and for an ideal structure with no interface roughness. In the former solar cell structure, microscopic roughness layers are also incorporated at the successive interfaces of the device (e.g., p/i,

i/n, n/ZnO) in proportion to that at the SnO_2/p interface as has been measured in previous RTSE studies (Koh *et al.*, 1995; Rovira *et al.*, 1999). The ZnO/Ag interface in both structures of Fig. 6.14(a), however, is assumed to be ideal. The lower panel of Fig. 6.14(a) shows the corresponding difference in the spectral reflectances for the two structures (rough–ideal). The most important effect of microscopic roughness at the solar cell interfaces is an increase in the total photon flux collected by the i-layer with the maximum gain observed near 550 nm. This gain is shown more clearly in Fig. 6.14(b). Here the potential increase in short-circuit current ΔJ_{SC} for the solar cell is plotted as a function of microscopic roughness layers thickness at the SnO_2/p interface. (Again the roughness layer thicknesses at the successive interfaces are scaled in proportion to that at the SnO_2/p interface; an exception is the ZnO/Ag interface, which is assumed to be perfect for all structures.) The quantity ΔJ_{SC} is computed by integrating the product of the optical quantum efficiency and the AM1.5 spectral photon flux over the range from 270 to 900 nm. The optical gains in Fig. 6.14(b) associated with the microscopic roughness layers are attributed to the suppression of refractive index discontinuities. In fact, the strongest effect occurs at the SnO_2/p interface, where the discontinuity is the largest and the roughness layer is the thickest. Thus, the microscopic roughness layer acts as an anti-reflecting layer for this interface; irradiance that would otherwise be reflected from the SnO_2/p interface in an ideal structure passes into the i-layer where it can be absorbed.

The upper panel of Fig. 6.15(a) shows the increase in back-reflector absorbance that results when a 13 nm ZnO/Ag interface layer is incorporated into the solar cell structure having 45 nm roughness at the SnO_2/p interface. The ZnO/Ag interface layer in this case is attributed both to microscopic roughness and to atomic-scale intermixing and interface reactions when Ag is sputtered on ZnO (or vice versa in an n-i-p solar cell) (Ferreira *et al.*, 2001). The optical properties of the interface layer are simulated as a 0.21/0.79 mixture of ZnO/Ag, applying the Bruggeman effective medium theory. The result of Fig. 6.15(a) shows a significant parasitic absorbance loss due to the interface layer in the spectral region from 500 to 700 nm. With decreasing wavelength below 500 nm, the decrease in absorbance loss is attributed to the fact that almost all incident

irradiance is absorbed by the overlying structure, whereas the decrease with increasing wavelength above 700 nm appears to be an effect of the optical properties of the interface layer. The latter effect is expected to be strongly dependent on the chemical and microstructural nature of the interface layer. The lower panel of Fig. 6.15(a) provides the corresponding difference in reflectance (interlayer – ideal), and Fig. 6.15(b) shows the potential gain in J_{SC} that would occur if all the parasitic absorbance losses in the ZnO/Ag interface region could be converted to useful current.

6.7 SUMMARY

In this chapter, a description was presented concerning the optical properties of many of the components of (a-Si:H)-based solar cells in terms of simple analytical expressions based on a few physically-determined parameters. Specifically, new analytical expressions have been developed for the optical functions of amorphous semiconductors absorber layers and doped microcrystalline contact layers. Such expressions will assist in the future in modeling the optical performance of the solar cells, and will allow the user to tailor the optical properties based on physical inputs such as the optical gaps of the i-layers, the free-carrier concentration of the TCOs, etc. This approach is quite general and can also be applied to other opto-electronic thin film technologies, as well.

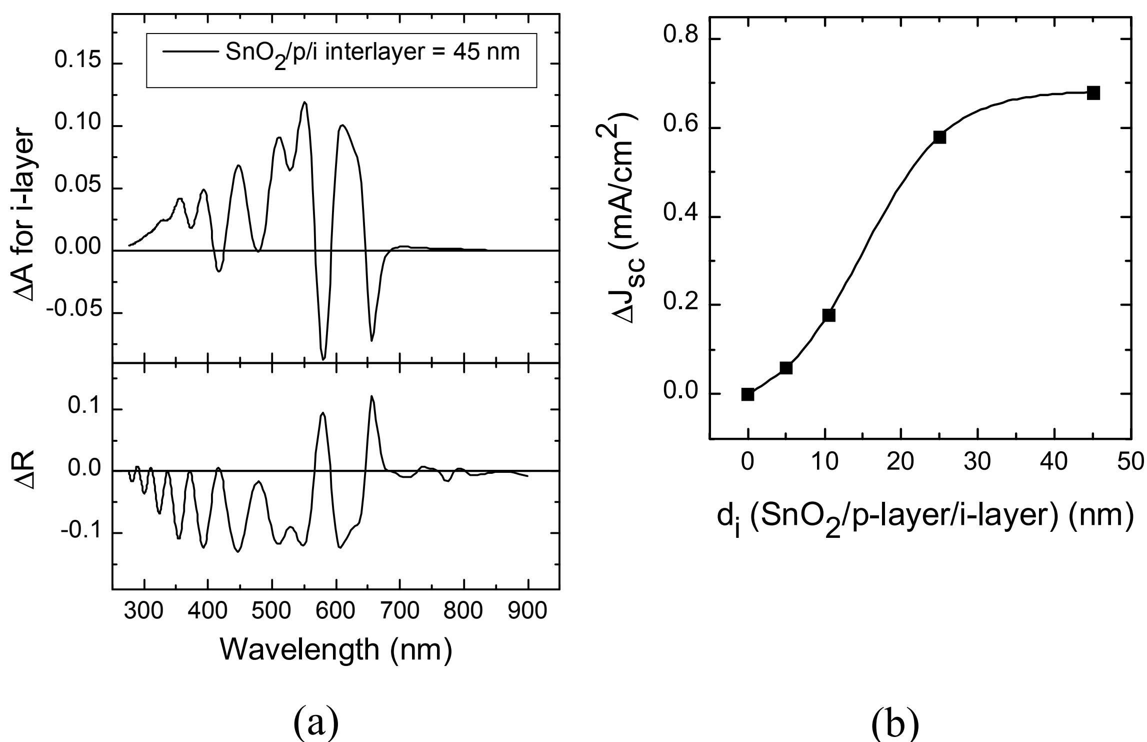

Figure 6.14 (a) Predicted increase in the i-layer absorbance spectrum (upper panel) for an a-Si:H-based single-junction p-i-n solar cell obtained by assuming a 45 nm microscopic roughness layer at the SnO_2/p-layer interface, over that for an "ideal" device without the interface roughness. The lower panel shows the difference (rough – ideal) in the solar cell reflectance; (b) potential current gain due to the antireflection effect of microscopic roughness of thickness d_i at the SnO_2/p-layer interface.

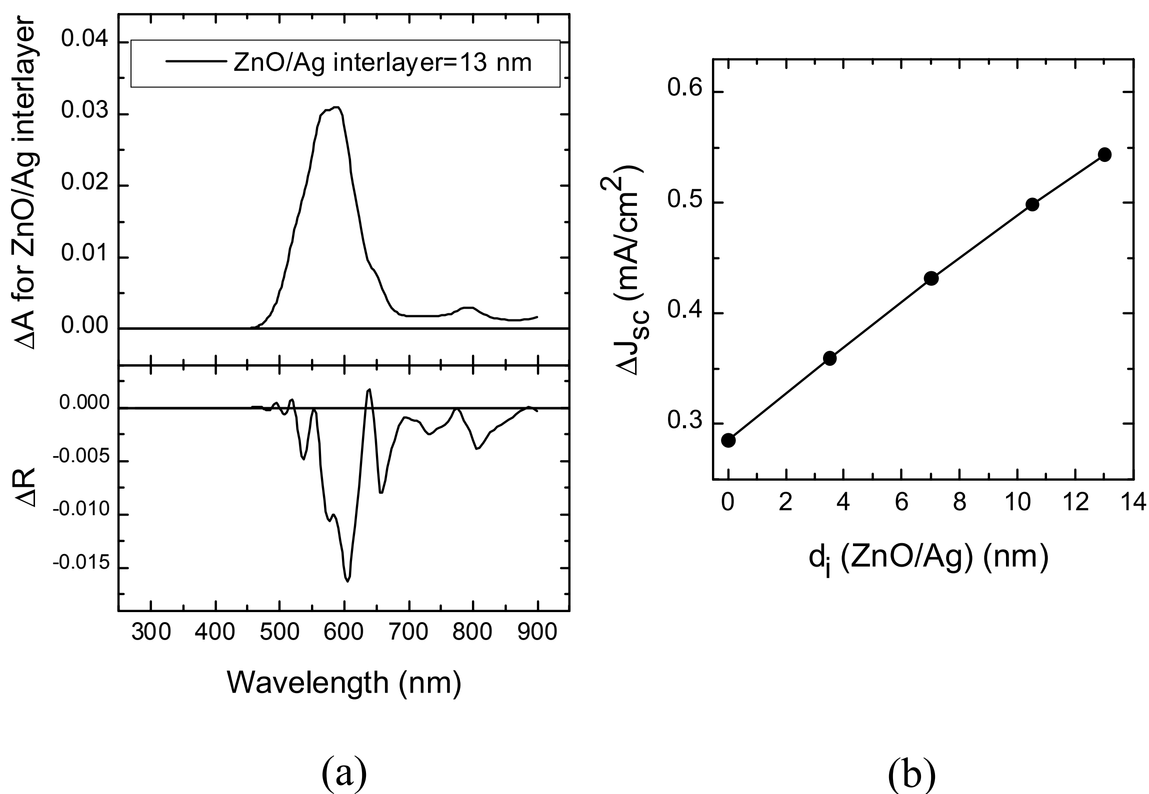

Figure 6.15 (a) Predicted increase in parasitic absorbance (upper panel) of the ZnO/Ag interface in the a-Si:H p-i-n solar cell obtained upon introduction of a 13 nm ZnO/Ag interlayer (21/79 vol.% ZnO/Ag). The lower panel shows the difference (interlayer − ideal) in the solar cell reflectance spectra; (b) potential current gain generated by the elimination of all parasitic absorbance at the ZnO/Ag interface, plotted versus the ZnO/Ag interface layer thickness d_i.

CHAPTER 7

CONCLUSION AND FUTURE WORK

7.1 CONCLUSION

In the first part of this thesis, the microstructural evolution and optical properties of Si:H films deposited by rf plasma-enhanced chemical vapor deposition (PECVD) were thoroughly characterized by real time spectroscopic ellipsometry (RTSE). The RTSE measurements and analyses were applied in the development of deposition phase diagrams. In correlations with solar cell results, the usefulness of such diagrams was demonstrated in providing insights into the Si:H film growth processes as well as guidelines for the optimization of intrinsic a-Si:H layers incorporated into a-Si:H-based solar cells.

Detailed investigations were performed whereby the RTSE measurements and analyses were complemented by ex situ atomic force microscopy (AFM) measurements and analyses in order to characterize the evolution of the surface roughness layer thickness versus the bulk layer thickness for Si:H films. Such investigations revealed that different growth regimes exist as a function of film thickness during Si:H PECVD, and that these regimes are controlled by the deposition conditions, particularly by the H_2-dilution level.

For Si:H films that are amorphous throughout growth, three main evolutionary regimes were identified as a function of the accumulated thickness, namely, (i) a surface smoothening regime due to the coalescence of nucleation-induced microstructure, (ii) a stable, smooth-surface regime, and (iii) a surface roughening regime. The onset of surface roughening defines "the amorphous roughening transition", so described because the film remains amorphous as the transition is crossed [a→a]. Theoretical simulations

reveal that these three regimes can be described in terms of a competition between surface roughening and smoothening mechanisms that act on different in-plane scales. Diffusion of adsorbed radicals on the surface was suggested to control which film growth regime dominates the microstructural evolution.

For Si:H films that evolve from the amorphous phase to the microcrystalline phase during growth, two transitions were identified that separate three different regimes in the phase evolution. It was shown that the nucleation of μc-Si:H grains from the a-Si:H matrix generates an onset of surface roughening identified as the amorphous–to–(mixed-phase microcrystalline) transition [a→(a+μc)]. In the mixed-phase regime, preferential growth of the μc-Si:H phase occurs at the expense of the a-Si:H phase such that, as the thickness evolves, the μc-Si:H grains eventually cover the entire film surface. This leads to a crystallite coalescence process and a subsequent single-phase μc-Si:H growth regime. The coalescence process is described as a (mixed-phase)–to–(single-phase) microcrystalline transition [(a+μc)→μc] and is reflected in a peak and subsequent decrease of the surface roughness layer thickness d_s. By comparing the RTSE results with AFM results, it was found that the sensitivity of RTSE to the development of the μc-Si:H phase at the a→(a+μc) transition is ~0.5% – 1% in the fractional area coverage. A growth model was proposed to describe the evolution of the crystalline component in the mixed-phase growth regime. The application of this model to a number of RTSE data sets suggests that the μc-Si:H grains can be described as capped cones having a relatively constant cone angle under a wide range of deposition conditions. The observed large differences in the [a→(a+μc)] and [(a+μc)→μc] transition thicknesses under the different deposition conditions, however, reflect a large variation in the nucleation density of the crystalline grains. For the first time, an RTSE analysis method was developed based on a four-medium virtual interface analysis that can provide the continuous evolution in the volume fraction of the μc-Si:H phase in the mixed-phase growth regime.

The transitions separating the different regimes as identified by RTSE were applied to the development of extended phase diagrams. These diagrams describe the

different regimes of Si:H film growth as a function of the bulk layer thickness and the H_2-dilution ratio R = $[H_2]/[SiH_4]$. Phase diagrams were developed for rf PECVD of Si:H on different substrates using wide ranges in the H_2-dilution ratio R. It was shown that an a-Si:H substrate suppresses the development of the μc-Si:H phase by imposing its structure on the overdeposited Si:H film. In contrast, μc-Si:H films development is favored for Si:H deposited on μc-Si:H substrates. In this case, the crystalline network of the substrate is believed to propagate to the overdeposited film by local epitaxial growth. The implications of such a substrate dependence on a-Si:H intrinsic layer deposition in solar cells has been clarified.

Comparisons between the phase diagrams and solar cell results reveal that optimum solar cell performance and stability is obtained for i-layer depositions performed using maximum H_2-dilution but without crossing the a→(a+μc) transition for the desired i-layer thickness. Moreover, it was shown that for low R values, the thickness at which the amorphous roughening transition is observed is an indicator of the electronic quality of the film. The optimum film/device properties are obtained for films in which the amorphous roughening transition occurs at the maximum thickness so that the stable, smooth-surface regime is observed throughout growth of even very thick layers (d_b~4000 Å).

The phase diagrams were also applied in an investigation of the effects of the rf PECVD parameters on Si:H film growth in order to obtain insights into i-layer deposition processes at high rates. It was shown that increases in rf plasma power lead to detrimental effects on film growth, and that moderate increases in substrate temperature exert only a small reversal of the effects of high power. This situation results in part because the a→(a+μc) transition shifts weakly to lower R at higher temperature. In contrast, increases in total gas pressure exert a large influence on the phase diagram, in particular, a shift in the a→(a+μc) transition to much larger R. As a result, there exists a large window in R, whereby the films are amorphous and exhibit smooth, stable surfaces up to relatively large bulk layer thicknesses. Such behavior indicates high electronic quality for these materials.

Finally, in the second part of this thesis, a database for the optical properties of the different materials incorporated into a-Si:H-based multijunction solar cells was established. In most cases, the optical functions of the different materials were described in terms of simple analytical expressions based on a few wavelength-independent parameters that describe the physical mechanisms of absorption. In particular, new analytical expressions have been developed for the optical functions of amorphous semiconductor absorber layers and doped microcrystalline layers. It was shown that for a set of high-quality intrinsic a-Si:H films and their alloys with Ge and C, the optical functions over the visible range can be described by a single parameter, the optical band-gap as determined by conventional methods.

7.2 FUTURE WORK

Future work is proposed on all topics covered by this thesis. Some of the possible research approaches are enumerated as follows.

More extensive studies of the amorphous roughening transition, the amorphous-to-(mixed-phase microcrystalline) roughening transition, and the (mixed-phase)-to-(single-phase) microcrystalline smoothening transition are warranted. This requires extending advanced RTSE and AFM analysis methods to a larger set of depositions and applying a broader set of characterization techniques.

(1) The approach used in this study to characterize the evolution of the surface roughness in both the amorphous and mixed-phase growth regimes by a combination of RTSE and AFM measurements can be extended to Si:H films deposited under different conditions. In addition, the in-plane distribution of the surface roughness features can be assessed by calculating the power spectral density of the AFM images. This information can be used together with theoretical growth models to provide an improved an improved *quantitative* description of the microstructural evolution in the amorphous regime.

(2) The recently-developed virtual interface (VI) analysis, which has been for applied for the first time in this thesis research to characterize the evolution of the volume fraction of the crystalline component in mixed-phase (a+μc)-Si:H film growth, can be extended in a reanalysis of the full set of samples of Fig. 3.19. In this way, more accurate values of the cone angle and the nucleation density may result, which in turn may lead to a better agreement with the direct values from AFM and TEM.

(3) The further characterization of Si:H films by cross sectional transmission electron microscopy (TEM), together with RTSE and AFM studies, is expected to provide a more complete picture of the microstructural evolution associated with the amorphous–to–microcrystalline transition. A collaboration with researchers at the National Renewable Energy Laboratory was initiated recently, and selected Si:H films prepared at Penn State will soon be characterized by TEM.

The systematic description of Si:H growth by means of phase diagrams can be used to continue investigations of high rate Si:H deposition processes. Different methods for achieving high rates while keeping satisfactory electronic quality can be explored.

(4) It is expected that the build up of large polymeric particles in the plasma at high power levels and high gas pressures are detrimental to film growth. It may be possible to suppress these particles by using pulsed RF plasma excitation.

(5) Collaborative work has been initiated between the groups at Penn State and the Institute of Photovoltaics, at the Research Center in Juelich (Juelich, Germany) in order to investigate a-Si:H and μc-Si:H films deposited by vhf-PECVD (50–100MHz). Plasma excitation with frequencies higher than rf is known to yield higher deposition rates at lower plasma power levels.

The phase diagram approach can also be used to assist in the optimization of a-Si:H doped and alloy layers.

(6) A recent study has suggested that, contrary to common belief in the amorphous semiconductor research community, the highest solar cell performance is obtained with p-type window layers deposited in the protocrystalline regime. Furthermore, the addition of doping gases is known to affect the transitions from amorphous to mixed-phase Si:H film growth. Therefore, important insights into p-layer

optimization for solar cells can be expected with the development of phase diagrams for doped Si:H film growth using different H_2-dilution and doping gas ratios.

(7) One of the current bottlenecks in attempts to improve the performance of amorphous silicon-based multijunction solar cells is the low electronic quality of the intrinsic material in the bottom cell of the tandem or triple-junction solar cell. The development of phase diagrams as a function of the hydrogen–to–silane gas flow ratio $R=[H_2]/[SiH_4]$, as well as the germane–to–total gas flow ratio $G=[GeH_4]/\{[SiH_4]+[GeH_4]\}$, will be extremely useful for the further optimization of the tandem or triple-junction solar cell.

Many concepts for improvements in solar cell performance are expected with the further development of optical simulation programs at Penn State. Possible future developments in the optical modeling along with their applications are enumerated as follows.

(8) The optical database for intrinsic amorphous layers can be extended to include the possibility of determining the optical functions in terms of parameters such as the hydrogen concentration in the films in addition to the band gap parameter.

(9) The optical database can be extended for transparent conducting oxides through systematic characterization and analysis of the optical properties of a wider variety of samples.

(10) Comparisons between the measured quantum efficiencies of solar cells and the simulated counterparts are required in order to identify the mechanisms leading to optical losses in the actual devices.

(11) It is important to incorporate routines into the optical simulation program that can treat the effects of light scattering generated by macroscopically rough surface and interface layers (i.e., the effects of texture).

(12) Further applications of the optical simulation program are required in order to investigate effects of microscopically rough and macroscopically rough interfaces, with special attention devoted to the distinguishing characteristics associated with the two types of roughness.

Finally, it is important to emphasize that RTSE measurements of Si:H film deposition are performed currently in a single-chamber reactor. Because of cross-contamination problems, however, the highest quality solar cell structures cannot be deposited in this reactor. Therefore, major advances in the investigation of (deposition process)/(device property) relationships are expected with the attachment of a rotating-compensator multichannel ellipsometer to a multi-chamber deposition system.

APPENDIX

Kramers-Kronig Transformation for Amorphous and Microcrystalline Semiconductors

Here the Kramers-Kronig integration is described for deducing the real part of the dielectric function $\varepsilon_1(E)$ from the imaginary part $\varepsilon_2(E)$, the latter given by Eq. 6.1 for the case of one Lorentz oscillator. The result for multiple oscillators is obtained easily by generalizing the approach described here, i.e., adding the $\varepsilon_1(E)$ expressions obtained in the integration for each oscillator. The expression for $\varepsilon_1(E)$ can be split into three terms, the constant contribution $\varepsilon_{1\infty}$, the Urbach tail contribution, and the above-gap contribution, respectively:

$$\varepsilon_1(E) = \varepsilon_{1\infty} + I_U(E) + I_L(E)\,, \tag{A1}$$

$$I_U(E) = \frac{2E_1}{\pi} P \int_0^{E_T} \frac{\exp[(E'-E_T)/E_U]}{E'^2 - E^2} dE', \tag{A2}$$

$$I_L(E) = \frac{2}{\pi} P \int_{E_T}^{\infty} \frac{E' G(E') L(E')}{E'^2 - E^2} dE'. \tag{A3}$$

In Eq. A2, E_1 is defined so that $\varepsilon_2(E)$ is continuous at E_T; thus

$$E_1 = E_T\, G(E_T)\, L(E_T)\,. \tag{A4}$$

Starting from the simplest expression for the gap function G(E) given by Eqs. 6.4 or 6.6, it is considered $E_T \geq E_G$, allowing the possibility of an Urbach tail contribution. Substituting Eq. 6.6b into Eq. A3 and setting $I_{TL} = I_L$ yields,

$$I_{TL}(a_{iT}; i = 1, 2, 3; c_{0T}, d_{0T}) = \frac{2}{\pi} A E_0 \Gamma \Big[a_{3T}\left\{\gamma^2 I_{1T} - \ln[L_D(E_T)]^{1/4}\right\} + a_{2T}\left(I_{0AT} + I_{0BT}\right)$$

$$+ a_{1T} I_{1T} + a_{0T} \frac{\left(I_{0AT} - I_{0BT}\right)}{E_0{}^2} - c_{0T} \ln|E - E_T| - d_{0T} \ln\left(E + E_T\right)\Big] \tag{A5}$$

where

$$I_{1T} = \frac{1}{2\alpha\Gamma}\left[\pi - 2\tan^{-1}\left(2\frac{E_T{}^2 - \gamma^2}{\alpha\Gamma}\right)\right], \qquad (A6)$$

$$I_{0AT} = \frac{1}{2\Gamma}\left[\pi - \tan^{-1}\left(\frac{2E_T + \alpha}{\Gamma}\right) + \tan^{-1}\left(\frac{-2E_T + \alpha}{\Gamma}\right)\right], \qquad (A7)$$

$$I_{0BT} = \frac{1}{4\alpha}\ln\left(\frac{E_T{}^2 + E_0{}^2 + \alpha E_T}{E_T{}^2 + E_0{}^2 - \alpha E_T}\right), \qquad (A8)$$

and

$$\gamma = [E_0^2 - (\Gamma^2/2)]^{1/2}, \qquad (A9)$$

$$\alpha = (4E_0^2 - \Gamma^2)^{1/2}, \qquad (A10)$$

$$c_{0T} = \frac{EG_T(E)}{2L_D(E)}, \qquad (A11)$$

$$d_{0T} = \frac{-(E + E_G)^2}{2EL_D(E)}, \qquad (A12)$$

$$a_{3T} = -(c_{0T} + d_{0T}), \qquad (A13)$$

$$a_{2T} = -E(c_{0T} - d_{0T}), \qquad (A14)$$

$$a_{1T} = -(E^2 - 2\gamma^2)(c_{0T} + d_{0T}), \qquad (A15)$$

$$a_{0T} = 1 - E(E^2 - 2\gamma^2)(c_{0T} - d_{0T}), \qquad (A16)$$

$$L_D(E) = (E^2 - E_0{}^2)^2 + \Gamma^2 E^2. \qquad (A17)$$

Here, two possibilities are retained: (i) E_T=E_G, in which case I_U=0, or (ii) E_T>E_G, in which case $I_U(E)$ must be evaluated. In addition, the subscripts on the oscillator parameters (A_1,E_{01},Γ_1) are suppressed, since only one oscillator is being considered. Furthermore, the fully expanded form of the expression for $\varepsilon_1(E)$ is used, rather than the reduced version given by Jellison and Modine (Jellison and Modine, 1996). With this approach, it is easier to adapt the expressions when the form of G(E) in Eq. A3 is modified. For this reason, a functional description of I_{TL} is adopted in terms of the

energy dependent coefficients.

Proceeding to the case of amorphous semiconductors, substituting Eq 6.5b into Eq. A3 and setting $I_{CL} = I_L$ [where "C" designates Cody's form of G(E)] yields,

$$I_{CL} = I_{TL}(a_{iC}; i = 1, 2, 3; c_{0C}, d_{0C}) + \frac{2}{\pi} A E_0 \Gamma \left[b_{1c} \left\{ E_G I_{0C} - \ln[(E_T - E_G)^2 + E_P{}^2]^{1/2} \right\} + b_{0C} I_{0C} \right], \tag{A18}$$

$$I_{0C} = \frac{1}{E_P} \left[\frac{\pi}{2} - \tan^{-1}\left(\frac{E_T - E_G}{E_P} \right) \right], \tag{A19}$$

$$c_{0C} = \frac{E G_C(E)}{2 L_D(E)}, \tag{A20}$$

$$d_{0C} = \frac{-(E + E_G)^2}{2 L_D(E) \left[(E + E_G)^2 + E_P{}^2 \right]}, \tag{A21}$$

$$b_{0C} = Y^4 F^2 \frac{L_D(E) \left[E^{-1}(c_{0C} - d_{0C}) + 2 E_G K^2 Y^{-4} (c_{0C} + d_{0C}) \right] - 1}{(K^2 - F^2) F^2 Y^4 + E_0^4 Y^4 + 4 E_G^2 F^2 K^4}, \tag{A22}$$

$$b_{1C} = Y^{-4} \left[2 E_G K^2 b_{0C} - L_D(E)(c_{0C} + d_{0C}) \right], \tag{A23}$$

$$a_{3C} = -(b_{1C} + c_{0C} + d_{0C}), \tag{A24}$$

$$a_{2C} = -\left[b_{0C} + 2 E_G b_{1C} + E(c_{0C} - d_{0C}) \right], \tag{A25}$$

$$a_{1C} = -\left[2 E_G b_{0C} - (K^2 - F^2) b_{1C} + (E^2 - 2\gamma^2)(c_{0C} + d_{0C}) \right], \tag{A26}$$

$$a_{0C} = 1 + (K^2 - F^2) b_{0C} + 2 E_G K^2 b_{1C} - E(E^2 - 2\gamma^2)(c_{0C} - d_{0C}), \tag{A27}$$

$$F^2 = E_P{}^2 + E_G{}^2, \tag{A28}$$

$$K^2 = 2F^2 + 2\gamma^2 - 4 E_G{}^2, \tag{A29}$$

$$Y^4 = E_0{}^2 + F^2 (K^2 - F^2) - 4 E_G{}^2 K^2, \tag{A30}$$

The integration of the Urbach contribution (Eq. A2) results in

$$I_U(E) = \frac{E_1}{\pi E}\left\{\exp\left(\frac{E-E_T}{E_U}\right)\left[\mathrm{Ei}\left(\frac{E_T-E}{E_U}\right)-\mathrm{Ei}\left(-\frac{E}{E_U}\right)\right]- \exp\left(-\frac{E+E_T}{E_U}\right)\left[\mathrm{Ei}\left(\frac{E_T+E}{E_U}\right)-\mathrm{Ei}\left(\frac{E}{E_U}\right)\right]\right\}, \qquad \text{(A31)}$$

where Ei(x) designates the exponential integral defined by

$$\mathrm{Ei}(x) = \int_{-\infty}^{x} \frac{\exp t}{t}\,dt\,. \qquad \text{(A32)}$$

Algorithms for the numerical evaluation of this integral can be found in the literature (Spanier and Oldham, 1987) and are provided in numerical library packages such as IMSL [Visual Numerics Inc.]. The addition of the Urbach tail to the Tauc-Lorentz or Cody-Lorentz formulations introduces difficulties in the evaluation of the two Kramers-Kronig integrals of Eqs. A2 and A3. Ei(x) diverges when $x \to 0$ leading to apparent divergences when $E \to 0$ or $E \to E_T$. However, $E \to 0$ corresponds to photon energies outside the visible range and the divergence in $E \to E_T$ is counterbalanced by the logarithmic term accompanying the c_{0T} coefficient in the Eq. A5 for I_{TL}. Thus, any residual features due to the discontinuity of the higher derivatives of ε_2 with respect to energy are so weak to be inconsequential for the fitting of experimental data.

REFERENCES

Abelson, J. R., "Plasma deposition of hydrogenated amorphous-silicon - studies of the growth surface." *Appl. Phys. A* **56**, 493 (1993).

An, I., Nguyen, H. V., Nguyen, N. V., and Collins, R. W., "Microstructural evolution of ultrathin amorphous-silicon films by real-time spectroscopic ellipsometry." *Phys. Rev. Lett.* **65**, 2274 (1990).

An, I., and Collins, R. W., "Wave-form analysis with optical multichannel detectors - applications for rapid-scan spectroscopic ellipsometry." *Rev. Sci. Instrum.* **62**, 1904 (1991).

An, I. , Cong, Y., Nguyen, N. V., Pudliner, B. S., and Collins, R. W., "Instrumentation considerations in multichannel ellipsometry for real-time spectroscopy." *Thin Solid Films* **206**, 300 (1991a).

An, I., Li, Y. M., Wronski, C. R., Nguyen, H. V., and Collins, R. W., "In situ determination of dielectric functions and optical gap of ultrathin amorphous-silicon by real-time spectroscopic ellipsometry." *Appl. Phys. Lett.* **59**, 2543 (1991b).

An, I., Li, Y. M., Nguyen, H. V., and Collins, R. W., "Spectroscopic ellipsometry on the millisecond time scale for real-time investigations of thin-film and surface phenomena." *Rev. Sci. Instrum.* **63**, 3842 (1992).

Andújar, J. L., Bertran, E., Canillas, A., Roch, C., and Morenza, J. L., "Influence of pressure and radio frequency power on deposition rate and structural properties of hydrogenated amorphous silicon thin films prepared by plasma deposition." *J. Vac. Sci. Technol. A* **9**, 2216 (1991).

Ashcroft, N. W., and Sturm, K., "Interband absorption and the optical properties of polyvalent metals." *Phys. Rev. B* **3**, 1898 (1971).

Aspnes, D. E., "Alignment of an optically active biplate compensator." *Applied Optics* **10**, 2545 (1971).

Aspnes, D. E., Theeten, J. B., and Hottier, F., "Investigation of effective-medium models of microscopic surface roughness by spectroscopic ellipsometry." *Phys. Rev. B* **20**, 3292 (1979).

Aspnes, D. E., "Optical properties of thin films." *Thin Solid Films* **89**, 249 (1982).

Aspnes, D. E., Studna, A. A., and Kinsbron, E., "Dielectric properties of heavily doped crystalline and amorphous silicon from 1.5 to 6.0 eV." *Phys. Rev. B* **29**, 768 (1984).

Aspnes, D. E., "Minimal-data approaches for determining outer-layer dielectric responses of films from kinetic reflectometry and ellipsometric measurements." *J. Opt. Soc. Am. A* **10**, 974 (1993).

Azzam, R. M. A., and Bashara, N. M., *Ellipsometry and Polarized Light*. Amsterdam, North-Holland, 1977.

Bales, G. S., Redfield, A. C., and Zangwill, A., "Growth dynamics of chemical vapor-deposition." *Phys. Rev. Lett.* **62**, 776 (1989).

Beckmann, P., and Spizzichino, A., *The Scattering of Electromagnetic Waves from Rough Surfaces*. Oxford, Pergamon, 1963.

Bennett, M., Rajan, K., and Kritikson, K., "Amorphous silicon based solar cells deposited from H_2-diluted SiH_4 at low temperatures." *Conference Record of the 23rd IEEE Photovoltaic Specialists Conference*, 845 (1993).

Bruno, G., Capezzuto, P., and Madan, A. (Eds.), *Plasma Deposition Processes of Amorphous Silicon-Based Materials*. Boston, Academic Press, 1995.

Cabarrocas, P. R. I., Morin, P., Chu, V., Conde, J. P., Liu, J. Z., Park, H. R., and Wagner, S., "Optoelectronic properties of hydrogenated amorphous-silicon films deposited under negative substrate bias." *J. Appl. Phys.* **69**, 2942 (1991).

Cahan, B. D., and Spanier, R. F., "A high speed precision automatic ellipsometer." *Surf. Sci.* **16**, 166 (1969).

Carlson, D. E., and Wronski, C. R., "Amorphous silicon solar cells." *Appl. Phys. Lett.* **28**, 671 (1976).

Chittick, R. C., Alexander, J. H., and Sterling, H. F., "The preparation and properties of amorphous silicon." *J. Electrochem. Soc.* **116**, 77 (1969).

Cody, G. D., "The optical absorption edge of a-Si:H". In Pankove, J. I. (Ed.), *Semiconductors and Semimetals* (Vol. 21B, pp. 11). New York, Academic, 1984.

Collins, R. W., and Yang, B. Y., "In situ ellipsometry of thin-film deposition - implications for amorphous and microcrystalline Si growth." *J. Vac. Sci. Technol. B* **7**, 1155 (1989).

Collins, R. W., "Automatic rotating element ellipsometers - calibration, operation, and real-time applications." *Rev. Sci. Instrum.* **61**, 2029 (1990).

Collins, R. W., and Vedam, K., "Optical properties of solids". In Trigg, G. L. (Ed.), *Encyclopedia of Applied Physics* (Vol. 12, pp. 285). New York, VCH, 1995.

Collins, R. W., Koh, J., Ferlauto, A. S., Rovira, P. I., Lee, Y. H., Koval, R. J., and Wronski, C. R., "Real time analysis of amorphous and microcrystalline silicon film growth by multichannel ellipsometry." *Thin Solid Films* **364**, 129 (2000).

Collins, R. W., An, I., Lee, J., and Zapien, J. A., "Multichannel ellipsometry". In Tompkins, H. G. and Irene, E. A. (Eds.), *Handbook of Ellipsometry*. New York, Noyes, 2001.

Cotter, T. M., Thomas, M. E., and Tropf, W. J., "Magnesium fluoride". In Palik, E. D. (Ed.), *Handbook of Optical Constant of Solids II* (pp. 899). Boston, Academic Press, 1991.

Curtins, H., Wyrsch, N., Favre, M., and Shah, A. V., "Influence of plasma excitation-frequency for a-Si:H thin-film deposition." *Plasma Chem. Plasma Process.* **7**, 267 (1987).

Danesh, P., Pantchev, B., Grambole, D., and Schmidt, B., "Depth distribution of hydrogen and intrinsic stress in a-Si:H films prepared from hydrogen-diluted silane." *J. Appl. Phys.* **90**, 3065 (2001).

Dawson, R. M., Li, Y. M., Gunes, M., Heller, D., Nag, S., Collins, R. W., Wronski, C. R., and Bennett, M., "Optical properties of hydrogenated amorphous silicon, silicon-germanium and silicon-carbon thin films." *Mater. Res. Soc. Symp. Proc.* **258**, 595 (1992).

Doughty, D. A., Doyle, J. R., Lin, G. H., and Gallagher, A., "Surface-reaction probability of film-producing radicals in silane glow-discharges." *J. Appl. Phys.* **67**, 6220 (1990).

Family, F., and Vicsek, T., "Dynamic scaling of the interface in 2-phase viscous flows in porous-media." *J. Physics A* **24**, L25 (1985).

Family, F., and Vicsek, T. (Eds.), *Dynamics of Fractal Surfaces*. Singapore, World Scientific, 1991.

Fejfar, A., Mates, T., Koch, C., Rezek, B., Svrcek, V., Fojtik, P., Stuchlikova, H., Stuchlik, J., and Kocka, J., "Microscopic aspects of charge transport in hydrogenated microcrystalline silicon." *Mater. Res. Soc. Symp. Proc.* **664**, A16.1 (2001).

Ferlauto, A. S., Koh, J., Rovira, P. I., Wronski, C. R., and Collins, R. W., "Microcrystalline silicon tunnel junctions for amorphous silicon-based multijunction solar cells." *Mater. Res. Soc. Symp. Proc.* **557**, 579 (1999).

Ferlauto, A. S., Koh, J., Rovira, P. I., Wronski, C. R., Collins, R. W., and Ganguly, G., "Modeling the dielectric functions of silicon-based films in the amorphous, nanocrystalline and microcrystalline regimes." *J. Non-Cryst. Solids* **266-269**, 269 (2000a).

Ferlauto, A. S., Rovira, P. I., Koval, R. J., Wronski, C. R., and Collins, R. W., "Study of the amorphous-to-microcrystalline transition during silicon film growth at increased rates: Extensions of the evolutionary phase diagram." *Mater. Res. Soc. Symp. Proc.* **609**, A2.2 (2000b).

Ferlauto, A. S., Ferreira, G. M., Chen, C., Rovira, P. I., Wronski, C. R., Collins, R. W., Deng, X., and Ganguly, G., "Optical metrology for the next generation of a-Si:H-based thin film photovoltaics". In McConnell, R. and Kapur, V. (Eds.), *Photovoltaics Beyond the 21st Century* (Vol. 2001-10, pp. 199). Pennington NJ, Electrochemical Society, 2001.

Ferreira, G. M., Ferlauto, A. S., Rovira, P. I., Chen, C., Nguyen, H. V., Wronski, C. R., and Collins, R. W., "Optical simulations of the effects of transparent conducting oxide interface layers on amorphous silicon solar cell performance." *Mater. Res. Soc. Symp. Proc.* **664**, A24.6 (2001).

Flavin, C., and Dunn, S., "Reiventing the energy system". In Brown, L. R., Flavin, C. and French, H. F. (Eds.), *State of the World 1999: A Worldwatch Institute Report on Progress Toward a Sustainable Society* (pp. 23). New York, W. W. Norton, 1999.

Flewitt, A. J., Robertson, J., and Milne, W. I., "Growth mechanism of hydrogenated amorphous silicon studied by *in situ* scanning tunneling microscopy." *J. Appl. Phys.* **85**, 8032 (1999).

Fujiwara, H., Koh, J., Wronski, C. R., and Collins, R. W., "Application of real time spectroscopic ellipsometry for high resolution depth profiling of compositionally graded amorphous silicon alloy thin films." *Appl. Phys. Lett.* **70**, 2150 (1997).

Fujiwara, H., Koh, J., Wronski, C. R., Collins, R. W., and Burnham, J. S., "Parameterization of the optical functions of a-$Si_{1-x}C_x$:H: Applications to C depth-profiling and surface temperature monitoring in solar cell preparation." *J. Non-Cryst. Solids* **230**, 460 (1998).

Fujiwara, H., Koh, J., Wronski, C. R., and Collins, R. W., "Analysis of contamination, hydrogen emission, and surface temperature variations using real time spectroscopic ellipsometry during p/i interface formation in amorphous silicon p-i-n solar cells." *Appl. Phys. Lett.* **74**, 3687 (1999a).

Fujiwara, H., Toyoshima, Y., Kondo, M., and Matsuda, A., "Interface-layer formation mechanism in a-Si:H thin-film growth studied by real-time spectroscopic ellipsometry and infrared spectroscopy." *Phys. Rev. B* **60**, 13598 (1999b).

Fujiwara, H., Koh, J., Rovira, P. I., and Collins, R. W., "Assessment of effective-medium theories in the analysis of nucleation and microscopic surface roughness evolution for semiconductor thin films." *Phys. Rev. B* **61**, 10832 (2000a).

Fujiwara, H., Toyoshima, Y., Kondo, M., and Matsuda, A., "Nucleation mechanism of microcrystalline silicon studied by real time spectroscopic ellipsometry and infrared spectroscopy." *Mater. Res. Symp. Soc. Proc.* **609**, A2.1 (2000b).

Fujiwara, H., Kondo, M., and Matsuda, A., "Effect of strained Si-Si bonds in amorphous silicon incubation layer on microcrystalline silicon nucleation." *Mater. Res. Soc Symp. Proc.* **664**, A1.2 (2001a).

Fujiwara, H., Kondo, M., and Matsuda, A., "Real-time spectroscopic ellipsometry studies of the nucleation and grain growth processes in microcrystalline silicon thin films." *Phys. Rev. B* **63**, 115306 (2001b).

Gallagher, A., "Neutral radical deposition from silane discharges." *J. Appl. Phys.* **63**, 2406 (1988).

Ganguly, G., and Matsuda, A., "Defect formation during growth of hydrogenated amorphous-silicon." *Phys. Rev. B* **47**, 3661 (1993).

Ganguly, G., and Matsuda, A., "A new deposition parameter to control the carrier drift mobility in a-Si:H." *J. Non-Cryst. Solids* **198-200**, 1003 (1996).

Griffith, J. E., and Grigg, D. A., "Dimensional metrology with scanning probe microscopes." *J. Appl. Phys.* **74**, R83 (1993).

Guha, S., Narasimhan, K. L., and Pietruszko, S. M., "On light-induced effects in hydrogenated amorphous silicon." *J. Appl. Phys.* **52**, 859 (1981).

Guha, S., Xu, X., Yang, J., and Banerjee, A., "High deposition rate amorphous silicon-based multijunction solar-cell." *Appl. Phys. Lett.* **66**, 595 (1995).

Guha, S., Yang, J., Williamson, D. L., Lubianiker, Y., Cohen, J. D., and Mahan, A. H., "Structural, defect, and device behavior of hydrogenated amorphous Si near and above the onset of microcrystallinity." *Appl. Phys. Lett.* **74**, 1860 (1999).

Guha, S., Yang, J., and Banerjee, A., "Amorphous silicon alloy photovoltaic research - present and future." *Prog. Photovoltaics* **8**, 141 (2000).

Guo, L., Kondo, M., Fukawa, M., Saitoh, K., and Matsuda, A., "High rate deposition of microcrystalline silicon using conventional plasma-enhanced chemical vapor deposition." *Jap. J. App. Phys.* **37**, L1116 (1998).

Guo, L., and Lin, R., "Studies on the formation of microcrystalline silicon with PECVD under low and high working pressure." *Thin Solid Films* **376**, 249 (2000).

Hecht, E., *Optics*. Reading, Addison-Wesley, 1987.

Herion, J., "Scanning tunneling microscopy of hydrogenated amorphous silicon: High-resolution topography and local apparent barrier heights." *Appl. Surf. Sci.* **151**, 73 (1999).

Hishikawa, Y., "Raman-study on the variation of the silicon network of a-Si-H." *J. Appl. Phys.* **62**, 3150 (1987).

Houben, L., Luysberg, M., Hapke, P., Carius, R., Finger, F., and Wagner, H., "Structural properties of microcrystalline silicon in the transition from highly crystalline to amorphous growth." *Phil. Mag. A* **77**, 1447 (1998).

Ikuta, K., Tanaka, K., Yamasaki, S., Miki, K., and Matsuda, A., "Nucleation and coalescence in hydrogenated amorphous silicon studied by scanning tunneling microscopy." *Appl. Phys. Lett.* **65**, 1760 (1994).

Ikuta, K., Toyoshima, Y., Yamasaki, S., Matsuda, A., and Tanaka, K., "STM observation on the initial growth of amorphous and microcrystalline silicon films." *Mater. Res. Soc. Symp. Proc.* **420**, 413 (1996).

Jellison, G. E., and Modine, F. A., "Parameterization of the optical functions of amorphous materials in the interband region." *Appl. Phys. Lett.* **69**, 371 (1996).

Jellison, G. E., "Spectroscopic ellipsometry data analysis: Measured versus calculated quantities." *Thin Solid Films* **313**, 33 (1998).

Jellison, G. E., and Boatner, L. A., "Optical functions of uniaxial ZnO determined by generalized ellipsometry." *Phys. Rev. B* **58**, 3586 (1998).

Jiao, L., Chen, I., Collins, R. W., Wronski, C. R., and Hata, N., "An improved analysis for band edge optical absorption spectra in hydrogenated amorphous silicon from optical and photoconductivity measurements." *Appl. Phys. Lett.* **72**, 1057 (1998).

Jin, Z. C., Hamberg, I., and Granqvist, C. G., "Optical-properties of sputter-deposited ZnO-al thin-films." *J. Appl. Phys.* **64**, 5117 (1988).

Kamei, T., Stradins, P., and Matsuda, A., "Effects of embedded crystallites in amorphous silicon on light-induced defect creation." *Appl. Phys. Lett.* **74**, 1707 (1999).

Kanicki, J. (Ed.), *Amorphous and Microcrystalline Semiconductor Devices: Optoelectronic Devices*. Boston, Artech House, 1991.

Kardar, M., Parisi, G., and Zhang, Y.-C., "Dynamic scaling of growing interfaces." *Phys. Rev. Lett.* **56**, 889 (1986).

Kardar, M., "Roughness and ordering of growing films." *Physica A* **281**, 295 (2000).

Kessels, W. M. M., Severens, R. J., Smets, A. H. M., Korevaar, B. A., Adriaenssens, G. J., Schram, D. C., and van de Sanden, M. C. M., "Hydrogenated amorphous silicon deposited at very high growth rates by an expanding Ar-H_2-SiH_4 plasma." *J. Appl. Phys.* **89**, 2404 (2001).

Kim, S., and Collins, R. W., "Optical characterization of continuous compositional gradients in thin-films by real-time spectroscopic ellipsometry." *Appl. Phys. Lett.* **67**, 3010 (1995).

Kim, S., Burnham, J. S., Koh, J., Jiao, L. H., Wronski, C. R., and Collins, R. W., "Real time spectroellipsometry characterization of optical gap profiles in compositionally-graded semiconductor structures: Applications to bandgap engineering in amorphous silicon-carbon alloy solar cells." *J. Appl. Phys.* **80**, 2420 (1996).

Koh, J., Lu, Y. W., Kim, S., Burnham, J. S., Wronski, C. R., and Collins, R. W., "Real-time spectroscopic ellipsometry study of hydrogenated amorphous-silicon p-i-n solar-cells - characterization of microstructural evolution and optical gaps." *Appl. Phys. Lett.* **67**, 2669 (1995).

Koh, J., Lu, Y. W., Wronski, C. R., Kuang, Y. L., Collins, R. W., Tsong, T. T., and Strausser, Y. E., "Correlation of real time spectroellipsometry and atomic force microscopy measurements of surface roughness on amorphous semiconductor thin films." *Appl. Phys. Lett.* **69**, 1297 (1996).

Koh, J., Lee, Y., Fujiwara, H., Wronski, C. R., and Collins, R. W., "Optimization of hydrogenated amorphous silicon p-i-n solar cells with two-step i layers guided by real-time spectroscopic ellipsometry." *Appl. Phys. Lett.* **73**, 1526 (1998).

Koh, J., Ferlauto, A. S., Rovira, P. I., Wronski, C. R., and Collins, R. W., "Evolutionary phase diagrams for plasma-enhanced chemical vapor deposition of silicon thin films from hydrogen-diluted silane." *Appl. Phys. Lett.* **75**, 2286 (1999a).

Koh, J., Fujiwara, H., Koval, R. J., Wronski, C. R., and Collins, R. W., "Real time spectroscopic ellipsometry studies of the nucleation and growth of p-type microcrystalline silicon films on amorphous silicon using B_2H_6, $B(CH_3)_3$, and BF_3 dopant source gases." *J. Appl. Phys.* **85**, 4141 (1999b).

Kondo, M., Fukawa, M., Guo, L., and Matsuda, A., "High rate growth of microcrystalline silicon at low temperatures." *J. Non-Cryst. Solids* **266-269**, 84 (2000).

Koval, R. J., *Microstructurally Engineered Improvements in the Performance and Stability of Si:H based Thin Film Solar Cells*, Ph.D. thesis, The Pennsylvania State University, University Park, 2001.

Koval, R. J., Pearce, J. M., Ferlauto, A. S., Collins, R. W., and Wronski, C. R., "Evolution of the mobility gap with thickness in hydrogen-diluted intrinsic Si:H materials in the phase transition region and its effect on p-i-n solar cell characteristics." *Mater. Res. Soc. Symp. Proc.* **664**, A16.4 (2001).

Kroll, U., Meier, J., Shah, A., Mikhailov, S., and Weber, J., "Hydrogen in amorphous and microcrystalline silicon films prepared by hydrogen dilution." *J. Appl. Phys.* **80**, 4971 (1996).

Lee, J., Rovira, P. I., An, I., and Collins, R. W., "Rotating-compensator multichannel ellipsometry: Applications for real time stokes vector spectroscopy of thin film growth." *Rev. Sci. Instrum.* **69**, 1800 (1998a).

Lee, J., Rovira, P. I., An, I., and Collins, R. W., "Rotating-compensator multichannel ellipsometry for characterization of the evolution of nonuniformities in diamond thin-film growth." *Appl. Phys. Lett.* **72**, 900 (1998b).

Lee, J., Rovira, P. I., An, I., and Collins, R. W., "Alignment and calibration of the MgF_2 biplate compensator for applications in rotating-compensator multichannel ellipsometry." *J. Opt. Soc. Am. A* **18**, 1980 (2001).

Lee, Y.-H., Jiao, L.-H., Liu, H.-Y., Lu, Z., Collins, R., and Wronski, C. R., "Stability of a-Si:H solar cells and corresponding intrinsic materials fabricated using hydrogen diluted silane." *Conference Record of the 25th IEEE Photovoltaic Specialists Conference*, 1165 (1996).

Li, Y. M., An, I., Nguyen, H. V., Wronski, C. R., and Collins, R. W., "Thin-film coalescence in hydrogenated amorphous-silicon probed by spectroscopic ellipsometry with millisecond-scale resolution." *Phys. Rev. Lett.* **68**, 2814 (1992).

Lu, Y., An, I. , Gunes, M., Wakagi, M., Wronski, C. R., and Collins, R. W., "Nucleation and growth of hydrogenated amorphous silicon-carbon alloys - effect of hydrogen dilution in plasma-enhanced chemical vapor deposition." *Appl. Phys. Lett.* **63**, 2228 (1993).

Lu, Y., Kim, S., Gunes, M., Lee, Y., Wronski, C. R., and Collins, R. W., "Process-property relationships for a-$Si_{1-x}C_x$:H deposition: Excursions in parameter space guided by real time spectroellipsometry." *Mater. Res. Soc. Symp. Proc.* **336**, 595 (1994).

Lucovsky, G., Nemanich, R. J., and Knights, J. C., "Structural interpretation of the vibrational spectra of a-Si:H alloys." *Phys. Rev. B* **19**, 2064 (1979).

Luft, W., and Tsuo, S., *Hydrogenated Amorphous Silicon Deposition Processes*. New York, Marcel Dekker, 1993.

Maeda, K., Kuroe, A., and Umezu, I., "Mechanism of surface-reaction in the deposition process of a-Si:H by rf glow-discharge." *Phys. Rev. B* **51**, 10635 (1995).

Mahan, A. H., Carapella, J., Nelson, B. P., Crandall, R. S., and Balberg, I., "Deposition of device quality, low H content amorphous-silicon." *J. Appl. Phys.* **69**, 6728 (1991).

Marra, D. C., Edelberg, E. A., Naone, R. L., and Aydil, E. S., "Silicon hydride composition of plasma-deposited hydrogenated amorphous and nanocrystalline silicon films and surfaces." *J. Vac. Sci. Technol. A* **16**, 3199 (1998).

Matsuda, A., and Tanaka, K., "Investigation of the growth-kinetics of glow-discharge hydrogenated amorphous-silicon using a radical separation technique." *J. Appl. Phys.* **60**, 2351 (1986).

Matsuda, A., and Tanaka, K., "Guiding principle for preparing highly photosensitive Si-based amorphous-alloys." *J. Non-Cryst. Solids* **97-98**, 1367 (1987).

Matsuda, A., and Goto, T., "Role of surface and growth-zone reactions in the formation process of μc-Si:H." *Mater. Res. Soc. Symp. Proc.* **164**, 3 (1990).

Matsuda, A., Nomoto, K., Takeuchi, Y., Suzuki, A., Yuuki, A., and Perrin, J., "Temperature-dependence of the sticking and loss probabilities of silyl radicals on hydrogenated amorphous-silicon." *Surf. Sci.* **227**, 50 (1990).

Matsuda, A., "Plasma and surface reactions for obtaining low defect density amorphous silicon at high growth rates." *J. Vac. Sci. Technol. A* **16**, 365 (1998).

Matsuda, A., "Growth mechanism of microcrystalline silicon obtained from reactive plasmas." *Thin Solid Films* **337**, 1 (1999).

Maycock, P., "Happy new millennium." *PV News* **1** (2000).

Mazor, A., Srolovitz, D. J., Hagan, P. S., and Bukiet, B. G., "Columnar growth in thin-films." *Phys. Rev. Lett.* **60**, 424 (1988).

Messier, R., Giri, A. P., and Roy, R. A., "Revised structure zone model for thin film physical structure." *J. Vac. Sci. Technol. A* **2**, 500 (1984).

Messier, R., Yehoda, J. E., and Pilione, L. J., "Ion-surface interactions: General understandings". In Rossnagel, S. M., Cuomo, J. J. and Westwood, W. D. (Eds.), *Handbook of Plasma Processing Technology* (pp. 448). Park Ridge NJ, Noyes, 1990.

Nguyen, H. V., An, I., and Collins, R. W., "Evolution of the optical functions of aluminum films during nucleation and growth determined by real-time spectroscopic ellipsometry." *Phys. Rev. Lett.* **68**, 994 (1992).

Nguyen, H. V., An, I., and Collins, R. W., "Evolution of the optical functions of thin-film aluminum - a real-time spectroscopic ellipsometry study." *Phys. Rev. B* **47**, 3947 (1993).

Nguyen, H. V., and Collins, R. W., "Finite-size effects on the optical functions of silicon microcrystallites - a real-time spectroscopic ellipsometry study." *Phys. Rev. B* **47**, 1911 (1993).

Okamoto, S., Hishikawa, Y., and Tsuda, S., "New interpretation of the effect of hydrogen dilution of silane on glow-discharged hydrogenated amorphous silicon for stable solar cells." *Jpn. J. Appl. Phys. Part 1* **35**, 26 (1996).

Osborne, I. S., Hata, N., and Matsuda, A., "Steady state defect density and annealing kinectics of light-induced defects in a-Si:H deposited from 'new' deposition techniques." *J. Non-Cryst. Solids* **198-200**, 991 (1996).

Oversluizen, G., and Lodders, W. H. M., "Optimization of plasma-enhanced chemical vapor deposition of hydrogenated amorphous silicon." *J. Appl. Phys.* **83**, 8002 (1998).

Palik, E. D., *Handbook of Optical Constants of Solids.* Academic, New York, 1985.

Palmer, B. J., and Gordon, R. G., "Local equilibrium-model of morphological instabilities in chemical vapor-deposition." *Thin Solid Films* **158**, 313 (1988).

Perrin, J., Cabarrocas, P. R. I., Allain, B., and Friedt, J., "A-Si:H deposition from SiH_4 and Si_2H_6 discharges: Pressure and temperature dependence of film growth in relation to α-γ discharge transition." *Jap. J. App. Phys.* **27**, 2041 (1988).

Perrin, J., Takeda, Y., Hirano, N., Takeuchi, Y., and Matsuda, A., "Sticking and recombination of the SiH_3 radical on hydrogenated amorphous-silicon - the catalytic effect of diborane." *Surf. Sci.* **210**, 114 (1989).

Perrin, J., "Reactor design for a-Si:H deposition". In Bruno, G., Capezzuto, P. and Madan, A. (Eds.), *Plasma Deposition of Amorphous Silicon-Based Materials* (pp. 177). Boston, Academic Press, 1995.

Perrin, J., Shiratani, M., Kae-Nune, P., Videlot, H., Jolly, J., and Guillon, J., "Surface reaction probabilities and kinetics of H, SiH_3, Si_2H_5, CH_3, and C_2H_5 during deposition of a-Si:H and a-C:H from H_2, SiH_4, and CH_2 discharges." *J. Vac. Sci. Technol. A* **16**, 278 (1998).

Rech, B., Wieder, S., Siebke, F., Beneking, C., and Wagner, H., "Material basis of highly stable a-Si:H solar cells." *Mater. Res. Soc. Symp. Proc.* **420**, 33 (1996).

Rech, B., Roschek, T., Muller, J., Wieder, S., and Wagner, H., "Amorphous and microcrystalline silicon solar cells prepared at high deposition rates using rf (13.56 MHz) plasma excitation frequencies." *Solar Energy Materials and Solar Cells* **66**, 267 (2001).

Robertson, J., "Deposition mechanism of hydrogenated amorphous silicon." *J. Appl. Phys.* **87**, 2608 (2000a).

Robertson, J., "Growth mechanism of hydrogenated amorphous silicon." *J. Non-Cryst. Solids* **266**, 79 (2000b).

Roschek, T., Repmann, T., Muller, J., Rech, B., and Wagner, H., "High rate deposition of microcrystalline silicon solar cells using 13.56 MHz PECVD." *Conference Record of the 28th IEEE Photovoltaic Specialists Conference*, 150 (2000).

Ross, C., Herion, J., and Wagner, H., "Nucleation and growth analysis of microcrystalline silicon by scanning probe microscopy: Substrate dependence, local structure and electronic properties of as-grown surfaces." *J. Non-Cryst. Solids* **266-269**, 69 (2000).

Rovira, P. I., Ferlauto, A. S., An, I., Fujiwara, H., Koh, J., Koval, R. J., Wronski, C. R., and Collins, R. W., "Real time optics of amorphous silicon solar cell fabrication on textured tin-oxide-coated glass." *Mater. Res. Soc. Symp. Proc.* **557**, 719 (1999).

Rovira, P. I., *Real Time Stokes Vector Spectroscopy and its Applications to the Characterization of Inhomogeneus Thin Films*, Ph.D. thesis, The Pennsylvania State University, University Park, 2000.

Rovira, P. I., Ferlauto, A. S., Koh, J., Wronski, C. R., and Collins, R. W., "Optics of textured amorphous silicon surfaces." *J. Non-Cryst. Solids* **266**, 279 (2000a).

Rovira, P. I., Ferlauto, A. S., Koval, R. J., Wronski, C. R., Collins, R. W., and Ganguly, G., "Real time optics of p-type microcrystalline silicon deposition on specular and textured ZnO-coated glass." *Mater. Res. Soc. Symp. Proc.* **609**, A19.6 (2000b).

Schropp, R. E. I., and Zeman, M., *Amorphous and Microcrystalline Silicon Solar Cells: Modeling, Materials and Device Technology.* Boston, Kluwer, 1998.

Shah, A., Torres, P., Tscharner, R., Wyrsch, N., and Keppner, H., "Photovoltaic technology: The case for thin-film solar cells." *Science* **285**, 692 (1999).

Shiles, E., Sasaki, T., Inokuti, M., and Smith, D. Y., "Self-consistency and sum-rule tests in the Kramers-Kronig analysis of optical data: Applications to aluminum." *Phys. Rev. B* **22**, 1612 (1980).

Shirai, H., Das, D., Hanna, J., and Shimizu, I., "A novel preparation technique for preparing hydrogenated amorphous-silicon with a more rigid and stable Si network." *Appl. Phys. Lett.* **59**, 1096 (1991).

Smets, A. H. M., Schram, D. C., and van den Sanden, M. C. M., "Surface roughness evolution of a-Si:H growth and its relation to the growth mechanism." *Mater. Res. Soc. Symp. Proc.* **609**, A7.6.1 (2000).

Sopori, B., Madjdpour, J., Zhang, Y., Chen, W., Guha, S., Yang, J., Banerjee, A., and Hegedus, S., "Optical modeling of a-Si solar cells." *Mater. Res. Soc. Symp. Proc.* **557**, 755 (1999).

Spanier J. and Oldham, K. B. *An Atlas of Functions*, New York, Hemisphere, 1987

Spear, W. E., and LeComber, P. G., "Substitutional doping of amorphous silicon." *Solid State Commun.* **17**, 1193 (1975).

Staebler, D. L., and Wronski, C. R., "Reversible conductivity changes in discharge-produced amorphous Si." *Appl. Phys. Lett.* **31**, 292 (1977).

Street, R. A., *Hydrogenated Amorphous Silicon*. Cambridge, Cambridge University Press, 1991.

Takagi, T., Hayashi, R., Ganguly, G., Kondo, M., and Matsuda, A., "Gas-phase diagnosis and high-rate growth of stable a-Si:H." *Thin Solid Films* **345**, 75 (1999).

Takai, M., Nishimoto, T., Takagi, T., Kondo, M., and Matsuda, A., "Guiding principles for obtaining stabilized amorphous silicon at larger growth rates." *J. Non-Cryst. Solids* **266**, 90 (2000).

Tanaka, K. (Ed.), *Glow-discharge Hydrogenated Amorphous Silicon.* Boston, Kluwer, 1989.

Tanenbaum, D. M., Laracuente, A. L., and Gallagher, A., "Surface roughening during plasma-enhanced chemical-vapor deposition of hydrogenated amorphous silicon on crystal silicon substrates." *Phys. Rev. B* **56**, 4243 (1997).

Terakawa, A., and Matsunami, K., "Hydrogen elimination model of the formation of hydrogen bonding structures during the growth of hydrogenated amorphous silicon by plasma CVD." *Phys. Rev. B* **62**, 16808 (2000).

Thiart, J. J., Hlavacek, V., and Viljoen, H. J., "Chemical vapor deposition and morphology problems." *Thin Solid Films* **365**, 275 (2000).

Toyoshima, Y., Arai, K., Matsuda, A., and Tanaka, K., "In situ characterization of the growing a-Si:H surface by IR spectroscopy." *J. Non-Cryst. Solids* **137**, 765 (1991).

Tsai, C. C., Knights, J. C., Chang, G., and Wacker, B., "Film formation mechanisms in the plasma deposition of hydrogenated amorphous-silicon." *J. Appl. Phys.* **59**, 2998 (1986).

Tsai, C. C., "Plasma deposition of amorphous and crystalline silicon: The effect of hydrogen on the growth structure, and electronic properties". In Fritzsche, H. (Ed.), *Advances in Disordered Semiconductors* (Vol. 1, pp. 123). Singapore, World Scientific, 1989.

Tsai, C. C., Anderson, G. B., and Thompson, R., "Low-temperature growth of epitaxial and amorphous-silicon in a hydrogen-diluted silane plasma." *J. Non-Cryst. Solids* **137**, 673 (1991).

Tsu, D. V., Chao, B. S., Ovshinsky, S. R., Guha, S., and Yang, J., "Effect of hydrogen dilution on the structure of amorphous silicon alloys." *Appl. Phys. Lett.* **71**, 1317 (1997).

Vallat-Sauvain, E., Kroll, U., Meier, J., Wyrsch, N., and Shah, A., "Microstructure and surface roughness of microcrystalline silicon prepared by very high frequency-glow discharge using hydrogen dilution." *J. Non-Cryst. Solids* **266-269**, 125 (2000).

Vedam, K., "Spectroscopic ellipsometry: A historical overview." *Thin Solid Films* **313-314**, 1 (1998).

Vetterl, O., Finger, F., Carius, R., Hapke, P., Houben, L., Kluth, O., Lambertz, A., Muck, A., Rech, B., and Wagner, H., "Intrinsic microcrystalline silicon: A new material for photovoltaics." *Solar Energy Materials and Solar Cells* **62**, 97 (2000).

Williams, R. S., Tong, W. M., and Ngo, T. T., "Film growth: Control of surface morphology from monodisperse nanoparticles through fractals to flat epitaxial heterostructures." *Mater. Res. Soc. Symp. Proc.* **367**, 273 (1995).

Wilson, W. L., Szajowski, P. F., and Brus, L. E., "Quantum confinement in size-selected, surface-oxidized silicon nanocrystals." *Science* **262**, 1242 (1993).

Wooten, F., *Optical properties of solids*. New York, Academic Press, 1972.

Yang, H.-N., Wang, G.-C., and Lu, T.-M., *Diffraction from Rough Surfaces and Dynamic Growth Fronts*, Singapore, World Scientific, 1993.

Yang, J., Xu, X., and Guha, S., "Stability studies of hydrogenated amorphous silicon alloy solar cells prepared with hydrogen dilution." *Mater. Res. Soc. Symp. Proc.* **336**, 687 (1994).

Yang, J., Banerjee, A., and Guha, S., "Triple-junction amorphous silicon alloy solar cell with 14.6% initial and 13.0% stable conversion efficiencies." *Appl. Phys. Lett.* **70**, 2975 (1997).

Yang, L., and Chen, L. F., "The effect of H_2-dilution on the stability of a-Si:H based solar cells." *Mater. Res. Soc. Symp. Proc.* **336**, 669 (1994).

Zapien, J. A., Collins, R. W., and Messier, R., "Multichannel ellipsometer for real time spectroscopy of thin film deposition from 1.5 to 6.5 eV." *Rev. Sci. Instrum.* **71**, 3451 (2000).

VITA

Andre Santarosa Ferlauto was born in São Paulo, Brazil, on October 9, 1972. He entered the University of São Paulo in 1990 and received a Bachelor of Science degree in Physics in 1993. In 1994, he began his graduate studies, concentrating his research in scanning tunneling microscopy of semiconductor thin films. He received a Master of Science degree in Solid State Physics in 1996 from the University of São Paulo. In the Summer of 1997, Andre came to The Pennsylvania State University and began his Ph. D. studies. He worked as a research assistant at the Electrical Engineering Department, at the Materials Research Laboratory and Center for Thin Film Devices.